UNIVERSITÀ DEGLI STUDI DI GENOVA

DOCTORAL THESIS

Inverse Problems in data-driven multi-scale Systems Medicine: application to cancer physiology

Author:
Mara SCUSSOLINI

Supervisors:
Prof. Dr. Michele PIANA
Prof. Giacomo CAVIGLIA

A Thesis submitted in fulfillment of the requirements for the degree of Doctor of Philosophy

in

Mathematics and Applications

Dipartimento di Matematica

December 20, 2018

"I give myself very good advice, but I very seldom follow it."

Alice *(Alice in Wonderland)*

Declaration of Authorship

I, Mara SCUSSOLINI, declare that this Thesis, titled "Inverse Problems in data-driven multi-scale Systems Medicine: application to cancer physiology", and the work presented in it are my own. I confirm that:

- This work was done wholly or mainly while in candidature for a research degree at this University.
- Where any part of this Thesis has previously been submitted for a degree or any other qualification at this University or any other institution, this has been clearly stated.
- Where I have consulted the published work of others, this is always clearly attributed.
- Where I have quoted from the work of others, the source is always given. With the exception of such quotations, this Thesis is entirely my own work.
- I have acknowledged all main sources of help.

Date:

December 20, 2018

Signed:

Mara Scussolini

Dissemination Achievements

Papers

Dorraji E., Oteiza A., Kuttner S., Martin-Armas M., Kanapathippillai P., Garbarino S., Kalda G., Scussolini M., Figenschau S.L., Piana M., Fenton K.A. (2018). "PET and SPECT imaging of Tertiary Lymphoid Structures (TLS) during the development of Lupus nephritis". In: *Journal of Nuclear Medicine* (submitted).

Scussolini M., Bauckneht M., Cossu V., Bruno S., Orengo A.M., Piccioli P., Capitanio S., Yosifov N., Ravera S., Morbelli S., Piana M., Sambuceti G., Caviglia G., and Marini C. (2018). "G6Pase location in the endoplasmic reticulum: Implications on compartmental analysis of FDG uptake in cancer cells". In: *Scientific Reports* (accepted for publication).

Scussolini M., Cossu V., Marini C., Sambuceti G., and Caviglia G. (2018). "FDG kinetics in cells and tissues: a biochemically-driven compartmental approach". In: *arXiv.org* q-bio.arXiv:1803.05025v1. URL: `https://arxiv.org/abs/1803.05025v1`

Principi E., Buschiazzo A., Papait A., Castagnola P., Costa D., Pece R., Maric I., Scussolini M., Marini C., Sambuceti G., Strollo F., and Tavella S. (2018). "Anthropometric and glucometabolic changes in an aged mouse model of lipocalin-2 overexpression". In: *International Journal of Obesity*. DOI: 10.1038/s41366-018-0171-5

Scussolini M., Garbarino S., Piana M., Sambuceti G., and Caviglia G. (2018). "Reference Tissue Models for FDG–PET Data: Identifiability and Solvability". In: *IEEE Transactions on Radiation and Plasma Medical Sciences* 2.3, pp. 177–186. DOI: 10.1109/TRPMS.2018.2801029

Scussolini M., Garbarino S., Sambuceti G., Caviglia G., and Piana M. (2017). "A physiology-based parametric imaging method for FDG–PET data". In: *Inverse Problems* 33.12, p. 125010. DOI: 10.1088/1361-6420/aa9544

Talks at international meetings

Scussolini M., Caviglia G., Piana M. (2018). "Inverse Problems in multiscale Systems Medicine: applications in oncology". *SIMAI 2018 - Italian Society of Applied and Industrial Mathematics*, Rome, Italy.

Poster presentations

Scussolini M., Garbarino S., Sambuceti G., Piana M., Buschiazzo A., Bauckneht M., Marini C., Caviglia G. (2017). "A Full Reference Tissue Model with Non-Vanishing Blood Volume Fractions for Kinetic Analysis of Dynamic FDG-PET Data". *EANM'17 - 30th Annual Congress of the European Association of Nuclear Medicine*, Vienna, Austria.

UNIVERSITÀ DEGLI STUDI DI GENOVA

Abstract

Ph.D. in Mathematics and Applications
Dipartimento di Matematica

Doctor of Philosophy

Inverse Problems in data-driven multi-scale Systems Medicine: application to cancer physiology

by Mara SCUSSOLINI

Systems Medicine is an interdisciplinary framework involving reciprocal feedback between clinical investigation and mathematical modeling/analysis. Its aim is to improve the understanding of complex diseases by integrating knowledge and data across multiple levels of biological organization. This Thesis focuses on three inverse problems, arising from three kinds of data and related to cancer physiology, at different scales: tissues, cells, molecules.

The general assumption of this piece of research is that cancer is associated to a pathological glucose consumption and, in fact, its functional behavior can be assessed by nuclear medicine experiments using [^{18}F]-fluorodeoxyglucose (FDG) as a radioactive tracer mimicking the glucose properties. At tissue-scale, this Thesis considers the Positron Emission Tomography (PET) imaging technique, and deals with two distinct issues within compartmental analysis. First, this Thesis presents a compartmental approach, referred to as reference tissue model, for the estimation of FDG kinetics inside cancer tissues when the arterial blood input of the system is unknown. Then, this Thesis proposes an efficient and reliable method for recovering the compartmental kinetic parameters for each PET image pixel in the context of parametric imaging, exploiting information on the tissue physiology.

Standard models in compartmental analysis assume that phosphorylation and dephosphorylation of FDG occur in the same intracellular cytosolic volume. Advances in cell biochemistry have shown that the appropriate location of dephosphorylation is the endoplasmic reticulum (ER). Therefore, at cell-scale, this Thesis formalizes a biochemically-driven compartmental model accounting for the specific role played by the ER, and applies it to the analysis of in vitro experiments on FDG uptake by cancer cell cultures obtained with a LigandTracer (LT) device.

Finally, at molecule-scale, this Thesis provides a preliminary mathematical investigation of a chemical reaction network (CRN), represented by a huge Molecular Interaction Map (MIM), describing the biochemical interactions occurring between signaling proteins in specific pathways within a cancer cell. The main issue addressed in this case is the network parameterization problem, i.e. how to determine the reaction rate coefficients from protein concentration data.

Contents

List of Figures

List of Tables

Introduction

Systems Medicine is a new approach to healthcare that draws from the principle of Systems Science and Systems Biology: *the whole is greater than the sum of the parts*. Every day modern medicine moves forward, but in over the 50% of all medical cases the chosen treatment does not benefit the individual patient. The main reason is the traditional fragmented approach to a patient's system, focusing on a single-scale perspective that limits the understanding of the overall clinical situation. Systems Medicine strives for measurable improvements of patient health through comprehensive systems-based approaches and practice.

The starting idea of Systems Medicine is that the structures constituting the whole of living organisms are more than the collection of their single components. This viewpoint recognizes the human body as a unified system of biochemical, physiological, and environmental interactions. Indeed, on a biological level, the human body is a complex machine made up of many networks that are integrated at multiple communicating scales, i.e. a network of networks. Organelles inside each cell interact with each other through chemical reactions to maintain the cell in a healthy functioning state, able to move, differentiate and die. These sub-cellular organelles and their processes govern cell signaling mechanisms to connect neighboring cells, and form multi-cellular systems called tissues. Different types of tissues join to form an organ that performs a specific duty, and different organs cooperate to compose organ systems that carry out complicated functions. All these organ systems together enable a living organism. The aim of Systems Medicine is to decipher the complexity of this human network system for improving the understanding, prevention, and treatment of diseases, through the integration of knowledge and data across multiple levels of biological organization.

Solving biomedical problems requires the development of cutting-edge computational technologies in order to explore undiscovered dimensions of data space, and new data types require innovative analytical tools tackling such vast amounts of information and making sense of all this. The latter cycle defines the fundamental interplay between medicine, technology, and computation supporting Systems Medicine. It is therefore straightforward to notice that the tasks of Systems Medicine can be achieved only in a multidisciplinary framework where clinicians, biologists, chemists, computer scientists, engineers, mathematicians, physicists, and others, work together. The collaboration of these many scientific profiles involves iterative and reciprocal feedback, and asks scientists to step beyond the borders of their field and engage for an interdisciplinary environment in which complementary skills and different attitudes allow to face the biological challenges and to get shareable insights more quickly. The team cooperates to combine the biomedical data into mathematical models describing the biological systems, to predict how these systems change over time and under varying conditions, and to develop solutions to the world's most urgent health issues.

The potential benefits of Systems Medicine are profound. In the long term, this methodology can (i) track diseases on various levels, from the human body down to organs, and to cellular and sub-cellular layers, (ii) provide a detailed portrait of the human physiology, based on multi-scale data and models, and (iii) deliver individual treatments for patients opening the way to personalized medicine.

This Thesis takes its inspiration from the world of Systems Medicine and pursues the idea that integration of information is more effective than reductionist approaches. A reasonable question is: what's the role of Mathematics within this framework? The relation between Mathematics and Systems Medicine has been so far mainly focused on the development and study of dynamical systems describing biological processes. This is a crucial point: bioinformatics addresses biological problems (almost) without the use of a preliminary mathematical model characterizing the system structure and equations, since, in some sense, the models are inferred from the available biological data; the application of Mathematics to Systems Medicine requires the formulation of mathematical models mimicking the biological processes, but is much less involved in the use of experimental data for assessing the reliability of the models. This Thesis follows an inverse problem approach to Systems Medicine: once the dynamical (forward) model is designed, the attention is shifted on what unknowns and measurements mean for clinicians and biologists, and therefore on the formulation of the inverse problem; then, a study on the identifiability of the unknowns with respect to the measurements is performed; afterwards, there is the need to develop suitable numerical methods able to determine the unknowns from the measurements in a reliable (numerically stable) way; finally, the algorithms are applied to both synthetic and experimental data, and the results are provided together with their biological interpretation.

The procedure adopted in this Thesis is data-driven and multi-scale. Three inverse problems are addressed, classified according to the level-type of data and described with a top-down strategy: from Positron Emission Tomography (PET) images at tissue-scale, down to LigandTracer (LT) signals at cell-scale, and eventually chemical reaction networks (CRNs) for protein-protein interactions within a cell at molecule-scale. At all levels, the main attention is devoted to cancer physiology. Roughly speaking, one of the primary effects visible in cancer tissues is an augmented pathological consumption of glucose, which is a consequence of altered enzymatic mechanisms processing glucose inside the diseased cells. The deep cause of this abnormal behavior is an uncontrolled proliferation, which essentially requires a lot of energy, due to genetic mutations affecting specific regulating proteins within the cell signaling network. In this scenario, the PET can image glucose metabolism by tissues, LT can collect signals of glucose uptake by cells, and a CRN can describe the network of the cell signaling chemical reactions. But, how is it possible to look into the specific characteristics of cancer starting from the available data? The answer is in a proper mathematical model.

The PET is a functional nuclear medicine imaging technique providing dynamical images of the metabolism under study. The PET acquisition can be performed after the injection of a radioactive tracer into the living organism. Then, the PET is able to detect the time-dependent spatial distribution of the decay of radioisotopes of the labeled tracer bound to known molecules. The raw PET data consist in the measured radioactivity, collected in a set of projections called sinograms; the PET images of tracer distribution are obtained by solving a well-known image reconstruction inverse problem involving the inversion of the Radon transform. If the study focuses on glucose metabolism, the most popular glucose analog tracer is the [^{18}F]-fluorodeoxyglucose (FDG), with a radioactivity elimination half-life of 110 minutes which makes PET with FDG widely exploitable from a clinical viewpoint. The distribution of FDG is a marker for the glucose uptake by tissues. Nevertheless, the FDG-PET dynamic images of tracer concentration are total signals which result from the superposition of multiple tracer sources arising from different metabolic states of the radioactive molecules. Compartmental analysis is the mathematical tool

dealing with the problem of reconstructing both the single tracer emitters and the flow of tracer between them, as indexes of the efficiency of tracer metabolism. Compartmental models are properly designed to include compartments, for representing the functional states of the basic radioactive molecules within a specific physiological system, and kinetic parameters, for representing the tracer flow as input/output rates of tracer for each compartment. The kinetics of the compartmental structure is described by a linear system of ordinary differential equations (ODEs), where the time-dependent concentrations of tracer in each compartment constitute the state variables, and the kinetic parameters are the system constant coefficients. The aim in compartmental analysis is to determine the unknown rate parameters assessing the system metabolism from PET measurements, and thus solving the compartmental inverse problem, which is non-linear and ill-posed. In this Thesis, two tissue-scale compartmental issues are addressed. First, the reference tissue model deals with the problem of estimating the kinetic parameters for tracer metabolism in a given target tissue when the blood input function that triggers the tracer kinetics of the system cannot be determined in a reliable manner, or is simply unknown. For overcoming this obstacle, a reference tissue is selected in order to replace the input. Here, a consistently reference tissue procedure is proposed, validated, and tested on FDG-PET data of cancer tissues. Second, the parametric imaging approach reconstructs the set of model parameters for every pixel of the PET images, and hence reproduces the spatial distribution of each exchange rate. This Thesis puts forward a computationally efficient imaging method capable of handling complex physiological systems, e.g. the renal system.

A nuclear medicine device looking at a thinner level than PET is LT, adopted for tracking in time specific enzymatic interactions within a group of isolated cells. LT comprises a detector, a rotating support, and a Petri dish in which the cell cultures are opportunely positioned. The cells are immersed in a prepared liquid medium containing the active substance to be monitored. LT counts the radioactivity emitted by the cell sources and provides a time-dependent signal which directly reflects the total substance consumption. In oncology, the LT coupled with the FDG radioactive tracer can be used to evaluate glucose uptake by different cultured cancer cells in several environmental conditions. This context allows for the application of compartmental analysis. Standard current models for FDG kinetics assume that both phosphorylation and dephosphorylation of FDG occur in the cell cytosol. Nevertheless, recent progresses in cell biology and biochemistry identify the endoplasmic reticulum (ER) as the correct location for the dephosphorylation process. In this Thesis, the true biochemical path of FDG inside a cell is analyzed and a cell-scale biochemically-driven model for FDG metabolism is finalized: the structure of a state-of-the-art model with two compartments is complicated to a three-compartment redesign accounting for a new pool, namely the ER compartment. Therefore, the novel compartmental outline is employed on FDG-LT cancer data, bringing out remarkable insights on the processing of FDG/glucose from cancer cells.

Within Systems Biology, CRNs are comprehensive mathematical models schematizing the chemical interactions between proteins and other molecules inside a cell. The kinetics of the network follows the law of mass action, for which the rate of a chemical reaction is proportional to the product of the concentrations of the reagents involved. This rule gives rise to a non-linear (polynomial) parameter-dependent system of ODEs: the concentrations of the chemical species constitute the state variables, and the reaction rate constants are the system constant coefficients. This Thesis considers a molecule-scale Molecular Interaction Map (MIM), as a graphical representation of a huge CRN, describing the protein-protein interactions occurring within the signaling network of a colorectal cancer cell. The CRN inverse problem is a parameterization problem: the measurable quantities are the concentrations of

the chemical species (all, or some of them) at a limited number of time points, while the rates of the chemical reactions (all, or some of them) are unknowns. This Thesis carries on a first test for solving the parameterization of a limited portion of the MIM, in particular the TGFβ-pathway. More time and more efforts are required to investigate in a deeper way the MIM parameterization, from both a qualitative and a quantitative point of view. In some sense, this is an open problem which uncovers the beginning of a next research challenge, rather than the end of a closed roadmap.

The mathematical ingredients needed and used for the accomplishment of this Thesis are: ODEs for the design of the dynamical models, functional analysis for the study of uniqueness of the model parameters with respect to the available data, regularization theory for the formulation of inversion methods undertaking the ill-posedness of the inverse problems and reducing the numerical instability, and numerical optimization for the implementation of the inversion procedures. However, the methodological peculiarity of the Thesis is in the fact that its general approach is systematic: regardless of the biological scale considered, the underlying strategy follows the entire chain that from the experimental data (PET images, LT signals, protein concentrations) leads to a reliable estimation of the model parameters fully characterizing the dynamical systems, and to the interpretation of the calibrated models within the specific biological frameworks. Therefore, the realization of this piece of research has been possible thanks to a continuous interaction with clinicians and biologists, for both recording the biomedical and biological data, setting up the mathematical models, and examining the results.

The Thesis is structured as follows. In Part I, the state-of-the-art mathematical models are presented. Chapter 1 defines the compartmental analysis in general terms, providing the modeling assumptions and equations, the formalization of the compartmental inverse problem, the discussion on the identifiability issues, and the description of the Newton-type method applied for the model reduction. Chapter 2 introduces the theory of CRNs and their modeling, starting from the basic principles and then deducing the CRN system in a matrix compact form useful to state some results on CRN equilibria and stability. Part II focuses on the tissue-scale. Chapter 3 describes the PET data formation and the PET image reconstruction problem. Chapter 4 concerns the reference tissue model, and Chapter 5 is devoted to the parametric imaging approach. For both problems, the specific compartmental models are delineated, then the methods are validated against simulated data, and finally applied on real FDG-PET measurements. Part III regards the cell-scale. Chapter 6 shows the LT technology, addresses the LT calibration routine, and characterizes the type of LT data. Chapter 7 proposes the new biochemically-driven compartmental model for the evaluation of FDG metabolism in cells, together with its properties and connections with standard models. Chapter 8 reports the results on FDG kinetics obtained from the application of the models on FDG-LT data of cancer cell cultures. Part IV considers the molecule-scale. Chapter 9 comments on the MIM model and supplies the chemical structure underneath the network. Chapter 10 deals with the MIM parameterization. After some generalities on the complexity of the problem, the parameterization of a specific part of the MIM, namely the TGFβ-pathway, by means of a Bayesian approach, is given as a first assessment on the solution feasibility. The conclusions, as open issues, are offered in Chapter 11.

A few rather technical contents are discussed in the appendices. Appendix A, Appendix B, and Appendix C provide the proofs of identifiability of the compartmental models for the reference tissue, renal system and biochemically-driven model, respectively. Appendix C details the lists of all chemical components of the TGFβ-pathway, the related system of ODEs and its dynamical properties.

Part I

Mathematical models: state-of-the-art

Chapter 1

Compartmental Analysis

This chapter is devoted to the description of compartmental analysis, to be regarded as the mathematical framework providing a quantitative description of a family of biological phenomena, occurring within a given biological system. In general, compartmental models are used in many fields including pharmacokinetics, epidemiology, biomedicine, systems theory, complexity theory, engineering, physics, information science and social science. In particular, compartmental design finds its natural application in nuclear medicine being a tool for the description and evaluation of tracer kinetics. Indeed, a typical nuclear medicine experiment consists in estimating glucose metabolism in a pathological system, e.g. in presence of cancer or diabetes; this issue is addressed by means of the diffusion of a glucose analog tracer and the employment of compartmental analysis.

Nuclear medicine datum is a composite of various superimposed signals emitted by tracer sources, reproducing different metabolic states of the radiolabeled molecules. Compartmental modeling identifies distinct homogeneous compartments in the biological system of interest, each one representing a specific functional state of the basic radioactive molecules. The radioactivity concentrations in the various compartments are the natural state variables of the system; tracer flow, resulting from interchange of radioactive molecules between compartments, is modeled by a Cauchy problem for a linear system of ordinary differential equations (ODEs) for concentrations; the constant coefficients, also called rate constants or kinetic parameters, represent first-order process tracer kinetics. From the collection of the dynamic distribution of tracer in the overall biological system by means of nuclear medicine techniques, the aim of compartmental analysis is to resolve the single emitters and to get information on the radioactive tracer exchange rates between compartments.

In the first section, the basic principles of compartmental modeling and the formal description of the model equations are illustrated. In the second section, the compartmental problem of retrieving the kinetic parameters from available nuclear medicine measurements is addressed using inverse problem theory and numerical optimization.

1.1 Compartmental modeling

Nuclear medicine studies analyze dynamic data of functional processes related to a specific metabolic activity. Nuclear medicine data are acquired by means of devices that detect the product of the decay of radioisotopes in a radioactive tracer, which is bound to molecules with known biological properties and diffused in a living organism. Within nuclear medicine imaging techniques, Positron Emission Tomography (PET) (Bailey et al., 2005; Ollinger and Fessler, 1997) is the most modern and sensitive modality, which permits to quantitatively and non-invasively measure regional

radioactivity concentration, and to produce high-quality images of tracer distribution by applying an appropriate image reconstruction algorithm. With an understanding of the biological fate of the tracer in the system of interest, it is possible to construct a mathematical model with a set of parameters that can be used to explain the observed time-dependent distribution of tracer.

1.1.1 Modeling assumptions

In general, tracers consist in labeled molecules, also known as radiotracers or radiopharmaceuticals, and are designed to provide information about a particular physiological function of interest. Basic characteristics of radioactive tracers are the following (Cherry, Sorenson, and Phelps, 2012).

- The behavior of the tracer should be identical or related in a known and predictable manner to that of the natural substance.
- The mass of tracer used should not alter the underlying physiological process being studied.
- The specific activity of the tracer should be sufficiently high to permit imaging and blood or plasma activity assays.
- There are no isotope effects, meaning that the act of labeling the tracer molecule with a radionuclide does not alter its properties.

A tracer may be either a direct radiolabeled version of a naturally occurring compound, an analog of a natural compound, or a unique compound, perhaps a radiolabeled drug (Carson, 2005). In particular, the analog tracer is a compound that possesses many of the properties of the natural compound to which it is related but with differences, e.g. chemical properties, that change the way the analog interacts with biological systems. In many cases, analog tracers are deliberately created to simplify the analysis of a biological function. The most common analog tracer in nuclear medicine is the glucose analog 2-deoxy-2-[^{18}F]-fluoro-D-glucose or [^{18}F]-fluorodeoxyglucose (FDG), produced to evaluate glucose metabolism. FDG and glucose enter cells by the same transport enzymes (GLUTs) and are both phosphorylated by the enzyme hexokinase (HK). However, FDG is not a substrate for the next enzyme in the glycolytic pathway; as a consequence, FDG-6-phosphate (FDG6P) accumulates in the biological system. In this way, the radioactive signal directly reflects the rate of glucose intake and uptake, since there is little clearance of metabolized tracer. FDG is one of the most utilized tracers for PET applications to oncology. In fact, FDG-PET experiments allow to detect and stage diseases related to pathological glucose consumption, such as cancer (Annibaldi and Widmann, 2010; Cairns, Harris, and Mak, 2011; Warburg, 1927) or diabetes (Basu et al., 2000; Iozzo et al., 2003).

Once a radioactive tracer has been selected for evaluation, there are a number of steps involved in developing a useful model and a model-based method. Compartmental modeling (Carson, 2005) is the most commonly used method for describing the flow and storage of radioactive tracers in biological tissues. Compartmental models assume that at any given time all molecules of tracer injected into the system will belong to one of possibly many compartments. Each compartment defines one possible state of the tracer, specifically its physical location (e.g. intravascular space, extracellular space, intracellular space, etc.) and its chemical state (i.e. its current metabolic form or its binding state to different biological elements, such as plasma

proteins, receptors, etc.). A single compartment may represent a number of these states lumped together. The compartmental model describes the possible transformations that can occur to the tracer, allowing it to "move" between compartments. The model defines the fraction or proportion of tracer molecules that will "move" to a different compartment within a specified time. This fractional rate of change of the tracer concentration in one compartment is called a rate constant, usually expressed as k, and has units of inverse time for first-order processes. The physiological interpretation of the source and destination compartments defines the meaning of the rate constants for movement of tracer between them.

For the applicability of compartmental analysis, some key assumptions must be satisfied (Morris et al., 2004).

- Any compartmental system requires an input to drive it.
- Each model compartment is well-mixed, i.e. there are no spatial concentration gradients within a single compartment (but only gradients in time).
- The amount of tracer injected is a trace amount; that is, the radioactive content exists at a negligible concentration with respect to the non-radioactive natural biological substrates and the presence of tracer causes no change in the physiology of the organism.
- The tracer is in steady state with the endogenous molecule that the tracer seeks to emulate.
- The parameters of the model are time-invariant, at least over the duration of the study.

1.1.2 Model equations

In a typical nuclear medicine experiment, the tracer is injected into the system with a concentration mathematically modeled by the input function (IF), usually assumed to be known. In FDG-PET measurements, the IF coincides with the time-dependent FDG concentration in the bloodstream. After injection, the tracer is carried by blood and perfuses the living biological system (e.g. an organ, a tissue, a system of cells). Then, compartmental analysis identifies different functional compartments in the physiological system of interest. The time-dependent concentrations of tracer in each compartment constitute the state variables. The net flux of tracer into each compartment is equal to the rate of change of the compartment concentration and can be defined as the sum of all the inflows minus the sum of all the outflows. Each of these components is symbolized by an arrow into or out of the compartment, and the magnitude of each flux is the product of the rate constant and the concentration in the related source compartment. Therefore, the time evolution of the state variables (i.e. the kinetics of the system) is modeled by a linear system of ODEs with constant coefficients, expressing the conservation of tracer during flow between compartments. The coefficients, identified with the rate constants, are real positive numbers and the plus or minus signs against them characterize incoming and outgoing fluxes, respectively.

Denote with C_n the concentration of the compartment n, and with k_{nm} the kinetic parameter describing the tracer exchange to the target compartment n from the source compartment m. Let $\mathbb{R}_+ = \{x \in \mathbb{R} : x > 0\}$ be the strictly positive real numbers, and $\mathbb{R}_+^* = \{x \in \mathbb{R} : x \geq 0\}$ be the non-negative real numbers. Accordingly, $\mathbb{R}_+^n = \{\boldsymbol{x} \in \mathbb{R}^n : x_i > 0 \; \forall i = 1, \ldots, n\}$, and $\mathbb{R}_+^{*n} = \{\boldsymbol{x} \in \mathbb{R}^n : x_i \geq 0 \; \forall i = 1, \ldots, n\}$.

In general, for a compartmental system of N compartments and input compartment i, the differential equation for a non-specific compartment concentration is

$$\frac{dC_n}{dt} = \dot{C}_n = -J_n^{\text{out}} + J_n^{\text{in}} \,, \tag{1.1}$$

where J_n^{out} and J_n^{in} indicate the net outflow and inflow of the compartment n, respectively, and are defined as

$$J_n^{\text{out}} = \sum_{l \in \mathbb{I}_n^{\text{out}}} k_{ln} C_n \,, \quad J_n^{\text{in}} = \sum_{l \in \mathbb{I}_n^{\text{in}}} k_{nl} C_l \,, \tag{1.2}$$

with $\mathbb{I}_n^{\text{out}} = \{l \in \{1,\dots,N\} \bigcup \{i\} \text{ s.t. } \exists k_{ln} \in \mathbb{R}_+\}$ and $\mathbb{I}_n^{\text{in}} = \{l \in \{1,\dots,N\} \bigcup \{i\} \text{ s.t. } \exists k_{nl} \in \mathbb{R}_+\}$ the sets of the labels of the compartments connected to n. Note that, the inflow J_n^{in} may contain also the contribution due to the external input of tracer.

The system of ODEs for the generic N-compartment model with single IF C_i can be written in compact form:

$$\dot{\boldsymbol{C}} = \boldsymbol{M}\boldsymbol{C} + \boldsymbol{W} \,, \tag{1.3}$$

with $\boldsymbol{C}$ and $\boldsymbol{W}$ N-dimensional vectors, $\boldsymbol{M}$ a $N \times N$ matrix, defined as

$$\boldsymbol{C} = \begin{pmatrix} C_1 \\ C_2 \\ \vdots \\ C_N \end{pmatrix} \,, \; \boldsymbol{M}_{n,m} = \begin{cases} -\sum_{l \in \mathbb{I}_n^{\text{out}}} k_{ln} & \text{if } n = m \\ k_{nm} & \text{if } m \in \mathbb{I}_n^{\text{in}} \setminus \{i\} \\ 0 & \text{if } m \notin \mathbb{I}_n^{\text{in}} \setminus \{i\} \end{cases} \,, \; \boldsymbol{W}_n = \begin{cases} k_{ni} C_i & \text{if } i \in \mathbb{I}_n^{\text{in}} \\ 0 & \text{if } i \notin \mathbb{I}_n^{\text{in}} \end{cases} .$$

Example of simple compartmental model configurations and the related systems of ODEs are shown in Figure 1.1.

We now report some state-of-the-art properties of a compartmental model.

The matrix $\boldsymbol{M}$ is a column weakly diagonally dominant matrix. Moreover, a general result holds for the matrix $\boldsymbol{M}$ of the N-compartment system (Hearon, 1963).

Theorem 1.1.1. *Let $k_{nm} \in \mathbb{R}_+$, $\forall n, m \in \{1,\dots,N\} \bigcup \{i\}$. Then, the eigenvalues of the matrix $\boldsymbol{M}$ have a non-positive real part, and if an eigenvalue has a zero real part then the eigenvalue is 0. Moreover, $dim(ker(\boldsymbol{M})) = m_0$, where m_0 is the multiplicity of 0.*

A compartmental model is supposed to be a connected system for which it is possible for the tracer to reach every compartment from every other compartment. Nevertheless, a compartmental system with no cycle is a system for which it is not possible for the tracer to pass from a given compartment through two or more other compartments back to the starting compartment. A particular case of compartmental model with no cycle is the catenary compartmental system, whose definition is the following.

Definition 1.1.1. A *N-compartment catenary system* is a N-compartment system s.t.

$$\begin{aligned} &k_{nm} \geq 0 \; n, m \in \{1,\dots,N\} \\ &k_{nm} > 0 \; n, m \in \{1,\dots,N\} \,, \; |n-m| = 1 \\ &k_{nm} = 0 \; n, m \in \{1,\dots,N\} \,, \; |n-m| > 1 \,. \end{aligned}$$

For the matrix $\boldsymbol{M}$ of a catenary compartmental model, we have the following result.

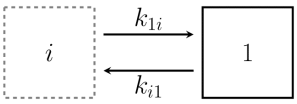

$$\dot{C}_1 = -k_{i1}C_1 + k_{1i}C_i$$

(a) One-compartment model.

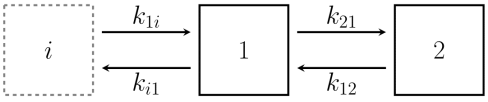

$$\begin{cases} \dot{C}_1 = -(k_{i1} + k_{21})C_1 + k_{12}C_2 + k_{1i}C_i \\ \dot{C}_2 = -k_{12}C_2 + k_{21}C_1 \end{cases}$$

(b) Two-compartment model.

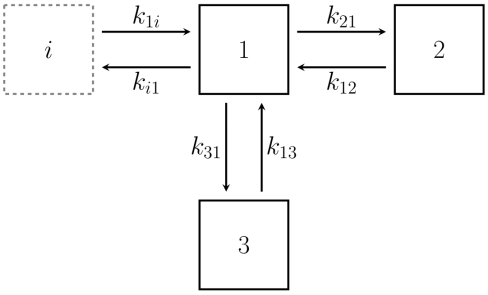

$$\begin{cases} \dot{C}_1 = -(k_{i1} + k_{21} + k_{31})C_1 + k_{12}C_2 + k_{13}C_3 + k_{1i}C_i \\ \dot{C}_2 = -k_{12}C_2 + k_{21}C_1 \\ \dot{C}_3 = -k_{13}C_3 + k_{31}C_1 \end{cases}$$

(c) Three-compartment model.

FIGURE 1.1: Example of compartmental models and corresponding model equations: C_i is the concentration of the input compartment i, considered as known, C_1, C_2, and C_3 are the concentrations in compartments 1–3, and k_{nm} for $n, m \in \{1, 2, 3\} \bigcup \{i\}$ are the rate constants that define the rate of tracer movement between compartments.

Theorem 1.1.2. *The matrix $\boldsymbol{M}$ of a N-compartment catenary system is diagonalizable and its eigenvalues are real, non-positive and simple. Moreover, 0 is an eigenvalue of $\boldsymbol{M}$ if and only if the system with no input is closed, that is $k_{in} = 0$, $\forall n \in \{1, \dots, N\}$.*

More general properties and results concerning N-compartment systems can be found in Delbary, Garbarino, and Vivaldi, 2016.

The analytical solution of the system of ODEs (1.3) with the initial conditions $\boldsymbol{C}(t_0) = \boldsymbol{C}_{t_0} = (C_1(t_0) \dots C_N(t_0))^T \in \mathbb{R}_+^{*N}$ is

$$\boldsymbol{C}(t; C_i, \boldsymbol{k}) = \int_{t_0}^{t} e^{(t-\tau)\boldsymbol{M}} \boldsymbol{W}(\tau)\, d\tau + e^{(t-t_0)\boldsymbol{M}} \boldsymbol{C}_{t_0}\,, \tag{1.4}$$

with $t \in \mathbb{R}_+$ the time variable, and $\boldsymbol{k} \in \mathbb{R}_+^P$ ($P \leq N^2 + N$) the vector of rate constants. Under the hypothesis $\boldsymbol{W} \colon \mathbb{R}_+ \to \mathbb{R}_+^N$, or simply $C_i \colon \mathbb{R}_+ \to \mathbb{R}_+$, the solution $\boldsymbol{C}$ verifies $C_n \geq 0$ $\forall n \in \{1, \dots, N\}$ and $t \in \mathbb{R}_+$; the positiveness of $\boldsymbol{C}$ agrees with the fact that physical concentrations are positive quantities. In standard application of compartmental analysis, the initial conditions are $\boldsymbol{C}(0) = \boldsymbol{C}_0 = (0 \dots 0)^T$, meaning that the nuclear medicine experiment starts at time $t = 0$ when there is no available tracer into the biological system. Equation (1.4) formally expresses the compartmental forward problem of evaluating the compartment concentrations $\boldsymbol{C}$ from the set of kinetic parameters $\boldsymbol{k}$.

1.2 Compartmental inverse problem

Compartmental analysis requires the determination of the tracer kinetic parameters, by utilizing measurements of tracer concentration provided by nuclear medicine. Given the forward model equation, as the analytical solution to the compartmental system of ODEs, the rate constants are regarded as unknown to be estimated. Hence we have to solve a compartmental inverse problem by applying an optimization scheme.

1.2.1 Measurement equation

Nuclear medicine data supply information on the IF C_i and provide an estimate of a linear combination of the concentrations of the different model compartments, at each time point of the acquisition. Denote by $\mathscr{C}$ the experimental total concentration of tracer in the biological system under consideration; the following equation connecting the data to the compartmental model holds:

$$\mathscr{C}(t; C_i, \boldsymbol{k}) = \sum_{n=1}^{N} V_n C_n(t; C_i, \boldsymbol{k}) + V_i C_i(t) \,, \quad \forall t \in \mathbb{R}_+ \,, \tag{1.5}$$

or, equivalently, in compact form

$$\mathscr{C}(t; C_i, \boldsymbol{k}) = \boldsymbol{\alpha}^T \boldsymbol{C}(t; C_i, \boldsymbol{k}) + V_i C_i(t) \,, \quad \forall t \in \mathbb{R}_+ \,, \quad \boldsymbol{\alpha} = \begin{pmatrix} V_1 \\ \vdots \\ V_N \end{pmatrix} . \tag{1.6}$$

The constant weight V_n, $n \in \{1, \ldots, N\}$, s.t. $V_n \in [0, 1]$, is a physiological parameter usually considered as a known quantity and identified with the volume fraction occupied by the compartment n. The parameter $V_i \in [0, 1]$ is the input volume fraction accounting for the direct contribution of the input tracer to the biological system, e.g. blood perfusion in PET-tissue analysis. Equation (1.6) is the basic equation for the formulation of the inverse problem of determining the rate constants, in that it relates measured quantities to formal expressions of the unknown vector $\boldsymbol{k}$ given by the analytical solution (1.4).

1.2.2 Identifiability issues

Before dealing with the optimization process for the solution of the compartmental inverse problem, the formal identifiability of compartmental models has to be discussed. The identifiability analysis wonders if the model parameters are uniquely determined by the given available data, under the assumption that they are not contaminated by noise (Miao et al., 2011; Yates, 2006). The proof of uniqueness may be regarded as an a priori test on the compartmental model, assuring that it is effective in providing a unique description of tracer kinetics, independently of the numerical values of the data.

The identifiability problem consists in theoretically establishing whether, given the model structure and a certain configuration of inputs and outputs, it is possible to univocally determine the unknown parameters, before attempting to actually estimate them. Obviously, only if the model is identifiable the procedure of parameter evaluation makes sense. If the model is unidentifiable, then, whatever the quality of the measurements may be, the same model with different parameter values would represent the observed quantities fairly well. In the case of non-identifiability, the

model complexity can be reduced by shrinking the number of compartments and rate constants or by adding some physical and biological constraints.

The basic definition of identifiability of a compartmental system is the following (Miao et al., 2011).

Definition 1.2.1. The N-compartment system of equations (1.4) and (1.6) is *identifiable* if $\boldsymbol{k}$ can be uniquely determined from the given system input $C_i(t)$ and the measurable system output $\mathscr{C}(t; C_i, \boldsymbol{k})$; otherwise, it is said to be *unidentifiable*.

The identifiability property of a system can be further subdivided, as first introduced by Ljung and Glad, 1994. Denote by $\Omega \subset \mathbb{R}^P$ the parameter space.

Definition 1.2.2. The N-compartment system of equations (1.4) and (1.6) is:

(i) *globally identifiable* if for any admissible input $C_i(t)$ and any two parameter vectors $\boldsymbol{k}_1, \boldsymbol{k}_2 \in \Omega$, $\mathscr{C}(t; C_i, \boldsymbol{k}_1) = \mathscr{C}(t; C_i, \boldsymbol{k}_2)$ holds if and only if $\boldsymbol{k}_1 = \boldsymbol{k}_2$;

(ii) *locally identifiable* if for any $\boldsymbol{k}$ within an open neighborhood of some $\boldsymbol{k}^* \in \Omega$, $\mathscr{C}(t; C_i, \boldsymbol{k}_1) = \mathscr{C}(t; C_i, \boldsymbol{k}_2)$ holds if and only if $\boldsymbol{k}_1 = \boldsymbol{k}_2$.

Both definitions use the concept of one-to-one mapping between parameters and system input/output. More in general, the notion of structural identifiability can be formulated, as Xia and Moog, 2003 proposed.

Definition 1.2.3. The N-compartment system of equations (1.4) and (1.6) is:

(i) *structurally globally identifiable* if it is globally identifiable for all $\boldsymbol{k} \in \Omega$;

(ii) *structurally locally identifiable* if it is locally identifiable for all $\boldsymbol{k} \in \Omega$.

It is hard to find a characterization for identifiability of a general N-compartment system, and it is convenient to analyze each model case-by-case. Some weak results, leading, in particular cases, to more precise identifiability results, are reported in Delbary, Garbarino, and Vivaldi, 2016. In particular, a uniqueness theorem for the general two-compartment catenary system (Figure 1.1(b)) is proven to hold.

Theorem 1.2.1. *The two-compartment catenary system, with given IF $C_i \in \mathcal{C}^0(\mathbb{R}_+, \mathbb{R}_+)$, of equations*

$$\begin{pmatrix} \dot{C}_1 \\ \dot{C}_2 \end{pmatrix} = \begin{pmatrix} -(k_{i1} + k_{21}) & k_{12} \\ k_{21} & -k_{12} \end{pmatrix} \begin{pmatrix} C_1 \\ C_2 \end{pmatrix} + \begin{pmatrix} k_{1i} C_i \\ 0 \end{pmatrix} , \tag{1.7}$$

with $C_1, C_2 \in \mathcal{C}^1(\mathbb{R}_+, \mathbb{R}_+)$, $C_1(0) = C_2(0) = 0$, and

$$\mathscr{C}(t; C_i, \boldsymbol{k}) = \begin{pmatrix} V_1 \\ V_2 \end{pmatrix}^T \begin{pmatrix} C_1(t; C_i, \boldsymbol{k}) \\ C_2(t; C_i, \boldsymbol{k}) \end{pmatrix} + V_i C_i(t) , \quad \forall t \in \mathbb{R}_+ , \tag{1.8}$$

with $\boldsymbol{k} = (k_{1i}, k_{i1}, k_{21}, k_{12})^T \in \mathbb{R}^4_+$, $V_1, V_2, V_i \in [0, 1]$, is structurally globally identifiable.

1.2.3 Regularized Gauss-Newton method

For the solution of the compartmental inverse problem, we make use of the Gauss-Newton method supplied with a regularizing term (Bauer, Hohage, and Munk, 2009; Nocedal and Wright, 2006; Vogel, 2002). It has been shown in Delbary and Garbarino, 2018 that Gauss-Newton regularization in the compartmental framework provides reconstructions of the kinetic parameters that are more stable with respect

to state-of-the-art Levenberg-Marquardt method (see Tables 1-3 in that paper). Further, the matrix differentiation step required at some stage of the optimization analysis is in this method performed analytically, thus avoiding time consuming numerical differentiation, and tackling one standard drawback of Newton methods. Also, by searching for zeroes of non-linear functionals, Newton methods do not need to a priori select a topology in the data space, as in the case of least squares approaches. On the other hand, this class of methods, as compared to standard optimization-through-minimization techniques, may lack in convergence if the starting point is taken too far away from the ground truth.

We rewrite equation (1.6) for the unknown vector of parameters $\boldsymbol{k} \in \mathbb{R}_+^P$ in the form

$$\boldsymbol{\alpha}^T \boldsymbol{C}(t; C_i, \boldsymbol{k}) + V_i C_i(t) - \mathscr{C}(t) := \mathcal{F}_t(\boldsymbol{k}) = 0 \,, \tag{1.9}$$

where $\mathcal{F}_t \colon \mathbb{R}_+^P \to C^1(\mathbb{R}_+, \mathbb{R})$ is a non-linear operator parameterized by the time variable $t \in \mathbb{R}_+$, and $\boldsymbol{C}$ is defined as in (1.4). The non-linear zero-finding problem of equation (1.9) is solved by means of the Gauss-Newton method. If we consider the first-order Taylor expansion of $\mathcal{F}_t$ at $\boldsymbol{k}$, it is possible to write

$$\mathcal{F}_t(\boldsymbol{k} + \boldsymbol{\delta}) = \mathcal{F}_t(\boldsymbol{k}) + \frac{d\mathcal{F}_t}{d\boldsymbol{k}}(\boldsymbol{k}; \boldsymbol{\delta}) \,, \tag{1.10}$$

where $d\mathcal{F}_t / d\boldsymbol{k}$ is the Fréchet derivative of $\mathcal{F}_t$, and $\boldsymbol{\delta}$ is the step-size. By assuming that $\mathcal{F}_t(\boldsymbol{k} + \boldsymbol{\delta}) = 0$, we can find the multi-dimensional root as $\boldsymbol{k} + \boldsymbol{\delta}$, where the step-size $\boldsymbol{\delta} \in \mathbb{R}^P$ is the solution of

$$\frac{d\mathcal{F}_t}{d\boldsymbol{k}}(\boldsymbol{k}; \boldsymbol{\delta}) = -\mathcal{F}_t(\boldsymbol{k}) \,. \tag{1.11}$$

The operator $\mathcal{F}_t$ is differentiable and even analytic, therefore it is possible to compute analytically its Fréchet derivative, which is the bounded and linear operator

$$\begin{aligned} \frac{d\mathcal{F}_t}{d\boldsymbol{k}}(\boldsymbol{k}) \colon \mathbb{R}^P &\to C^1(\mathbb{R}_+, \mathbb{R}) \\ \boldsymbol{\delta} &\mapsto \Big[t \mapsto \nabla_{\boldsymbol{k}} \mathcal{F}_t(\boldsymbol{k}) \cdot \boldsymbol{\delta} \Big] \,. \end{aligned}$$

Denote with $\check{\boldsymbol{k}} \in \mathbb{R}_+^{\check{P}}$ ($\check{P} \leq N$) the components of $\boldsymbol{k}$ contained in the forcing vector $\boldsymbol{W}$, and with $\hat{\boldsymbol{k}} \in \mathbb{R}_+^{\hat{P}}$ ($\hat{P} \leq N^2$) the components of $\boldsymbol{k}$ contained in the system matrix $\boldsymbol{M}$. For all $t \in \mathbb{R}_+$, the gradient of $\mathcal{F}_t$ with respect to $\boldsymbol{k}$ is given by

$$\nabla_{\boldsymbol{k}} \mathcal{F}_t = \begin{pmatrix} \nabla_{\check{\boldsymbol{k}}} \mathcal{F}_t \\ \nabla_{\hat{\boldsymbol{k}}} \mathcal{F}_t \end{pmatrix} \,,$$

where $\nabla_{\check{\boldsymbol{k}}}$ indicates the gradient with respect to $\check{\boldsymbol{k}}$, and $\nabla_{\hat{\boldsymbol{k}}}$ the gradient with respect to $\hat{\boldsymbol{k}}$. Therefore, explicitly, the Fréchet derivative of $\mathcal{F}_t$, for all $t \in \mathbb{R}_+$, is

$$\frac{d\mathcal{F}_t}{d\boldsymbol{k}}(\boldsymbol{k}; \boldsymbol{\delta}) = \nabla_{\boldsymbol{k}} \mathcal{F}_t(\boldsymbol{k}) \cdot \boldsymbol{\delta} = \begin{pmatrix} \left(\boldsymbol{\alpha}^T \int_{t_0}^t e^{(t-\tau)\boldsymbol{M}} \boldsymbol{e}_1 \, d\tau \right) \cdot \boldsymbol{\delta} \\ \vdots \\ \left(\boldsymbol{\alpha}^T \int_{t_0}^t e^{(t-\tau)\boldsymbol{M}} \boldsymbol{e}_{\check{P}} \, d\tau \right) \cdot \boldsymbol{\delta} \\ \boldsymbol{\alpha}^T \int_{t_0}^t e^{(t-\tau)\boldsymbol{M}} \boldsymbol{M}(\hat{\boldsymbol{\delta}}) \boldsymbol{C}(\tau) \, d\tau \end{pmatrix} \,, \tag{1.12}$$

where $\boldsymbol{e}_p$ is the N-dimensional unit vector s.t. $\boldsymbol{e}_{p,p} = 1$ and $\boldsymbol{e}_{p,j} = 0$ $j \neq p$, for $p, j \in \{1, \ldots, \check{P}\}$.

In real applications, only noisy versions of $\mathscr{C}(t)$ and $C_i(t)$ for a finite number of sampling time points $t_1, \ldots, t_T \in \mathbb{R}_+$ are available. Therefore, equation (1.11) becomes the discretized linear system

$$\boldsymbol{F}\boldsymbol{\delta} = \boldsymbol{Y}\,, \tag{1.13}$$

where

$$\boldsymbol{F} = \begin{pmatrix} \nabla_{\boldsymbol{k}} \mathcal{F}_{t_1}(\boldsymbol{k})^T \\ \vdots \\ \nabla_{\boldsymbol{k}} \mathcal{F}_{t_T}(\boldsymbol{k})^T \end{pmatrix}\,,\ \boldsymbol{Y} = \begin{pmatrix} \mathscr{C}(t_1) - V_i C_i(t_1) - \boldsymbol{\alpha}^T \boldsymbol{C}(t_1; C_i, \boldsymbol{k}) \\ \vdots \\ \mathscr{C}(t_T) - V_i C_i(t_T) - \boldsymbol{\alpha}^T \boldsymbol{C}(t_T; C_i, \boldsymbol{k}) \end{pmatrix}\,. \tag{1.14}$$

The system (1.13), with the step-size vector $\boldsymbol{\delta}$ as unknown, constitutes a classic linear ill-posed inverse problem, since the solution may not exist, may not be unique, and may not be stable. Regularization is needed in order to find a unique stable solution of (1.13). We consider a Tikhonov-type regularization (Tikhonov, Goncharsky, and Yagola, 1995), with the Tikhonov penalty on the step-size vector, which leads to the regularized system

$$(r\boldsymbol{I}_P + \boldsymbol{F}^T\boldsymbol{F})\boldsymbol{\delta} = \boldsymbol{F}^T\boldsymbol{Y}\,, \tag{1.15}$$

where $\boldsymbol{I}_P$ is the $P \times P$ identity matrix, and $r \in \mathbb{R}_+$ is the regularization parameter which may be fixed a priori or selected with a proper method, e.g. the Generalized Cross Validation (GCV) method (Golub, Heath, and Wahba, 1979; O'Sullivan, 1999). The advantages in using the GCV are mainly that it can be applied without any *a priori* information on the error on the data or on peculiar properties of the solution, and that it requires just the computation of the SVD of the matrix of the problem. The step-size $\boldsymbol{\delta}$ is the least-square solution of (1.15). Note that solving the problem by means of Tikhonov regularization is equivalent to asking for the solution of the original system (1.13) with a small norm, i.e. limiting the step-size length. This property allows to avoid divergence of the iterative algorithm. The role of the regularization parameter is crucial, since in general it supervises the importance of the regularization term, and in particular it defines the direction along which look for the solution. For example, for large values of the regularization parameter the step-size is taken approximately in the direction of the gradient.

The regularized Gauss-Newton (reg-GN) optimization algorithm performs the following iterative scheme.

Algorithm 1.1. [reg-GN]

Step 1. Choose the initial guess $\boldsymbol{k}^{(0)} \in \mathbb{R}_+^P$.

Step 2. Compute $\boldsymbol{F}^{(0)}$ and $\boldsymbol{Y}^{(0)}$, defined as in (1.14) and evaluated in $\boldsymbol{k}^{(0)}$.

Step 3. Solve for $\boldsymbol{\delta}^{(0)} \in \mathbb{R}^P$

$$(r^{(0)}\boldsymbol{I}_P + {\boldsymbol{F}^{(0)}}^T\boldsymbol{F}^{(0)})\boldsymbol{\delta}^{(0)} = {\boldsymbol{F}^{(0)}}^T\boldsymbol{Y}^{(0)}\,,$$

with the regularization parameter $r^{(0)}$ allowed to change at every iteration.

Step 4. Project onto zero the components of the step-size vector $\boldsymbol{\delta}^{(0)}$ that make negative the components of the parameter vector $\boldsymbol{k}^{(0)}$, by means of the $P \times P$ projection matrix $\boldsymbol{P}^{(0)}$ s.t.

$$\boldsymbol{P}^{(0)}(q,r) = \begin{cases} 0 & \text{if } q \neq r \\ 0 & \text{if } q = r \text{ and } \boldsymbol{k}_q^{(0)} + \boldsymbol{\delta}_q^{(0)} < 0 \\ 1 & \text{if } q = r \text{ and } \boldsymbol{k}_q^{(0)} + \boldsymbol{\delta}_q^{(0)} > 0 \end{cases} .$$

Step 5. Update $\boldsymbol{k}^{(0)}$ with the projected step-size

$$\boldsymbol{k}^{(1)} = \boldsymbol{k}^{(0)} + \boldsymbol{P}^{(0)}\boldsymbol{\delta}^{(0)} .$$

Step 6. Iterate.

The iterative scheme is stopped when the relative error between the given experimental dynamic concentration and the model-predicted one is less than an appropriate threshold, i.e. at a generic iteration h

$$\frac{||\mathscr{C}(t) - V_i C_i(t) - \boldsymbol{\alpha}^T \boldsymbol{C}(t; C_i, \boldsymbol{k}^{(h)})||_2}{||\mathscr{C}(t)||_2} \leq \epsilon , \tag{1.16}$$

where ϵ depends on the noise level on data.

Chapter 2

Chemical Reaction Networks

This chapter introduces the mathematical formulation describing the modeling and dynamics of chemical reaction networks (CRNs for short), to be regarded as compositions of interconnected chemical reactions occurring between chemical species. CRNs are a special form of compartmental systems, which involve mass- and energy-balance relations.

Typical reaction networks in living cells involve several hundreds of chemical species and reactions. According to the functions carried out inside the cells, different networks can be modeled, such as regulatory interaction networks, metabolic networks, signaling networks, and protein-protein interaction networks. These large-scale CRNs arise abundantly in systems biology and bioengineering, being a tool to decipher the molecular basis of biological processes and diseases. In fact, CRNs provide a systems-level understanding of the mechanisms underlying biological processes, by serving as a model for data integration and analysis. They have been used to gain insight into disease mechanisms, study comorbidities, analyze therapeutic drugs and their targets, and discover novel network-based biomarkers.

The most basic law prescribing the dynamics of the concentrations of the various species in the CRNs is the law of mass action, stating that the rate of a chemical reaction is proportional to the product of the concentrations of the reactants involved. The proportionality constant is the reaction rate constant, defining the speed at which the reaction occurs. Therefore, the mass action kinetics allows the formulation of the CRN dynamics by means of polynomial parameter-dependent systems of ordinary differential equations (ODEs), in which the species concentrations are the state variables and the reaction rate constants are the system constant coefficients.

In the first section, the chemical reactions are introduced and illustrated by means of well-known state-of-the-art examples, and the CRNs are formalized in mathematical terms as direct graphs provided by a suitable kinetics. In the second section, the non-linear system of ODEs associated with the CRN is rewritten in a matrix compact form, as done for standard linear systems, and some important results on CRN equilibria and stability are provided.

2.1 CRN modeling

The structural theory of CRNs finds its foundation in the pioneering works of Horn, Jackson, and Feinberg in the 1970s. The starting point of, e.g., Horn and Jackson, 1972, Horn, 1972, Feinberg, 1972, is the definition of a graph structure for CRNs based on the chemical complexes, i.e. the combination of chemical species appearing on the left-hand (reactant) and right-hand (product) sides of every reaction, as the vertices of a graph and the reactions as its edges. This enables the formulation of the dynamics of the reaction network as a dynamical system on the graph of complexes. The reaction rates of CRNs are modeled through the law of mass action, and

therefore CRN dynamics is characterized by an intrinsic nonlinearity. Note that the CRN as graph of complexes is not the only possible choice; indeed, CRNs can be interpreted by various graphs, as described in Domijan and Kirkilionis, 2008.

In this section we survey the notion of a chemical reaction, the basic topological structure of the CRN, and the characterization of the CRN kinetics.

2.1.1 Basics of chemical reactions

Molecules inside the cell undergo various transformations, e.g. a molecule can transform from one kind to another, two molecules of the same or different kinds can combine to form another molecule of a third kind, and so on. At the basic level these transformations are known as chemical reactions (Ullah, 2011).

A chemical reaction is described schematically by an arrow with reactants on the left and products on the right. The molecules involved in the chemical reaction are chemical species, and a single molecule of a species A is referred to as an A-molecule. The chemical complexes are the objects that appear before and after the reaction arrows (Horn and Jackson, 1972). Three elementary and irreversible reactions can be identified, as follows.

- *Conversion* (or modification, isomerization):

  $$A \to B \,,$$

  an A-molecule transforms to a B-molecule.

- *Association* (or synthesis):

  $$A + B \to C \,,$$

  an A-molecule associates with a B-molecule to form a non-covalently-bound complex C.

- *Dissociation* (or decomposition):

  $$C \to A + B \,,$$

  the complex C-molecule dissociates into an A- and a B-molecule.

Note that the plus sign between the species is a standard chemical notation for indicating the combination of them as binding of molecules.

Every chemical reaction can always be broken down into a mechanism that consists of combinations of these three elementary processes (conversion, association, dissociation). For example, the probable mechanism of the chemical reaction

$$A + B \rightleftarrows C$$

would be

$$A + B \rightleftarrows AB \to C \,,$$

where C is a covalent modification of AB. Each single arrow denotes one of the elementary reactions.

A species that is not of interest (e.g., because its abundance does not change over time) is represented by the symbol $\varnothing$, and referred to as the *null species* or *zero complex*. The reaction

$$A \to \varnothing$$

represents the *degradation* of an A-molecule to a form not of interest; similarly,

$$\varnothing \rightarrow B$$

indicates the *production* of a B-molecule when the reactants are disregarded.

Different rate functions for a chemical reaction can be chosen; the most used and standard one is the *law of mass action* (Waage and Gulberg, 1986):

> "when two reactants, A and B, react together at a given temperature in a substitution reaction, the affinity, or chemical force between them, is directly proportional to the product of the active masses of the reactants $k[A][B]$".

The active mass was defined as "the amount of substance in the sphere of action", and for a species in solution active mass is equal to concentration. The proportionality constant k was called affinity constant, actually named rate constant, and was regarded as an empirical constant to be determined by experiments. The law evolved from the work of the French chemist C.L. Berthollet (Berthollet, 1803), was first formulated by C.M. Guldberg and P. Waage in the 1860's (Waage and Gulberg, 1986), and later clarified by the Dutch chemist J. van't Hoff (van't Hoff, 1877).

Essentially, the law of mass action is a semi-empirical law, and find its phenomenological justification as a macroscopic version of collision theory. In fact, reactions happen because molecules collide with each other, forming and destroying chemical bonds. Constraints to the law of mass action validity are:

- constant temperature;
- compartment in which the reactions occur must be well-mixed;
- the number of molecules must be high ($\simeq 10^{23}$ Avogadro number).

2.1.2 Literature examples of CRNs

Academic examples of biochemical networks (Ullah, 2011) are now presented. These well-known CRNs are very simple, but relevant to molecular and cell biology.

Example 1. The *Lotka-Volterra predator-prey model* was initially proposed by A.J. Lotka in the theory of autocatalytic chemical reactions (Lotka, 1909), and then investigated in the context of population biology by both A.J. Lotka (Lotka, 1925) and V. Volterra (Volterra, 1928). The reaction scheme is the following:

$$\begin{aligned} X_1 + A &\xrightarrow{k_1} 2X_1 \\ X_1 + X_2 &\xrightarrow{k_2} 2X_2 \\ X_2 &\xrightarrow{k_3} \varnothing \end{aligned} .$$

The model involves two interacting species, X_1 (the prey) and X_2 (the predator); the substrate (food) A is assumed to be constantly replenished and it is available for X_1, which reproduces, with rate coefficient k_1, after consuming one unit of A. An encounter between the two species, with rate coefficient k_2, results in the disappearance of X_1 and the replication of X_2. This is the only way X_1 degrades (dies), whereas X_2 has a natural degradation (death) with rate coefficient k_3. This reaction scheme was proposed as a simple mechanism of oscillating reactions.

Example 2. A basic chemical reaction occurring within a cell environment is the *enzyme kinetic reaction*, depicted in Figure 2.1. The conversion of a substrate to a product is made easier by specialized proteins called enzymes that bind to the substrate and lower the activation energy required for conversion to the product. The reaction scheme is composed by three elementary steps:

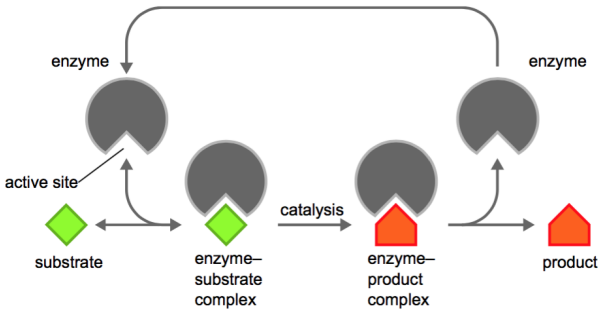

FIGURE 2.1: Enzyme-catalyzed conversion of a substrate to a product: the enzyme binds to the substrate to make its conversion to product energetically favorable (from Ullah, 2011).

$$E + S \underset{k_2}{\overset{k_1}{\rightleftarrows}} ES \xrightarrow{k_1} E + P \,,$$

in which the enzyme E catalyzes a substrate S into a product P that involves an intermediary complex ES.

Example 3. A simplified regulatory mechanism for *gene regulation* is illustrated in Figure 2.2, as a feedback loop regulatory network. The protein product from gene expression binds to a regulatory region on the DNA and represses transcription. The regulatory mechanism is simplified by not showing the contributions of RNA polymerase and any cofactors. The reaction scheme for the system is

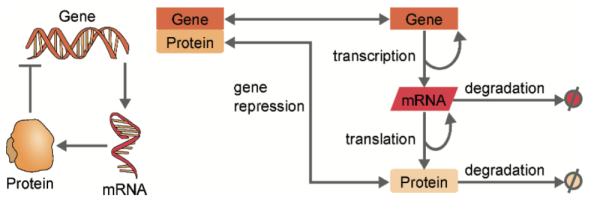

FIGURE 2.2: A simplified model for gene regulation: on the left-hand side a pictorial representation, on the right-hand side the reaction scheme (from Ullah, 2011).

$$G \xrightarrow{k_m} G + M \qquad \text{(transcription)}$$

$$M \xrightarrow{k_p} M + P \qquad \text{(translation)}$$

$$G + P \underset{k_u}{\overset{k_b}{\rightleftarrows}} GP \qquad \text{(binding/unbinding)}$$

$$M \xrightarrow{k_m^-} \varnothing \,, \; P \xrightarrow{k_p^-} \varnothing \qquad \text{(degradation)}$$

where the gene G is transcribed to the mRNA M with rate constant k_m, the mRNA is translated to the protein P with rate constant k_p, and the protein binds to (and represses) the gene with rate constant k_b and unbinds back with rate constant k_u. The mRNA and protein are degraded with respective rate constants k_m^- and k_p^-.

2.1.3 CRN formalization

Consider a homogeneous, well-stirred, isothermal reactor of constant volume, i.e. a reactor in which its content remains spatially homogeneous for all time and is maintained at fixed temperature and total volume. This of course does not mean that the chemical composition of the mixture will remain constant in time, for the occurrence of chemical reactions will serve to consume certain species and generate others. Suppose that the chemistry within the reactor is reasonably well-modeled by a reaction network. Then, following Feinberg, 1979, Feinberg, 1987, and Arceo et al., 2015, the networks of chemical reactions can be formalized as follows.

Definition 2.1.1. A *chemical reaction network* (CRN) consists of a list of three finite sets $(\mathcal{S}, \mathcal{C}, \mathcal{R})$:

- $\mathcal{S}$ the set of *species* undergoing the chemical reactions;
- $\mathcal{C}$ the set of *complexes* as finite non-negative integer combinations of species, used and produced in all reactions, s.t.

$$\bigcup_{c \in \mathcal{C}} \operatorname{supp} c = \mathcal{S} \,,$$

  where $\operatorname{supp} c \subset \mathcal{S}$ is the set of species appearing in the complex c, i.e. each element of $\mathcal{S}$ appears in at least one complex;

- $\mathcal{R}$ the set of *reactions* between complexes, $\mathcal{R} \subset \mathcal{C} \times \mathcal{C}$ s.t.
  (a) $(c, c) \notin \mathcal{R}\ \forall c \in \mathcal{C}$, i.e. no complex reacts to itself;
  (b) for each $c \in \mathcal{C}$ there exists $c' \in \mathcal{C}$ s.t. $(c, c') \in \mathcal{R}$ or $(c', c) \in \mathcal{R}$, i.e. no complex is isolated.

  For a reaction $(c, c') = c \to c'$, c is called the *reactant* complex and c' the *product* complex. A reaction $c \to c'$ is *reversible* if its reverse reaction $c' \to c$ is also in $\mathcal{R}$; these reactions may be depicted as $c \rightleftarrows c'$.

The complexes can be characterized in different equivalent ways.

Definition 2.1.2. A complex $c \in \mathcal{C}$ is a formal weighted sum of species, where the weights are non-negative integer numbers:

$$c = \sum_{s \in \mathcal{S}} c_s s \,,$$

with $c_s \in \mathbb{N}$, $\forall s \in \mathcal{S}$. Each non-negative integer coefficient c_s is called *stoichiometric coefficient* of species s in complex c.

Remark 2.1.1. Note that a complex $c \in \mathcal{C}$ is uniquely identified by a vector in $\mathbb{N}^m$, with $m \in \mathbb{N} \setminus \{0\}$ the finite dimension of $\mathcal{S}$, whose elements are the stoichiometric coefficients c_s, $\forall s \in \mathcal{S}$. Further, a complex c can be seen as a function $\mathcal{S} \to \mathbb{N}$, associating at each species its stoichiometric coefficient.

Definition 2.1.3. Let $(\mathcal{S}, \mathcal{C}, \mathcal{R})$ be a CRN. The *reaction vector* of reaction $c \to c' \in \mathcal{R}$ is the vector $c' - c$ s.t the component of $c' - c$ corresponding to species $s \in \mathcal{S}$ is $c'_s - c_s$, i.e. the difference between the stoichiometric coefficient of s in the product complex c' and in the reactant complex c. The integer value $c'_s - c_s$ is the net number of molecules of s produced with each occurrence of the reaction $c \to c'$.

The network structure of a CRN cannot be directly captured by a graph involving the chemical species, since generally there are more than two species involved in a reaction. Instead, the graph originating from the CRN reactions can be modeled by means of the complexes.

Definition 2.1.4. A CRN can be viewed as a directed graph whose nodes are complexes and whose edges correspond to the reactions, called *graph of complexes*. A *linkage class* is a connected component of the CRN directed graph: the complexes c and c' belong to the same linkage class if and only if there is a sequences of complexes $c^{(0)} = c, c^{(1)}, \dots, c^{(l-1)}, c^{(l)} = c'$ such that either $c^{(j)} \to c^{(j+1)}$ or $c^{(j+1)} \to c^{(j)}$ is a reaction for all $0 \leq j \leq l-1$. A CRN is said to be *weakly reversible* if every connected component of the network is strongly connected.

We need to clarify some notations. Let $\mathbb{R}_+ = \{x \in \mathbb{R} : x > 0\}$ be the strictly positive real numbers, and $\mathbb{R}^*_+ = \{x \in \mathbb{R} : x \geq 0\}$ be the non-negative real numbers. Accordingly, $\mathbb{R}^n_+ = \{\boldsymbol{x} \in \mathbb{R}^n : x_i > 0 \ \forall i = 1, \dots, n\}$, and $\mathbb{R}^{*n}_+ = \{\boldsymbol{x} \in \mathbb{R}^n : x_i \geq 0 \ \forall i = 1, \dots, n\}$. If $\mathcal{I}$ is a finite set, $\mathbb{R}^{\mathcal{I}}$ denotes the space of real-valued functions with domain $\mathcal{I}$. If $x \in \mathbb{R}^{\mathcal{I}}$, then the symbol x_i indicates the number that x assigns to $i \in \mathcal{I}$. The support of $x \in \mathbb{R}^{\mathcal{I}}$ is the subset of $\mathcal{I}$ assigned non-zero values by x, i.e. $\operatorname{supp} x = \{i \in \mathcal{I} : x_i \neq 0\}$.

Many characteristics and relationships of CRNs can be expressed in terms of the associated finite-dimensional spaces $\mathbb{R}^{\mathcal{S}}$, $\mathbb{R}^{\mathcal{C}}$, and $\mathbb{R}^{\mathcal{R}}$, simply called the spaces of species compositions, complex compositions and reaction compositions, respectively (Arceo et al., 2015). These spaces can be viewed as the spaces of functions from each set to $\mathbb{R}$. For example, complexes are elements of $\mathbb{N}^{\mathcal{S}} \subset \mathbb{R}^{\mathcal{S}}$.

With each species in the CRN there is associated a non-negative molar concentration, indicating the instantaneous amount of that species presents in the reactor.

Definition 2.1.5. A *composition state* for a CRN is a function $x \colon \mathcal{S} \to \mathbb{R}^*_+$, i.e. $x \in \mathbb{R}^{*\mathcal{S}}_+$, assigning to each species $s \in \mathcal{S}$ its instantaneous non-negative molar concentration x_s.

To formulate differential equations describing how the various species concentrations evolve in time, we must first specify how the instantaneous occurrence rates of the individual reactions in the network depend upon the instantaneous composition state of the reactor (Feinberg, 1987).

Definition 2.1.6. A *kinetics* κ for a CRN $(\mathcal{S}, \mathcal{C}, \mathcal{R})$ is an assignment to each reaction $c \to c' \in \mathcal{R}$ of a continuous *rate function* $\kappa_{c \to c'} \colon \mathbb{R}^{*\mathcal{S}}_+ \to \mathbb{R}^*_+$ s.t. $\kappa_{c \to c'}(x) > 0$ if and only if $\operatorname{supp} c = \{s \in \mathcal{S} : c_s \neq 0\} \subset \operatorname{supp} x = \{s \in \mathcal{S} : x_s \neq 0\}$.

Remark 2.1.2. Note that for strictly positive x, that is $x \in \mathbb{R}^{\mathcal{S}}_+$, it holds $\operatorname{supp} c \subset \operatorname{supp} x$ $\forall c \in \mathcal{C}$. Thus, for $x \in \mathbb{R}^{\mathcal{S}}_+$, it holds $\kappa_{c \to c'}(x) > 0$ for all $c \to c' \in \mathcal{R}$.

Remark 2.1.3. Given a kinetics κ, each rate function $\kappa_{c \to c'}$, with $c \to c' \in \mathcal{R}$, is an element of $\mathbb{R}^{*\,(\mathbb{R}^{*\mathcal{S}}_+)}_+$. Since a kinetics is an assignment to each reaction of a rate function, then a kinetics κ is itself a function $\kappa \colon \mathcal{R} \to \mathbb{R}^{*\,(\mathbb{R}^{*\mathcal{S}}_+)}_+$.

Definition 2.1.7. A *reaction system* $(\mathcal{S}, \mathcal{C}, \mathcal{R}, \kappa)$ is a CRN endowed with a kinetics κ.

Our interest is in reaction systems for which the rate functions are of the standard mass action form.

Definition 2.1.8. A kinetics κ for a CRN $(\mathcal{S}, \mathcal{C}, \mathcal{R})$ is *mass action* if for each $c \to c' \in \mathcal{R}$, there exist a positive number $k_{c\to c'}$ s.t.

$$\kappa_{c\to c'}(x) = k_{c\to c'} \prod_{s\in\mathcal{S}} (x_s)^{c_s} \, .$$

The positive number $k_{c\to c'}$ is called *rate constant* for the reaction $c \to c'$.

Definition 2.1.9. A reaction system for which the kinetics is mass action is called *mass action system*.

With mass action kinetics the rate of each reaction is proportional to the product of all the molar species concentrations of the reactants, each raised to a power given by the corresponding stoichiometric coefficient in the reactant complex. A mass action kinetics for a CRN is completely specified by an assignment to each reaction $c \to c' \in \mathcal{R}$ of a positive constant $k_{c\to c'}$. Therefore, a mass action kinetics is specified by an element $k \in \mathbb{R}_+^{\mathcal{R}}$.

Definition 2.1.10. In a mass action system, the rate of forward reactions are called *forward rate constants* and are denoted by k_f, the rate for reverse reactions are called *reverse rate constants* and are denoted by k_r.

Now it is possible to describe the time evolution of the composition state, i.e. of the species molar concentrations, and therefore to define the differential equations for a CRN.

Definition 2.1.11. Given a reaction system $(\mathcal{S}, \mathcal{C}, \mathcal{R}, \kappa)$, the *vector differential equation* for the composition state is

$$\frac{dx}{dt} = \dot{x} = \sum_{c\to c'\in\mathcal{R}} \kappa_{c\to c'}(x)(c' - c) \, , \tag{2.1}$$

where $x \in \mathbb{R}_+^{*\mathcal{S}}$, and t is the time variable. The *scalar differential equation* for a single species is simply given by

$$\dot{x_s} = \sum_{c\to c'\in\mathcal{R}} \kappa_{c\to c'}(x)(c'_s - c_s) \, , \quad \forall s \in \mathcal{S} \, . \tag{2.2}$$

For a mass action system, the vector differential equation takes the form:

$$\dot{x} = \sum_{c\to c'\in\mathcal{R}} k_{c\to c'} \left(\prod_{s\in\mathcal{S}} (x_s)^{c_s} \right) (c' - c) \, . \tag{2.3}$$

Finally, a *steady state* of a reaction system is a composition state $\bar{x} \in \mathbb{R}_+^{*\mathcal{S}}$ s.t.

$$0 = \sum_{c\to c'\in\mathcal{R}} \kappa_{c\to c'}(\bar{x})(c' - c) \, , \tag{2.4}$$

and a steady state is positive if $\bar{x} \in \mathbb{R}_+^{\mathcal{S}}$, i.e. all species concentrations are positive.

In Figure 2.3, we report an example of CRN with its formal set of species, set of complexes, set of reactions, and the differential equations of mass action form for the kinetics of the network. The CRN counts four species, four complexes and

five elementary reactions, each one associated with a rate constant. The differential equations in terms of the species concentrations are non-linear with respect to the concentrations, and linear with respect to the rate constants. Each formal expression indicates how the concentration change over time when the related species undergoes specified CRN reactions.

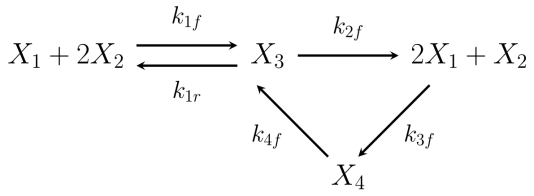

$$\mathcal{S} = \{X_1\,, X_2\,, X_3\,, X_4\} = \{s_1, s_2, s_3, s_4\}$$
$$\mathcal{C} = \{X_1 + 2X_2\,, X_3\,, 2X_1 + X_2\,, X_4\} = \{c_1, c_2, c_3, c_4\}$$
$$\mathcal{R} = \{c_1 \underset{k_{1r}}{\overset{k_{1f}}{\rightleftarrows}} c_2\,, c_2 \xrightarrow{k_{2f}} c_3\,, c_3 \xrightarrow{k_{3f}} c_4\,, c_4 \xrightarrow{k_{4f}} c_2\}$$
$$\kappa = \{k_{1f}, k_{1r}, k_{2f}, k_{3f}, k_{4f}\}$$

$$\begin{aligned}
\dot{x}_1 &= -k_{1f}x_1x_2^2 + k_{1r}x_3 + 2k_{2f}x_3 - 2k_{3f}x_1^2x_2 \\
\dot{x}_2 &= -2k_{1f}x_1x_2^2 + 2k_{1r}x_3 + k_{2f}x_3 - k_{3f}x_1^2x_2 \\
\dot{x}_3 &= k_{1f}x_1x_2^2 - k_{1r}x_3 - k_{2f}x_3 + k_{4f}x_4 \\
\dot{x}_4 &= k_{3f}x_1^2x_2 - k_{4f}x_4
\end{aligned}$$

FIGURE 2.3: Example of CRN and its formalization.

2.2 CRN kinetics

A CRN, taken together with a specification of reaction rate functions, gives rise to a system of ODEs, non-linear in case of mass action kinetics. The CRN mass action system is then well described by a polynomial system of ODEs with the molar species concentrations as state variables and the reaction rate constants as system constant coefficients. The CRN dynamical system can be qualitative characterized by looking at both its stoichiometry and its associated direct graph of complexes.

In the following, let $\mathbb{R}_+ = \{x \in \mathbb{R} : x > 0\}$ be the strictly positive real numbers, and $\mathbb{R}_+^* = \{x \in \mathbb{R} : x \geq 0\}$ be the non-negative real numbers. Accordingly, $\mathbb{R}_+^n = \{\boldsymbol{x} \in \mathbb{R}^n : x_i > 0\ \forall i = 1, \ldots, n\}$, and $\mathbb{R}_+^{*n} = \{\boldsymbol{x} \in \mathbb{R}^n : x_i \geq 0\ \forall i = 1, \ldots, n\}$.

2.2.1 CRN system

Following van der Schaft, Rao, and Jayawardhana, 2013; van der Schaft, Rao, and Jayawardhana, 2016; Rao, Schaft, and Jayawardhana, 2013, it is possible to write the system of ODEs of the mass action CRN in a matrix compact form.

Consider a CRN with $m \in \mathbb{N} \setminus \{0\}$ species, $n \in \mathbb{N} \setminus \{0\}$ complexes, and $r \in \mathbb{N} \setminus \{0\}$ reactions. Let $\boldsymbol{x} \in \mathbb{R}_+^m$ be the vector of species concentrations x_i, for $i = 1, \ldots, m$, and $\boldsymbol{k} \in \mathbb{R}_+^r$ be the vector of reaction rate constants. The ODEs for the CRN takes

the form

$$\frac{d\boldsymbol{x}}{dt} = \dot{\boldsymbol{x}} = \boldsymbol{S}\boldsymbol{v}(\boldsymbol{x}, \boldsymbol{k}) \,, \tag{2.5}$$

where $\boldsymbol{S}$ is a $m \times r$ matrix, called *stoichiometric matrix*, whose elements in $\mathbb{Z}$ are the reaction vectors, and $\boldsymbol{v}(\boldsymbol{x}, \boldsymbol{k}) \in \mathbb{R}^r_+$ is the vector of *reaction fluxes* containing the products of species concentrations and rate constants, as governed by the law of mass action. The system of ODEs (2.5) is equivalent to the vector differential equation (2.3) of Definition 2.1.11.

The stoichiometric matrix embodies the topology of a CRN, and describes the contribution of each reaction to the rate of each species concentration. The rows of $\boldsymbol{S}$ correspond to the chemical species and the columns correspond to the reactions. If we look at $\boldsymbol{S}$ column-wise, there is a minus sign in front of the stoichiometric coefficients of the substrates, and a plus sign in case of products. Row-wise, the non-zero entries of the i-th row of $\boldsymbol{S}$ correspond to the reactions in which x_i is involved either as substrate (with a minus sign) or as a product (with a plus sign).

The formalization of the complexes allows to split the stoichiometric matrix into the product of two matrices, encoding the information from species to complexes and from complexes to reactions. The expression of the complexes as non-negative integer combinations of species is formalized by a $m \times n$ *complex stoichiometric matrix* $\boldsymbol{Z}$: each element $\boldsymbol{Z}(i, j) \in \mathbb{N}$ indicates how many times the $i-$th species appears in the $j-$th complex. Essentially, each element of $\boldsymbol{Z}$ is a stoichiometric coefficient. As detailed in subsection 2.1.3, a CRN leads to a graph of complexes where the nodes are the complexes and the edges are the reactions. The CRN graph with n nodes and r edges, as any other directed graph, is defined by a $n \times r$ *incidence matrix* $\boldsymbol{B}$: each element $\boldsymbol{B}(i, j) \in \{-1, 0, 1\}$ indicates if the $i-$th complex is a reactant (-1), product $(+1)$, or does not appear (0), in the $j-$th reaction. Therefore, the relationship between the complex stoichiometric matrix $\boldsymbol{Z}$ and the standard stoichiometric matrix $\boldsymbol{S}$ is expressed as

$$\boldsymbol{S} = \boldsymbol{Z}\boldsymbol{B} \,. \tag{2.6}$$

In general, the mass action reaction rate of the $j-$th reaction of a CRN, from a substrate complex S_j to a product complex P_j (i.e. $S_j \to P_j$), is given as (Rao, Schaft, and Jayawardhana, 2013)

$$v_j(\boldsymbol{x}, k_j) = k_j \prod_{i=1}^{m} x_i^{z_{i,S_j}} \,, \tag{2.7}$$

where $z_{i,S_j} = \boldsymbol{Z}(i, S_j)$, i.e. the element of row index i and column index S_j of the complex stoichiometric matrix $\boldsymbol{Z}$, and k_j the rate constant of the $j-$th reaction. Without loss of generality, we will throughout assume that, for every $j = 1, \ldots, r$, the constant k_j is strictly positive (since otherwise the $j-$th reaction does not occur).

Define the mapping

$$\begin{aligned} \mathrm{Ln} : \mathbb{R}^m_+ &\to \mathbb{R}^m \,, \qquad \text{s.t. } (\mathrm{Ln}(\boldsymbol{x}))_i = \ln(x_i) \,, \\ \boldsymbol{x} &\mapsto \mathrm{Ln}(\boldsymbol{x}) \end{aligned}$$

and, similarly,

$$\begin{aligned} \mathrm{Exp} : \mathbb{R}^m &\to \mathbb{R}^m_+ \,, \qquad \text{s.t. } (\mathrm{Exp}(\boldsymbol{x}))_i = \exp(x_i) \,. \\ \boldsymbol{x} &\mapsto \mathrm{Exp}(\boldsymbol{x}) \end{aligned}$$

Let $\boldsymbol{Z}_{S_j}$ be the column of $\boldsymbol{Z}$ corresponding to the substrate complex S_j of the $j-$th reaction. Then, equation (2.7), can be rewritten as

$$v_j(\boldsymbol{x}, k_j) = k_j \exp\left(\boldsymbol{Z}_{S_j}^T \mathrm{Ln}(\boldsymbol{x})\right) . \tag{2.8}$$

Define the $r \times n$ matrix $\boldsymbol{K}$, s.t. $\boldsymbol{K}(j,i) = k_j$ if the $i-$th complex is the substrate complex for the $j-$th reaction, and $\boldsymbol{K}(j,i) = 0$ otherwise. The matrix $\boldsymbol{K}$ is called *outgoing co-incidence matrix*, since the $i-$th column of $\boldsymbol{K}$ specifies the weighted outgoing edges from vertex i. Then, it holds (van der Schaft, Rao, and Jayawardhana, 2016)

$$\boldsymbol{v}(\boldsymbol{x}, \boldsymbol{k}) = \boldsymbol{K}\mathrm{Exp}(\boldsymbol{Z}^T \mathrm{Ln}(\boldsymbol{x})) . \tag{2.9}$$

Note that, essentially, the vector $\mathrm{Exp}(\boldsymbol{Z}^T Ln(\boldsymbol{x})) \in \mathbb{R}_+^n$ contains the products of the species concentrations composing the complexes, properly sorted.

Therefore, by means of equations (2.6) and (2.9), the CRN system of ODEs (2.5) can be rewritten as

$$\dot{\boldsymbol{x}} = \boldsymbol{Z}\boldsymbol{B}\boldsymbol{K}\mathrm{Exp}(\boldsymbol{Z}^T \mathrm{Ln}(\boldsymbol{x})) . \tag{2.10}$$

Moreover, by defining the $n \times n$ matrix

$$\boldsymbol{L} = -\boldsymbol{B}\boldsymbol{K} , \tag{2.11}$$

the system (2.10) becomes

$$\dot{\boldsymbol{x}} = -\boldsymbol{Z}\boldsymbol{L}\mathrm{Exp}(\boldsymbol{Z}^T \mathrm{Ln}(\boldsymbol{x})) . \tag{2.12}$$

It can be verified that the matrix $\boldsymbol{L}$ has non-negative diagonal elements and non-positive off-diagonal elements. Moreover, the column sums of $\boldsymbol{L}$ are all zero. Hence, $\boldsymbol{L}$ defines (a transposed version of) a weighted Laplacian matrix, simply called *Laplacian matrix* of the graph of complexes (van der Schaft, Rao, and Jayawardhana, 2016). Figure 2.4 shows an example of CRN, the same network of subsection 2.1.3 reported in Figure 2.3, with the system of ODEs for the dynamics of the CRN species concentrations expressed in compact form.

2.2.2 CRN equilibria and stability

One of the most widespread research area on CRNs deals with the study of the relationship between the structure of a CRN and properties of the induced system of differential equations, regardless of the numerical values of the species concentrations or of the rate constants. Qualitative properties and general results concerning the CRNs, e.g. the deficiency of a network, the existence and uniqueness of positive equilibria, the stability of positive equilibria, can be found in Feinberg, 1972; Feinberg, 1987; Feinberg, 1995; Arceo et al., 2015; Rao, Schaft, and Jayawardhana, 2013; van der Schaft, Rao, and Jayawardhana, 2013; van der Schaft, Rao, and Jayawardhana, 2016. Here we report the most important results on the CRN system dynamics, concerning equilibria and stability for a particular class of CRNs exhibiting the same type of dynamics. The proofs are not reported.

Remark 2.2.1. Note that for all possible fluxes, the solutions of the system of ODEs (2.5), starting from an initial state $\boldsymbol{x}_0 = \boldsymbol{x}(0)$, will always remain within the affine space

$$\mathbb{S}_{\boldsymbol{x}_0} = \{\boldsymbol{x} \in \mathbb{R}_+^m : \boldsymbol{x} - \boldsymbol{x}_0 \in \mathrm{Im}(\boldsymbol{S})\} , \tag{2.13}$$

referred to as *positive stoichiometric compatibility class* (corresponding to $\boldsymbol{x}_0$).

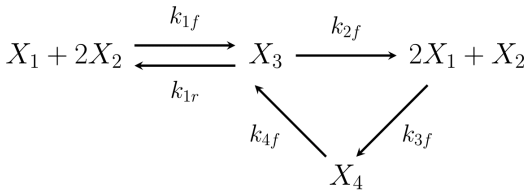

$$\dot{\boldsymbol{x}} = \boldsymbol{S}\boldsymbol{v}(\boldsymbol{x}, \boldsymbol{k})$$

$$\begin{pmatrix} \dot{x}_1 \\ \dot{x}_2 \\ \dot{x}_3 \\ \dot{x}_4 \end{pmatrix} = \begin{pmatrix} -1 & 1 & 2 & -2 & 0 \\ -2 & 2 & 1 & -1 & 0 \\ 1 & -1 & -1 & 0 & 1 \\ 0 & 0 & 0 & 1 & -1 \end{pmatrix} \begin{pmatrix} k_1^f x_1 x_2^2 \\ k_1^r x_3 \\ k_2^f x_3 \\ k_3^f x_1^2 x_2 \\ k_4^f x_4 \end{pmatrix}$$

$$\dot{\boldsymbol{x}} = \boldsymbol{Z}\boldsymbol{B}\boldsymbol{K}\mathrm{Exp}(\boldsymbol{Z}^T Ln(\boldsymbol{x}))$$

$$\begin{pmatrix} \dot{x}_1 \\ \dot{x}_2 \\ \dot{x}_3 \\ \dot{x}_4 \end{pmatrix} = \begin{pmatrix} 1 & 0 & 2 & 0 \\ 2 & 0 & 1 & 0 \\ 0 & 1 & 0 & 0 \\ 0 & 0 & 0 & 1 \end{pmatrix} \begin{pmatrix} -1 & 1 & 0 & 0 & 0 \\ 1 & -1 & -1 & 0 & 1 \\ 0 & 0 & 1 & -1 & 0 \\ 0 & 0 & 0 & 1 & -1 \end{pmatrix} \begin{pmatrix} k_1^f & 0 & 0 & 0 \\ 0 & k_1^r & 0 & 0 \\ 0 & k_2^f & 0 & 0 \\ 0 & 0 & k_3^f & 0 \\ 0 & 0 & 0 & k_4^f \end{pmatrix} \begin{pmatrix} x_1 x_2^2 \\ x_3 \\ x_1^2 x_2 \\ x_4 \end{pmatrix}$$

$$\dot{\boldsymbol{x}} = -\boldsymbol{Z}\boldsymbol{L}\mathrm{Exp}(\boldsymbol{Z}^T \mathrm{Ln}(\boldsymbol{x}))$$

$$\begin{pmatrix} \dot{x}_1 \\ \dot{x}_2 \\ \dot{x}_3 \\ \dot{x}_4 \end{pmatrix} = - \begin{pmatrix} 1 & 0 & 2 & 0 \\ 2 & 0 & 1 & 0 \\ 0 & 1 & 0 & 0 \\ 0 & 0 & 0 & 1 \end{pmatrix} \begin{pmatrix} k_{1f} & -k_{1r} & 0 & 0 \\ -k_{1f} & k_{1r} + k_{2f} & 0 & -k_{4f} \\ 0 & -k_{2f} & k_{3f} & 0 \\ 0 & 0 & -k_{3f} & k_{4f} \end{pmatrix} \begin{pmatrix} x_1 x_2^2 \\ x_3 \\ x_1^2 x_2 \\ x_4 \end{pmatrix}$$

FIGURE 2.4: Example of CRN and its system of ODEs in compact form.

Since the vector $\boldsymbol{x}$ represents the species concentrations, it must be and remain non-negative.

Theorem 2.2.1. *Consider a CRN with with m species, n complexes, and r reactions. If the initial conditions for the species concentrations is s.t.* $\boldsymbol{x}(0) \in \mathbb{R}_+^{*m}$*, then the solution of the system of ODEs* (2.5) *satisfies* $x(t) \in \mathbb{R}_+^{*m}$, $\forall t \in \mathbb{R}_+$ *and* $\forall \boldsymbol{k} \in \mathbb{R}_+^r$.

Special classes of CRNs can be identified, by looking at the system at equilibrium.

Definition 2.2.1. Consider a CRN with dynamics given by equation (2.5). A vector of concentrations $\bar{\boldsymbol{x}} \in \mathbb{R}_+^m$ is called *complex-equilibrium* if $\boldsymbol{B}\boldsymbol{v}(\bar{\boldsymbol{x}}, \boldsymbol{k}) = 0$. Furthermore, a CRN is called *complex-balanced* if it admits a complex-equilibrium.

Remark 2.2.2. Note that any complex-equilibrium is an equilibrium for the network, but the other way round need not be true (since in general $\boldsymbol{Z}$ is not injective). At a complex-equilibrium, the combined rate of outgoing reactions from any complex is equal to the combined rate of incoming reactions to the complex. In other words, at a complex-equilibrium, not only the chemical species but also every complex involved in the network is at equilibrium.

Definition 2.2.2. Consider a CRN with dynamics given by equation (2.5). A vector of concentrations $\bar{\boldsymbol{x}} \in \mathbb{R}^m_+$ is called *thermodynamic equilibrium* if $\boldsymbol{v}(\bar{\boldsymbol{x}}, \boldsymbol{k}) = 0$. Furthermore, a CRN is called *thermodynamically balanced* or *detailed-balanced* if it admits a thermodynamic equilibrium.

Remark 2.2.3. Note that detailed-balanced networks are necessarily reversible (van der Schaft, Rao, and Jayawardhana, 2013). Moreover, every thermodynamically balanced network is complex-balanced.

In order to derive stability properties, we rewrite the dynamical equations (2.12) for complex-balanced networks in terms of a known complex-equilibrium $\bar{\boldsymbol{x}} \in \mathbb{R}^m_+$ (Rao, Schaft, and Jayawardhana, 2013). Define the $n \times n$ matrix

$$\boldsymbol{\Theta}(\bar{\boldsymbol{x}}) = \operatorname{diag}\big(\exp(\boldsymbol{Z}_i^T \operatorname{Ln}(\bar{\boldsymbol{x}}))_{i=1,\dots,n}\,,$$

where $\boldsymbol{Z}_i$ denotes the $i-$th column of $\boldsymbol{Z}$, and thus the $n \times n$ matrix

$$\mathcal{L}(\bar{\boldsymbol{x}}) = \boldsymbol{L}\boldsymbol{\Theta}(\bar{\boldsymbol{x}})\,,$$

called *weighted Laplacian matrix* of the graph of complexes, associated with the given complex-balanced network. Both the row and column sums of the weighted Laplacian $\mathcal{L}(\bar{\boldsymbol{x}})$ are equal to zero. As shown in Rao, Schaft, and Jayawardhana, 2013, the matrix $\mathcal{L}(\bar{\boldsymbol{x}})$ is independent of the choice of the complex-balanced equilibrium $\bar{\boldsymbol{x}}$ up to a multiplicative factor for every connected component of the CRN direct graph. The system of ODEs (2.12) for the complex-balanced network can be written as

$$\dot{\boldsymbol{x}} = -\boldsymbol{Z}\mathcal{L}(\bar{\boldsymbol{x}})\operatorname{Exp}(\boldsymbol{Z}^T \operatorname{Ln}(\boldsymbol{x}/\bar{\boldsymbol{x}}))\,. \tag{2.14}$$

Theorem 2.2.2. *Consider a complex-balanced network governed by mass action kinetics. Let $\boldsymbol{S}$ denote the stoichiometric matrix and assume that $\bar{\boldsymbol{x}} \in \mathbb{R}^m_+$ is a complex-equilibrium for the network. The following hold:*

1. *$\bar{\bar{\boldsymbol{x}}} \in \mathbb{R}^m_+$ is another equilibrium for the network if and only if $\boldsymbol{S}^T Ln(\bar{\bar{\boldsymbol{x}}}/\bar{\boldsymbol{x}}) = 0$;*
2. *every positive equilibrium of the network is a complex-equilibrium.*

We now define the notion of deficiency of a CRN and of zero-deficient CRN, first introduced in Feinberg, 1972 in order to relate the stoichiometry of a given network to the structure of the associated graph of complexes.

Definition 2.2.3. The *deficiency* δ of a CRN with complex stoichiometric matrix $\boldsymbol{Z}$, incidence matrix $\boldsymbol{B}$ and stoichiometric matrix $\boldsymbol{S}$ is defined as

$$\delta = \operatorname{rank}(\boldsymbol{B}) - \operatorname{rank}(\boldsymbol{Z}\boldsymbol{B}) = \operatorname{rank}(\boldsymbol{B}) - \operatorname{rank}(\boldsymbol{S}) \geq 0\,.$$

A CRN has zero-deficiency if $\delta = 0$, and is called *zero-deficient* CRN.

Remark 2.2.4. Note that zero-deficiency is equivalent to $\operatorname{Ker}(\boldsymbol{Z}) \cap \operatorname{Im}(\boldsymbol{B}) = 0$, or with the mapping $\boldsymbol{Z}\colon \operatorname{Im}(\boldsymbol{B}) \subset \mathbb{R}^n \to \mathbb{R}^m$ being injective.

Remark 2.2.5. In the work Feinberg, 1972, the deficiency of a CRN has been defined in a different way. Denote by l the number of linkage classes of a given CRN. Note that $l = n - \operatorname{rank}(\boldsymbol{B})$. Then, the deficiency δ was defined as

$$\delta = n - l - \operatorname{rank}(\boldsymbol{S})\,.$$

Hence, in the zero-deficiency case there is a one-to-one correspondence between the rate vector $\dot{\boldsymbol{x}} \in \mathrm{Im}(\boldsymbol{S}) \subset \mathbb{R}^m$ of chemical species $\boldsymbol{x} \in \mathbb{R}^m_+$ and the rate vector $\dot{\boldsymbol{c}} \in \mathrm{Im}(\boldsymbol{B}) \subset \mathbb{R}^n$ of complexes $\boldsymbol{c} \in \mathbb{R}^n$. Many CRNs are zero-deficient, although with growing complexity deficiency greater than zero is likely to occur. The deficiency of a reaction mechanism can be considered as a measure for the linear independence of necessary reactions: if a reaction is a linear combination of other reactions in the system, but cannot be eliminated to simplify the reaction mechanism, then the deficiency of the mechanism will be greater than zero.

The characterization of the possible equilibria for a CRNs strictly connected with the deficiency property is contained in two famous theorems, the deficiency zero theorem and the deficiency one theorem, formulated in Feinberg, 1987; Feinberg, 1995. Both theorems are based on the concept of weak reversibility of the CRN graph of complexes. A reaction mechanism is said to be weakly reversible if for any two complexes in a graph component which are connected by a directed path, there exists a directed path connecting the two complexes in the reverse direction. The zero-deficiency theorem assert two properties of zero-deficient CRNs that hold for any arbitrary choice of rate constants (Feinberg, 1995): (i) if the CRN is weakly reversible, it possesses a single steady state which is asymptotically stable. (ii) If the CRN is not weakly reversible, there exists neither a steady state where all species concentrations are greater than zero, nor is there a periodic trajectory in which all species concentrations are positive. Essentially, the theorem states that only reaction networks with $\delta > 0$ may show non-linear dynamics such as oscillations.

What is possible to prove is that every zero-deficient CRN that admits an equilibrium is complex-balanced. Consequently, all the results holding for a complex-balanced network also apply for a zero-deficient CRN that admits an equilibrium (Rao, Schaft, and Jayawardhana, 2013).

Theorem 2.2.3. *If a CRN is zero-deficient and admits an equilibrium, then it is complex-balanced.*

In order to establish the asymptotic stability of a complex-balanced CRN, in the following a Lyapunov function for the system (2.14) is defined, together with the related properties.

Theorem 2.2.4. *Consider a complex-balanced CRN with stoichiometric matrix $\boldsymbol{S}$, an equilibrium $\bar{\boldsymbol{x}} \in \mathbb{R}^m_+$ and dynamics given by equation* (2.14)*. Define*

$$G(\boldsymbol{x}) = \boldsymbol{x}^T Ln\left(\frac{\boldsymbol{x}}{\bar{\boldsymbol{x}}}\right) + (\bar{\boldsymbol{x}} - \boldsymbol{x})^T \mathbb{1}_m \,, \tag{2.15}$$

where $\mathbb{1}_m$ denotes a vector of dimension m with all entries equal to 1. Then G has a strict minimum at $\bar{\boldsymbol{x}}$, and for $\boldsymbol{x} \in \mathbb{R}^m_+$ it holds

$$\dot{G}(\boldsymbol{x}) \leq 0 \,, \quad \dot{G}(\boldsymbol{x}) = 0 \text{ if and only if } \boldsymbol{x} \in \mathcal{E} \,,$$

where

$$\mathcal{E} = \{\bar{\tilde{\boldsymbol{x}}} \in \mathbb{R}^m_+ \colon \boldsymbol{S}^T Ln(\bar{\tilde{\boldsymbol{x}}}) = \boldsymbol{S}^T Ln(\bar{\boldsymbol{x}})\} \,. \tag{2.16}$$

Remark 2.2.6. The Lyapunov function G is in $\mathbb{R}^{*m}_+$, then the fact that $\dot{G}(\boldsymbol{x}) \leq 0$ implies that the state trajectory $\boldsymbol{x}(\cdot)$ is bounded in $\mathbb{R}^m_+$.

Theorem 2.2.4 does not directly prevent the solution trajectories of the dynamical system (2.14) to approach the boundary equilibria of (2.14) for $t \to \infty$.

Theorem 2.2.5. *Consider the complex-balanced CRN with dynamics given by equation* (2.14) *and equilibrium set $\mathcal{E}$ given by* (2.16). *Then, for every $\boldsymbol{x}_0 \in \mathbb{R}^m_+$ there exists a unique $\boldsymbol{x}_1 \in \mathcal{E} \cap \mathbb{S}_{\boldsymbol{x}_0}$, with $\mathbb{S}_{\boldsymbol{x}_0}$ given by* (2.13). *The equilibrium $\boldsymbol{x}_1$ is (locally) asymptotically stable with respect to all initial conditions in $\mathbb{S}_{\boldsymbol{x}_0}$ nearby $\boldsymbol{x}_1$. Furthermore, if the network is persistent, i.e. for every $\boldsymbol{x}_0 \in \mathbb{R}^m_+$ the w-limit set $w(\boldsymbol{x}_0)$ does not intersect the boundary of $\mathbb{R}^{*m}_+$, then $\boldsymbol{x}_1$ is globally asymptotically stable with respect to all initial conditions in $\mathbb{S}_{\boldsymbol{x}_0}$.*

Essentially, the dynamics of complex-balanced CRNs is characterized by the property that for every initial condition of the concentrations there exists a unique positive equilibrium to which the system will converge. Other dynamics, such as multistability or presence of oscillations, can therefore only occur within CRNs violating these conditions. For an overview of results on CRNs and current research in this direction see Angeli, Leenheer, and Sontag, 2010; Joshi and Shiu, 2015 and the references therein cited.

Part II

Tissue-scale

Chapter 3

Positron Emission Tomography

Positron Emission Tomography (PET) is a nuclear medicine imaging technique which allows the diagnosis and monitoring of various diseases through the production of functional images of biochemical processes occurring in the organism under examination, i.e. providing physiological information. These images are acquired by diffusing a radioactive tracer in the biological system and by mapping the decay of radioisotopes bound to molecules with specific metabolic properties. The PET has an important application in oncology: the distribution of the glucose analog radioactive tracer [^{18}F]-fluorodeoxyglucose (FDG) may show pathological glucose uptake in the presence of tumors. Often functional medical imaging techniques are combined with morphological methods, such as Computed Tomography (CT) and Magnetic Resonance Imaging (MRI), which provide anatomical information, in order to obtain dynamic images of tracer metabolism anatomically well defined.

In this chapter a PET experiment is described. In the first section, the PET physical principles and the process of data formation are illustrated. The second section deals with the well-known inverse problem of image reconstruction, for whose solution two distinct approaches are presented: the analytical method Filtered Back-Projection (FBP), based on the inversion of the Radon transform, and the statistical method Maximum Likelihood Expectation Maximization (MLEM), utilizing iterative techniques for the estimation of the solution.

3.1 PET data formation

PET (Bailey et al., 2005; Ollinger and Fessler, 1997) is an imaging technique that can detect the spatial and temporal distribution of pico-molar quantities of a radioactive tracer, which is diffused in a living body or in one of its parts, such as an organ or a tissue. The PET study begins after the injection of a radiopharmaceutical (composed of a substrate, added to a radioisotope, easily metabolized by the cells) and a delay ranging from seconds to minutes needed for the tracer to distribute uniformly in the body under examination. When the radiopharmaceutical reaches the cells, the substrate is metabolized causing the release of the radioisotope, a non-stable atom that naturally decays into another stable atom. In the case of PET, the radioisotopes decay emitting a positron ($\beta+$), which travels for a short distance (typically 1mm) before interacting with an electron ($e-$) of the body. The interaction determines the *annihilation* of both particles, with conversion into energy of the masses and the production of two high-energy gamma photons (511 keV) which propagate in opposite direction along a line called line of response (LOR). This physical process is illustrated in Figure 3.1.

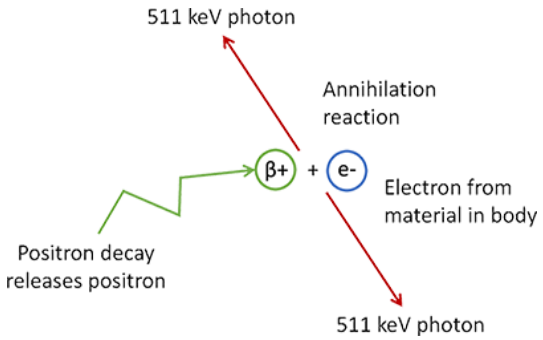

FIGURE 3.1: Scheme of the PET annihilation process: the $\beta+$ emitted positron interacts with an electron $e-$ producing two gamma-photons of 511 keV energy that propagate along opposite directions (from Radiology Cafe website).

The gamma rays reach the scintillation crystals inside the PET scanner and are subsequently detected by the photomultiplier tubes. Basically, the photon interacting with the crystal releases, partially or totally, its energy, which is then converted into visible light and directed towards the photomultiplier tube to be transformed into an electrical impulse. The scintillation crystals and the photomultiplier tubes constitute a single block called *detector*; more detectors are combined to form cylindrical rings placed next to each other and composing the scanner, which surrounds the body during the PET study (Figure 3.2).

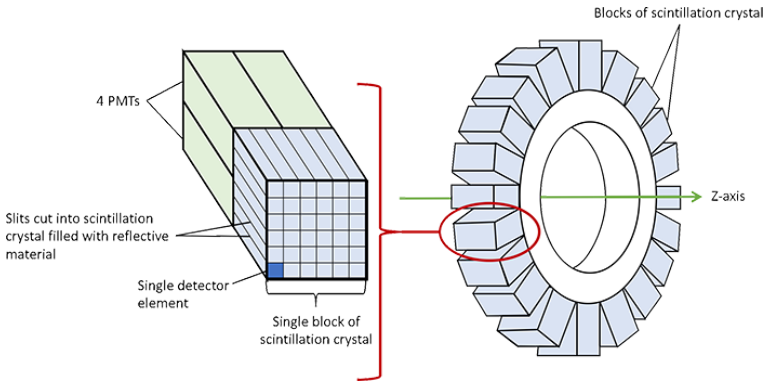

FIGURE 3.2: PET detector ring in a cylindrical geometry scanner: each block consists of the scintillation crystals and the photomultiplier tubes (PMTs) (from Radiology Cafe website).

The PET scanner has the task of detecting the emitted gamma rays and reconstructing the precise location of the emission source, but not all the produced photon pairs can be acquired. Photons not reaching the detector within a time frame of a few nanoseconds are not taken into account. If, on the other hand, the two photons are received in a short predefined timing window (about 10 nsec), an event is recorded along the line connecting the two detectors that have detected the gamma rays. Summing many such events results in quantities that approximate the line integrals through the radioisotope distribution. Obviously, the number and the quality of the recorded counts can have a significant influence on the validity of this approximation: the more reliable counts one is able to collect, the more accurate approximation of the line integrals is obtained, which leads to a better reconstruction of the radioisotope distribution. For this reason, in addition to a timing window, an energy window is added, in order to collect photons in a small energy interval around

511 keV (about 350-650 keV). In this energy range there is a possible photon-electron scattering phenomenon: the *Compton effect*. In a Compton interaction, a photon interacts with a free electron that that deflects its path, causing a loss of energy. In PET, most scattered photons are deflected out of the field of view (FOV) of the scanner and are lost. The effect of these interactions is called *attenuation*; the probability of a photon not to interact with an electron along its LOR is called *narrow-beam attenuation*. Because of the large number of scattered photons, it happens that for many annihilation processes only one of the two photons is actually detected. These events are called *singles*.

An emission signal correctly recorded is called coincidence event. Figure 3.3 shows the different types of coincidence events occurring in the PET scanner:

- a *true coincidence* is an event that originates from a single positron-electron annihilation in which the generated photons do not undergo any interaction before being detected;
- an *accidental coincidence* is recorded when two photons originating in two distinct annihilations (e.g. two singles) are considered to be a single event, as they are simultaneously detected; the system will identify as origin point a non-existent point placed halfway between the two original annihilations;
- a *scattered coincidence* occurs when one or both of the emitted photons underwent a Compton interaction before reaching the detector; the system will identify a virtual origin point.

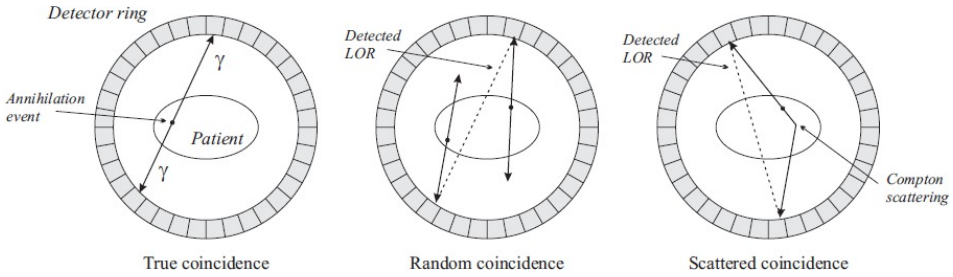

FIGURE 3.3: The different types of coincidence events occurring in the PET scanner.

For the accuracy of the measurements it is essential that each registered LOR reflects a real event so as to obtain a reliable estimate of the tracer distribution and not to add noise to the final image. Accidental coincidences and scattered coincidences give rise to LORs not containing the emission source. Therefore, these types of events have to be identified and then corrected; suitable techniques able to address such problems can be consulted in Bailey et al., 2005.

The counting rate of a PET scanner is also dependent on the *detector deadtime*. In fact, the time required for the scanner to process an event influences the collection of the events: each event processing begins with the detection a photon impulse by the detector involved, then the impulse is integrated for some time interval, and finally the scanner performs position calculations and energy discrimination. The involved detector is dead to new events during this time, and it is not able to detect and measure any of the photons that collide its crystal.

If statistical effects are ignored, all the previous physical factors can be incorporated into a model for the total number of recorded events, leading to the following

equation of PET data formation (Ollinger and Fessler, 1997):

$$Y_{(s,\phi)} = \gamma^{d}_{(s,\phi)}(\eta^{t}_{(s,\phi)}\eta^{a}_{(s,\phi)}M_{(s,\phi)} + \eta^{r}_{(s,\phi)}r_{(s,\phi)} + \eta^{f}_{(s,\phi)}f_{(s,\phi)}) \,, \tag{3.1}$$

where, for each LOR, identified with the couple (s,ϕ), $Y_{(s,\phi)}$ is the total number of recorded events, $M_{(s,\phi)}$ is the number of annihilations with photons emitted along the LOR, $\eta^{t}_{(s,\phi)}$ is the probability of detection for true events, $\eta^{a}_{(s,\phi)}$ is the narrow-beam attenuation, $\eta^{r}_{(s,\phi)}$ is the probability of detection for accidental coincidences, $r_{(s,\phi)}$ is the number of accidental coincidences, $\eta^{f}_{(s,\phi)}$ is the probability of detection for scattered events, $f_{(s,\phi)}$ is the number of scattered events, $\gamma^{d}_{(s,\phi)}$ is the probability of an event not being lost due to the deadtime of the PET scanner.

3.2 PET image reconstruction

The aim of PET image reconstruction is to obtain the dynamic distribution of radiotracer concentration from the PET measurements collected in the PET sinograms. This type of inverse problem is well-known and for its solution there exist essentially two different approaches: analytical inverse formula and statistical iterative techniques.

The values of PET data can be modeled through both deterministic and stochastic variables. If we assume that the datum is deterministic, then the noise introduced by the measurement is a deterministic number and, if known, we can find the exact solution of the image reconstruction problem. To tackle this problem, methods involving the inversion of the Radon transform (Natterer, 2001) are used, e.g. FBP.

Actually, the data values are intrinsically stochastic, due to the physical effects involved in the measurement procedure: the positron decay process, the effects of attenuation, the addition of scattered and random events, and the photon detection process. Therefore, the noise is well described by a random process. As a consequence, the exact solution for the problem cannot be found and estimation techniques are needed, leading to a good approximate solution only through some form of regularization. In the field of tomographic reconstruction, these methods consist of statistical iterative algorithms (Lalush and Wernick, 2004), requiring specific assumption on data noise (Gaussian or Poisson), e.g. MLEM (Shepp and Vardi, 1982) and its accelerated version Ordered Subsets Expectation Maximization (OSEM) (Hudson and Larkin, 1994).

3.2.1 PET imaging system

The PET scanner consists of multiple rings placed one next to each other composed of detectors. During a PET acquisition, it may happen that a coincidence event involves the same ring or two distinct rings. This difference gives rise to the two possible ways of acquiring PET data (Figure 3.4):

- 2D imaging collects direct LORs (direct planes), belonging to the same detector ring, and crossed LORs (crossed planes), connecting adjacent rings; to image a volumetric object it is necessary to repeat the 2D acquisition for multiple axial slices;
- 3D imaging records both direct LORs and oblique LORs (oblique planes), lying on planes that are oblique with respect to the detector rings and placed within a predefined volume.

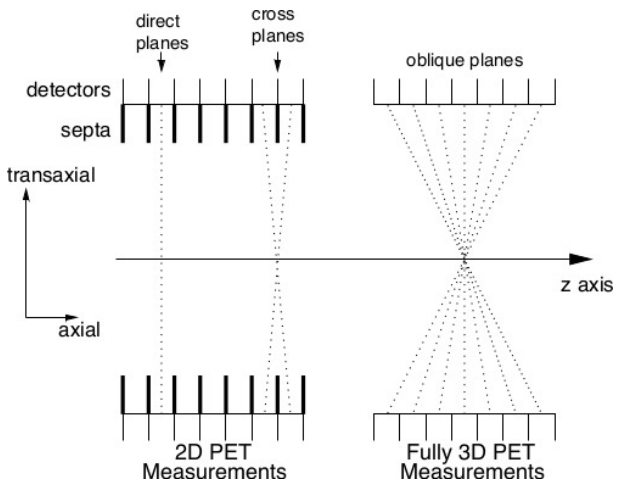

FIGURE 3.4: Comparison of 2D and 3D PET imaging systems. In the 2D measurements, the direct planes and the crossed planes are collected; in 3D measurements, also the oblique planes are considered.

The 3D PET scanner collects a greater number of LORs with a substantial gain in terms of sensitivity, and thus lowers the photon counting noise, compared to 2D acquisition. However, 3D measurements require more storage of data, and involve a significant increase in accidental and scattered events, which must be corrected with an elevated computational cost in the management of data.

Let consider the 2D PET mode. The acquired data are collocated along LORs through the object $f(x, y)$ (Figure 3.5). The LORs are organized into sets of projections, i.e. line integrals for all s for a fixed direction ϕ. The collection of all projections $p(s, \phi)$ forms the two-dimensional sinogram of the object $f(x, y)$: in the case of a point source, s varies sinusoidally with ϕ when it is stored in an array with columns indexed by s and the rows by ϕ. A sinogram for a general object will be the superposition of all sinusoids corresponding to each point of activity in the object (Figure 3.6). The volumetric object $f(x, y, z)$ is formed by stacking together the two-dimensional images obtained for multiple axial slices z.

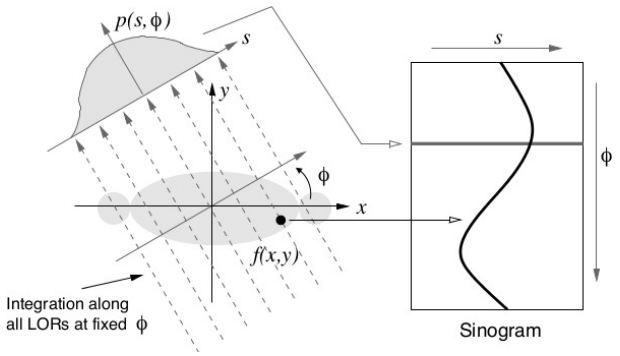

FIGURE 3.5: A projection $p(s, \phi)$ formed from integration along all parallel LORs at an angle ϕ crossing the object $f(x, y)$. The projections are organized into a sinogram.

In general, the PET imaging system is represented by the linear equation

$$p = \mathcal{R}f + n \,, \tag{3.2}$$

where p is the datum (the set of projections or the sinogram), $\mathcal{R}$ is the known system

model, f is the unknown image, and n is the noise introduced by the measurement process. The reconstruction of PET images aims at determining the image f from the projections p obtained with the imaging system, by solving an inverse problem.

FIGURE 3.6: During the 2D PET acquisition, the object emitting radioactivity on the left-hand side provides the sinogram on the right-hand side.

3.2.2 Analytical inverse formula

By assuming a deterministic datum, we are able to find the exact solution f of the PET imaging inverse problem, defined by equation $p = \mathcal{R}f$, where the additive deterministic noise is omitted. We first introduce some definition and notation.

Definition 3.2.1. The *Schwartz space* $\mathcal{S}(\mathbb{R}^n)$ is defined as

$$\mathcal{S}(\mathbb{R}^n) := \{f \in \mathcal{C}^\infty(\mathbb{R}^n) : \sup_{x\in\mathbb{R}^n} |x^l \partial^k f(x)| < +\infty,\ \forall l,k \in \mathbb{Z}_+^n\}\ ,$$

where l and k are multi-indexes in $\mathbb{Z}_+^n$.

Definition 3.2.2. Let $C^n := \{(\theta, s) : \theta \in S^{n-1},\ s \in \mathbb{R}\}$ be the cylinder in $\mathbb{R}^n$, where S^{n-1} is the sphere in $\mathbb{R}^{n-1}$. The Schwartz space on the cylinder $\mathcal{S}(C^n)$ is defined as

$$\mathcal{S}(C^n) := \{f \in \mathcal{C}^\infty(C^n) : \sup_{\theta\in S^{n-1}, s\in\mathbb{R}} \left| s^l \frac{\partial^k \partial^j f(\theta,s)}{\partial\theta^k \partial s^j} \right| < +\infty,\ \forall l,j \in \mathbb{Z}_+,\ \forall k \in \mathbb{Z}_+^{n-1}\}\ .$$

Definition 3.2.3. Let $f \in L^1(\mathbb{R}^n)$. The *Fourier transform* of f is defined as

$$\hat{f}(\xi) := (2\pi)^{-n/2} \int_{\mathbb{R}^n} f(x) e^{-ix\cdot\xi}\, dx\ .$$

Remark 3.2.1. If $f \in \mathcal{S}(\mathbb{R}^n)$, then $\hat{f} \in \mathcal{S}(\mathbb{R}^n)$. Furthermore, it is possible to define the *inverse Fourier transform*

$$\tilde{f}(x) := (2\pi)^{-n/2} \int_{\mathbb{R}^n} \hat{f}(\xi) e^{ix\cdot\xi}\, d\xi\ ,$$

s.t. $\tilde{f} \in \mathcal{S}(\mathbb{R}^n)$ and $\hat{\tilde{f}} = \tilde{\hat{f}} = f$, i.e. the Fourier transform on $\mathcal{S}(\mathbb{R}^n)$ is bijective.

Definition 3.2.4. Let $H(\theta, s) := \{x \in \mathbb{R}^n : x \cdot \theta = s\}$ be the hyperplane in $\mathbb{R}^n$ perpendicular to $\theta \in S^{n-1}$ with distance s from the origin. The *Radon transform* $\mathcal{R}$ is the bounded integral operator defined as

$$\begin{aligned} \mathcal{R}\colon \mathcal{S}(\mathbb{R}^n) &\to \mathcal{S}(C^n) \\ f &\mapsto \int_{H(\theta,s)} f(x)\, dx = \int_{\theta^\perp} f(s\theta + y)\, dy\ . \end{aligned}$$

Definition 3.2.5. A *projection* of f at direction $\theta \in [0, \pi)$ is the integral operator $\mathcal{R}_\theta \colon \mathcal{S}(\mathbb{R}^n) \to \mathcal{S}(\mathbb{R})$ s.t. $(\mathcal{R}_\theta f)(s) = \mathcal{R}f(\theta, s)$.

The following result states a fundamental property that links the Fourier transform with the Radon transform of suitable functions, and essential in order to prove that there exists the inverse of the Radon transform (Bertero and Boccacci, 1998).

Theorem 3.2.1 (Fourier Slice Theorem)**.** *If $f \in \mathcal{S}(\mathbb{R}^n)$, then $(\widehat{\mathcal{R}_\theta f})(\sigma) = (2\pi)^{\frac{n-1}{2}} \hat{f}(\sigma\theta)$.*

An essential step in image reconstruction is the backprojection, which is the adjoint to forward projection process that forms the projections of the object.

Definition 3.2.6. The adjoint of the projection is the backprojection $\mathcal{R}_\theta^{\#} \colon \mathcal{S}(\mathbb{R}) \to \mathcal{S}(\mathbb{R}^n)$ s.t. $(\mathcal{R}_\theta^{\#} p)(x) = p(x \cdot \theta)$. Therefore, the backprojection of the Radon transform $\mathcal{R}^{\#}$ is defined as

$$\begin{aligned} \mathcal{R}^{\#} \colon \mathcal{S}(C^n) &\to \mathcal{S}(\mathbb{R}^n) \\ p &\mapsto \mathcal{R}^{\#} p \,, \end{aligned}$$

where $(\mathcal{R}^{\#} p)(x) := \int_{S^{n-1}} p(\theta, x \cdot \theta)\, d\theta$.

Theorem 3.2.2 (Inversion of the Radon transform)**.** *If $f \in \mathcal{S}(\mathbb{R}^n)$ and $p = \mathcal{R}f$, then*

$$f(x) = \frac{1}{2}(2\pi)^{1-n}(\mathcal{I}^{-\alpha}\mathcal{R}^{\#}\mathcal{I}^{\alpha+1-n} p)(x) \,, \tag{3.3}$$

where $\mathcal{I}^\alpha$ is the linear Riesz potential s.t. $(\widehat{\mathcal{I}^\alpha f})(\xi) = |\xi|^{-\alpha} \hat{f}(\xi)$, for $f \in \mathcal{S}(\mathbb{R}^n)$ and $\alpha \in \mathbb{R}$ s.t. $\alpha < n$.

Remark 3.2.2. We point out some remarks.

- Since $\alpha < n$, then $\widehat{\mathcal{I}^\alpha} \in L^1(\mathbb{R}^n)$. Therefore, it is possible to perform the inverse Fourier transform and define the inverse of the Riesz potential as $\mathcal{I}^{-\alpha}$, s.t. $\mathcal{I}^{-\alpha}\mathcal{I}^\alpha f = f$.
- The formula for the inversion of the Radon transform (3.3) is a one-parameter family of formulas, varying for $\alpha \in \mathbb{R}$ s.t. $\alpha < n$.
- If $\alpha = 0$, then $f(x) = \frac{1}{2}(2\pi)^{1-n}(\mathcal{R}^{\#}\mathcal{I}^{1-n} p)(x)$, where $\mathcal{I}^{1-n}$ acts on a function of $\mathbb{R}$. For a function $g \in \mathcal{S}(\mathbb{R})$, define the Hilbert transform $\mathcal{H}$ as

  $$(\mathcal{H}g)(x) := \frac{1}{\pi} \int_{\mathbb{R}} \frac{g(y)}{x - y}\, dy \,,$$

  and its Fourier transform

  $$(\widehat{\mathcal{H}g})(\xi) = -i \operatorname{sign}(\xi) \hat{g}(\xi) \,.$$

  Then, it holds

  $$(\widehat{\mathcal{I}^{1-n} g})(\xi) = |\xi|^{n-1} \hat{g}(\xi) = \operatorname{sign}(\xi)^{n-1} \xi^{n-1} \hat{g}(\xi) \,,$$

  and thus,

  $$\mathcal{I}^{1-n} g = \mathcal{H}^{n-1} g^{(n-1)} \,,$$

with $g^{(n-1)}$ the $(n-1)$th derivative of g. By applying this property in the inverse formula for f, we get

$$f(x) = \frac{1}{2}(2\pi)^{1-n}(\mathcal{R}^{\#}\mathcal{H}^{n-1}p^{(n-1)})(x)\,, \tag{3.4}$$

where the $(n-1)$th derivative is taken with respect to the first argument. The Hilbert transform has the following property

$$\mathcal{H}^{n-1} = \begin{cases} (-1)^{(n-2)/2}\mathcal{H} & \text{if } n \text{ even} \\ (-1)^{(n-1)/2} & \text{if } n \text{ odd} \end{cases},$$

equation (3.4) can be rewritten as

$$f(x) = \frac{1}{2}(2\pi)^{1-n} \begin{cases} (-1)^{(n-2)/2} \int_{S^{n-1}} \mathcal{H}p^{(n-1)}(\theta, x\cdot\theta)\,d\theta & \text{if } n \text{ even} \\ (-1)^{(n-1)/2} \int_{S^{n-1}} p^{(n-1)}(\theta, x\cdot\theta)\,d\theta & \text{if } n \text{ odd} \end{cases}. \tag{3.5}$$

The fact that $\mathcal{H}$ appears only in the even cases has an important consequence. Since $p(\theta, x\cdot\theta)$ is the integral of f over the hyperplane perpendicular to θ that contains x, the reconstruction of f is local in the odd cases: the evaluation of equation (3.5) at some point x requires the integrals of f along all hyperplanes meeting a neighbor of x. On the contrary, if n is even, the problem of reconstructing f is not local since $\mathcal{H}$ is not local: equation (3.5) is evaluated at some point x by computing the integrals along all hyperplanes meeting the support of the function.

- In the framework of PET reconstruction problem, the Radon transform is a compact operator; therefore, the inverse of the Radon transform is not bounded and in order to reconstruct the image f a form of regularization is needed.

Theorem 3.2.3 (Filtered backprojection)**.** *If $f \in \mathcal{S}(\mathbb{R}^n)$ and $p = \mathcal{R}f$, then*

$$f(x) = \frac{1}{2}(2\pi)^{1-n}(\mathcal{I}^{-\alpha}\mathcal{R}^{\#}\mathcal{I}^{\alpha+1-n}(w_c * p))(x)\,, \tag{3.6}$$

where $*$ denotes the convolution operation, and w_c is a ramp filter that filters the projections before applying the backprojection operator.

This result ensures that it is possible to filter the projections p before the backprojection step and obtain again the objective function f, yielding an exploitable inversion formula for the Radon transform, that could be used in practice. Regularization is obtained by means of an optimal choice of the cut-off frequency c of the filter w_c (Bertero and Boccacci, 1998).

2D FBP method

The 2D PET image reconstruction problem consists in finding $f \in \mathcal{S}(\mathbb{R}^2)$ s.t. $p = \mathcal{R}f$, where $p \in \mathcal{S}(C^2)$ is the known set of projections measured by the PET system and $\mathcal{R}$ is the Radon transform. In order to obtain the image f, it is necessary to invert the Radon transform. In this context, the Radon transform defines a compact operator between (weighted) L^2-spaces, and therefore its inverse is not bounded. Then the solution does not depend continuously on the data, generating an intrinsic numerical instability which, in the presence of noise on the data, amplifies the noise on the solution.

Suppose that the body under examination lies at the center of a LOR connecting two detectors, and consider only direct planes. We introduce a system of coordinates $\boldsymbol{x} = (x_1, x_2)$ with origin in the positron annihilation point, and a variable coordinate system $\boldsymbol{\theta} = (cos(\phi), sin(\phi))$ indicating the LOR direction. Then, the two-dimensional backprojection (BP) is given by

$$f(\boldsymbol{x}) = \frac{1}{4\pi} \int_0^{2\pi} (2\pi)^{-1/2} \int_{-\infty}^{+\infty} (\hat{\mathcal{R}_{\boldsymbol{\theta}} f})(\xi) |\xi| e^{i\xi \boldsymbol{\theta} \cdot \boldsymbol{x}} \, d\xi \, d\phi \, . \tag{3.7}$$

Given the Radon projections $p_{\boldsymbol{\theta}} = \mathcal{R}_{\boldsymbol{\theta}} f$, f can be reconstructed by filtering the Radon transform by means of the ramp filter $|\xi|$, by inverting its filtered Fourier transform, and then by backprojecting it by means of the two-dimensional backprojection operator $(\mathcal{R}^{\#} p_{\boldsymbol{\theta}})(\boldsymbol{x}) = \int_0^{2\pi} p_{\boldsymbol{\theta}}(\boldsymbol{x} \cdot \boldsymbol{\theta}) \, d\phi$.

In presence of noise on the data, the BP is modified into the FBP by introducing the additional low-pass filter w_c, which attenuates the signal with frequencies higher than the cutoff frequency c. Equation (3.7) becomes

$$f(\boldsymbol{x}) = \frac{1}{4\pi} \int_0^{2\pi} (2\pi)^{-1/2} \int_{-\infty}^{+\infty} (\hat{\mathcal{R}_{\boldsymbol{\theta}} f})(\xi) |\xi| w_c(\xi) e^{i\xi \boldsymbol{\theta} \cdot \boldsymbol{x}} \, d\xi \, d\phi \, . \tag{3.8}$$

A typical low-pass filter used in tomography is the Hamming filter:

$$w_c^{ham}(\xi) = \begin{cases} 1/2(1 + cos(\pi \xi / c)) & \text{if } |\xi| < c \\ 0 & \text{if } |\xi| \geq c \end{cases} .$$

By summarizing, the FBP algorithm for the 2D PET image reconstruction problem is the following (Natterer, 2001).

Algorithm 3.1. [2D-FBP]

Step 1. Given the 2D PET projections $p_{\boldsymbol{\theta}} = \mathcal{R}_{\boldsymbol{\theta}} f$, compute $\hat{p_{\boldsymbol{\theta}}}$.

Step 2. Multiply $\hat{p_{\boldsymbol{\theta}}}(\xi)$ by the ramp filter $|\xi|$.

Step 3. Multiply by the low-pass filter w_c.

Step 4. Compute the one-dimensional inverse Fourier transform.

Step 5. Apply the backprojection $\mathcal{R}^{\#}$.

Step 6. Multiply by $1/4\pi$.

3.2.3 Statistical iterative technique

By assuming that the data can be modeled through stochastic variables, then statistical iterative reconstruction techniques can be used, accounting for the structure of the noise on the data and thus able to describe the model of the problem with more reliability. However, the improvement in the quality of the reconstruction comes at the cost of an increased complexity in the mathematical formulation and a loss of speed in the reconstruction algorithm.

Unlike the analytical inversion formula of the deterministic case, applying a statistical technique to the PET image reconstruction problem does not provide an exact solution but relies on the estimation of the solution. The iterative reconstruction algorithms are based on the discrete representation of both the data and the image, in contrast to analytical methods that introduce the discrete character of the problem

a posteriori. Furthermore, the development of iterative algorithms is completely independent of the geometry of the imaging system and is therefore applicable in an equivalent way to the acquisition of the 2D and 3D PET data.

MLEM method

The Maximum Likelihood (ML) approach estimates the object f from noisy data p, satisfying $p = \mathcal{R}f + n$. The method is based on the assumption that the data p are observed values of a random process P with mean $\mathcal{R}f$. The density function of P is given by the joint probability density function $\mathcal{P}_\eta(p, \mathcal{R}f)$, where η indicates a generic random process. When this density is thought of as a function of f given p, we call it the likelihood

$$\mathcal{L}_p(f) = \mathcal{P}_\eta(p, \mathcal{R}f) \,. \tag{3.9}$$

Once the operator $\mathcal{R}$ and the data p are given, ML obtains the estimation of the solution f when the likelihood reaches its maximum value. The nature of the problem implies the physical constraint of non-negative estimate; therefore, the constrained ML estimator is

$$\tilde{f} = \arg\max_{f \geq 0} \mathcal{L}_p(f) \,. \tag{3.10}$$

Usually, it is more convenient to minimize the negative logarithm of the likelihood instead of maximizing it; then, the constrained ML problem (3.10) is equivalent to

$$\tilde{f} = \arg\min_{f \geq 0}(-\log(\mathcal{L}_p(f))) \,. \tag{3.11}$$

In general, when both the likelihood function and the constraint are convex, the necessary and sufficient conditions for f to be the constrained ML estimator are the Karush-Khun-Tucker (KKT) conditions (Boyd and Vandenberghe, 2004), which take the form

$$f\nabla(-\log(\mathcal{L}_p(f))) = 0 \,, \quad f \geq 0 \,. \tag{3.12}$$

The statistical model to be adopted follows the type of measurement. In the case of PET, data are obtained by collecting the photos of annihilation in a finite time interval and thus PET measurements consist in a counting process with Poisson noise. Then, PET data are modeled by independent random variables with Poisson distribution. When η is a vector of independent and identically distributed Poisson variables with rate parameter $\mathcal{R}f$, the negative logarithm of the likelihood is the Kullback Leibler divergence

$$-\log(\mathcal{L}_p(f)) = p \, \log\left(\frac{p}{\mathcal{R}f}\right) + \mathcal{R}f - p \,. \tag{3.13}$$

Hence, the constrained ML problem (3.11) is equivalent to the minimization of the divergence (3.13) under the non-negativity constraint. In the Poisson case, the KKT conditions lead to the Expectation Maximization (EM) iterative algorithm (Carson and Lange, 1985; Lalush and Wernick, 2004), that reads:

$$f^{(i+1)} = \frac{f^{(i)}}{\mathcal{R}^T\mathbb{1}}\mathcal{R}^T\frac{p}{\mathcal{R}f^{(i)}} \,, \tag{3.14}$$

where i represents the iteration step in the estimation procedure, and $f^{(i)}$ is the i-th estimate of f.

The PET image reconstruction problem is to determine a non-negative f, given the projections p affected by Poisson noise, s.t. $p = \mathcal{R}f$. The MLEM iterative procedure for the estimation of f as the maximum-likelihood solution is the following (Shepp and Vardi, 1982).

Algorithm 3.2. [MLEM]

Step 1. Choose the initial guess $f^{(0)}$.

Step 2. Project forwardly $f^{(0)}$ into the projection domain by computing $\mathcal{R}f^{(0)}$.

Step 3. Compare with the given projections p as $p/\mathcal{R}f^{(0)}$.

Step 4. Backproject into the image domain through $\mathcal{R}^T$.

Step 5. Multiply by $f^{(0)}$, normalized by a weighting term.

Step 6. A new mage estimate $f^{(1)}$ is obtained; iterate.

With the purpose of reducing the reconstruction time of MLEM for applications in clinical practice, OSEM was introduced by Hudson and Larkin, 1994. The OSEM iterative algorithm is based on equation

$$f^{(i+1)} = \frac{f^{(i)}}{(\mathcal{R}_{|S_a})^T \mathbb{1}} (\mathcal{R}_{|S_a})^T \frac{p}{\mathcal{R}f^{(i)}} \,, \tag{3.15}$$

where the backprojection step sum only over a subset S_a of a total of A projection subset. OSEM is a computationally convenient method, A times faster than MLEM, but it does not ensures convergence to the ML solution.

Chapter 4

Reference Tissue Model

In general, compartmental analysis aims at the determination of the rate constants from the time concentration curves of tracer in a specific target tissue (TT) and in the arterial blood. The time-dependent concentrations are recovered by drawing regions of interest (ROIs) on the reconstructed Positron Emission Tomography (PET) images of tracer distribution. In principle, the blood input function (IF) can be determined by computing the image content of a ROI positioned over a sufficiently large blood pool, such as the left ventricle. However, the procedure is subject to systematic errors arising from, e.g., partial volume effects, spillover, cardiac motion, and the low resolution of PET cameras (see Zanotti-Fregonara et al., 2011 and the references therein cited).

To avoid direct reference to the IF, alternative approaches have been developed which have been referred to as reference tissue models (RTMs). The idea is that a time concentration curve measured over a ROI belonging to a suitably chosen reference tissue (RT) may be used to provide an estimate of the IF (Schmidt and Turkheimer, 2002). Reference tissue approaches are reported to provide robust estimates of the unknown parameters if the RT can be modeled as a one-compartment system, e.g., in the case of a radiotracer with reasonably fast kinetics or negligible specific binding (Lammertsma and Hume, 1996; Schmidt and Turkheimer, 2002; Tichauer et al., 2012a; Zhou et al., 2003; Zhou et al., 2007; Ginovart et al., 2001). Rather similar approaches (dual-tracer models) have also been developed such that, in place of considering the RT, a second untargeted tracer is injected and diffused inside the TT (Tichauer et al., 2012a; Tichauer et al., 2012b; Tichauer et al., 2014; Tomasi et al., 2012).

The procedure proposed (Scussolini et al., 2018c) may be regarded as a revisitation of reference tissue approaches. We consider a RTM for the analysis of [^{18}F]-fluorodeoxyglucose (FDG) kinetics, which is composed by a two-compartment TT, a one-compartment RT, and six kinetic parameters. It is shown that the RTM is identifiable, i.e. the rate constants are uniquely retrievable, provided that a selection criterion for one of the coefficients is introduced. The RTM together with the procedure for the solution of the compartmental inverse problem are validated on synthetic data and applied to a group of micro-PET experimental data of murine models with murine cancer cell lines CT26.

The first section provides the mathematical setup of the RTM and discusses the model identifiability. The second section deals with the numerical validation of the computational method for the reduction of the RTM, while the third section applies the method against the experimental datasets.

4.1 Mathematical models

A RTM is a compartmental approach to the estimation of the kinetic parameters of the tracer flow in a given TT without explicit knowledge of the blood IF as the time concentration curve of the arterial blood. The idea of reference tissue approaches is to utilize the time-dependent tracer concentration of a suitably chosen RT providing an indirect measure of arterial concentration. The RTM is formed by the RT and the TT. We assume that the conditions for applicability of compartmental analysis are satisfied (for details see subsection 1.1.1), and we adopt the usual notations of compartmental analysis (as in Chapter 1).

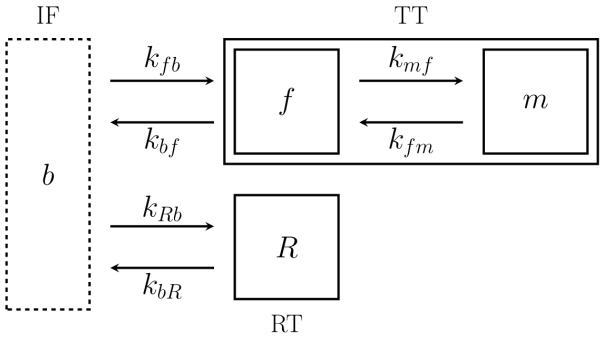

FIGURE 4.1: The RTM accounting for a two-compartment TT, a one-compartment RT, and six rate constants connecting the TT and RT through the blood IF.

We consider an RTM (Figure 4.1) comprising:

- a two-compartment TT for both free (f) and metabolized (m) tracer;
- a one-compartment RT (R), supposed to be free of tracer receptors;
- six kinetic parameters, $k_{fb}, k_{bf}, k_{mf}, k_{fm}$ for the TT, and k_{Rb}, k_{bR} for the RT.

The blood (b) compartment is formally introduced in order to describe the tracer kinetics in the TT and RT. The arterial blood concentration C_b supplies the IF. The time concentration curves of the TT and the RT are reconstructed from suitable ROIs on PET image data. No a priori restrictions on rate coefficients are introduced; in particular, we do not require any equality of volume distributions for TT and RT, a rather strong assumption which has been subject to criticism (Tichauer et al., 2012a; Tichauer et al., 2012b).

4.1.1 One-compartment reference tissue

The concentration of bound tracer in the RT is taken as significantly low to be neglected (Lammertsma and Hume, 1996; Schmidt and Turkheimer, 2002; Tichauer et al., 2012a; Zhou et al., 2003; Zhou et al., 2007; Ginovart et al., 2001). Thus the RT is modeled as a single compartment (R) of tracer concentration C_R. As a consequence of the balance equation for tracer, it is found that C_R solves the Cauchy problem

$$\dot{C}_R = -k_{bR}C_R + k_{Rb}C_b\,, \quad C_R(0) = 0\,, \tag{4.1}$$

where k_{Rb} and k_{bR} (min^{-1}) are the rate constants for tracer exchange from arterial blood to reference tissue, and conversely. The analytical solution of the Cauchy

problem (4.1) is

$$C_R(t; C_b, \boldsymbol{k}_R) = k_{Rb} \int_0^t e^{-k_{bR}(t-\tau)} C_b(\tau)\, d\tau \,, \tag{4.2}$$

where $t \in \mathbb{R}_+$, and $\boldsymbol{k}_R = (k_{Rb}, k_{bR})^T \in \mathbb{R}^2_+$.

We assume that the volume fraction occupied by blood in RT V_{bR} can be estimated or measured a priori. Thus the total radioactivity concentration in RT $\mathscr{C}_R$ is given by

$$\mathscr{C}_R(t; C_b, \boldsymbol{k}_R) = (1 - V_{bR}) C_R(t; C_b, \boldsymbol{k}_R) + V_{bR} C_b(t) \,. \tag{4.3}$$

We let

$$k_{bR} = \lambda k_{Rb} \,. \tag{4.4}$$

The interpretation of the constant adimensional parameter λ follows from the observation that

$$\lambda = \frac{k_{bR}}{k_{Rb}} = \frac{1}{DV_{\mathrm{RT}}} \,, \tag{4.5}$$

where DV_{RT} is the distribution volume of the RT (Zhou et al., 2003).

It is found from (4.1), (4.3), and the definition of λ (4.5) that

$$\int_{t_0}^t \mathscr{C}_R(\tau)\, d\tau = \beta_1 \int_{t_0}^t C_b(\tau)\, d\tau + \frac{(1 - V_{bR})}{k_{bR}} (C_R(t_0) - C_R(t)) \,,$$

where

$$\beta_1 = (1 - V_{bR}) \frac{1}{\lambda} + V_{bR} \,, \tag{4.6}$$

and $t_0 < t$. Division by $\mathscr{C}_R$ leads to equation

$$Y = \beta_1 X + \beta_2 \,, \tag{4.7}$$

with

$$Y = \frac{\int_{t_0}^t \mathscr{C}_R}{\mathscr{C}_R} \,, \quad X = \frac{\int_{t_0}^t C_b}{\mathscr{C}_R} \,, \quad \beta_2 = \frac{(1 - V_{bR})}{k_{bR}} \left(\frac{C_R(t_0) - C_R(t)}{\mathscr{C}_R} \right) \,, \tag{4.8}$$

known as *asymptotic Logan plot* of the RT. In the plane referred to Cartesian axes (X, Y), equation (4.7) represents a curve parameterized by t. If we assume that t_0 is sufficiently large that $\mathscr{C}_R(t_0)$ is close to the asymptotic equilibrium value, then the curve (4.7) is well approximated by a line of slope β_1. Therefore, we can determine β_1 by means of a polynomial curve (of degree one) fitting procedure on (4.7), utilizing the measured asymptotic values of $\mathscr{C}_R$ and C_b. From the knowledge of β_1 and V_{bR}, is straightforward to obtain λ through equation (4.6); therefore, from now on the parameter λ is regarded as known.

Since the concentration $\mathscr{C}_R$ can be measured with more accuracy than C_b, in the following analysis we replace C_b with its expression in terms of $\mathscr{C}_R$. By time-deriving equation (4.3) and by substituting $\dot{C}_R$ through the RT balance equation (4.1), we find

$$\dot{C}_b = -\gamma k_{Rb} C_b + \frac{1}{V_{bR}} (\dot{\mathscr{C}}_R + \lambda k_{Rb} \mathscr{C}_R) \,, \tag{4.9}$$

where

$$\gamma = (V_{bR}^{-1} - 1) + \lambda \,,$$

is a known parameter. Now, equation (4.9) is regarded as a differential equation in C_b, whose solution (when $C_b(0) = 0$) is

$$C_b(t; \mathscr{C}_R, k_{Rb}) = \frac{1}{V_{bR}} \int_0^t e^{-\gamma k_{Rb}(t-\tau)} (\dot{\mathscr{C}}_R(\tau) + \lambda k_{Rb} \mathscr{C}_R(\tau))\, d\tau \,, \tag{4.10}$$

also expressed as

$$C_b(t; \mathscr{C}_R, k_{Rb}) = \frac{1}{V_{bR}} \left(\mathscr{C}_R(t) - (V_{bR}^{-1} - 1) k_{Rb} \int_0^t e^{-\gamma k_{Rb}(t-\tau)} \mathscr{C}_R(\tau)\, d\tau \right) . \tag{4.11}$$

Here k_{Rb} is regarded as a free parameter. By (4.11), we will get rid of explicit reference to the blood IF C_b in the analysis of the TT.

4.1.2 Two-compartment target tissue

The TT consists of a compartment of tracer concentration C_f, accounting for free tracer, and a compartment of concentration C_m, accounting for metabolized tracer. The state variables C_f and C_m satisfy the Cauchy problem for a linear system of ordinary differential equations (ODEs)

$$\dot{\boldsymbol{C}} = \boldsymbol{M}\boldsymbol{C} + k_{fb}\boldsymbol{e}_1 C_b \,, \quad \boldsymbol{C}(0) = 0 \,, \tag{4.12}$$

where

$$\boldsymbol{C} = \begin{pmatrix} C_f \\ C_m \end{pmatrix} \,, \quad \boldsymbol{M} = \begin{pmatrix} -(k_{bf} + k_{mf}) & k_{fm} \\ k_{mf} & -k_{fm} \end{pmatrix} \,, \quad \boldsymbol{e}_1 = \begin{pmatrix} 1 \\ 0 \end{pmatrix} \,. \tag{4.13}$$

The rate constants k_{fb}, k_{bf} (min^{-1}) describe transfer from arterial blood to free tracer, and conversely; similarly, k_{mf} and k_{fm} (min^{-1}) refer to transfer from free to metabolized tracer, and conversely. The analytical solution of the Cauchy problem (4.12)–(4.13) is

$$\boldsymbol{C}(t; C_b, \boldsymbol{k}_T) = k_{fb} \int_0^t e^{(t-\tau)\boldsymbol{M}} C_b(\tau) \boldsymbol{e}_1\, d\tau \,, \tag{4.14}$$

where $t \in \mathbb{R}_+$, and $\boldsymbol{k}_T = (k_{fb}, k_{bf}, k_{mf}, k_{fm})^T \in \mathbb{R}_+^4$.

By denoting with V_{bT} the fraction of blood volume occupying the TT, the total radioactivity concentration in TT $\mathscr{C}_T$ satisfies

$$\mathscr{C}_T(t; C_b, \boldsymbol{k}_T) = \boldsymbol{\alpha}^T \boldsymbol{C}(t; C_b, \boldsymbol{k}_T) + V_{bT} C_b(t) \,, \tag{4.15}$$

where

$$\boldsymbol{\alpha} = \begin{pmatrix} 1 - V_{bT} \\ 1 - V_{bT} \end{pmatrix} \,, \tag{4.16}$$

and $\mathbf{C}$ is the analytical solution (4.14).

4.1.3 RTM

The previous models of RT and TT are put together to define the RTM. Replacement of C_b by its expression in terms of $\mathscr{C}_R$ (4.11) in equation (4.12) gives

$$\dot{\boldsymbol{C}} = \boldsymbol{M}\boldsymbol{C} + \frac{k_{fb}\boldsymbol{e}_1}{V_{bR}} \left(\mathscr{C}_R(t) - (V_{bR}^{-1} - 1) k_{Rb} \int_0^t e^{-\gamma k_{Rb}(t-\tau)} \mathscr{C}_R(\tau)\, d\tau \right). \tag{4.17}$$

Equation (4.17) shows the connection between the TT state variables and the rate constants of TT and RT. It may be regarded as the differential formulation of the RTM mathematical model.

Consider the differential equation (4.17), with the initial condition $\boldsymbol{C}(0) = 0$. The solution $\boldsymbol{C}$ in terms of $\mathscr{C}_R$ is given by

$$\boldsymbol{C}(t;\mathscr{C}_R,\boldsymbol{k}_{RTM}) = \frac{k_{fb}}{V_{bR}} \int_0^t e^{\boldsymbol{M}(t-\tau)}\boldsymbol{e}_1 \left(\mathscr{C}_R(\tau) - (V_{bR}^{-1}-1)k_{Rb} \int_0^\tau e^{-\gamma k_{Rb}(\tau-\sigma)} \mathscr{C}_R(\sigma)\, d\sigma \right) d\tau \,, \tag{4.18}$$

where $t \in \mathbb{R}_+$, and $\boldsymbol{k}_{RTM} = (k_{Rb}, k_{fb}, k_{bf}, k_{mf}, k_{fm})^T \in \mathbb{R}^5_+$ is the vector of RTM rate constants. Equation (4.18) is the integral form of the RTM mathematical model.

In principle, the RT and the TT involve six rate coefficients, but the condition that λ is known reduces the total number of parameters to five. All of them enter equations (4.17) and (4.18), characterizing the RTM. A simplified formulation of the RTM is obtained under the assumption that $k_{mf} = k_{fm} = 0$, which means that the TT contributes only to two rate constants, instead of the four considered here. This case is known as simplified reference tissue model (SRTM, as in Lammertsma and Hume, 1996).

We also remark that in a number of approaches to reference tissue modeling (Schmidt and Turkheimer, 2002; Zhou et al., 2003; Zhou et al., 2007) the total number of the unknown parameters for the RTM is reduced by the assumption that the distribution volumes of tracer of the two tissues are equal. In our notations, this means that

$$\frac{k_{fb}}{k_{bf}} = \frac{k_{Rb}}{k_{bR}} \,, \tag{4.19}$$

in the simplest cases. Due to recent criticism on this assumption (Tichauer et al., 2012a; Tomasi et al., 2012) especially in the framework of tumor modeling, we have simply considered the ratio $k_{Rb}/k_{bR} = DV_{RT}$ as experimentally determined by the asymptotic Logan plot of the RT.

The total radioactivity concentration $\mathscr{C}_R$ in RT and $\mathscr{C}_T$ in TT are measured by drawing ROIs on the overall tissues selected to work as a reference and as a target, respectively. Therefore, the equation connecting the data with the RTM follows from equation (4.15), after substitution of the IF in terms of the RT:

$$\mathscr{C}_T(t;\mathscr{C}_R,\boldsymbol{k}_{RTM}) = \boldsymbol{\alpha}^T \boldsymbol{C}(t;\mathscr{C}_R,\boldsymbol{k}_{RTM}) + V_{bT} C_b(t;\mathscr{C}_R,k_{Rb}) \,, \tag{4.20}$$

where $C_b(t;\mathscr{C}_R,k_{Rb})$ is defined as in (4.11), and $\boldsymbol{C}(t;\mathscr{C}_R,\boldsymbol{k}_{RTM})$ is given by (4.18). In an explicit form, equation (4.20) can be rewritten as

$$\begin{aligned} \boldsymbol{\alpha}^T \Bigg(& k_{fb} \int_0^t e^{\boldsymbol{M}(t-\tau)}\boldsymbol{e}_1 \left(\mathscr{C}_R(\tau) - (V_{bR}^{-1}-1)k_{Rb} \int_0^\tau e^{-\gamma k_{Rb}(\tau-\sigma)} \mathscr{C}_R(\sigma)\, d\sigma \right) d\tau \Bigg) \\ & - V_{bT}(V_{bR}^{-1}-1)k_{Rb} \int_0^t e^{-\gamma k_{Rb}\,(t-\tau)} \mathscr{C}_R(\tau)\, d\tau \\ & + V_{bT}\mathscr{C}_R(t) - V_{bR}\mathscr{C}_T(t) = 0 \,. \end{aligned} \tag{4.21}$$

Equation (4.21) is the starting point for the compartmental inverse problem of finding the exchange coefficients k_{Rb}, k_{fb}, k_{bf}, k_{mf}, and k_{fm} when the total concentrations of the reference tissue $\mathscr{C}_R$, the target tissue $\mathscr{C}_T$, and the blood volume fractions V_{bT}, V_{bR} are known. The zero-finding problem (4.21) is solved by means of the regularized Gauss-Newton (reg-GN) iterative procedure (Algorithm 1.1, described in subsection 1.2.3).

4.1.4 RTM identifiability

Before proceeding to the numerical evaluation of the rate coefficients, we need to discuss the formal identifiability of the RTM problem, namely whether the rate coefficients $\boldsymbol{k}_{RTM} = (k_{Rb}, k_{fb}, k_{bf}, k_{mf}, k_{fm})^T \in \mathbb{R}^5_+$ are uniquely determined by the given RT datum $\mathscr{C}_R$ and TT datum $\mathscr{C}_T$, under the assumption that they are not contaminated by noise. For the RTM, we can state the following result.

Theorem 4.1.1. *Assume that the polynomials*

$$\begin{aligned} Q(s;\boldsymbol{k}_{RTM}) = s^3 &+ (\bar{k}_{fb} + \lambda k_{Rb} + k_{bf} + k_{mf} + k_{fm})s^2 \\ &+ (\lambda k_{Rb}(\bar{k}_{fb} + k_{bf} + k_{mf} + k_{fm}) + \bar{k}_{fb}(k_{mf} + k_{fm}) + k_{bf}k_{fm})s \\ &+ \lambda k_{Rb}(\bar{k}_{fb}(k_{mf} + k_{fm}) + k_{bf}k_{fm}) \,, \end{aligned}$$

and

$$\begin{aligned} D(s;\boldsymbol{k}_{RTM}) = s^3 &+ (\bar{k}_{Rb} + \lambda k_{Rb} + k_{bf} + k_{mf} + k_{fm})s^2 \\ &+ ((\bar{k}_{Rb} + \lambda k_{Rb})(k_{bf} + k_{mf} + k_{fm}) + k_{bf}k_{fm})s \\ &+ (\bar{k}_{Rb} + \lambda k_{Rb})k_{bf}k_{fm} \,, \end{aligned}$$

where

$$\bar{k}_{fb} = (V_{bT}^{-1} - 1)k_{fb} \,, \quad \bar{k}_{Rb} = (V_{bR}^{-1} - 1)k_{Rb} \,,$$

are coprime. If $\boldsymbol{k}_{RTM} = (k_{Rb}, k_{fb}, k_{bf}, k_{mf}, k_{fm})^T \in \mathbb{R}^5_+$ is generic, then $\boldsymbol{k}_{RTM}$ is uniquely determined by $\mathscr{C}_R$ and $\mathscr{C}_T$, and the RTM of equations (4.17) *and* (4.20) *is globally identifiable.*

Theorem 4.1.1 ensures uniqueness for the RTM when the rate coefficient k_{bR} is constrained as λk_{Rb}, and λ is estimated thanks to the asymptotic Logan plot approach and equation (4.6). The proof of Theorem 4.1.1 follows the procedure used in Delbary, Garbarino, and Vivaldi, 2016, and is reported in Appendix A.

We point out some remarks characterizing RTM identifiability under special cases.

Remark 4.1.1. We observe that if one of the blood volume fractions V_{bR} or V_{bT} is negligible, then we still have uniqueness. On the contrary, uniqueness does not hold if both blood volume fractions are set to zero ($V_{bR} = V_{bT} = 0$), and under these conditions the RTM is not identifiable. Indeed, suppose that $\boldsymbol{h}_{RTM} = (h_{1R}, h_1, h_2, h_3, h_4)^T \in \mathbb{R}^5_+$ is an alternative choice of rate coefficients consistent with the data of the problem; then it may be shown that two different sets of rate constants satisfy the RTM problem:

$$\boldsymbol{h}_{RTM}{}^{(1)} = \boldsymbol{k}_{RTM} \,,$$

and

$$\boldsymbol{h}^{(2)}_{RTM} = \left(\frac{k_{mf} + k_{fm}}{\lambda}, \frac{k_{fb}}{k_{Rb}} h_{1R}, k_{bf} + k_{mf} + k_{fm} - \lambda k_{Rb}, \lambda k_{Rb} - \frac{k_{bf}k_{fm}}{h_2}, \frac{k_{bf}k_{fm}}{h_2} \right).$$

In this case, uniqueness is ensured only if the value of k_{Rb} is a priori fixed. Although the kinetic coefficients are not generally identifiable, some macro-parameters of clinical interest, such as the total volumes of distribution, are here shown to be identifiable. Indeed, the total volume of distribution for RT is $DV_{\mathrm{RT}} = 1/\lambda$ as in equation (4.5), that in our framework is estimated by means of the asymptotic Logan plot (and therefore is obviously identifiable). The total volume of distribution for TT is

$$DV_{TT}(\boldsymbol{k}_{RTM}) = \frac{k_{fb}}{k_{bf}} \left(1 + \frac{k_{mf}}{k_{fm}} \right) ;$$

if $\boldsymbol{h}_{RTM} = \boldsymbol{h}^{(1)}_{RTM}$, then clearly $DV_{\mathrm{TT}}(\boldsymbol{h}_{RTM}) = DV_{\mathrm{TT}}(\boldsymbol{k}_{RTM})$ holds. If $\boldsymbol{h}_{RTM} = \boldsymbol{h}^{(2)}_{RTM}$, then

$$\begin{aligned} DV_{\mathrm{TT}}(\boldsymbol{h}_{RTM}) &= \frac{h^{(2)}_1}{h^{(2)}_2}\left(1+\frac{h^{(2)}_3}{h^{(2)}_4}\right) \\ &= \frac{k_{fb}(k_{mf}+k_{fm})}{\lambda k_{Rb}(k_{bf}+k_{mf}+k_{fm}-\lambda k_{Rb})}\,\frac{\lambda k_{Rb}(k_{bf}+k_{mf}+k_{fm}-\lambda k_{Rb})}{k_{bf}k_{fm}} \\ &= \frac{k_{fb}}{k_{bf}}\left(1+\frac{k_{mf}}{k_{fm}}\right). \end{aligned} \tag{4.22}$$

Therefore, DV_{TT} is identifiable. The distribution volume ratio (with respect to the reference tissue) is also identifiable, being $DV_{\mathrm{TT}}/DV_{\mathrm{RT}}$.

Remark 4.1.2. The asymptotic Logan plot step to estimate λ is necessary; indeed, if we consider the RTM with six free parameters (i.e. k_{bR} free) then identifiability does not hold.

Remark 4.1.3. Identifiability of the RTM is ensured if the dephosphorylation inside the TT is assumed to be negligible, i.e. if $k_{fm} = 0$.

Remark 4.1.4. The SRTM, corresponding to the case $k_{mf} = k_{fm} = 0$, is identifiable.

4.2 Numerical validation

In this section we describe the performance of our approach to reference tissue compartmental analysis in the case of synthetic data simulated by mimicking the behavior of a real micro-PET system. We remark that all the computational part has been implemented in the Matlab programming environment.

The first simulation is presented to test the reliability of our proposed reg-GN iterative procedure (Algorithm 1.1) against the state-of-the-art Levenberg-Marquardt (LM) algorithm (Levenberg, 1944; Marquardt, 1962). The second simulation is set up in order to test the robustness of our model when the assumption of a priori knowledge of the blood volume fractions is broken. Indeed, in this case, we simulate many data with varying blood volume fractions (for both RT and TT) and then reconstruct the kinetic parameters by imposing known blood volume fractions, different from the one used to generate the data. The obtained kinetic parameters are almost unaffected by errors on the blood fractions up to a 40% factor. Further, we show the sensitivity of standard RTM (std-RTM) (Zhou et al., 2003) when the assumption of equal distribution volumes (4.19) is broken. Under this condition, the std-RTM fails in returning fair values of the kinetic coefficients. The results are compared with a full compartmental model (full-CM) for the TT with known IF C_b.

In all the scenarios, in order to produce the synthetic data, we initially choose realistic ground truth values for the adimensional parameter λ and the tracer kinetic parameters k_{Rb}, k_{fb}, k_{bf}, k_{mf}, k_{fm}. We select $V_{bR} = 0.025$ and $V_{bT} = 0.15$ to be the realistic values for the blood volume fractions of the RT and the TT, respectively.

The synthetic IF C_b is created by fitting with a gamma variate function (Golish et al., 2001) a set of real measurements acquired from a healthy mouse in a controlled experiment. We recall that the IF is not directly involved in the numerical reduction except for its asymptotic values, but in this framework the whole IF is needed for the construction of the reference and target tissue synthetic data. The RT concentration is obtained by computing first equation (4.2) for C_R with the given parameters k_{Rb}, $k_{bR} = \lambda k_{Rb}$, and then equation (4.3) for $\mathscr{C}_R$ with the given V_{bR}. Next, equation (4.17)

is solved for $\boldsymbol{C}$. The total TT concentration $\mathscr{C}_T$ is computed by equation (4.20) with the given V_{bT}. Finally, the data are affected by white Gaussian noise, by means of the Matlab function awgn with a signal-to-noise ratio of 30 dB, to produce realistic signals for the activity of the radiotracer in tissues.

The synthetic data for $\mathscr{C}_R$ and $\mathscr{C}_T$ are used to estimate the RTM parameters. The angular coefficient β_1 is obtained from the asymptotic values of $\mathscr{C}_R$ and C_b by means of equation (4.7), where t_0 is identified with a time point where the concentrations started being almost constant. Consequently, by equation (4.6) with the selected value for V_{bR}, an estimate of λ is obtained, and inserted into the subsequent inversion procedure.

The full-CM is built by considering the synthetic IF C_b, i.e. by computing equations (4.14)–(4.15). For the std-RTM, we generate the synthetic data without assumption of equal volumes of distribution, and reconstruct the coefficients by imposing the condition $k_{fb}/k_{bf} = \epsilon k_{Rb}/k_{bR}$, with $\epsilon \in U_1$ (a neighbor of 1). The case $\epsilon = 1$ obviously corresponds to the std-RTM assumption, $\epsilon < 1$ to some weaker std-RTM assumption, and $\epsilon > 1$ to some stronger one, testing the limit of sensitivity of the model. For both the std-RTM and the full-CM, the kinetic parameters are estimated by means of the state-of-the-art LM algorithm.

The reg-GN scheme is applied to synthetic data in order to reconstruct the RTM rate constants k_{Rb}, k_{fb}, k_{bf}, k_{mf}, k_{fm}. The starting point of the method is randomly chosen in the interval $(0, 1)$. To stop the iterative algorithm we check the relative error between the original noisy TT concentration (the datum in the real data context) and the model-reconstructed one, using a threshold of order $O(10^{-2})$ as a stopping criterion. The regularization parameter is optimized at each iteration through the Generalized Cross Validation (GCV) method (Golub, Heath, and Wahba, 1979), by the requirement of a predefined range of variability (between 10^4 and 10^6).

Table 4.1 shows the comparison between the ground truth and the estimated values of the parameters retrieved with reg-GN, providing information about the reliability of the inversion procedure. It is apparent that the means provide a good approximation of the ground truth values while the standard deviations are systematically small, thus showing the notable numerical stability of the iterative reconstruction scheme with respect to noise. Moreover, the observation that the complete inversion procedure has been based on an approximate value of λ shows that the algorithm is very robust. The reg-GN algorithm is also clearly compatible with the state-of-the-art LM algorithm, by producing the same mean values and comparable standard deviations. It has indeed the advantage of being faster, given that in reg-GN it is possible to compute the gradient of the functional to be minimized in an analytical form, thus avoiding time-consuming numerical differentiation step. The computational burden is about 10 seconds for one run of LM and about 2 seconds for one run of reg-GN (on an Intel Core i7, 3.1GHz).

In order to test the sensitivity of our RTM to a non-precise estimation of blood volume fractions, we choose different $V_{bR} = \{0.015, 0.020, 0.025, 0.030, 0.035\}$ and $V_{bT} = \{0.05, 0.10, 0.15, 0.20, 0.25\}$ to be the values in order to compute the RT and TT data. The proposed RTM shows a good robustness with respect to mis-estimation (up to a 40%) of both volume fractions. In fact, Table 4.2 shows that the reconstruction of the RTM kinetic parameters is unaffected by errors on V_{bR} and V_{bT}.

The std-RTM exhibits a lower stability, as shown in Table 4.3. In this case, data are built imposing the condition $\epsilon = 0.6$, and the reconstruction is performed with varying ϵ. We can observe that the reconstruction fails for $\epsilon = 1$, meaning that the std-RTM assumptions is not reliable when there is a 40% mis-estimation. For weaker std-RTM conditions ($\epsilon < 1$) the reconstructions gradually approach the true values,

while going beyond ($\epsilon > 1$) the reconstructions get worse. This result shows that the std-RTM assumption is very sensitive to the model hypothesis of equal volumes of distribution.

	λ	k_{Rb}	k_{fb}	k_{bf}	k_{mf}	k_{fm}
g.t.	2.5	0.08	0.1	0.4	0.2	0.05
reg-GN	2.261	0.082 ± 0.005	0.106 ± 0.014	0.383 ± 0.084	0.211 ± 0.044	0.053 ± 0.009
LM	2.261	0.084 ± 0.011	0.121 ± 0.061	0.447 ± 0.271	0.202 ± 0.049	0.051 ± 0.010

TABLE 4.1: Algorithm validation: ground truth (g.t.) and reconstructed values for the adimensional parameter λ, with the asymptotic Logan plot approach, and for the tracer kinetic parameters, with the reg-GN and LM methods. Means and standard deviations are computed over 50 different runs of the algorithm, with 50 different random initialization values. Here $V_{bR} = 0.025$ and $V_{bT} = 0.15$.

	λ	k_{Rb}	k_{fb}	k_{bf}	k_{mf}	k_{fm}
g.t.	2	0.1	0.3	0.2	0.05	0.02
RTM ($V_{bR} = 0.015$ $V_{bT} = 0.15$)	1.917	0.097 ± 0.009	0.311 ± 0.036	0.208 ± 0.033	0.061 ± 0.015	0.019 ± 0.009
RTM ($V_{bR} = 0.020$ $V_{bT} = 0.15$)	1.826	0.101 ± 0.008	0.316 ± 0.028	0.200 ± 0.030	0.058 ± 0.016	0.023 ± 0.011
RTM ($V_{bR} = 0.025$ $V_{bT} = 0.15$)	1.811	0.099 ± 0.009	0.300 ± 0.033	0.181 ± 0.031	0.055 ± 0.015	0.023 ± 0.010
RTM ($V_{bR} = 0.030$ $V_{bT} = 0.15$)	1.802	0.102 ± 0.008	0.300 ± 0.029	0.184 ± 0.028	0.055 ± 0.016	0.022 ± 0.011
RTM ($V_{bR} = 0.035$ $V_{bT} = 0.15$)	1.793	0.105 ± 0.010	0.293 ± 0.031	0.187 ± 0.033	0.061 ± 0.019	0.026 ± 0.011
RTM ($V_{bR} = 0.025$ $V_{bT} = 0.05$)	1.811	0.106 ± 0.007	0.293 ± 0.025	0.158 ± 0.031	0.052 ± 0.017	0.021 ± 0.011
RTM ($V_{bR} = 0.025$ $V_{bT} = 0.10$)	1.811	0.108 ± 0.008	0.289 ± 0.023	0.169 ± 0.022	0.058 ± 0.015	0.026 ± 0.011
RTM ($V_{bR} = 0.025$ $V_{bT} = 0.15$)	1.811	0.103 ± 0.008	0.311 ± 0.027	0.193 ± 0.027	0.058 ± 0.014	0.026 ± 0.012
RTM ($V_{bR} = 0.025$ $V_{bT} = 0.20$)	1.811	0.099 ± 0.009	0.329 ± 0.038	0.218 ± 0.037	0.061 ± 0.021	0.027 ± 0.013
RTM ($V_{bR} = 0.025$ $V_{bT} = 0.25$)	1.811	0.096 ± 0.008	0.327 ± 0.033	0.236 ± 0.029	0.065 ± 0.015	0.029 ± 0.008
full-CM	–	–	0.301 ± 0.009	0.204 ± 0.019	0.052 ± 0.012	0.021 ± 0.011

TABLE 4.2: Proposed RTM validation: ground truth (g.t.) and reconstructed values for the adimensional parameter λ, with the asymptotic Logan plot approach, and for the tracer kinetic parameters, with the reg-GN method, in the case of data generated with varying blood volume fractions (for both RT and TT). For the inversion procedure, $V_{bR} = 0.025$ and $V_{bT} = 0.15$. The full-CM model is optimized through the LM method and $V_{bT} = 0.15$ fixed. Means and standard deviations are computed over 50 different runs of the algorithm, with 50 different random initialization values.

4.3 Application to FDG-PET cancer data

The micro-PET system Albira (Bruker, 2012) produced by Carestream Health is currently operational at the Nuclear Medicine Department, IRCCS San Martino IST, Genova (Italy), and experiments with mice are performed by using different tracers, mainly for applications to oncology. In this section, we show the results of our reference tissue compartmental approach for the tumor environment on real experiments, concerning murine models and FDG-PET acquisitions.

	λ	k_{Rb}	k_{fb}	k_{bf}	k_{mf}	k_{fm}
g.t.	4	0.05	0.5	1.2	0.1	0.04
std-RTM ($\epsilon = 0.6$)	3.613	0.054 ± 0.001	0.538 ± 0.028	1.166 ± 0.061	0.102 ± 0.005	0.041 ± 0.004
std-RTM ($\epsilon = 0.7$)	3.613	0.047 ± 0.002	0.478 ± 0.031	1.208 ± 0.078	0.137 ± 0.007	0.046 ± 0.005
std-RTM ($\epsilon = 0.8$)	3.613	0.043 ± 0.001	0.438 ± 0.023	1.266 ± 0.065	0.165 ± 0.008	0.047 ± 0.005
std-RTM ($\epsilon = 0.9$)	3.613	0.039 ± 0.001	0.414 ± 0.026	1.345 ± 0.085	0.193 ± 0.008	0.047 ± 0.004
std-RTM ($\epsilon = 1.0$)	3.613	0.037 ± 0.001	0.393 ± 0.025	1.421 ± 0.089	0.220 ± 0.011	0.047 ± 0.005
std-RTM ($\epsilon = 1.1$)	3.613	0.035 ± 0.001	0.383 ± 0.026	1.521 ± 0.102	0.244 ± 0.011	0.046 ± 0.004
std-RTM ($\epsilon = 1.2$)	3.613	0.033 ± 0.001	0.376 ± 0.026	1.631 ± 0.111	0.269 ± 0.009	0.046 ± 0.003
std-RTM ($\epsilon = 1.3$)	3.613	0.032 ± 0.001	0.369 ± 0.024	1.736 ± 0.113	0.288 ± 0.012	0.044 ± 0.003
std-RTM ($\epsilon = 1.4$)	3.613	0.031 ± 0.001	0.363 ± 0.027	1.835 ± 0.135	0.311 ± 0.015	0.043 ± 0.004
full-CM	–	–	0.498 ± 0.020	1.188 ± 0.081	0.097 ± 0.009	0.038 ± 0.005

TABLE 4.3: Standard RTM (std-RTM) validation: ground truth (g.t.) and reconstructed values for the adimensional parameter λ, with the asymptotic Logan plot approach, and for the tracer kinetic parameters, with the LM method, in the case of synthetic data generated without assumption of equal distribution volumes. For the inversion procedure, the condition $k_{fb}/k_{bf} = \epsilon k_{Rb}/k_{bR}$, with varying ϵ, is imposed. The full-CM model is optimized through the LM method. Means and standard deviations are computed over 50 different runs of the algorithm, with 50 different random initialization values. Here $V_{bR} = 0.025$ and $V_{bT} = 0.15$.

All animals were studied after a fasting period of six hours to ensure a steady state of substrate and hormones governing glucose metabolism. Animals were positioned on the bed of Albira micro-PET system whose two-ring configuration permits to cover the whole animal body in a single bed position. A dose of 3 to 4 MBq of FDG was injected through a tail vein, soon after the start of a dynamic list mode acquisition lasting 40 minutes. The acquisition was reconstructed using the following framing rate: $10 \times 15\text{s} + 1 \times 22\text{s} + 4 \times 30\text{s} + 5 \times 60\text{s} + 2 \times 150\text{s} + 5 \times 300\text{s}$ and PET data were reconstructed using a Maximum Likelihood Expectation Maximization (MLEM) method (Algorithm 3.2, described in subsection 3.2.3). Animals were inoculated subcutaneously in the dorsal hip muscles with 2×10^5 murine cancer cell lines CT26 (colon carcinoma cell lines). In this context, the tumor is the TT. We choose a leg muscle to work as RT, since under resting conditions muscles exhibit a negligible hexokinase activity (Lackner et al., 1984) and thus a negligible FDG metabolism. More information on the sex, weight, and glycaemia of the animals are reported in Table 4.4.

In order to obtain the experimental concentrations (kBq/ml), each image dataset was reviewed by an experienced observer who drew three ROIs: one over the cancer lesion, one around the resting thigh muscle, and one over the left ventricle in order to compute the IF. The determination of the IF is a challenging task in the case of mice. To accomplish it, for each animal model the tracer first pass was viewed in cine mode. Then a ROI was drawn in the aortic arc, in a frame where the left ventricle was particularly visible, and maintained it for all time points. An example of micro-PET data of a mouse model and related time-dependent tracer concentrations of the ROIs around the TT and RT is represented in Figure 4.2. The blood volume fractions are set to $V_{bT} = 0.15$ and $V_{bR} = 0.025$ for the TT and the RT, respectively, according to Montet et al., 2007 (for tumor in CT26-tumor bearing mice), Bertoldo et al., 2001 and Hindel et al., 2017 (for the muscle).

The experimental data obtained for a group of four mice are processed by the

proposed RTM approach. Estimates of the parameters obtained for each member of the group are shown in Table 4.5. Means and standard deviations are computed by using 50 runs of the code for the reg-GN method (Algorithm 1.1), where the initialization of the kinetic parameters is performed by picking up numbers in the interval $(0, 1)$ with uniform distribution, and the regularization parameter is determined at each iteration through the GCV method (with a confidence interval ranging between 10^5 and 10^7). The starting time point for the graphical analysis is chosen as the time point at which the IF curve reaches a plateau, that is, becomes approximately asymptotic (and thus stable) to the time axis.

Table 4.5 clearly shows that the proposed RTM is able to effectively reconstruct the kinetic coefficients, with good agreement with the ones reconstructed by means of the gold-standard full-CM comprising the IF. Moreover, in Figure 4.3 it is possible to observe that the IF generated by the reconstructed parameters through equation (4.11) provides a good approximation of the experimental IF, measured on the ROI around the left ventricle, for all mice considered in our analysis. The red points describe the experimental IF curve, together with its standard deviation (computed according to the experimental noise level), while the black points represent the reconstructed IF curve, computed with the averaged value of the k_{Rb} parameter resulting from the 50 different runs of the algorithm, together with its standard deviation. It is also possible to observe that the reconstructed IF curves tend to be smoother than the measured ones, as expectable, given that they are model-based; this effect is particularly visible when the measured IF has some oscillations (as, for instance, times 7min-17min of Figure 4.3(b) for m2).

In general, the inter-animal variability of the estimated rate constants for the TT is quite low, meaning that the inter-tumor variability is not significant since in all animals the inoculated cancer cell lines are of the same type. Although, the third model (m3) appears to slightly underestimate all the parameters. This effect is visible in Figure 4.3(c), where the comparison between the reconstructed IF and the experimental one shows a subtle underestimation of the first points, that we hypothesize is the reason for the underestimation of k_{fb} and consequently of the other coefficients. Finally, we observe that the second mouse model (m2) appears to have a lower λ and a higher k_{Rb} with respect to the values reconstructed for the other murine models. This could be due to the quite low blood sugar levels of m2 (the glycaemia is 30 mg/dl, see Table 4.4): when glycaemia is low, the FDG is highly absorbed by the cells, due the shortage of sugar in blood. This appears to cause a higher absorption rate in the RT and therefore an increase in k_{Rb}. This effect is not visible in the parameters concerning the target tissue kinetics, which instead are consistent with the values for the other mice. This can be considered a consequence of the fact that the tumor is a pathological tissue less affected by the environment conditions than physiological tissues.

	Cell line type	Weight [g]	Sex	Glycaemia [mg/dl]
m1	CT26	17.2	F	84
m2	CT26	16.8	F	30
m3	CT26	15.9	F	53
m4	CT26	16.1	F	81

TABLE 4.4: Cell line type, weight, sex and glycaemia information for the four murine models.

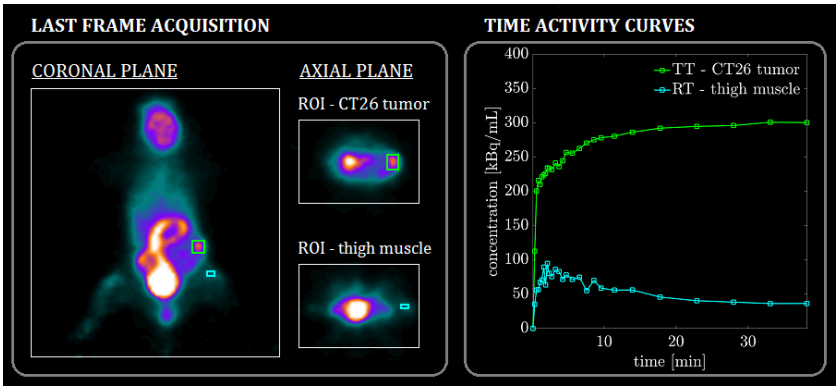

FIGURE 4.2: Left panel: last frame of the FDG-micro-PET acquisition of a murine model with ROIs around the CT26 tumor (green color) and the thigh muscle (light blue color). Right panel: time-dependent tracer concentrations of the CT26 tumor as TT (green color) and of the thigh muscle as RT (light blue color).

		λ	k_{Rb}	k_{fb}	k_{bf}	k_{mf}	k_{fm}
m1	RTM	4.373	0.039 ± 0.003	0.206 ± 0.034	0.426 ± 0.097	0.099 ± 0.022	0.032 ± 0.009
m1	full-CM	–	–	0.213 ± 0.001	0.441 ± 0.007	0.101 ± 0.003	0.033 ± 0.001
m2	RTM	1.858	0.433 ± 0.024	0.292 ± 0.033	0.468 ± 0.117	0.091 ± 0.035	0.033 ± 0.014
m2	full-CM	–	–	0.229 ± 0.004	0.481 ± 0.022	0.096 ± 0.006	0.017 ± 0.002
m3	RTM	5.049	0.111 ± 0.002	0.223 ± 0.025	0.493 ± 0.071	0.069 ± 0.019	0.023 ± 0.011
m3	full-CM	–	–	0.279 ± 0.004	0.586 ± 0.017	0.112 ± 0.004	0.031 ± 0.001
m4	RTM	5.844	0.036 ± 0.003	0.238 ± 0.029	0.350 ± 0.075	0.161 ± 0.035	0.054 ± 0.015
m4	full-CM	–	–	0.231 ± 0.003	0.435 ± 0.011	0.151 ± 0.003	0.035 ± 0.001

TABLE 4.5: Real data validation: reconstructed values for the dimensionless parameter λ and for the tracer kinetic parameters of FDG-PET experiments involving four mice. Both the RTM and the full-CM models are optimized through the reg-GN method. The uncertainties are computed as standard deviations over 50 runs of the algorithm with 50 different random initialization values. Here $V_{bR} = 0.025$ and $V_{bT} = 0.15$.

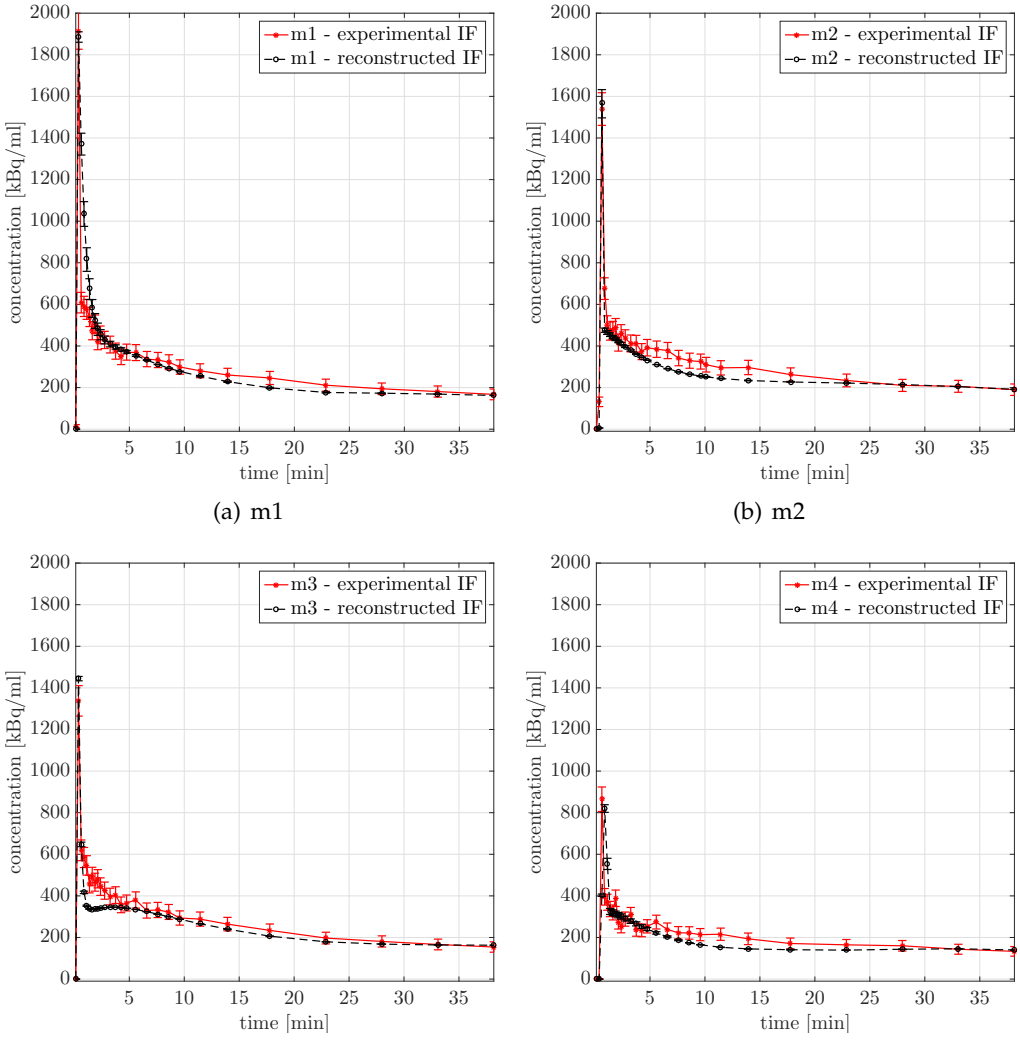

(a) m1 (b) m2

(c) m3 (d) m4

FIGURE 4.3: Experimental IF (red curve) together with RTM reconstructed IF (black curve) and their standard deviations, for the four murine models.

Chapter 5

Physiology-based parametric imaging

Compartmental analysis can be mainly subdivided in two classes (Figure 5.1): region of interest (ROI) kinetic modeling and parametric imaging. ROI-based methods (Carson, 2005; Vanzi et al., 2004) return a single set of tracer kinetic parameters for a homogeneous region of tissue, whose time concentration curve is obtained averaging the Positron Emission Tomography (PET) measurements over the region at each time frame. On the other hand, parametric imaging (Reader and Verhaeghe, 2014) aims at evaluating the set of model rate constants for every pixel of the PET images, thus providing the spatial distribution of each model parameter. This approach is particularly useful when the tissue under examination cannot be effectively segmented into homogeneous regions that could be modeled with a single kinetic parameter set.

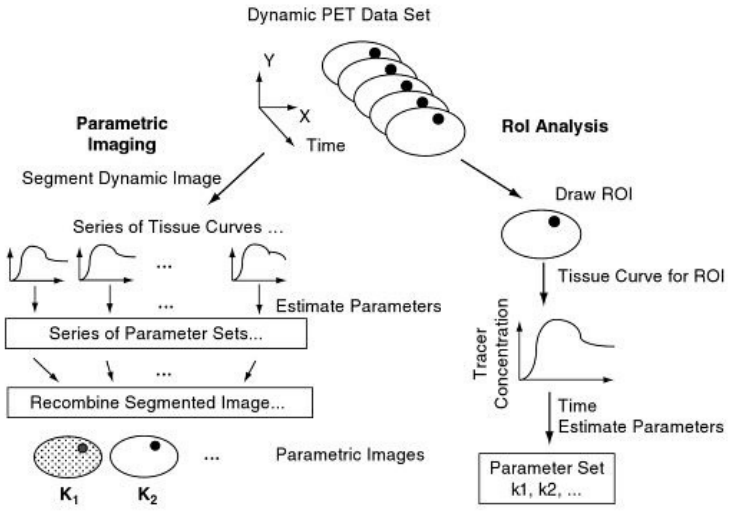

FIGURE 5.1: Parametric imaging versus ROI-based approaches in compartmental analysis.

There exist indirect and direct approaches to parametric imaging. Indirect methods work by first reconstructing the dynamic PET images and then estimating the kinetic parameters at each pixel (Zhou, Huang, and Bergsneider, 2001; Zhou et al., 2002). Direct methods estimate directly the space-varying kinetic parameters from the measured PET sinograms (Wang and Qi, 2013). The direct approach has been proven to reduce the signal-to-noise ratio with respect to indirect techniques (O'Sullivan, 1999), although strongly relies on the implementation of an efficient inversion algorithm capable of reconstructing the parameters on a dense set of pixels

(Kamasak et al., 2005). However, most parametric imaging methods (both direct and indirect) rely on linearized compartmental models and/or provide parametric images of algebraic combinations of the kinetic coefficients (Logan et al., 1990; Logan, 2003; Patlak, Blasberg, and Fenstermacher, 1983; Thie, Smith, and Hubner, 1997; Tsoumpas, Turkheimer, and Thielemans, 2008). Rather few methods are able to reconstruct maps of each single parameter, and most of them consider simple one- and two- compartment models (Carson and Lange, 1985; Huesman et al., 1998; Kamasak et al., 2005; Limber et al., 1995).

We want to exploit recent advances in ROI-based analysis (Garbarino et al., 2014; Garbarino et al., 2015; Watabe et al., 2006) in order to realize a novel and computationally efficient imaging procedure that can be used for parametric imaging in the case of complex physiological systems (Scussolini et al., 2017). We consider [^{18}F]-fluorodeoxyglucose (FDG) PET data and analyze the two-compartment catenary model, describing the standard FDG metabolism in an homogeneous tissue, and the three-compartment non-catenary model, representing the renal physiology. We provide a uniqueness theorem for the three-compartment non-catenary system, by exploiting physiological constraints. The proposed imaging method starts from the reconstructed FDG-PET images of tracer concentration, and preliminarily applies image processing algorithms for noise reduction and image segmentation. The optimization procedure solves pixel-wise the non-linear compartmental inverse problem of determining the kinetic parameters from dynamic concentration data through the regularized Gauss-Newton iterative algorithm. The reliability of the proposed imaging method is validated on synthetic data mimicking a standard two-compartment system for a generic homogeneous tissue, and is applied against micro-PET experimental measurements concerning the three-compartment renal system of murine models.

In the first section, the mathematical background of both the two-compartment and the three-compartment models is presented, concerning the compartmental forward and inverse problems and the discussion of identifiability. The second section describes the proposed parametric imaging method. The third section provides the numerical validation of the computational method in the case of the two-compartment catenary model. The fourth section shows the results obtained from the application against experimental murine data for the analysis of the renal three-compartment non-catenary system.

5.1 Mathematical models

Compartmental analysis identifies different functional compartments in the physiological system of interest, each one associated with a specific metabolic state of the tracer. The tracer typically is injected into the blood and the tracer concentration in the blood is the input function (IF) of the compartmental system. The blood IF is assumed to be known as it can be obtained by drawing ROIs on reconstructed PET images in correspondence with the left ventricle. When the IF is not given, suitable reference tissue models have to be taken into account (as described in Chapter 4).

This section is devoted to the description of the standard two-compartment catenary model and a three-compartment non-catenary model developed for the renal physiology (Garbarino et al., 2014). We assume that the conditions for applicability of compartmental analysis are satisfied (for details see subsection 1.1.1), and we adopt the usual notations of compartmental analysis (as in Chapter 1).

Note that, in the following analysis, the spatial dependence on the pixel index in the compartment concentrations and in the kinetic parameters is omitted but implied. We indicate a generic ROI compartment concentration with the apex ROI.

5.1.1 Two-compartment catenary system

The compartmental model describing the FDG metabolism of phosphorylation and dephosphorylation is the two-compartment catenary model shown in Figure 5.2 (Sokoloff et al., 1977). This model represents standard FDG kinetics within a living tissue, such as the tumor.

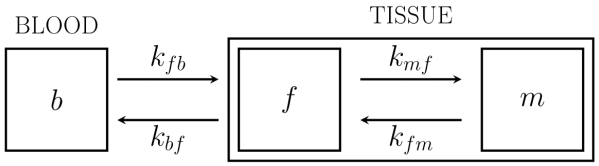

FIGURE 5.2: The compartmental model for the two-compartment catenary system describing the FDG kinetics in a generic tissue.

The two-compartment catenary model consists of:

- a blood compartment b;
- two functional compartments: compartment f, accounting for free FDG, and compartment m, accounting for metabolized FDG;
- four exchange coefficients: k_{fb} and k_{bf} (min^{-1}) between the blood and the free compartment, k_{mf} and k_{fm} (min^{-1}) between the free and the metabolized ones.

Balance of tracer concentrations leads to the following Cauchy problem for a linear system of ordinary differential equations (ODEs):

$$\dot{\boldsymbol{C}} = \boldsymbol{M}\boldsymbol{C} + \boldsymbol{W}\,, \quad \boldsymbol{C}(0) = 0\,, \tag{5.1}$$

where

$$\begin{aligned} \boldsymbol{C} &= \begin{pmatrix} C_f \\ C_m \end{pmatrix}\,, \quad \boldsymbol{M} = \begin{pmatrix} -(k_{bf}+k_{mf}) & k_{fm} \\ k_{mf} & -k_{fm} \end{pmatrix}\,, \\ \boldsymbol{W} &= k_{fb}C_b^{\text{ROI}}\boldsymbol{e}_1 = \begin{pmatrix} k_{fb}C_b^{\text{ROI}} \\ 0 \end{pmatrix}\,, \quad \boldsymbol{e}_1 = \begin{pmatrix} 1 \\ 0 \end{pmatrix}\,. \end{aligned} \tag{5.2}$$

The blood ROI compartment concentration C_b^{ROI} plays the role of the ROI IF of the two-compartment model. The analytical solution of (5.1)–(5.2), formally expressing the forward problem of evaluating the concentrations from the kinetic parameters $\boldsymbol{k}_T = (k_{fb}, k_{bf}, k_{mf}, k_{fm})^T \in \mathbb{R}^4_+$, is given by

$$\boldsymbol{C}(t; C_b^{\text{ROI}}, \boldsymbol{k}_T) = \int_0^t e^{(t-\tau)\boldsymbol{M}}\boldsymbol{W}(\tau)\,d\tau = k_{fb}\int_0^t e^{(t-\tau)\boldsymbol{M}}C_b^{\text{ROI}}(\tau)\boldsymbol{e}_1\,d\tau\,, \tag{5.3}$$

with the time variable $t \in \mathbb{R}_+$, and the blood IF C_b^{ROI} a known function.

Denote by $\mathscr{C}_T$ the pixel-dependent PET experimental concentration within a specific tissue, and by V_{bT} the volume fraction of the tissue occupied by blood. In principle, V_{bT} may depend on the position within the tissue but, with a good approximation, it can be considered constant since the blood perfusion, under physiological

conditions, is homogeneous inside the same organ. Therefore, the compartmental inverse problem equation connecting the two-compartment catenary model and the data is

$$\mathscr{C}_T(t; C_b^{\mathrm{ROI}}, \boldsymbol{k}_T) = \boldsymbol{\alpha}^T \boldsymbol{C}(t; C_b^{\mathrm{ROI}}, \boldsymbol{k}_T) + V_{bT} C_b^{\mathrm{ROI}}(t)\,, \quad \boldsymbol{\alpha} = \begin{pmatrix} 1 - V_{bT} \\ 1 - V_{bT} \end{pmatrix}\,, \tag{5.4}$$

where $\boldsymbol{C}$ is given by equation (5.3), and V_{bT} is assumed to be a known quantity.

As shown in Delbary, Garbarino, and Vivaldi, 2016 and as reported in Theorem 1.2.1, the two-compartment catenary systems describing the basic FDG metabolism is always identifiable, i.e. the following result holds.

Theorem 5.1.1. *The kinetic parameters* $\boldsymbol{k}_T = (k_{fb}, k_{bf}, k_{mf}, k_{fm})^T \in \mathbb{R}^4_+$ *are uniquely determined by* C_b^{ROI} *and* $\mathscr{C}_T$*, and the two-compartment catenary model of equations* (5.1)–(5.2) *and* (5.4) *is structurally globally identifiable.*

5.1.2 Three-compartment non-catenary system

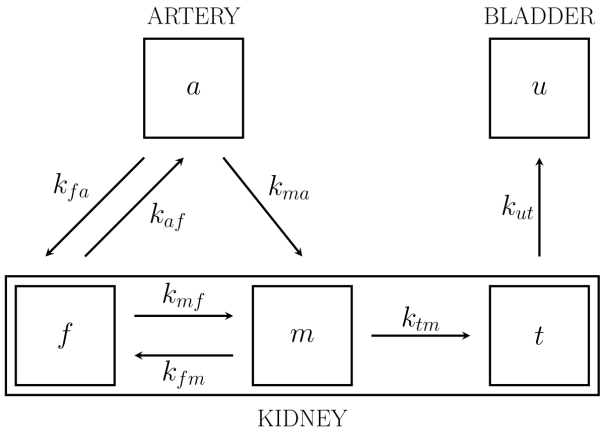

FIGURE 5.3: The compartmental model for the three-compartment non-catenary system describing the FDG kinetics inside the kidney.

The FDG availability within a living organism is influenced by several variables, among which kidney function plays a relevant role as, differently from glucose, FDG is poorly reabsorbed in the renal tubule and is largely excreted in the urine, with accumulation in the bladder, as reported by Shreve, Anzai, and Wahl, 1999. Indeed, urinary loss of glucose and of FDG might modify the diagnostic interpretation of PET studies in diabetic patients with cancer. In order to study FDG kinetics in the kidney, the model represented in Figure 5.3 is designed (Garbarino et al., 2014; Qiao et al., 2007).

Once injected into the system, the tracer reaches the kidneys and infuses the organs via the blood stream through the renal artery (a). Here, we consider the usual two-compartment model describing the FDG phosphorylation/dephosphorylation processes, obtaining the free tracer (f) and the metabolized tracer (m), both located in the extravascular kidney tissue. However, in order to study the role of the mechanisms carrying glucose back to the metabolism, we need to include the reabsorption compartment (t), anatomically identified with the renal tubule. Moreover, we add the external urine compartment (u), anatomically identified with the bladder, accounting for the tracer there accumulated, thanks to the excretion mechanism.

The resulting three-compartment non-catenary model has the following kinetic parameters (min^{-1}):

- k_{fa} and k_{af} between the arterial IF and the free FDG compartment;
- k_{ma} from the arterial compartment to the metabolized FDG one (filtration);
- k_{fm} and k_{mf} between the free FDG and the metabolized FDG compartments (phosphorylation and dephosphorylation);
- k_{tm} from the metabolized FDG compartment to the tubule (reabsorption);
- k_{ut} from the tubule compartment to the bladder pool (excretion).

The state variables C_f, C_m, and C_t satisfy the Cauchy problem for a linear system of ODEs

$$\dot{\boldsymbol{C}} = \boldsymbol{M}\boldsymbol{C} + \boldsymbol{W}\,, \quad \boldsymbol{C}(0) = 0\,, \tag{5.5}$$

where

$$\begin{gathered}\boldsymbol{C} = \begin{pmatrix} C_f \\ C_m \\ C_t \end{pmatrix}\,, \quad \boldsymbol{M} = \begin{pmatrix} -(k_{af}+k_{mf}) & k_{fm} & 0 \\ k_{mf} & -(k_{fm}+k_{tm}) & 0 \\ 0 & k_{tm} & -k_{ut} \end{pmatrix}\,, \\ \boldsymbol{W} = k_{fa}C_a^{\text{ROI}}\boldsymbol{e}_1 + k_{ma}C_a^{\text{ROI}}\boldsymbol{e}_2 = \begin{pmatrix} k_{fa}C_a^{\text{ROI}} \\ k_{ma}C_a^{\text{ROI}} \\ 0 \end{pmatrix}\,, \quad \boldsymbol{e}_1 = \begin{pmatrix} 1 \\ 0 \\ 0 \end{pmatrix}\,, \quad \boldsymbol{e}_2 = \begin{pmatrix} 0 \\ 1 \\ 0 \end{pmatrix}\,.\end{gathered} \tag{5.6}$$

The ROI compartment concentration of arterial blood C_a^{ROI} is the IF of the renal compartmental model. The analytical solution of (5.5)–(5.6) for $\boldsymbol{C}$ in terms of the kinetic coefficients $\boldsymbol{k}_K = (k_{fa}, k_{ma}, k_{af}, k_{mf}, k_{fm}, k_{tm}, k_{ut})^T \in \mathbb{R}_+^7$ is given by

$$\begin{aligned}\boldsymbol{C}(t; C_a^{\text{ROI}}, \boldsymbol{k}_K) &= \int_0^t e^{(t-\tau)\boldsymbol{M}}\boldsymbol{W}(\tau)\,d\tau = \\ &= k_{fa}\int_0^t e^{(t-\tau)\boldsymbol{M}}C_a^{\text{ROI}}(\tau)\boldsymbol{e}_1\,d\tau + k_{ma}\int_0^t e^{(t-\tau)\boldsymbol{M}}C_a^{\text{ROI}}(\tau)\boldsymbol{e}_2\,d\tau\,,\end{aligned} \tag{5.7}$$

with the time variable $t \in \mathbb{R}_+$, and the arterial IF C_a^{ROI} a known function.

Denote by $\mathscr{C}_K$ the pixel-dependent PET experimental concentration within the tissue of the kidney, and by V_{bK} the position-independent fraction of renal volume occupied by arterial blood. The compartmental inverse problem equation connecting the three-compartment non-catenary renal model and the data is

$$\mathscr{C}_K(t; C_a^{\text{ROI}}, \boldsymbol{k}_K) = \boldsymbol{\alpha}^T\boldsymbol{C}(t; C_a^{\text{ROI}}, \boldsymbol{k}_K) + V_{bK}C_a^{\text{ROI}}(t)\,, \quad \boldsymbol{\alpha} = \begin{pmatrix} 1-V_{bK} \\ 1-V_{bK} \\ 1-V_{bK} \end{pmatrix}\,, \tag{5.8}$$

where $\boldsymbol{C}$ is given by equation (5.7), and V_{bK} is assumed to be a known quantity.

Renal model identifiability.

We expect that in general the three-compartment system is not identifiable in that it is a non-catenary model involving seven unknown rate constants. Identifiability is achieved by reducing the number of unknowns through the introduction of constraints coming from renal physiology. It is shown in the course of the discussion

that the constraints are used effectively in the discussion of uniqueness but they cannot be applied in the procedure for the solution of the inverse problem.

To introduce the restrictions, we first consider tracer kinetics within the ROI-based framework, by looking at the overall bulk flow of tracer between the ROI compartments tubule and bladder. The pertinent properties are then extended to the pixel framework, in analogy with the extension of ROI-based features of other compartments, e.g. the dynamical system of tracer exchange between model compartments. Specifically, we have to reconsider the role of the bladder, which accumulates urine and tracer in the course of the experiment. The bladder is connected to the kidneys but is not part of the kidneys, and is related to a strictly global behavior of the renal system. The influence of bladder in tracer kinetics has to be inserted into the description of the characteristic features of the pixel constituents of the renal compartment system, although pixels are not physically connected to the bladder. The following points describe a few aspects of bladder involvement in tracer kinetics that are relevant to parametric modeling and are applied in the subsequent analysis of identifiability. We assume that the volume and the activity of bladder are known, although we do not need the corresponding explicit values.

1. The bladder compartment of tracer density C_u^{ROI} is the only compartment whose volume significantly changes (specifically increases) in time. The condition of tracer balance for bladder is expressed by equation

$$\frac{d}{dt}(V_u C_u^{\mathrm{ROI}}) = F_{ut}^{\mathrm{ROI}} C_t^{\mathrm{ROI}} \,, \quad C_u^{\mathrm{ROI}}(0) = 0 \,, \tag{5.9}$$

   where V_u (ml) indicates the bladder volume, and F_{ut}^{ROI} (ml min^{-1}) is the bulk flow entering the bladder from the tubule region. In words, equation (5.9) states that the (positive) time rate of the tracer content of bladder equals the amount of tracer carried inward by the flux of urine.

2. We assume that the accumulation rate of urine is constant, consistently with the assumption of stationarity and the condition of resting state of the subject during PET acquisition. Therefore, the growth of the bladder volume V_u during time is linear and hence the flux rate of urine into bladder satisfies (Garbarino et al., 2014)

$$F_{ut}^{\mathrm{ROI}} = \frac{V_u(t_f) - V_u(\bar{t})}{t_f - \bar{t}} \,, \tag{5.10}$$

   where t_f is the end time point and $\bar{t}$ is a generic time instant. In principle, an estimate of F_{ut}^{ROI} is obtained from experimental values of V_u at different time points. As a consequence, we find that

$$C_t^{\mathrm{ROI}} = \frac{1}{F_{ut}^{\mathrm{ROI}}} \frac{d}{dt}(V_u C_u^{\mathrm{ROI}}) \,, \tag{5.11}$$

   showing that C_t^{ROI} can be estimated from measurements performed on bladder.

3. Consider the renal tubule ROI compartment. We regard as a result from physiology the existence of a direct proportionality between the bulk ingoing flow F_{tm}^{ROI} (ml min^{-1}), entering the renal tubule system from the metabolized compartment, and the bulk outgoing flow F_{ut}^{ROI}, directed towards bladder. Accordingly, we can write

$$F_{tm}^{\mathrm{ROI}} = \gamma F_{ut}^{\mathrm{ROI}} \,, \tag{5.12}$$

where γ is a constant factor establishing the order of magnitude of the bulk quantity passing from the tubule to the bladder. For example, for the mouse model the value of γ is typically equal to 10^2 (Meneton et al., 2000). Substitution of (5.10) into (5.12) provides F_{tm}^{ROI} in terms of data.

4. The balance of tracer flow inside the overall tubule system is given by (Garbarino et al., 2014)

$$\frac{d}{dt}(V_K V_t C_t^{\mathrm{ROI}}) = F_{tm}^{\mathrm{ROI}} C_m^{\mathrm{ROI}} - F_{ut}^{\mathrm{ROI}} C_t^{\mathrm{ROI}} , \tag{5.13}$$

where V_K (ml) is the renal volume, V_t the fraction of the tubule volume, and thus $V_K V_t$ (ml) is the total volume of the tubule. Equation (5.13) may be written in the equivalent form

$$\dot{C}_t^{\mathrm{ROI}} = k_{tm}^{\mathrm{ROI}} C_m^{\mathrm{ROI}} - k_{ut}^{\mathrm{ROI}} C_t^{\mathrm{ROI}} , \tag{5.14}$$

where the ROI parameters k_{tm}^{ROI} and k_{ut}^{ROI} are defined by

$$k_{tm}^{\mathrm{ROI}} = \frac{F_{tm}^{\mathrm{ROI}}}{V_K V_t}, \qquad k_{ut}^{\mathrm{ROI}} = \frac{F_{ut}^{\mathrm{ROI}}}{V_K V_t} , \tag{5.15}$$

with

$$k_{tm}^{\mathrm{ROI}} = \gamma k_{ut}^{\mathrm{ROI}} . \tag{5.16}$$

The last equality follows from equation (5.12). Also k_{tm}^{ROI} and k_{ut}^{ROI} are determined by data through F_{tm}^{ROI}, F_{ut}^{ROI}, V_K, and V_t.

We now come to the parametric formulation. As already observed, we reproduce at the pixel level a few relevant features of the ROI approach; in particular, each pixel is regarded as capable of interchanging carrier fluid and tracer with bladder. In line with equation (5.11), we assume that, at each pixel,

$$C_t = \frac{1}{F_{ut}} \frac{d}{dt}(V_u C_u^{\mathrm{ROI}}) , \tag{5.17}$$

where F_{ut} describes the contribution to bladder volume change per unit time arising from the flux of fluid through the single pixel. The coefficient F_{ut} is dependent on the position within the renal tissue and is considered as fixed, in analogy with (5.11). The correspondent of equation (5.14) is postulated as

$$\dot{C}_t = k_{tm} C_m - k_{ut} C_t , \tag{5.18}$$

accounting for the dynamic of the pixel tubule compartment. As expected, equation (5.18) coincides with the third differential equation of the system (5.5). The rate coefficient k_{tm} and k_{ut} are position-dependent, as in (5.5), and are regarded as fixed.

To summarize, for the pixel-dependent tubule concentration and rate coefficients, we have obtained from physiology the conditions that C_t, k_{tm}, k_{ut} are fixed, and that $k_{tm} = \gamma k_{ut}$. These modeling assumptions are essential to prove identifiability of the renal three-compartment non-catenary system, for which we can state the following result.

Theorem 5.1.2. *Let C_t, k_{tm}, and k_{ut} be fixed. By assuming that the polynomials*

$$P(s; \boldsymbol{k}_K) = k_{ma}(s + k_{af} + k_{mf}) + k_{fa} k_{mf}$$

and

$$Q(s;\boldsymbol{k}_K) = k_{fa}(s + k_{fm} + k_{tm}) + k_{ma}k_{fm}$$

are both coprime with the polynomial

$$D(s;\boldsymbol{k}_K) = (s + k_{af} + k_{mf})(s + k_{fm} + k_{tm}) - k_{mf}k_{fm}\,,$$

the kinetic parameters $\boldsymbol{k}_K = (k_{fa}, k_{ma}, k_{af}, k_{mf}, k_{fm}, k_{tm}, k_{ut})^T \in \mathbb{R}^7_+$ *are uniquely determined by* C_a^{ROI} *and* $\mathscr{C}_K$*, and the three-compartment non-catenary model of equations* (5.5)–(5.6) *and* (5.8) *is structurally globally identifiable.*

The proof of Theorem 5.1.2 follows the idea presented in (Delbary, Garbarino, and Vivaldi, 2016), and is reported in Appendix B.

It is important to remark that, although C_t, k_{tm}, and k_{ut} are fixed by physiology, the corresponding time dependence and values are not known explicitly. This means that they are still to be determined through optimization.

5.2 Imaging method

We present a parametric imaging method which relies upon the application of image pre-processing algorithms and of a rather general optimization scheme based on the regularized Gauss-Newton (reg-GN) method (Algorithm 1.1, described in subsection 1.2.3) able to solve the compartmental inverse problem pixel-wise. The proposed method is general enough to work for both two- and three- compartment models, effective enough to provide maps of all the kinetic coefficients involved, and in principle can be extended to envisage more than one model for a single PET image and physiologies described by more than three compartments. Therefore, our method is potentially applicable to any generic compartmental model, provided an ad hoc identifiability study and taking into account the compartment-dependent increase of the computational cost.

We start from the set of N reconstructed dynamic FDG-PET images:

$$(\boldsymbol{f}_1^{(t)}, \boldsymbol{f}_2^{(t)}, \dots, \boldsymbol{f}_N^{(t)}) \text{ for } t = 1, \dots, T\,, \tag{5.19}$$

where $\boldsymbol{f}_n^{(t)}$ is the $n-$th PET image at $t-$th time point of tracer concentration $\mathscr{C}$, i.e.

$$\boldsymbol{f}_n^{(t)}(i,j) = \mathscr{C}_{(i,j)}(t) \text{ for } i = 1, \dots, I,\ j = 1, \dots, J\,, \tag{5.20}$$

and I, J are the image dimensions.

We select the tissue of interest and the compartmental model reliable for its functional description. For each dynamic PET image $(\boldsymbol{f}_{\bar{n}}^{(1)}, \dots, \boldsymbol{f}_{\bar{n}}^{(T)})$, $\bar{n} \in \{1, \dots, N\}$, i.e. a PET slice, our imaging method follows the steps described below.

Step 1. *Gaussian smoothing.* In order to reduce the noise due to data acquisition, we apply a truncated Gaussian smoothing filter through the convolution operation

$$\tilde{\boldsymbol{f}}_{\bar{n}}^{(t)} = \boldsymbol{f}_{\bar{n}}^{(t)} * \boldsymbol{G}_{0,\sigma}\ \forall t = 1, \dots, T\,, \tag{5.21}$$

where

$$\boldsymbol{G}_{0,\sigma}(i,j) = \frac{1}{2\pi\sigma^2} e^{-\frac{x(i,j)^2 + y(i,j)^2}{2\sigma^2}}\,,$$
$$\boldsymbol{x}(i,j), \boldsymbol{y}(i,j) \in \{-\frac{L-1}{2}, \dots, \frac{L-1}{2}\} \times \{-\frac{L-1}{2}, \dots, \frac{L-1}{2}\}\,,$$

and L is the (odd) dimension of the window. In all our applications, we use a Gaussian convolution matrix $\boldsymbol{G}_{0,\sigma}$ with zero mean, standard deviation $\sigma = 1$ and dimension $L = 3$.

Step 2. *Image segmentation.* We model the outer region of the organ of interest with a standard two-compartment model; the ROI $\boldsymbol{A}$ delimiting the organ of physiologic interest is described by the most reliable compartmental model (according to the organ physiology). To extract the ROI $\boldsymbol{A}$ we apply the following image segmentation method.

1. Compute the PET image averaged in time: $\tilde{\boldsymbol{f}}_{\bar{n}} = \dfrac{1}{T}\sum_{t=1}^{T} \tilde{\boldsymbol{f}}_{\bar{n}}^{(t)}$.
2. Consider the pixel with maximum intensity: $(\bar{i}, \bar{j}) = \max_{i,j} \tilde{\boldsymbol{f}}_{\bar{n}}(i,j)$.
3. Approximate the profile of the $\bar{i}-$th matrix row with a family of one–dimensional Gaussian functions $G_{\bar{j},\sigma}$ of mean $\bar{j}$, variable variance σ, and s.t. $G_{\bar{j},\sigma}(\bar{j}) = \tilde{\boldsymbol{f}}_{\bar{n}}(\bar{i}, \bar{j})$, by means of a curve fitting process. This consists in computing
$$\bar{\sigma}_{\bar{i}} = \arg\min_{\sigma} ||\tilde{\boldsymbol{f}}_{\bar{n}}(\bar{i}, j) - G_{\bar{j},\sigma}(j)||_2 \,. \tag{5.22}$$
4. Determine the activity's lower bound in the ROI as the value $\bar{c}$ at which the two curves $\tilde{\boldsymbol{f}}_{\bar{n}}(\bar{i}, j)$ and $G_{\bar{j},\bar{\sigma}_{\bar{i}}}(j)$ separate from each other. Formally, this consists in evaluating
$$\begin{cases} j^* = \underset{j\in(\bar{j}-\gamma,\bar{j}+\gamma)}{\arg\max} \; |\tilde{\boldsymbol{f}}_{\bar{n}}(\bar{i}, j) - G_{\bar{j},\bar{\sigma}_{\bar{i}}}(j)| \\ \bar{c} = \tilde{\boldsymbol{f}}_{\bar{n}}(\bar{i}, j^*) \end{cases} , \tag{5.23}$$
in a suitably chosen neighborhood of $\bar{j}$ (i.e. for a suitable choice of $\gamma > 0$). The ROI encompassing the organ is thus defined as
$$\boldsymbol{A}(i,j) = \begin{cases} 0 & \text{if } \tilde{\boldsymbol{f}}_{\bar{n}}(i,j) < \bar{c} \\ 1 & \text{if } \tilde{\boldsymbol{f}}_{\bar{n}}(i,j) \geq \bar{c} \end{cases} . \tag{5.24}$$

Step 3. *Parameter estimation.* We apply the reg-GN algorithm pixel-by-pixel, considering each pixel with its specific compartmental model. In general, for a compartmental model with P arbitrary kinetic parameters $\boldsymbol{k} \in \mathbb{R}^P_+$, for a image pixel $(i,j) \in \{1,\dots,I\} \times \{1,\dots,J\}$, the reconstruction iterative algorithm reads as follows.

1. Check whether the measured radioactivity is significant: fix a constant value $\tau > 0$ discriminating between background noise and tissue activity.
   - If $||\mathscr{C}_{(i,j)}(t)||_2 \leq \tau$, then assign $\boldsymbol{k} = 0$ and stop;
   - if $||\mathscr{C}_{(i,j)}(t)||_2 > \tau$, then continue.
2. Choose the initial guess: $\boldsymbol{k}^{(0)}_{(i,j)} \in \mathbb{R}^P_+$.
3. Solve for $\boldsymbol{\delta}^{(0)}_{(i,j)} \in \mathbb{R}^P$
$$(r^{(0)}\boldsymbol{I}_{[P]} + \boldsymbol{F}^{(0)\,T}_{(i,j)}\boldsymbol{F}^{(0)}_{(i,j)})\boldsymbol{\delta}^{(0)}_{(i,j)} = \boldsymbol{F}^{(0)\,T}_{(i,j)}\boldsymbol{Y}^{(0)}_{(i,j)} \,, \tag{5.25}$$

where $\boldsymbol{F}_{(i,j)}^{(0)}$ encodes the Frèchet derivatives with respect to the kinetic parameters, $\boldsymbol{Y}_{(i,j)}^{(0)}$ is the discrepancy between the measured datum $\mathscr{C}_{(i,j)}$ and the model-predicted total concentration, $\boldsymbol{I}_P \in M_P(\{0,1\})$ is the $P \times P$ identity matrix, and $r^{(0)} \in \mathbb{R}_+$ is the regularization parameter automatically selected by means of the Generalized Cross Validation (GCV) method (Golub, Heath, and Wahba, 1979; O'Sullivan, 1999). The advantages in using the GCV are mainly that it can be applied without any a priori information on the error on the data or on peculiar properties of the solution, and that it requires just the computation of the SVD of the matrix of the problem.

4. Update $\boldsymbol{k}_{(i,j)}^{(0)}$ with the projected step-size:

$$\boldsymbol{k}_{(i,j)}^{(1)} = \boldsymbol{k}_{(i,j)}^{(0)} + \boldsymbol{P}_{(i,j)}^{(0)} \boldsymbol{\delta}_{(i,j)}^{(0)} , \tag{5.26}$$

where the projection matrix $\boldsymbol{P}_{(i,j)}^{(0)} \in M_P(\{0,1\})$ is defined as

$$\boldsymbol{P}_{(i,j)}^{(0)}(q,r) = \begin{cases} 0 & \text{if } q \neq r \\ 0 & \text{if } q = r \text{ and } (\boldsymbol{k}_{(i,j)}^{(0)})_q + (\boldsymbol{\delta}_{(i,j)}^{(0)})_q < 0 \\ 1 & \text{if } q = r \text{ and } (\boldsymbol{k}_{(i,j)}^{(0)})_q + (\boldsymbol{\delta}_{(i,j)}^{(0)})_q > 0 \end{cases} , \tag{5.27}$$

and iterate.

The iterative scheme is stopped when the relative error between the experimental dynamic concentration and the model-predicted one is less than an appropriate threshold, i.e. at a generic iteration h

$$\frac{||\mathscr{C}_{(i,j)}(t) - V_b C_b^{\mathrm{ROI}}(t) - \boldsymbol{\alpha}^T \boldsymbol{C}_{(i,j)}(t; C_b^{\mathrm{ROI}}, \boldsymbol{k}_{(i,j)}^{(h)})||_2}{||\mathscr{C}_{(i,j)}(t)||_2} \leq \epsilon , \tag{5.28}$$

where C_b^{ROI} is the generic given blood IF of the system, V_b is the known constant blood volume fraction for the selected region, and ϵ depends on the noise level on data.

Step 4. *Parametric images.* Once we obtain the set of exchange coefficients of the model for each image pixel, we build up the parametric images $\boldsymbol{K}_1, \ldots, \boldsymbol{K}_P$:

$$\boldsymbol{K}_1(i,j) = \boldsymbol{k}_{(i,j)}(1), \ \ldots \ , \boldsymbol{K}_P(i,j) = \boldsymbol{k}_{(i,j)}(P) . \tag{5.29}$$

Regarding Step 1. and Step 2., other imaging processing methods can be used to smooth and segment PET images; the impact of other approaches on the accuracy of compartmental analysis is under investigation. However, simple Gaussian smoothing, as in Step 1., and our ad hoc image segmentation process, as in Step 2., provide good results regardless of the limited resolution of PET images involved in the analysis.

5.3 Numerical validation

The proposed parametric imaging method is validated against synthetic FDG-PET images constructed by simulating the two-compartment catenary model, described

in subsection 5.1.1. We remark that all the computational part has been implemented in the Matlab programming environment.

Synthetic data are created mimicking a real FDG-micro-PET acquisition: first we choose a phantom (Figure 5.4(a)) encompassing four homogeneous regions; for every region, a set of realistic kinetic parameters of a two-compartmental problem is assigned as ground truth, and a realistic value for the blood volume fraction V_{bT} is selected (Table 5.1). We obtain four synthetic parametric images $\boldsymbol{K}_{fb}, \boldsymbol{K}_{bf}, \boldsymbol{K}_{mf}, \boldsymbol{K}_{fm}$, each one characterized by a specific set of kinetic parameters. The ground truth parametric images are displayed in Figure 5.5.

	k_{fb}	k_{bf}	k_{mf}	k_{fm}	V_{bT}
region 1	0.80	0.60	0.07	0.07	0.10
region 2	1.00	1.00	0.20	0.20	0.20
region 3	1.10	0.90	0.50	0.40	0.05
region 4	0.50	0.50	0.10	0.01	0.30

TABLE 5.1: Ground truth numerical values of the kinetic parameters $k_{fb}, k_{bf}, k_{mf}, k_{fm}$ (min^{-1}), and of the blood volume fraction V_{bT}, for each one of the four homogeneous regions.

The dynamic PET images of tracer concentration are generated following the scheme below. For each pixel:

1. compute the values of the integral (5.3) using the ground truth values of the parameters and a simulated blood IF (Figure 5.4(b)), the latter obtained by fitting with a gamma variate function (Golish et al., 2001) a set of real measurements acquired from a healthy mouse in a controlled experiment;

2. evaluate the synthetic concentration by means of equation (5.4), with the numerical value of V_{bT} related to the homogeneous region at which the pixel belongs;

3. sample on time interval $[t_1; t_T]$ of 27 time frames equivalent to the typical total acquisition time of the FDG experiments performed with the micro-PET scanner Albira (Bruker, 2012), produced by Carestream Health, Genova, and in agreement with usual time points of the experiments (10×15s, 1×22s, 4×30s, 5×60s, 2×150s and 5×300s).

Once the noise-free dynamic PET images are obtained:

4. project the images into the sinogram space by means of the Radon transform, yielding projected noise-free sinogram data;

5. add mixed Poisson-Gaussian noise (Luisier, Blu, and Unser, 2011; Santarelli, Positano, and Landini, 2017) to the projected data: apply Poisson noise to account for the stochastic nature of the photon counting process at the detectors, and then corrupt the Poisson model with additive Gaussian noise to account for the intrinsic thermal and electronic fluctuations of the acquisition device. Note that errors arising from instrumental and physical effects, such as attenuation, scattered events, decay and accidental coincidences, are not simulated;

6. reconstruct the noisy dynamic PET images of tracer concentration by means of the Filtered Back Projection (FBP) applied on the two-dimensional noisy sinogram data (Algorithm 3.1, described in subsection 3.2.2).

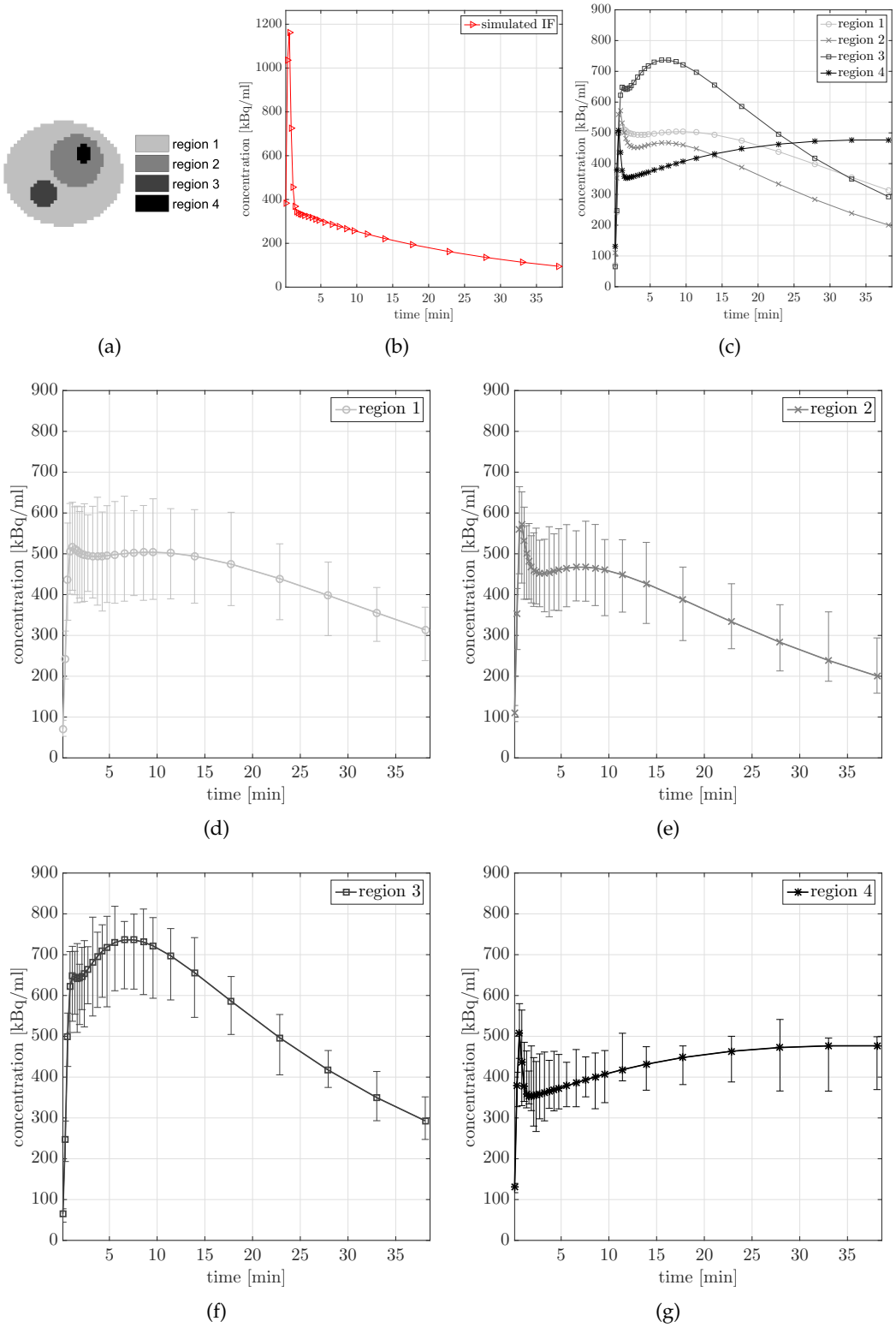

FIGURE 5.4: The FDG-PET simulation setting. (a) Phantom composed by four homogeneous regions. (b) Simulated blood IF. (c) Characteristic noise-free time concentration curves for the four regions. (d-g) Noisy time concentration curves for each region: the error bars identify the variability on the concentrations introduced by the noise.

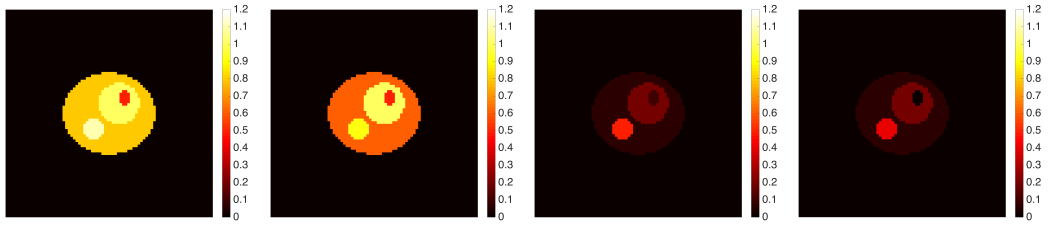

(a) $\boldsymbol{K}_{fb}$ (b) $\boldsymbol{K}_{bf}$ (c) $\boldsymbol{K}_{mf}$ (d) $\boldsymbol{K}_{fm}$

FIGURE 5.5: The ground truth parametric images $\boldsymbol{K}_{fb}, \boldsymbol{K}_{bf}, \boldsymbol{K}_{mf}, \boldsymbol{K}_{fm}$ of the two-compartment catenary system.

We create fifty independent identically-distributed noisy datasets. Characteristic noise-free TACs of the four regions are shown in Figure 5.4(c), whereas the noisy TACs are reported in Figure 5.4(d)–5.4(g). The Poisson noise is applied by using the Matlab function poissrnd, and the white Gaussian noise by means of the Matlab function awgn with a signal-to-noise ratio of 20 dB.

For each dataset, we follow the reconstruction steps of Section 5.2, i.e. we apply the Gaussian smoothing filter ($\sigma = 1$, window 3×3) on the dynamic PET images and solve pixel-wise the compartmental inverse problem by means of the reg-GN iterative procedure (Algorithm 1.1). For each pixel, the starting point of our method is randomly chosen in the interval $(0, 1)$ and the regularization parameter is optimized at each iteration through the GCV method, by the requirement of a predefined range of variability (between 10^4 and 10^6). We do not need to apply the image segmentation step because in this simulation we model the same two-compartment scheme for all the pixels.

Once the entire set of kinetic parameters $k_{fb}, k_{bf}, k_{mf}, k_{fm}$ for each pixel are retrieved, we build up the parametric images $\boldsymbol{K}_{fb}, \boldsymbol{K}_{bf}, \boldsymbol{K}_{mf}, \boldsymbol{K}_{fm}$. Figure 5.6 shows the mean images (first row) and the standard deviation images (second row), computed over the fifty reconstructions. The mean images provide a reliable approximation of the ground truth parametric images, demonstrating the consistency of the parametric inversion procedure. Note that the artifacts occurring at the edges of the homogeneous regions, observable especially around the first and second regions, are consequences of the application of the Gaussian filter. The standard deviation images keep systematically small values, proving that the iterative reconstruction scheme is numerically stable with respect to noise. Table 5.2 reports the mean and the standard deviation of the kinetic parameters over the four homogeneous regions. Comparison between the ground truth values of Table 5.1 and the reconstructed values of Table 5.2 clearly shows the reliability of our approach.

From the computational viewpoint, the parametric reconstruction takes almost 45 minutes. Please note that the algorithm was implemented in the Matlab programming environment and the algorithm was executed on a computer with a processor Intel core i5. Despite that, for a single pixel, the reg-GN iterative scheme requires about 5-10 iterations before it converges and the operations carried out in a single iteration for computing the Newton step-size are not computationally demanding (the matrices in the game have small size). Therefore, the high computational cost of the method depends only on the application of the reduction scheme on a dense set of pixels. Nevertheless, the computational complexity of our parametric imaging method is consistent with standard parametric methods.

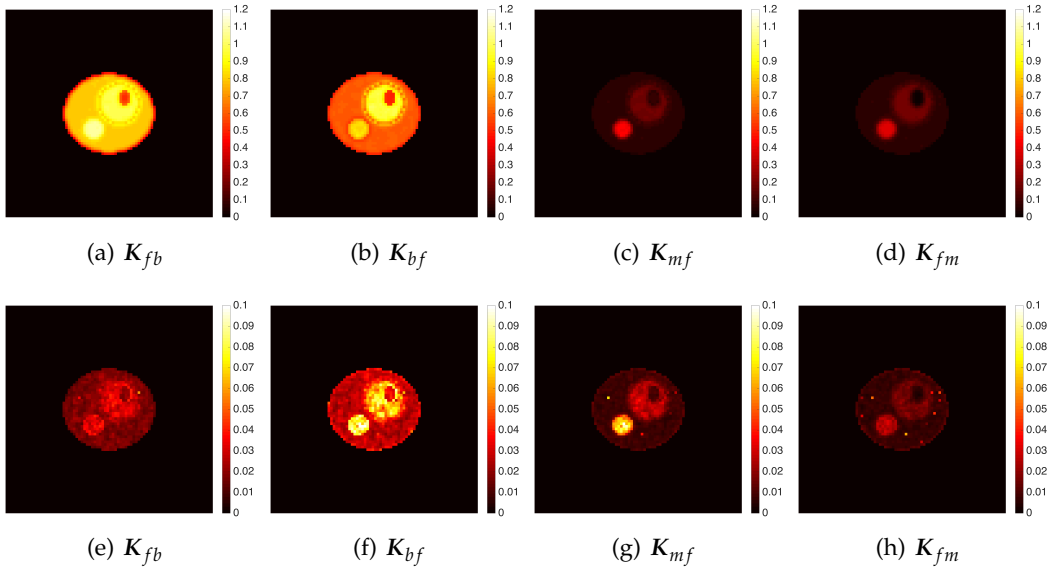

(a) $\boldsymbol{K}_{fb}$ (b) $\boldsymbol{K}_{bf}$ (c) $\boldsymbol{K}_{mf}$ (d) $\boldsymbol{K}_{fm}$

(e) $\boldsymbol{K}_{fb}$ (f) $\boldsymbol{K}_{bf}$ (g) $\boldsymbol{K}_{mf}$ (h) $\boldsymbol{K}_{fm}$

FIGURE 5.6: Mean images (first row) and standard deviation images (second row) of $\boldsymbol{K}_{fb}, \boldsymbol{K}_{bf}, \boldsymbol{K}_{mf}, \boldsymbol{K}_{fm}$, computed over the fifty parametric reconstructions.

	k_{fb}	k_{bf}	k_{mf}	k_{fm}
region 1	0.75 ± 0.02	0.59 ± 0.03	0.07 ± 0.01	0.07 ± 0.01
region 2	0.93 ± 0.03	0.87 ± 0.06	0.16 ± 0.02	0.16 ± 0.01
region 3	1.04 ± 0.03	0.79 ± 0.08	0.33 ± 0.06	0.31 ± 0.02
region 4	0.58 ± 0.02	0.51 ± 0.03	0.08 ± 0.01	0.02 ± 0.01

TABLE 5.2: Mean and standard deviation of the kinetic parameters $k_{fb}, k_{bf}, k_{mf}, k_{fm}$ (min^{-1}), for each one of the four homogeneous region, computed over the fifty parametric reconstructions.

5.4 Application to FDG-PET renal data

We test the proposed parametric imaging method on real FDG-PET experiments in the case of the three-compartment non-catenary model representing the renal physiology, described in subsection 5.1.2.

We analyze FDG-PET real data of murine models obtained by means of the dedicated Albira micro-PET system (Bruker, 2012) currently operational at our lab (Nuclear Medicine Department, IRCCS San Martino IST, Genova, Italy). Following the experimental protocol for FDG-PET experiments, utilized during a study on the metabolic effects of metformin (Massollo et al., 2013), the animals were studied after a fasting period of six hours to ensure a steady state of substrate and hormones governing glucose metabolism. Then, the animals were properly anesthetized and positioned on the bed of the micro-PET system whose two-ring configuration covers the whole animal body in a single bed position. A dose of 3 to 4 MBq of FDG was injected through the tail vein, soon after the start of a dynamic list mode acquisition lasting 40 minutes. The acquisition was reconstructed using the following framing rate: 10×15s, 1×22s, 4×30s, 5×60s, 2×150s and 5×300s. The dynamic PET images of tracer concentration (kBq/ml) were reconstructed using a Maximum Likelihood Expectation Maximization (MLEM) method (Algorithm 3.2, described in

subsection 3.2.3). The complete dataset is composed by 100 images of 80×80 pixels, each one reproducing an axial section, by the total number of time points of the experiment. For this test, we consider a mouse in a control (CTR) condition and a mouse in a starved (STS) condition (food deprivation, with free access to water, for 48 hours). We focus on the analysis of the renal physiology and select a single PET slice containing an axial section of the right kidney, the same slice for both animals. The entire FDG kinetic process is initialized by the arterial IF. The determination of the IF is a challenging task in the case of mice. To accomplish it, for each animal model the tracer first pass was viewed in cine mode. Then a ROI was drawn in the aortic arc by an experienced observer, in a frame where the left ventricle was particularly visible, and maintained it for all time points. For both analysis, the blood volume fraction is assumed to be equal to $V_{bK} = 0.2$, a typical value for the kidney of the mouse (Garbarino et al., 2014).

We apply our imaging method on the selected dynamic PET slice of the CTR mouse and of the STS mouse. More specifically, we smooth the data by means of a Gaussian filter of standard deviation $\sigma = 1$ and size 3×3; we select the ROI within the axial section of the kidney through the image segmentation process determining the minimum value of activity recorded inside the organ, and reconstruct the kinetic parameters $k_{fa}, k_{ma}, k_{af}, k_{mf}, k_{fm}, k_{tm}, k_{ut}$ of the three-compartment system for each pixel by means of the reg-GN method (Algorithm 1.1). The initial guesses are randomly selected in the interval $(0, 1)$ and the regularization parameter is chosen by the GCV method (with a confidence interval ranging between 10^4 and 10^6). The reconstructed parametric images $\boldsymbol{K}_{fa}, \boldsymbol{K}_{ma}, \boldsymbol{K}_{af}, \boldsymbol{K}_{mf}, \boldsymbol{K}_{fm}, \boldsymbol{K}_{tm}, \boldsymbol{K}_{ut}$ for the renal compartmental model are presented in Figure 5.7 and Figure 5.8: in each figure, the first row shows the parametric images for the CTR mouse, the second row for the STS mouse.

It should be pointed out that in general patient's motion during PET measurements contaminates the acquired data; this holds even true for rodents in anesthesia as the scans are rather long. Obviously, these motion artifacts affect the pixel-by-pixel analysis. Note that in our parametric reconstruction the effects of motion can be excluded and are not investigated.

All parametric images, of both the CTR mouse and the STS mouse, show values of the parameters that vary quite largely from pixel to pixel, bringing out the lack of homogeneity of the renal tissue. Indeed, the parametric images point out the different structures composing the kidney and characterizing the distinct functions of the organ (Meneton et al., 2000). This is consistent with the architecture of the renal compartmental model we have designed (subsection 5.1.2). The higher activity of the parameters is located in a specific part of the outer portion of the axial section of the kidney, which is attributable to the renal cortex, in which most of the renal processes are carried out. Moreover, for both the CTR and STS conditions, we can observe that the parametric images $\boldsymbol{K}_{tm}$ and $\boldsymbol{K}_{ut}$ linked to the tubule compartment have a very similar distribution while the physiologically sound condition $k_{tm} \simeq 10^2 k_{ut}$ is maintained pixel-wise (without any constraint in the inversion procedure). Instead, the fundamental difference between the CTR and the STS parametric images relies on the numerical values of the parameters. In particular, the values of the exchange coefficients associated with the blood input, that are k_{fa}, k_{ma}, k_{af}, exhibit a different behavior with respect to the two conditions. From the CTR mouse to the STS mouse: the input parameter from the blood k_{fa} increases (almost duplicates), the filtration process described by k_{ma} decreases (is almost reduced by a factor of three), and the output parameter to the blood k_{af} remains approximately equal. This trend reflects the response of the kidney to the different physiological conditions of the

two mice analyzed, coherently with what already observed (Garbarino et al., 2014). Finally, we notice that the parameters linked to FDG metabolism, k_{mf} and k_{fm}, and the parameters representing the reabsorption and excretion processes, k_{tm} and k_{ut} respectively, remain basically unchanged in the two conditions.

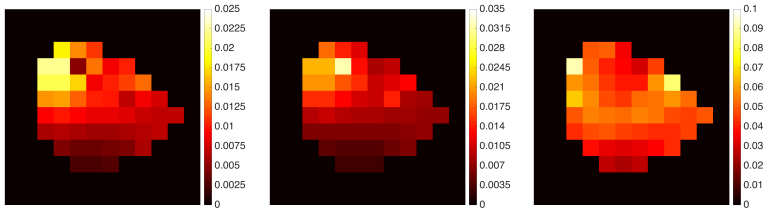

(a) $\boldsymbol{K}_{fa}$ (b) $\boldsymbol{K}_{ma}$ (c) $\boldsymbol{K}_{af}$

(d) $\boldsymbol{K}_{fa}$ (e) $\boldsymbol{K}_{ma}$ (f) $\boldsymbol{K}_{af}$

FIGURE 5.7: Parametric images $\boldsymbol{K}_{fa}, \boldsymbol{K}_{ma}, \boldsymbol{K}_{af}$: first row for the CTR mouse, second row for the STS mouse.

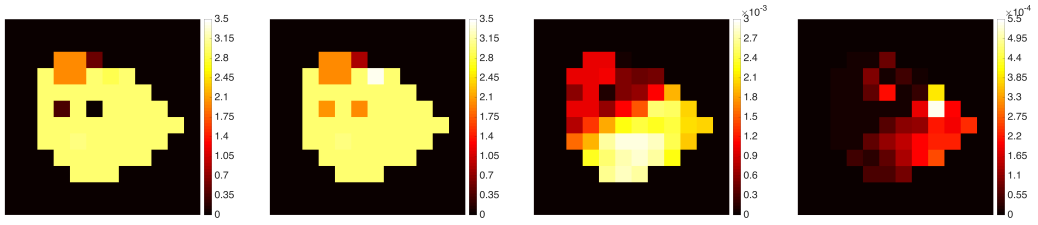

(a) $\boldsymbol{K}_{mf}$ (b) $\boldsymbol{K}_{fm}$ (c) $\boldsymbol{K}_{tm}$ (d) $\boldsymbol{K}_{ut}$

(e) $\boldsymbol{K}_{mf}$ (f) $\boldsymbol{K}_{fm}$ (g) $\boldsymbol{K}_{tm}$ (h) $\boldsymbol{K}_{ut}$

FIGURE 5.8: Parametric images $\boldsymbol{K}_{mf}, \boldsymbol{K}_{fm}, \boldsymbol{K}_{tm}, \boldsymbol{K}_{ut}$: first row for the CTR mouse, second row for the STS mouse.

Part III

Cell-scale

Chapter 6

LigandTracer technology

The LigandTracer (LT) technology (Ridgeview Instruments AB, Uppsala, Sweden) is devoted to real-time monitoring molecular interactions on cells, and a LT prototype is currently operational at our lab (Nuclear Medicine Department, IRCCS San Martino IST, Genova, Italy). The device measures the affinity of radiolabeled ligands interacting with cell-surface receptors, which is a common measurement in different fields of biology and biochemistry, including cancer research. The provided dynamic data of bound ligand amount can be processed to obtain kinetic parameters describing reliably the cell-ligand interaction.

Standard LT applications focus on the study of protein-cell interaction processes in vitro, in particular cellular uptake and cellular retention. In the area of biotechnology for the development of therapeutic agents (such as proteins, monoclonal antibodies, and antibody fragments in the pharmaceutical industry), assessing the rate of uptake may be of importance for the prediction of dosage of a therapeutic protein, and the retention time is a probable predictor of the duration of the effect caused by the protein.

We lead a novel application involving the LT device, in which the glucose analog radioactive tracer [^{18}F]-fluorodeoxyglucose (FDG) is used to evaluate the glucose uptake by cultured cancer cells (Scussolini et al., 2018b). LT measurements in vitro offer a quick and inexpensive method with less assay variability compared to in vivo studies: LT allows for repeated experiments under constant conditions, whereas experiments on tracer uptake in vivo may be influenced by absorption by other organs, specific tissue environment, blood perfusion, and so on. Moreover, LT measurements ensure a direct estimate of FDG consumption, and thus of glucose consumption, without any distortion introduced by physical corrections or signal reconstruction algorithms, which are essential steps to be made in, e.g., Positron Emission Tomography.

In this chapter we provide a detailed description of the LT experimental setting. In the first section, the operating principles of the device are outlined, concerning the LT technical characteristics and its geometrical properties. The second section describes the LT calibration procedure. In the third section, we formalize the time-dependent activity curves defining the LT data.

6.1 LT acquisition

The LT prototype (Figure 6.1) was previously described in Björke and Andersson, 2006a and Björke and Andersson, 2006b. It essentially consists in a circular Petri dish (PD) placed on a tilted rotating support of the instrument, and a detector. The PD contains a suitably prepared incubation liquid medium with the radioligand, and the seeded cell culture. The detector is capable of performing repeated radioactivity

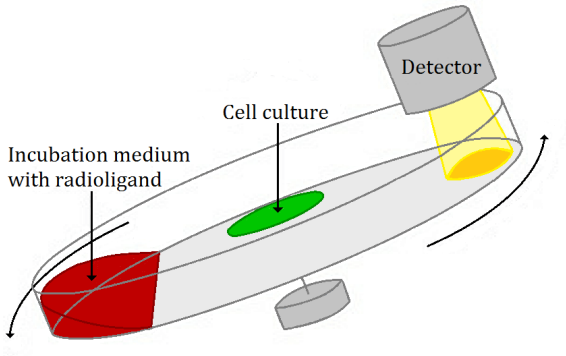

FIGURE 6.1: Measurement principles of the LT device: the Petri dish containing attached target cells is placed on an tilted and rotating support; the incubation medium with the radioligand occupies the lower part of the dish, due to the dish inclination; the detector points towards the upper part of the dish. The measurement of the cell-ligand interaction is performed once per rotation in the upper position.

measurements at predefined time points and positions. We make use of the LT White device, and we consider the glucose analog radiotracer FDG.

The LT has a solid state radioactivity detector (5CXS-S80, Crystal GmbH, Germany) capable of detecting gamma radiation in the energy range 10–69 keV. In the LT White device, the sensor is a photodiode, rectangular in shape with area 80 mm^2 (8 by 10 mm), encapsulated with a detection window made of 25 μm thick titanium foil. The sensor can register the beta particles emitted by the radionuclide fluorine-18 in the range of 38 keV to 1200 keV, with correct counting up to $3 \cdot 10^4$ Counts Per Seconds (CPS). The sensor sends TTL compatible pulses to a counter in the internal electronics of the instrument.

The cell culture to be analyzed is cultured prior to each experiment on a 100 mm diameter PD inclined at 30 degrees from the horizontal plane, so as to limit the presence of cells to a specific area of the PD. The PD is then placed in the LT, tilted at the same angle, and contains the incubation liquid medium of volume 3 mL in the lowest part of the dish. The radioligand is added to the medium right before the beginning of the experiment. The detector is inclined at an angle of 20 degrees to the plane of the PD and points at the top of the dish. In this configuration, the tilt of the detector ensures that radioactivity emitted by the medium in the lower part of the dish does not significantly contribute to counts.

The LT device rotates periodically around the axis inclined at an angle of 30 degrees from the vertical. By allowing the LT to rotate the PD continuously, the level of radioactivity accumulated by the cells can be measured in real-time with high temporal resolution. Each rotation cycle is divided into four time intervals, that for our experiments have been fixed as follows:

(a) 25 seconds with cell culture in the rotation nadir and hence fully immersed in the radioactive medium;

(b) 5 seconds for a counter-clockwise rotation of 180 degrees;

(c) 25 seconds with cell culture in the rotation zenith and thus under the detector;

(d) 5 seconds for another counter-clockwise rotation of 180 degrees, leading to cycle restart.

The detector collects the counts in phases (a) and (c) in order to measure the counting rates of the background area (devoid of cells) and the target area (with cells). For each t-th cycle, lasting one minute, the *background counts* $\mathcal{B}^c$ and the *target counts* $\mathcal{T}^c$ are defined as the normalized counts (CPS)

$$\mathcal{B}^c(t) = \frac{n_{\mathcal{B}}(t)}{25\ \text{sec}}\,, \quad \mathcal{T}^c(t) = \frac{n_{\mathcal{T}}(t)}{25\ \text{sec}}\,,$$

where n specifies the total number of counts detected in the time window of recording (in our case, 25 seconds). The apex c refers systematically to CPS.

Counts of the target region result from emission by cells and the residual of the liquid medium stuck to the dish. Therefore, the effective *LT counts* $\mathcal{A}^c_{\text{LT}}$ coming only from the cells under the detection window are determined as the difference between the target counts and the background counts at each measurement cycle, i.e.

$$\mathcal{A}^c_{\text{LT}}(t) = \mathcal{T}^c(t) - \mathcal{B}^c(t)\,. \tag{6.1}$$

The counts are corrected for physical decay through multiplication by the exponential factor $e^{\lambda t}$, where λ is the ^{18}F decay constant of the FDG radioactive tracer ($\lambda = \ln 2/110\ \text{min}^{-1}$).

6.2 LT calibration

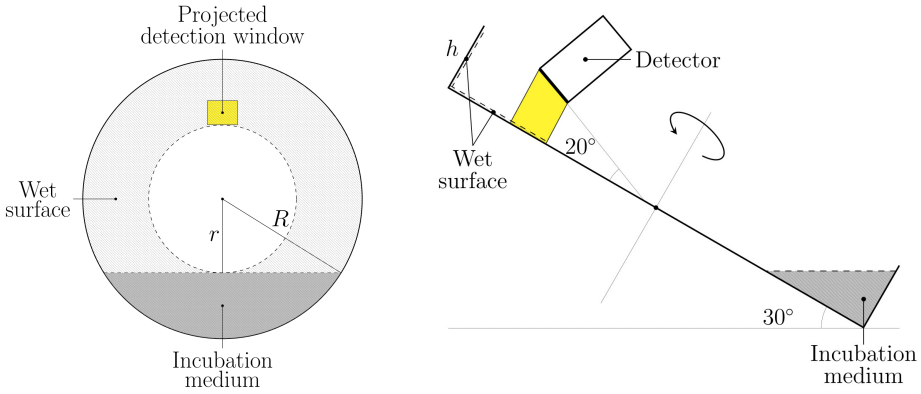

(a) Front view. (b) Lateral view.

FIGURE 6.2: LT geometry: (a) $R = 43.5$ mm; $r = 23$ mm; cells are attached to the circular segment of central angle $2\cos^{-1}(r/R)$ which is wet by the incubation medium; (b) height of the wet lateral surface $h = 11.85$ mm.

The amount of FDG added to the medium at each experiment is measured in Bq, while the time curves of counts provided by the LT are given in CPS. A calibration factor is thus needed in order to convert observed counting rates for the available FDG dose. The connection between Bq put into the medium and CPS measured by the detector is found as a consequence of the conservation law of the activity, which can be applied because LT represents a *closed system*: at each time, tracer molecules of the dose injected in the PD distribute exhaustively in the incubation medium, in the wet subsurface of the PD, and in the cells. Therefore, we apply a tracer conservation condition, formulated as follows: the total activity uptake from the incubation medium in the time interval of the experiment duration (in Bq) is proportional to

the total activity content external to the incubation medium (in CPS) at the end time. The proportionality constant provides the calibration factor allowing the conversion from Bq to CPS, and vice versa.

As described in Scussolini et al., 2018b, the LT calibration is performed by conducting controlled experiments in the absence of attached cells, in order to avoid uncontrolled variations in the measurements resulting from tracer uptake by cells, following essentially the same procedure of cell experiments. Input vial containing four mL of incubation medium is enriched with FDG; three mL of this radioactive fluid are spilled in the PD lodged in the LT, and measurements are performed for a time interval of 60 minutes, at most.

Radioactivity external to the incubation medium is emitted only from the total background area, which, because of periodic immersions of the PD due to LT rotations, consists of the surface of the circular ring of radii R and r, plus the lateral surface of the cylinder of radius R and height h (see Figure 6.2). This subsurface of the PD contaminated by radioactive molecules, i.e. the wet region, reflects the fluid adhesion to the plastic structure of the PD, which may be considered with fixed properties within the same experimental setting. Elementary geometric considerations, based on Figure 6.2, lead to estimate the total emitting area of the wet region as $S_W \simeq 7.5 \cdot 10^3$ mm^2.

The background counts $\mathcal{B}^c$ measured by the LT reaches instantly (in the first minute of the experiment) its maximum value, which is maintained constant in time. Moreover, the background counting is independent of the position on the PD surface, as verified with repeated experiments made with more than one background counting (i.e. with several pauses for each LT cycle in different positions). Therefore, the radioactive tracer is assumed to be uniformly distributed over the wet region. Accordingly, positrons received by the detector are regarded as coming from the orthogonal projection of the detection window over the PD surface. The LT detection window of area 80 mm^2 points toward the PD with an angle of 20 degrees with respect to the normal, accounting for an area of the projected detection window (pdw) on the PD surface of $S_{\text{pdw}} \simeq 75$ mm^2. Thus, we associate with S_{pdw} the measured value $\mathcal{B}^c$ in CPS. Owing to the uniform distribution, we estimate the radioactivity contaminating the wet region of the PD of area S_W by applying the law of direct proportionality between CPS and areas. The *wet counts* $\mathcal{A}^c_W$ associated with the wet region is found from the proportion

$$\frac{\mathcal{A}^c_W}{S_W} = \frac{\mathcal{B}^c}{S_{\text{pdw}}} ,$$

which leads to

$$\mathcal{A}^c_W = \frac{S_W}{S_{\text{pdw}}} \mathcal{B}^c \simeq 10^2 \mathcal{B}^c . \tag{6.2}$$

At the end of the experiment, the incubation medium is accurately removed from the PD, in order to evaluate the sequestration of tracer radioactivity by the wet region. Both the initial amount of tracer injected in the PD $\mathcal{D}$ and the final radioactivity content in the medium $\mathcal{D}_f$ are measured in Bq through a sodium iodide (NaI) scintillation counters (dose calibrator). The decay corrected difference in fluid radioactivity $\mathcal{D} - \mathcal{D}_f$ in Bq is thus compared with the counted radioactivity of the wet region in CPS.

The conservation law of activity for the closed LT system is expressed by the linear equation

$$\mathcal{D} - \mathcal{D}_f = e \mathcal{A}^c_W , \tag{6.3}$$

which is regarded as the definition of the *efficiency coefficient* e to be applied in the conversion from CPS to Bq.

Twelve cell-free experiments have been performed, denoted by qi, with $i \in \{1, \dots, 12\}$, at variable FDG amounts, either without glucose or with glucose concentration set at 5.5 mM (1 g/L) and 11.1 mM (2 g/L). Figure 6.3 shows the counting rates of the measured background $\mathcal{B}^C$ of one experiment for each different medium composition, namely q3 (no glucose), q7 (glucose concentration at 5.5 mM), and q11 (glucose concentration at 11.1 mM). Since these three experiments are carried out at comparable initial amount of FDG, the difference in the counts registered by LT depends on the glucose concentration. More precisely, the presence of glucose influences, or better increases, the tracer adhesion to the PD. In Table 6.1, for each experiment, we report glucose concentration, initial FDG dose $\mathcal{D}$, final value of radioactivity in the medium $\mathcal{D}_f$, estimated wet counts $\mathcal{A}_W^c$, and percentage of FDG removal off the medium (computed as the difference $\mathcal{D} - \mathcal{D}_f$ over $\mathcal{D}$).

We consider the data set consisting of the twelve couples $\{(\mathcal{A}_W^c, \mathcal{D} - \mathcal{D}_f)_i\}_{i=1}^{12}$. In support of the assumption of linearity of equation (6.3), the Pearson correlation coefficient evaluating the linear correlation between the variables $\mathcal{D} - \mathcal{D}_f$ and $\mathcal{A}_W^c$ assumes the value 0.95 with a p-value of $3 \cdot 10^{-6}$, showing a tight linear correlation regardless either glucose or radioactivity concentrations in the spilled fluid. Therefore, we determine the efficiency coefficient e through simple linear regression applied to the experimental set, as shown in Figure 6.4. We find the value $e = 3$ Bq/CPS combined with a standard error of the estimate of 0.24 and a coefficient of determination r^2 equal to 76%, which proves the goodness of fit and therefore the reliability of the estimated value of e.

We assume that the efficiency value e is maintained for experiments conducted with cell cultures.

	Glucose [mM]	$\mathcal{D}$ [MBq]	$\mathcal{D}_f$ [MBq]	$\mathcal{A}_W^c$ [CPS]	% removal
q1	0	6.79	6.78	$1.57 \cdot 10^4$	0.11
q2	0	5.17	4.95	$6.45 \cdot 10^4$	4.42
q3	0	4.41	4.40	$9.63 \cdot 10^3$	0.18
q4	0	4.25	4.08	$5.33 \cdot 10^4$	3.96
q5	5.5	5.83	5.74	$4.49 \cdot 10^4$	1.62
q6	5.5	4.40	4.35	$3.31 \cdot 10^4$	1.21
q7	5.5	3.01	2.99	$2.33 \cdot 10^4$	0.48
q8	5.5	1.49	1.44	$1.18 \cdot 10^4$	2.90
q9	11	6.56	6.37	$5.84 \cdot 10^4$	2.94
q10	11	4.67	4.55	$3.71 \cdot 10^4$	2.54
q11	11	3.93	3.84	$3.24 \cdot 10^4$	2.25
q12	11	2.15	2.11	$1.76 \cdot 10^4$	1.75

TABLE 6.1: Experimental values for each LT cell-free experiment qi, $i \in \{1, \dots, 12\}$: glucose concentration, administered FDG activity $\mathcal{D}$, final FDG activity $\mathcal{D}_f$, wet activity $\mathcal{A}_W^c$, and percentage of FDG removal off the medium (computed as the difference $\mathcal{D} - \mathcal{D}_f$ over $\mathcal{D}$).

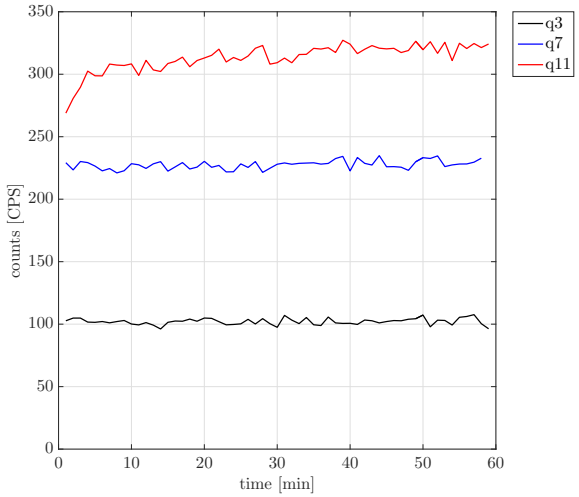

FIGURE 6.3: Counting rates of the measured background $\mathcal{B}^c$ for three selected LT cell-free experiments: q3 at zero glucose (black line), q7 at glucose concentration 5.5 mM (blue line), and q11 at glucose concentration 11.1 mM (red line).

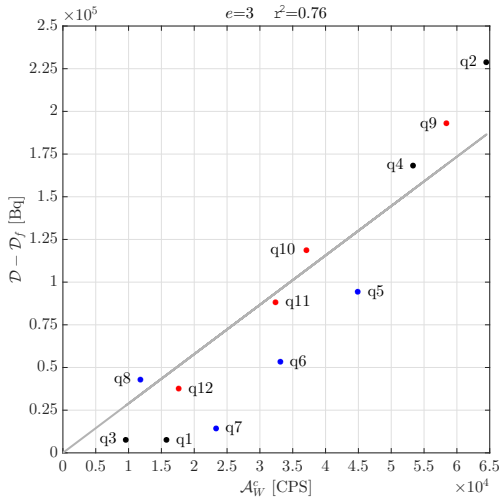

FIGURE 6.4: Simple linear regression on the data set $\{(\mathcal{A}_W^c, \mathcal{D} - \mathcal{D}_f)_i\}_{i=1}^{12}$ for the LT cell-free experiments q_i, $i \in \{1, \ldots, 12\}$, made at glucose concentration zero (black points), 5.5 mM (blue points) and 11.1 mM (red points).

6.3 LT data

For each experiment, the available LT data consist of the time-dependent counts of radioactive emission by the cells under the detection window $\mathcal{A}_{\text{LT}}^c$, and the injected FDG activity $\mathcal{D}$. The time activity curve (TAC) of tracer uptake by the whole cell culture in the PD, and the time curse of tracer activity in the incubation medium, are then reconstructed in terms of the LT data.

6.3.1 TAC of tracer inside cells

Starting from the LT measure $\mathcal{A}_{\text{LT}}^c$, counting the radiation emitted by only the cells under the detection window, we need to reconstruct the time curse of the activity emitted by the entire cell culture seeded in the PD.

We assume that cells in the culture cannot be distinguished between each other, and that they are uniformly distributed over the surface covered by the incubation medium, represented by the circular segment in Figure 6.2(a) covering the area $S_C \simeq 1.1 \cdot 10^3$ mm^2. The LT device provides the counts $\mathcal{A}^c_{\mathrm{LT}}$ associated with the area S_{pdw} of the projected detection window. Owing to uniformity, we apply a proportionality law between measured CPS and areas to find

$$\mathscr{A}^c_T = \frac{S_C}{S_{\mathrm{pdw}}} \mathcal{A}^c_{\mathrm{LT}} \simeq 0.14 \cdot 10^2 \mathcal{A}^c_{\mathrm{LT}} \,, \tag{6.4}$$

with the *cell culture counts* $\mathscr{A}^c_T$ representing the estimated time-dependent radioactivity counts to be associated with all cells.

In Bq, the TAC of tracer inside the cell culture, i.e. the *cell culture activity* $\mathscr{A}_T$, is simply obtained by applying the efficiency coefficient e to the counts:

$$\mathscr{A}_T = e\mathscr{A}^c_T \,, \tag{6.5}$$

where $e = 3$ Bq/CPS is estimated as shown in Section 6.2.

6.3.2 TAC of tracer inside the medium

Consider a typical LT experiment of tracer uptake by a cell culture. During the uptake phase, tracer molecules initially in the incubation medium are partially dispersed over the wet surfaces of the PD and partially adsorbed by cells. As a consequence, the decay corrected activity in the medium decreases with time. The TAC of tracer in the medium is unknown, and it can be reconstructed by exploiting the conservation principle of the diffusion process of radioactive molecules in the closed LT system.

First we examine tracer distribution at the very beginning of the LT experiment. As already observed, the tracer dose $\mathcal{D}$ injected into the PD is distributed, without loss, among incubation medium, wet background area, and cells. The counts of the background $\mathcal{B}^c$ reach the (maximum) stationary value in a very short time interval; in the meanwhile, the radiation content inside cells, which is zero at the time $t = 0$, does not grow significantly, since cell uptake is a much slower process. Denote by $A_i(t)$ (Bq) the time course of activity in the medium. Then, the initial value at $t = 0$, $A_{i0} = A_i(0)$, can be expressed as

$$A_{i0} = \mathcal{D} - e\mathcal{A}^c_W \,, \tag{6.6}$$

where the wet activity $\mathcal{A}^c_W$ is defined by equation (6.2). In words, the process of distribution of radioactivity over the wet background area is regarded as instantaneous with respect to cell uptake, so that the initial value A_{i0} of the activity inside the medium available for cells is given by the difference between the injected dose and the wet area sequestration.

The conservation of the decay corrected activities for the closed LT system leads to the following equation:

$$\mathcal{D} = A_i(t) + e\frac{S_W}{S_{\mathrm{pdw}}} \mathcal{B}^c(t) + e\frac{S_C}{S_{\mathrm{pdw}}} \mathcal{A}^c_{\mathrm{LT}} \,,$$

or, equivalently, with the definitions of the wet activity (6.2) and the cell culture activity (6.4),

$$\mathcal{D} = A_i(t) + e\mathcal{A}^c_W + e\mathscr{A}^c_T \,. \tag{6.7}$$

Indeed, the first term in the right-hand side is the *medium activity* A_i; the second term estimates the total contribution from the wet region (in Bq); the third term accounts for the contribution due to the cell culture (in Bq).

From the definition of the initial value of the medium activity (6.6) and the LT conservation principle (6.7), the TAC of tracer inside the incubation medium is reconstructed as

$$A_i(t) = A_{i0} - \mathscr{A}_T(t) \; . \tag{6.8}$$

Chapter 7

Biochemically-driven models

The glucose analog radioactive tracer [^{18}F]-fluorodeoxyglucose (FDG) is widely used in nuclear medicine to reconstruct glucose metabolism in cells and tissues. Following glucose path, FDG is first transported through cell membranes and is then trapped inside cells by phosphorylation. However, unlike phosphorylated glucose, phosphorylated FDG tends to accumulate in cells. For this reason, the measurable radioactive amount of FDG is considered an accurate marker of overall glucose uptake and consumption by cells and tissues (Cherry, Sorenson, and Phelps, 2012; Schmidt and Turkheimer, 2002; Morris et al., 2004). In addition, FDG assumption by cancer cells is increased by the Warburg effects for glucose (Vander-Heiden, Cantley, and Thompson, 2009); consequently, FDG is used in cancer detection and staging, and to assess the effectiveness of medical treatments.

The analysis of data on the time course of FDG tracer distribution is performed by the use of compartmental analysis. Classical compartmental models have been developed under the assumption that phosphorylation and dephosphorylation of FDG occur in the same intracellular cytosolic volume, as described by Sokoloff et al., 1977 and Morris et al., 2004. Recent progresses in cell biochemistry have shown that the appropriate location of dephosphorylation is the endoplasmic reticulum (ER), which is spatially separated from cytosol. Following this pattern for FDG kinetics in the cell, we describe and formalize a new model composed of three compartments, accounting for free FDG in cytosol, phosphorylated FDG in cytosol, and phosphorylated FDG in ER. The new biochemically-driven compartmental model is referred to as BCM (Scussolini et al., 2018a); the classical simplified compartmental model (SCM) is recovered from the proposed model under the assumption that the ER is removed from consideration. The introduction of the SCM is motivated by the need for comparison.

In order to test the effectiveness of the BCM in the description of FDG kinetics in cancer, we consider the time-dependent activity curves of FDG uptake by cancer cell cultures in vitro, obtained by the use of the LigandTracer (LT) device. Application of the BCM to cell cultures is in natural relation with the biochemical origin of the model. Note that the BCM can be adapted for analyzing FDG-PET tissue data (see Scussolini et al., 2018a).

In the first section, we illustrate the role of the ER in glucose metabolism and FDG uptake within a cell. The second section deals with the mathematical formulation of the compartmental models, namely the BCM and the SCM: the model equations are illustrated, together with the inverse problem of determining the model parameters from available LT data and the related identifiability results. Moreover, a general relation between the BCM and SCM kinetic parameters is shown. Finally, we formally study the influence of the LT calibration on the model rate constants, in order to assess the magnitude of potential errors arising from inaccurate estimation of the LT efficiency coefficient.

7.1 The role of the endoplasmic reticulum

Although measuring the continuous flux of glucose molecules through lesion populating cells is extremely difficult, this paradigm became a clinical standard to distinguish tumor from healthy tissues, to stage tumor burden and to assess treatment effectiveness. The task is possible due to the peculiar kinetic features of the radioactive glucose analog FDG.

Cancer imaging with FDG is based on two key concepts: 1) FDG competes with glucose for transmembrane transport and phosphorylation, and 2) differently from glucose, intracellular tracer cannot be degraded to diffusible radioactive product, and once trapped, it cannot be lost. Indeed, FDG is transported through cell membranes by the same glucose transporter membrane proteins (GLUT) as glucose, and it is trapped into the cytosol by phosphorylation catalyzed by the same enzyme hexokinase (HK). Differently from glucose-6-phosphate (G6P), the radioactive analog FDG-6-phosphate (FDG6P) is a false substrate for downstream enzymes channeling G6P to glycolysis (G6P-isomerase) or pentose-phosphate pathway (G6P-dehydrogenase). Nevertheless, FDG6P can be partially dephosphorylated by the enzyme glucose-6-phosphatase (G6Pase), and thus can be released from the cell.

The slow radioactivity loss from the tumor is generally attributed to low levels of G6Pase, and FDG accumulation is therefore considered an accurate marker of overall cell glucose consumption. This perspective has been formalized by Sokoloff et al., 1977 in a seminal paper that represents the theoretical basis for the experimental use of ^{14}C-2DG and for the clinical value of FDG uptake.

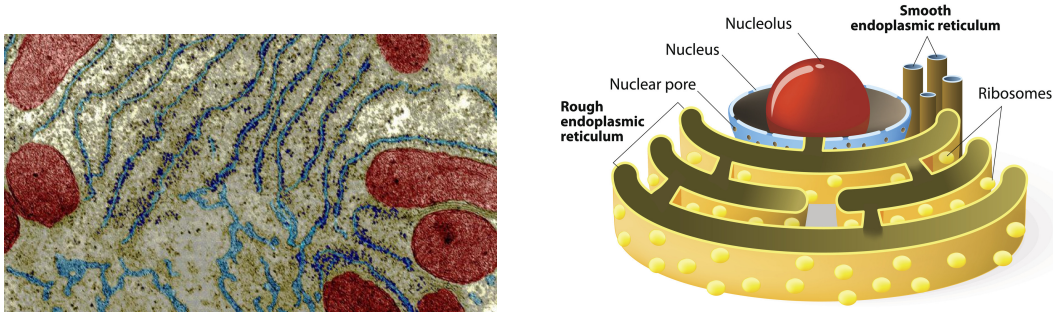

(a) ER micrograph.

(b) ER picture.

FIGURE 7.1: The ER. (a) A colored transmission electron micrograph (from University of Edinburgh/Wellcome Collection) of mitochondria (red) and both rough and smooth endoplasmic reticulum (blue). The rough endoplasmic reticulum appears darker due to the ribosomes (dark blue) dotted on its surface. (b) Pictorial representation of the ER.

Recent findings in biochemistry documented that G6Pase is compartmentalized within the endoplasmic reticulum (ER) (Ghosh et al., 2002). The ER was first observed with light microscopy by Garnier, 1897, who coined the term "ergastoplasm". With electron microscopy, the lacy membranes of the ER were first seen by Porter, Claude, and Fullam, 1945. Later, the word "reticulum", which means network, was applied by K.R. Porter in 1953 to describe this fabric of membranes. The ER (Figure 7.1) is a continuous membrane system that forms an interconnected network of flattened sacs and tubes within the cytoplasm of every nucleated cell, and serves

multiple functions, being important particularly in the synthesis, folding, modification, and transport of proteins and lipids. Its internal part, the ER lumen, is completely separated from the cytosol. Indeed, abundant biochemical, pharmacological, clinical and genetic data indicate that the barrier function of the lipid bilayer and specific transport activities in the membrane make the ER a distinct metabolic compartment (Csala, Bánhegyi, and Benedetti, 2006). However, the luminal enzyme activities are integrated in the cellular metabolism, and strongly connected to the cytosolic processes.

The ER can be classified in two functionally distinct forms: the rough endoplasmic reticulum and the smooth endoplasmic reticulum. Rough ER, a series of flattened sacs, is named for its rough appearance, which is due to the ribosomes attached to its outer cytoplasmic surface. Rough ER lies immediately adjacent to the cell nucleus, and its membrane is continuous with the outer membrane of the nuclear envelope. The ribosomes on rough ER specialize in the synthesis of proteins, mostly glycoproteins, that possess a signal sequence that directs them specifically to the ER for processing. Smooth ER, a meshwork of fine tubular membrane vesicles, is involved in the synthesis of lipids, including cholesterol and phospholipids, which are used in the production of new cellular membrane.

The transport of selected substrates across the ER membrane is an additional point where the enzyme activity can be potentially regulated (Csala et al., 2007). Glucose-6-phosphate transporter (G6PT) is the transmembrane protein providing a selective channel between the ER lumen and the cytosol. This important enzyme complex is located within the membrane of the ER, and catalyzes the terminal reactions in both glycogenolysis and gluconeogenesis. In particular, G6PT transports G6P from the cytosol into the lumen of the ER, where it is hydrolyzed by the catalytic subunit of G6Pase. Defective G6P transport leads to insufficient substrate supply to G6Pase in gluconeogenic tissues; therefore, G6PT mimics the true enzyme deficiency (Csala et al., 2007).

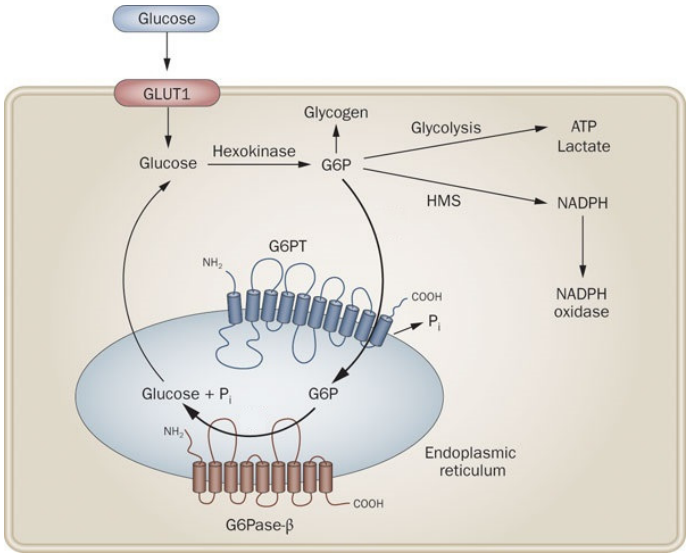

FIGURE 7.2: Biochemical path of glucose inside the cell (from Chou, Jun, and Mansfield, 2010).

Inside a cell, the biochemical path of glucose (schematized in Figure 7.2) and of its radioactive analog FDG may be characterized according to the scheme below.

1. Glucose and FDG are transported into the cytosol, and back, by GLUT proteins.

2. Inside the cell, glucose and FDG are phosphorylated by HK to G6P and FDG6P, respectively.

3. Once phosphorylated, glucose continues along the metabolic pathway of glycolysis and pentose-phosphate pathway or participates to glycogen synthesis; instead, FDG cannot follow the same channels and accumulates intracellularly as FDG6P.

4. G6P and FDG6P are substrates for G6Pase, which is anchored to the ER, so that its action of hydrolysis, resulting in the creation of a phosphate group and free glucose and tracer, occurs after the phosphorylated forms have been transported into the ER lumen by G6PT.

5. Free glucose and free FDG are released into the cytosol.

In general, the presence of a measurable, though limited, hydrolysis of FDG6P in virtually all tissues intrinsically implies a specific mechanism for its transport across the ER membrane. Indeed, FDG release is found to be related to the expression of the reticular G6PT more than that of G6Pase. This concept might explain the apparent disagreement of FDG accumulation kinetics despite the high G6Pase activity observed in cancer (Marini et al., 2016).

7.2 Mathematical models

The radioactive tracer FDG provides an analog of glucose metabolism, and allows a quantification of functions in living cells, such as rates of activity of enzymes. Starting from local measurements on the diffusion of the FDG radioactive molecules, the aim is to reconstruct FDG kinetics. Therefore, by means of compartmental analysis, a suitable set of different functional compartments is identified in the assigned target, where each compartment is associated with a specific metabolic state of the tracer, possibly contained in a predefined physiological volume. Tracer flow corresponds to exchange of radioactive molecules between compartments.

In this section we describe the compartmental models formalizing the biochemical path of FDG inside the cell. In particular, the biochemically-driven compartmental model accounting for the role of the ER, and its simplified form considering only the cytosolic pool. The simplified model is examined for the ease of comparison with most diffused existing models. We assume that standard assumptions for application of compartmental analysis are satisfied (for details see subsection 1.1.1), and we adopt the usual notations of compartmental analysis (as in Chapter 1).

Since available data on the time course of radioactivity for a cell culture are given by the LT device in terms of total activities, we provide the forward model equations for the compartment activities, instead of the usual compartmental formulation for concentrations. Next, we write the compartmental inverse problem for the determination of the kinetic parameters from LT data, and we discuss the identifiability properties of the models. By observing asymptotic characteristics of the BCM and SCM systems, consistent with the same LT data, we find a general relation between the BCM and SCM rate constants, and we analyze the dependence of the model rate constants on LT calibration.

7.2.1 Three-compartment BCM

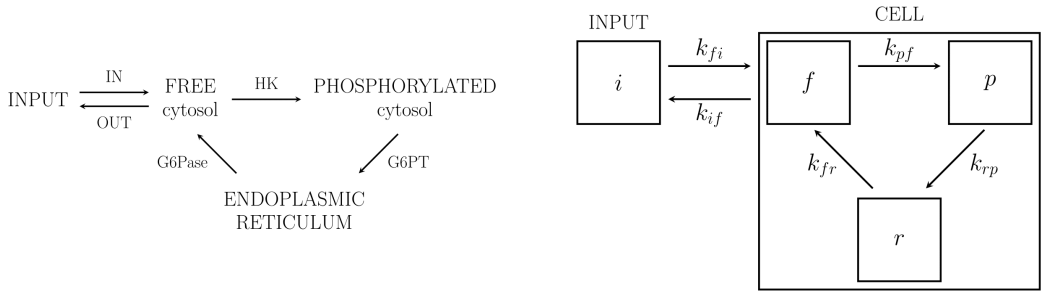

(a) FDG biochemical path. (b) BCM.

FIGURE 7.3: The biochemically-driven model for FDG metabolism inside a cell: (a) the ER-accounting biochemical FDG path, and (b) its compartmental representation. The model schematizes the three functional/metabolic states of the tracer: free, cytosolic-phosphorylated, ER-phosphorylated. The arrows connecting the compartments represent the enzyme actions and the model kinetic parameters.

Consider a cell which is in contact with a liquid containing glucose at physiological concentration and FDG at a smaller concentration, so that FDG may be regarded as a perturbation of glucose. This general situation is representative of any cells coming into contact with glucose and FDG, both in vitro and in vivo. As schematized in Figure 7.3(a), the FDG moves in and out the cell environment thanks to GLUT transporters; once inside the cytosol of the cell, free FDG is phosphorylated by HK, and the phosphorylated FDG can enter the ER transported by G6PT; only inside the ER, FDG6P can be dephosphorylated by G6Pase, after which the FDG turns back in a free status and is released out into the cytosol. This pattern is reflected in the three-compartment biochemically-driven model of Figure 7.3(b), referred to as BCM (Scussolini et al., 2018a), composed by:

- the pool i for tracer outside the cell environment, acting as input of the system;
- a compartment f for free tracer in free status in the cytosol of the cell;
- a compartment p for phosphorylated tracer in the cytosol of the cell;
- a compartment r for phosphorylated tracer in the ER;
- five kinetic parameters $k_{fi}, k_{if}, k_{pf}, k_{rp}, k_{fr}$ (min^{-1}).

The rate constants represent the rate of the action of the enzymes processing the tracer: k_{fi} and k_{if} reflect the transport by GLUT of FDG across the cell membrane; k_{pf} is the HK phosphorylation rate of FDG; k_{rp} represents FDG6P transport by G6PT from cytosol to ER; k_{fr} refers to the G6Pase dephosphorylation rate of FDG6P to FDG.

In principle, a pool for free tracer in ER could also be considered, which receives tracer also from the free compartment in cytosol; here we assume that its equilibrium value is reached almost instantaneously at the beginning of the tracer flow process and represents a small fraction of tracer contained in ER, so that it is discarded. Moreover, since the dephosphorylation occurs only inside the ER, a parameter k_{fp}, corresponding to an arrow from p to f, is not considered.

The crucial point is the remark that, usually, a single cell is not accessible to measurements of radiation emitted in time. Indeed, applications are based on observation of the time course of radiation emitted by cell cultures in vitro. Thus the model in Figure 7.3(b) has to be adapted to applications on a higher scale. If we consider a colony of N cells, reasonably of the same type and with the same characteristics, it is natural to define the volume of the colony as N-times the volume of the single cell, and the activity for the colony as N-times the activity of the single cell. Accordingly, with a good approximation, tracer concentration of the colony equals the tracer concentration of the single cell.

We introduce the state variables C_f, C_p, and C_r which describe the time-dependent and decay corrected concentrations for a cell culture of free tracer, phosphorylated tracer in cytosol, and phosphorylated tracer ER, respectively. The concentration of tracer in the external liquid medium, C_i, is the given input function of the system. The linear system of ordinary differential equations (ODEs) in terms of concentrations for the BCM is

$$\begin{cases} \dot{C}_f = -(k_{if} + k_{pf})C_f + k_{fr}C_r + k_{fi}C_i \\ \dot{C}_p = k_{pf}C_f - k_{rp}C_p \\ \dot{C}_r = k_{rp}C_p - k_{fr}C_r \end{cases} , \tag{7.1}$$

with initial conditions $C_f(0) = C_p(0) = C_r(0) = 0$, which mean that there is no tracer amount in the cells at the beginning of the experiment. The rate constants describe the first-order process of tracer transfer between compartments.

Available data on the time course of radioactivity for a cell culture are given in terms of total activity. In principle, rephrasing of the data in concentrations was allowed but this required, at least, the knowledge of parameters such as the total number of cells, and the volumes of cytosol and ER. These parameters are only roughly known. Besides other advantages, the reformulation of the system (7.1) in activities allows to reduce the number of external parameters to one, precisely, the ratio between the volumes of the ER and cytosol, which can be estimated and is independent of the number of cells.

Concentrations and corresponding activities of the cell culture are related by

$$C_f = \frac{A_f}{V_{cyt}} , \quad C_p = \frac{A_p}{V_{cyt}} , \quad C_r = \frac{A_r}{V_{er}} , \quad C_i = \frac{A_i}{V_i} , \tag{7.2}$$

where V_{cyt}, V_{er}, and V_i are the volumes of the total cytosolic region, ER, and external liquid, respectively. Substitution of the activities into the system (7.1) leads to the formulation of the Cauchy problem

$$\dot{\boldsymbol{A}} = \boldsymbol{M}\boldsymbol{A} + \bar{k}_{fi}A_i\boldsymbol{e}_1 , \quad \boldsymbol{A}(0) = 0 , \tag{7.3}$$

where

$$\boldsymbol{A} = \begin{pmatrix} A_f \\ A_p \\ \bar{A}_r \end{pmatrix} , \quad \boldsymbol{M} = \begin{pmatrix} -(k_{if} + k_{pf}) & 0 & k_{fr} \\ k_{pf} & -k_{rp} & 0 \\ 0 & k_{rp} & -k_{fr} \end{pmatrix} , \quad \boldsymbol{e}_1 = \begin{pmatrix} 1 \\ 0 \\ 0 \end{pmatrix} \tag{7.4}$$
$$\bar{A}_r = A_r\frac{V_{cyt}}{V_{er}} , \quad \bar{k}_{fi} = k_{fi}\frac{V_{cyt}}{V_i} ,$$

and where A_i is the given input function, representing in our case the total activity of the incubation medium in which cells are immersed. The coefficient $\bar{k}_{fi} = k_{fi}V_{cyt}/V_i$

provides the rate constant adapted to the description in terms of activities and plays the same role as k_{fi}. The other coefficients k_{if}, k_{pf}, k_{rp}, and k_{fr} are left unchanged by the transformation of the state variables from concentrations to activities, and thus preserve their interpretation as rate constants and the numerical values pertaining to the system (7.1). The auxiliary variable $\bar{A}_r$ is related to the "natural" activity A_r of the ER through the adimensional ratio V_{cyt}/V_{er}, which is independent of the number of cells. Accordingly, we find

$$A_r = v\bar{A}_r\,, \quad v = \frac{V_{er}}{V_{cyt}}\,, \tag{7.5}$$

where in particular $v < 1$ (Milo and Phillips, 2015), since the ER is contained into the cytosol and the ER volume is smaller than the cytosol volume.

The analytic solution of the Cauchy problem (7.3) takes the form

$$\boldsymbol{A}(t; A_i, \bar{\boldsymbol{k}}_{BCM}) = \bar{k}_{fi} \int_0^t e^{\boldsymbol{M}(t-\tau)} \boldsymbol{e}_1 A_i(\tau)\, d\tau\,, \tag{7.6}$$

where, by a slight abuse of language, we let $\bar{\boldsymbol{k}}_{BCM} = (\bar{k}_{fi}, k_{if}, k_{pf}, k_{rp}, k_{fr})^T \in \mathbb{R}^5_+$.

Denote as $\mathscr{A}_T$ the measured time-dependent total activity of the cell culture. Then, $\mathscr{A}_T$ equals the sum of activities of the model compartments, and we have

$$\mathscr{A}_T = A_f + A_p + A_r = A_f + A_p + v\bar{A}_r\,. \tag{7.7}$$

Equation (7.7) may be written in compact form as

$$\mathscr{A}_T(t) = \boldsymbol{\alpha}^T \boldsymbol{A}(t; A_i, \bar{\boldsymbol{k}}_{BCM})\,, \quad \boldsymbol{\alpha} = \begin{pmatrix} 1 \\ 1 \\ v \end{pmatrix}\,. \tag{7.8}$$

Equation (7.9) constitutes the compartmental inverse problem of finding the BCM rate constants $\bar{\boldsymbol{k}}_{BCM}$ starting from the known LT data, namely the activity of the medium and the total activity of the cell culture. By rewriting (7.9) as the zero-finding problem

$$\boldsymbol{\alpha}^T \boldsymbol{A}(t; A_i, \bar{\boldsymbol{k}}_{BCM}) - \mathscr{A}_T(t) = 0\,, \tag{7.9}$$

we can solve it by means of the regularized Gauss-Newton iterative procedure (reg-GN algorithm 1.1, described in subsection 1.2.3).

Concerning the identifiability problem, we state the following result ensuring uniqueness of the BCM rate constants.

Theorem 7.2.1. *Assume that the polynomials*

$$Q(s; \bar{\boldsymbol{k}}_{BCM}) = s^2 + (k_{pf} + k_{rp} + k_{fr})\, s + (k_{pf} + k_{rp})\, k_{fr} + v\, k_{pf}\, k_{rp}$$

and

$$D(s; \bar{\boldsymbol{k}}_{BCM}) = s^3 + (k_{if} + k_{pf} + k_{rp} + k_{fr})\, s^2 + [(k_{if} + k_{pf})\,(k_{rp} + k_{fr}) + k_{rp}\, k_{fr}]\, s + k_{if}\, k_{rp}\, k_{fr}$$

are coprime. If $\bar{\boldsymbol{k}}_{BCM} = (\bar{k}_{fi}, k_{if}, k_{pf}, k_{rp}, k_{fr})^T \in \mathbb{R}^5_+$ is generic, then $\bar{\boldsymbol{k}}_{BCM}$ is uniquely determined by A_i and $\mathscr{A}_T$, and the BCM of equations (7.3)–(7.4) *and* (7.9) *is globally identifiable.*

The proof of Theorem 7.2.1 follows the procedure used in Delbary, Garbarino, and Vivaldi, 2016 and is reported in Appendix C.

7.2.2 Two-compartment SCM

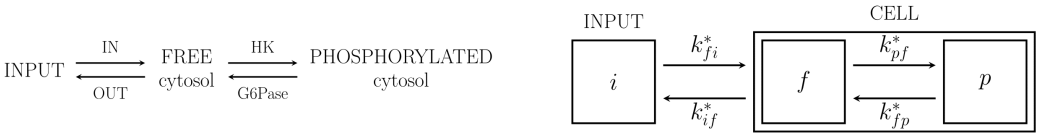

(a) Simplified FDG biochemical path. (b) SCM.

FIGURE 7.4: The simplified model for FDG metabolism inside a cell: (a) the cytosolic biochemical FDG path, and (b) its compartmental representation. The model schematizes the two functional/metabolic states of the tracer: free, cytosolic-phosphorylated. The arrows connecting the compartments represent the enzyme actions and the model kinetic parameters.

When not considering the role of the ER in the cell-processing of FDG, we deal with a simplified biochemical path for FDG, as in Figure 7.4(a), which account only for the cytosol. The simplified compartmental model, referred to as SCM, is the two-compartment model shown in Figure 7.4(b). Similarly to the BCM, tracer is first exchanged between the input compartment and the compartment for free tracer, with rate coefficients k^*_{fi} and k^*_{if} (min^{-1}). Unlike the BCM, there is only one cytosolic pool for phosphorylated FDG. The kinetic parameters k^*_{pf} and k^*_{fp} (min^{-1}), providing phosphorylation and dephosphorylation rates, can be regarded as the functional correspondent of k_{pf} and k_{fr}, respectively. The SCM is known conventionally as the Sokoloff model, first introduced by Sokoloff et al., 1977. Note that the apex star is used systematically to refer to quantities pertaining to the simplified model.

By denoting with C^*_f and C^*_p the time-dependent and decay corrected concentrations for a cell culture of free and phosphorylated tracer in cytosol, respectively, we can write the following system of ODEs for the SCM:

$$\begin{cases} \dot{C}^*_f = -(k^*_{if} + k^*_{pf})C^*_f + k^*_{fp}C^*_p + k^*_{fi}C_i \\ \dot{C}^*_p = k^*_{pf}C^*_f - k^*_{fp}C^*_p \end{cases}, \tag{7.10}$$

with initial conditions $C^*_f(0) = C^*_p(0) = 0$, and given tracer concentration in the external liquid C_i.

In the modeling of a cell culture, we consider as state variables A^*_f and A^*_p, the time-dependent and decay corrected activities for the cell culture of free and phosphorylated tracer in the cytosol, respectively. The system of ODEs in terms of activities is obtained by starting from the ODEs (7.10) for the concentrations and then substituting the relations between concentrations and activities, i.e. $C^*_f = A^*_f/V_{cyt}$ and $C^*_p = A^*_p/V_{cyt}$. The Cauchy problem in terms of activities for the SCM takes the form

$$\dot{\boldsymbol{A}}^* = \boldsymbol{M}^*\boldsymbol{A}^* + \bar{k}^*_{fi}A_i\boldsymbol{e}_1\,, \quad \boldsymbol{A}^*(0) = 0\,, \tag{7.11}$$

where

$$\boldsymbol{A}^* = \begin{pmatrix} A^*_f \\ A^*_p \end{pmatrix}\,, \quad \boldsymbol{M}^* = \begin{pmatrix} -(k^*_{if} + k^*_{pf}) & k^*_{fp} \\ k^*_{pf} & -k^*_{fp} \end{pmatrix}\,, \quad \boldsymbol{e}_1 = \begin{pmatrix} 1 \\ 0 \end{pmatrix}\,, \tag{7.12}$$

with $\bar{k}^*_{fi} = k^*_{fi}V_{cyt}/V_i$, and given input function A_i.

We denote by $\bar{\boldsymbol{k}}^*_{SCM} = (\bar{k}^*_{fi}, k^*_{if}, k^*_{pf}, k^*_{fp})^T \in \mathbb{R}^4_+$ the vector of parameters of the simplified formulation. The analytic solution of the Cauchy problem (7.11) is

$$\boldsymbol{A}^*(t; A_i, \bar{\boldsymbol{k}}^*_{SCM}) = \bar{k}^*_{fi} \int_0^t e^{\boldsymbol{M}^*(t-\tau)} \boldsymbol{e}_1 A_i(\tau)\, d\tau \,. \tag{7.13}$$

The connection between the cell culture datum $\mathscr{A}_T$ and the state variables is given by

$$\mathscr{A}_T = A^*_f + A^*_p = \boldsymbol{\alpha}^T \boldsymbol{A}^*(t; A_i, \bar{\boldsymbol{k}}^*_{SCM}) \,, \quad \boldsymbol{\alpha} = \begin{pmatrix} 1 \\ 1 \end{pmatrix} \,. \tag{7.14}$$

Equation (7.14) is the starting point for the compartmental inverse problem of finding the SCM rate constants $\bar{\boldsymbol{k}}^*_{SCM}$ from LT data $\mathscr{A}_T$ and A_i, which is solved by means of the regularized Gauss-Newton (reg-GN) iterative procedure (Algorithm 1.1, described in subsection 1.2.3).

The two-compartment SCM is known to be identifiable (see Theorem 1.2.1 of subsection 1.2.2). Differently from usual formulations, here the SCM is modified in terms of activities in order to describe the cell culture system. Nevertheless, the identifiability property is not affected from such reformulation, and the following result holds.

Theorem 7.2.2. *The kinetic parameters $\bar{\boldsymbol{k}}^*_{SCM} = (\bar{k}^*_{fi}, k^*_{if}, k^*_{pf}, k^*_{fp})^T \in \mathbb{R}^4_+$ are uniquely determined by A_i and $\mathscr{A}_T$, and the SCM of equations* (7.11)–(7.12) *and* (7.14) *is structurally globally identifiable.*

7.2.3 Connection between BCM and SCM

With the aim of performing a qualitative analysis on the two models BCM and SCM, the following considerations are in order. It is well-known that the dephosphorylation rate is rather small (Sokoloff et al., 1977); therefore, we assume that k_{fr} and k^*_{fp} are small with respect to the other coefficients, so that their contribution can be neglected. Next, we suppose that the concentrations C_i, C_f, C_p, and C^*_f are almost constant at large time values, and that C_r and C^*_p grow over time as the concentrations of the pools where tracer accumulates. Under these hypotheses, the systems of ODEs (7.1) and (7.10) reduce to the algebraic conditions

$$\begin{cases} (k_{if} + k_{pf})\hat{C}_f = k_{fi}\hat{C}_i \\ k_{pf}\hat{C}_f = k_{rp}\hat{C}_p \\ \dot{C}_r = k_{rp}\,\hat{C}_p \end{cases} , \tag{7.15}$$

and

$$\begin{cases} (k^*_{if} + k^*_{pf})\,\hat{C}^*_f = k^*_{fi}\,\hat{C}_i \\ \dot{C}^*_p = k^*_{pf}\,\hat{C}^*_f \end{cases} , \tag{7.16}$$

where the superposed hat refers to the constant values of the concentrations and $\hat{C}_i$ is the common forcing contribution, independent of the model. The constant rates of growth of phosphorylated FDG are given by

$$\dot{C}_r = \frac{k_{fi}\,k_{pf}}{k_{if} + k_{pf}} \hat{C}_i \,, \tag{7.17}$$

$$\dot{C}_p^* = \frac{k_{fi}^* k_{pf}^*}{k_{if}^* + k_{pf}^*} \hat{C}_i \,. \tag{7.18}$$

Consider the case of a cell culture, and suppose that the two models BCM and SCM are consistent with the same data. Comparison of equations (7.7) and (7.14) for the total activity shows that

$$\mathscr{A}_T = A_f + A_p + A_r = A_f^* + A_p^* \,. \tag{7.19}$$

In view of the assumptions, also the activities A_f, A_p, and A_f^* are almost constant at large time values. Therefore, evaluation of the time derivative of (7.19) leads to $\dot{A}_r = \dot{A}_p^*$, which, after comparison with (7.2), is written in the equivalent form

$$V_{er}\dot{C}_r = V_{cyt}\dot{C}_p^* \,. \tag{7.20}$$

Substitution into (7.20) of (7.17) and (7.18), and the definition of $\bar{k}_{fi}$, lead to

$$v\frac{\bar{k}_{fi}k_{pf}}{k_{if} + k_{pf}} = \frac{\bar{k}_{fi}^* k_{pf}^*}{k_{if}^* + k_{pf}^*} \,, \tag{7.21}$$

where we recall that $v = V_{er}/V_{cyt}$. The general relation (7.21) arises as direct consequence of the modeling assumptions, and may be used as a check on the effectiveness of the numerical reconstructions. Moreover, If

$$\begin{aligned} \bar{k}_{fi} &\simeq \bar{k}_{fi}^* \\ k_{if} &\simeq k_{if}^* \\ k_{pf} &\leq k_{if} \\ k_{pf}^* &\leq k_{if}^* \end{aligned} \,, \tag{7.22}$$

then equation (7.21) simplifies to

$$v k_{pf} \approx k_{pf}^* \,. \tag{7.23}$$

This shows that the factor v connects the reconstructed phosphorylation rates of BCM and SCM.

7.2.4 Model dependence on LT calibration

The calibration procedure for the LT, discussed in Section 6.2, was needed in order to convert measured counting rates (CPS) in activity (Bq), and thus to write dimensionally consistent equations. Despite an apparent reliability of the estimated efficiency coefficient e, several errors might have been caused by inaccurate evaluations of initial and final medium activities, non-uniform FDG distribution on the wet surface, or non-orthogonal emission from the surface under the detector. Moreover, the relatively poor correlation between the points in Figure 6.4 might have altered the value of e, with a subsequent impact on the accuracy of all downstream measurements. Accordingly, in order to further test consequences arising from errors on e, we formally investigate the dependence of the model rate constants on the calibration procedure, starting from the model equations and the definition of e.

We consider the system of ODEs (7.3)–(7.4) for the activities of the BCM. We assume a dephosphorylation rate k_{fr} small enough to discard the contribution $k_{fr}\bar{A}_r$,

and an asymptotic condition where A_f, A_p, and A_i assume almost constant values. It follows that

$$\dot{\hat{A}}_r = k_{rp}\hat{A}_p = \frac{k_{pf}}{k_{if}+k_{pf}}\bar{k}_{fi}\hat{A}_i \,, \tag{7.24}$$

where the superposed hat refers to the constant values of the activities. Under the assumptions, the time derivative of (7.7) reduces to $\dot{\mathscr{A}}_T = v\dot{\hat{A}}_r$, where both $\dot{\mathscr{A}}_T$ and $\dot{\hat{A}}_r$ are constant. Combination of this result with (7.24) leads to

$$\bar{k}_{fi}\frac{k_{pf}}{k_{if}+k_{pf}} = \frac{\dot{\mathscr{A}}_T}{v}\frac{1}{\hat{A}_i} \,, \tag{7.25}$$

with $v = V_{er}/V_{cyt}$ the known physiological parameter. We approximate the constant value of the medium activity with its starting value, i.e. $\hat{A}_i \simeq A_{i0} = \mathcal{D} - e\mathcal{A}^c_W$, and we consider the total activity $\mathscr{A}_T = e\mathscr{A}^c_T$. Then, equation (7.25) becomes

$$\bar{k}_{fi}\frac{k_{pf}}{k_{if}+k_{pf}} = \frac{\dot{\mathscr{A}}^c_T}{v}\frac{1}{\mathcal{D}/e - \mathcal{A}^c_W} \,. \tag{7.26}$$

The relation (7.26) implies the equality between a non-linear combination of kinetic parameters, at the left-hand side, and a constant quantity dependent on LT data and e, at the right-hand side. The fraction $k_{pf}/(k_{if}+k_{pf}) = 1/(k_{if}/k_{pf}+1)$ is a positive number smaller than one, and even if k_{if} or k_{pf} may depend on e, the ratio k_{if}/k_{pf} may not. Therefore, equation (7.26) can be rewritten as

$$\bar{k}_{fi} = \frac{k_{if}+k_{pf}}{k_{pf}}\frac{\dot{\mathscr{A}}^c_T}{v}\frac{1}{\mathcal{D}/e - \mathcal{A}^c_W} = \frac{\gamma}{\mathcal{D}/e - \mathcal{A}^c_W} \,, \tag{7.27}$$

with γ, $\mathcal{D}$, and A_{i0} constant quantities independent of e. According to (7.27), the input parameter $\bar{k}_{fi}$ is highly influenced by the value assigned to the LT efficiency coefficient e, more precisely, growth of e implies necessarily increase in the value of $\bar{k}_{fi}$ and conversely.

The same procedure can be made for the SCM, by considering the system of ODEs (7.11)–(7.12), negligible dephosphorylation flux $k_{fp}A_p$, and asymptotic constant values of A^*_f and A_i. The final result (7.27) holds also for the SCM, i.e. in details,

$$\bar{k}^*_{fi} = \frac{k^*_{if}+k^*_{pf}}{k^*_{pf}}\dot{\mathscr{A}}^c_T\frac{1}{\mathcal{D}/e - \mathcal{A}^c_W} = \frac{\gamma^*}{\mathcal{D}/e - \mathcal{A}^c_W} \,. \tag{7.28}$$

Chapter 8

Application to FDG-LT cancer data

Once the LigandTracer (LT) device for measurement of [^{18}F]-fluorodeoxyglucose (FDG) uptake by cell cultures has been described, and the compartmental schemes for FDG path at cell-scale have been formalized, we can perform experiments with cultured cancer cells and analyze the data to characterize FDG kinetics. Similar results can be found in Scussolini et al., 2018a and Scussolini et al., 2018b.

Our application involves murine 4T1 breast cancer cells. Two groups of experiments are considered, with glucose concentration in the liquid medium of 1 g/L and 2 g/L, and with variable amount of FDG. The aim is to (i) assess the competition between glucose and its non-degradable analog, (ii) verify whether glucose-6-phosphatase (G6Pase) sequestration in the endoplasmic reticulum (ER) lumen is compatible with the accumulation kinetics of FDG, and (iii) compare the different descriptions of FDG transformations arising from reduction of LT data by means of the biochemically-driven compartmental model (BCM) and the simplified compartmental model (SCM). In the analysis, we test the sensitivity of our compartmental approach with respect to mis-estimation of the LT calibration coefficient.

The results show that the rate of phosphorylation predicted by the BCM is higher than the one produced by the classical SCM, and that tracer tends to accumulate in the ER, rather than cytosol. This latter phenomenon is also confirmed by directly imaging the fluorescent FDG analog 2NBDG.

The first section presents the experimental setting: how the cancer cells are cultured prior to LT measurements, and the type of experiments carried out. In the second section, we describe the application of the two competing compartmental models, namely the BCM and SCM, to the data obtained from the two sets of experiments, and we show the results on FDG kinetics.

8.1 LT experimental setting

Murine 4T1 breast cancer cells are cultured in standard Petri dishes (PDs) with 100 mm diameter, inclined at 30 degrees from the horizontal plane so as to limit cell presence to the lowest segment of the circular ring. Once seeded, cells are maintained in DMEM[1] with glucose concentration set at 11.1 mM (2 g/L) enriched with 10% fetal bovine serum, for at least twenty-four hours. For each experiment, a pair of twin cultures is prepared, one for cell counting and one for radioactivity counting. The PD with the cell culture intended for the measurements is placed on the platform

[1]DMEM (Dulbecco's Modified Eagle Medium) is a widely used basal medium for supporting the growth of many different mammalian cells. DMEM is a modification of Basal Medium Eagle (BME) that contains a four-fold higher concentration of amino acids and vitamins, as well as additional supplementary components. The original DMEM formula contains 1 g/L of glucose and was first reported for culturing embryonic mouse cells.

of the LT instrument, as illustrated in Section 6.1. Cultures are washed with PBS[2] before the administration of 3 mLs of incubation medium, containing both FDG and glucose. In general, administered FDG concentration varies from 1 to 2 MBq/mL, while glucose is set at two distinct concentrations, 5.5 mM (1 g/L) or 11.1 mM (2 g/L), to evaluate the competition FDG/glucose in different environment situations.

By the use of the LT device sixteen experiments on 4T1 cell cultures are performed, with acquisitions lasting 180 minutes. The experiments are grouped into two sets, according to the glucose concentration in the medium:

- group Gl1includes experiments e$i^{[1]}$, with $i = 1, \dots, 8$, at glucose concentration 1 g/L, approximating normal blood sugar levels in vivo;
- group Gl2 includes experiments e$i^{[2]}$, with $i = 1, \dots, 8$, at glucose concentration 2 g/L, approximating sugar level of diabetic disease.

For each experiment, the injected initial dose $\mathcal{D}$ of FDG is of the order of 10^6 Bq; therefore, the amount of FDG is negligible with respect to that of glucose, i.e., FDG is to be regarded as a perturbation of glucose.

The data obtained with the LT are the background and target counts, counting cell-free area and cell area radioactivities under the detector. First, the collected counts (CPS) are transformed in activities (Bq) by applying the efficiency coefficients $e = 3$ Bq/CPS, estimated in Section 6.2; then, following the procedures outlined in Section 6.3, the time-dependent total activity in the incubation medium A_i and the time-dependent activity of the entire cell culture $\mathscr{A}_T$ are reconstructed. For all experiments, Table 8.1 reports the number of cells N_c, the administered FDG dose $\mathcal{D}$, the initial amount of FDG in the medium A_{i0}, the end-time total activity of the cell culture $\mathscr{A}_T$, and the slope of the line approximating $\mathscr{A}_T$ (by means of linear regression, with a coefficient of determination r^2 oscillating between 0.97 and 0.99), as an estimate of the growth rate of the activity of cells. All the time activity curves (TACs) of the cell cultures $\mathscr{A}_T$ are shown in Figure 8.1(a) for the Gl1 group and in Figure 8.1(b) for the Gl2 group.

In general, the graph of $\mathscr{A}_T$ exhibits a certain degree of variability among the experiments because of the different experimental setup, e.g. different values of the initial FDG dose and different number of cells seeded at each experiment. Nevertheless, the qualitative behavior of the uptake curves is relatively well defined: at each experiment $\mathscr{A}_T$ grows almost linearly, with small random oscillations that should be due to experimental errors. A similar behavior has already been observed both in vitro and in vivo (see, e.g., Mertens et al., 2012 and references cited therein). Moreover, tracer uptake is highly influenced by the concentration of glucose in the medium. The growth rate is a first index of the FDG/glucose competition in FDG uptake by cells: as glucose concentration doubles, the growth rate decreases of at least one order of magnitude. This effect is directly visible by looking at the TACs in Figure 8.2(a), comparing $\mathscr{A}_T$ of experiments e$3^{[1]}$ and e$2^{[2]}$, performed at similar injected dose $\mathcal{D}$ and number of cells N_c but owing to the two different Gl groups. More precisely, it is evident an inverse correlation between FDG uptake and glucose concentration, whereby $\mathscr{A}_T$ is notably higher and grows at a higher rate in the group Gl1 with respect to the group Gl2.

[2]PBS (phosphate buffered saline) is a balanced water-based salt solution used for a variety of cell culture applications, such as washing cells before dissociation, transporting cells or tissue, diluting cells for counting, and preparing reagents. The purpose of PBS is to maintain the constant pH and the osmolarity of the cells. PBS washing is needed to remove the serum of media, before the administration of substances under analysis.

	N_c [M]	$\mathcal{D}$ [MBq]	A_{i0} [MBq]	$\mathscr{A}_T(180)$ [Bq]	Growth rate [Bq min^{-1}]
e1[1]	0.80	8.37	8.05	$1.73 \cdot 10^5$	911
e2[1]	0.45	6.00	5.63	$1.46 \cdot 10^5$	759
e3[1]	0.50	5.34	5.04	$1.11 \cdot 10^5$	585
e4[1]	0.80	6.94	6.39	$1.01 \cdot 10^5$	545
e5[1]	0.80	9.11	8.37	$9.16 \cdot 10^4$	412
e6[1]	0.20	7.75	7.44	$8.88 \cdot 10^4$	440
e7[1]	0.96	5.77	5.46	$7.72 \cdot 10^4$	348
e8[1]	0.40	5.80	5.46	$6.61 \cdot 10^4$	305
e1[2]	0.60	5.65	5.32	$2.30 \cdot 10^4$	86
e2[2]	0.35	5.22	4.90	$2.29 \cdot 10^4$	106
e3[2]	0.80	4.40	4.05	$2.16 \cdot 10^4$	74
e4[2]	0.30	4.73	4.45	$2.14 \cdot 10^4$	89
e5[2]	0.30	5.50	5.20	$2.10 \cdot 10^4$	81
e6[2]	0.35	5.04	4.74	$2.03 \cdot 10^4$	75
e7[2]	0.60	4.70	4.31	$1.10 \cdot 10^4$	27
e8[2]	0.80	1.70	1.56	$7.11 \cdot 10^3$	21

TABLE 8.1: Experimental values of the number of cells N_c, the administered FDG dose $\mathcal{D}$, the initial FDG activity in the medium A_{i0}, the final total activity of cells $\mathscr{A}_T(180)$, and the growth rate of $\mathscr{A}_T$ as the slope of the line approximating the curve, for each LT experiment at Gl1 and Gl2. Note that [M] refers to multiplication by 10^6.

An example of total activity in the incubation medium can be seen in Figure 8.2(b), where we report A_i for the experiments e3[1] and e2[2], belonging to group Gl1 and Gl2, respectively. In all cases, the graph of A_i is almost constant, in that the relative loss of tracer from the medium with respect to the initial amount, in the total time-interval of 180 minutes, is about 1%; in other terms, the cell culture uptake of tracer from the incubation medium is small with respect to the total amount of tracer in the medium. Moreover, the medium activity decreases with time almost linearly, since, according to the definition (6.8) of A_i given in subsection 6.3.2, the cell culture activity $\mathscr{A}_T$ itself is almost linear. The difference in the medium activity of the Gl1 experiment with respect to the Gl2 one is in the decrease rate, which is more rapid in the Gl1 curve than the Gl2 curve, reflecting the fact that the uptake of tracer from the medium is greater in the case of lower glucose concentration. Note that, even if e3[1] and e2[2] were conducted at almost equal initial dose $\mathcal{D}$, there is a slight difference in the initial values of the two A_i curves, depending on the subtraction of the wet activity at $t = 0$ (see definition (6.6) of A_{i0} in subsection 6.3.2) which appears different in the two experiments.

8.2 FDG kinetics

Direct inspection of the collected LT data, namely the cell culture activity $\mathscr{A}_T$ and medium activity A_i, does not answer questions concerning, e.g., the amount of tracer contained in cells in a free form, or the efficiency of the phosphorylation process. To investigate in quantitative terms the details of FDG kinetics, we analyze LT data

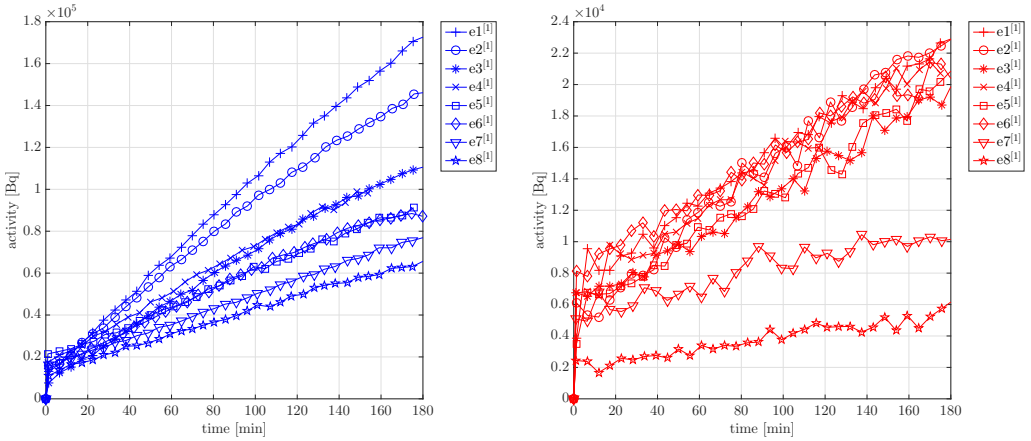

(a) $\mathscr{A}_T$ for Gl1. (b) $\mathscr{A}_T$ for Gl2.

FIGURE 8.1: TACs of FDG uptake by the cell cultures for: (a) all Gl1 group, (b) all Gl2 group.

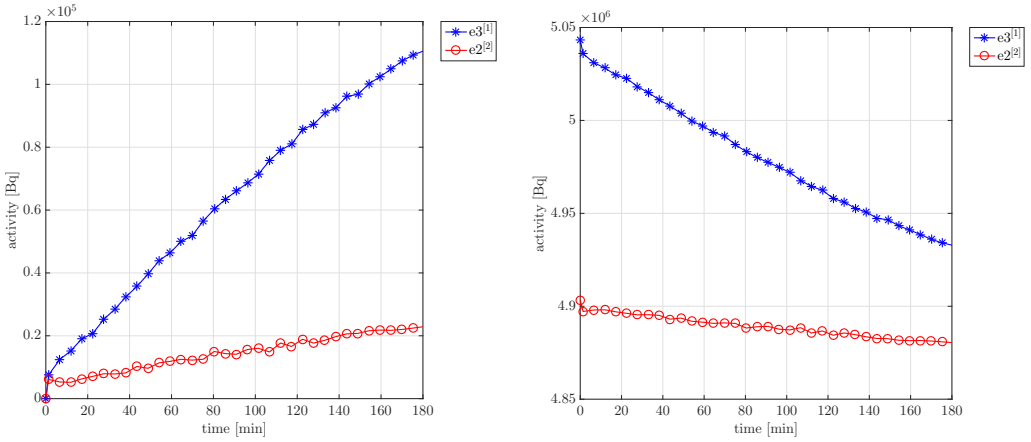

(a) $\mathscr{A}_T$. (b) A_i.

FIGURE 8.2: Example of TACs for two selected experiments, $e3^{[1]}$ in Gl1 and $e2^{[2]}$ in Gl2, of (a) cell culture activity $\mathscr{A}_T$, and (b) medium activity A_i.

by application of two compartmental model approaches: the new BCM (see subsection 7.2.1) accounting for the presence of the ER (described in Section 7.1), and the standard SCM (see subsection 7.2.2) considering only cytosolic pools. In both cases, the related compartmental inverse problem is solved through the regularized Gauss-Newton (reg-GN) computational method (Algorithm 1.1, described in subsection 1.2.3), and we determine the model rate coefficients, representing the rate of the action of the enzymes processing the FDG, and the corresponding compartment activities, indicating the amount of tracer contained in each pool. In our analysis, we also test the effects of a wrong estimate of the LT calibration coefficient on the reconstructed values of the rate constants.

In order to apply the BCM, we need to fix the value of the intracellular relative size of the ER with respect to the cytosol; following Milo and Phillips, 2015, we have chosen $v = 0.17$, which holds for a rough ER in a liver hepatocyte cell and can be considered a good approximation for a cancer cell.

8.2.1 BCM and SCM rate constants

We analyze 4T1 cell culture data of the Gl1 and Gl2 experiments with both the BCM and SCM. In general, the reconstructed values of the rate coefficients depend on the available data, the mathematical model applied for their reduction, and the specific conditions of each experiment (information reported in Table 8.1). As already observed, experiments differ slightly from each other as to the value of the injected FDG dose and the number of cells. Accordingly, we expect a reasonable variability in the values of the rate constants among the experiments of the same Gl group.

The reconstructed rate constants of the Gl1 group are reported in Table 8.2 for the BCM and in Table 8.3 for the SCM; the results of the Gl2 group are shown in Table 8.4 for the BCM and in Table 8.5 for the SCM. For each experiment, means and standard deviations are computed over fifty runs of the reg-GN iterative algorithm, with different initialization of the kinetic parameters, randomly chosen in the interval $(0, 1)$ with uniform distribution. The reg-GN algorithm is rather robust with respect to the choice of the regularization parameter, as shown in Delbary and Garbarino, 2018; in this application the regularization parameter is fixed for each iteration at the value of 10^6. The iterative algorithm is stopped when the relative error between the experimental cell culture activity and the model-predicted one, computed with the L^2 norm, is lower than a threshold of the order of 10^{-2}. Note that the standard deviation of each rate constant keeps systematically small with respect to the mean value, showing the robustness of the Newton-based inversion procedure. The BCM shows a variation of the estimates relatively greater than the SCM, which can be ascribed to the increase in the model complexity.

Before commenting on the results characterizing FDG kinetics, we focus on a test on the model dependence on LT calibration by considering errors on the estimated value of the efficiency coefficient $e = 3$ Bq/CPS. To this purpose, we analyze each experiment with two more e values, namely $e = 1.8$ Bq/CPS as minimum, and $e = 4.2$ Bq/CPS as maximum, thus accounting for a variability up to 40%. Figure 8.3 shows, as bar plots, the reconstructed rate constants of the Gl1 and Gl2 groups by means of both the BCM and SCM: the mean values are referred to $e = 3$ Bq/CPS and are computed over the experiments of the same Gl group, while the standard deviations indicate the estimates variability with respect to 40% of changes on e. Independently of the glucose concentration in the medium, increasing or decreasing e value actually modified significantly $\bar{k}_{fi}$ and $\bar{k}^*_{fi}$, with standard deviations about 50% with respect to the averages. The high variability of the input parameters of the two models inherently depends on the modeling assumptions, as shown in subsection 7.2.4. On the contrary, the uncertainty of the efficiency coefficient does not affect estimated rate constants of intracellular processes. The output parameters k_{if} and k^*_{if} are sufficiently stable with respect to changes in e showing a 10% of variability, while the BCM ER-input parameter k_{rp} presents a standard deviation of 15%. Finally, it is evident that k_{pf} and k_{fr} of the BCM, k^*_{pf} and k^*_{fp} of the SCM, are almost unaltered by errors on e, since the standard deviations are smaller than 4% of the coefficients mean values.

To summarize the outcomes on FDG kinetics given by the two models, we can observe that the results show a systematic difference in the rate coefficients of the groups Gl1 and Gl2, both in the case of BCM and SCM. In general, each rate constant is higher in group Gl1 than Gl2, showing an inverse correlation with glucose concentration in the medium. As to comparison between models, the values of $(\bar{k}_{fi}, \bar{k}^*_{fi})$ and (k_{if}, k^*_{if}) are essentially coincident, which means that they cannot be used to discriminate, and the same holds for k_{fr} and its equivalent k^*_{fp}. The values of (k_{pf}, k^*_{pf}) are highly dependent on the model, while k_{rp} has a unique representation in the BCM.

	$\bar{k}_{fi}$	k_{if}	k_{pf}	k_{rp}	k_{fr}
e1[1]	0.0055 ± 0.0001	4.5202 ± 0.1203	0.7183 ± 0.0057	4.5278 ± 0.3462	0.0015 ± 0.0000
e2[1]	0.0080 ± 0.0003	4.5295 ± 0.2208	0.6450 ± 0.0824	4.2957 ± 0.7072	0.0033 ± 0.0027
e3[1]	0.0042 ± 0.0003	3.3684 ± 0.3673	0.8670 ± 0.0053	3.4819 ± 0.0694	0.0033 ± 0.0001
e4[1]	0.0152 ± 0.0018	6.3674 ± 0.8135	0.2586 ± 0.0009	3.8728 ± 0.2840	0.0021 ± 0.0000
e5[1]	0.0153 ± 0.0012	7.1280 ± 0.5583	0.1510 ± 0.0002	4.5027 ± 0.1900	0.0009 ± 0.0000
e6[1]	0.0070 ± 0.0001	4.4340 ± 0.0597	0.3169 ± 0.0007	3.5029 ± 0.1061	0.0035 ± 0.0000
e7[1]	0.0083 ± 0.0007	2.8722 ± 0.2710	0.1340 ± 0.0021	2.0803 ± 0.3009	0.0001 ± 0.0000
e8[1]	0.0050 ± 0.0006	2.4056 ± 0.3527	0.1939 ± 0.0030	2.2454 ± 0.6789	0.0014 ± 0.0000
mean	0.0086	4.4532	0.4106	3.5637	0.0020
std	0.0044	1.6344	0.2880	0.9555	0.0013

TABLE 8.2: Reconstructed BCM rate constants (min^{-1}) for the 4T1 cell cultures of the Gl1 group, as means and standard deviations over 50 runs of the reg-GN algorithm. The last two lines report mean and standard deviation of each parameter computed over the mean estimates of the eight experiments.

	$\bar{k}^*_{fi}$	k^*_{if}	k^*_{pf}	k^*_{fp}
e1[1]	0.0060 ± 0.0000	4.9263 ± 0.0229	0.1080 ± 0.0000	0.0013 ± 0.0000
e2[1]	0.0084 ± 0.0003	4.7329 ± 0.1855	0.0995 ± 0.0001	0.0026 ± 0.0000
e3[1]	0.0047 ± 0.0003	3.7799 ± 0.2512	0.1226 ± 0.0002	0.0027 ± 0.0000
e4[1]	0.0144 ± 0.0001	5.8915 ± 0.0450	0.0417 ± 0.0000	0.0020 ± 0.0000
e5[1]	0.0150 ± 0.0002	6.9155 ± 0.0966	0.0250 ± 0.0000	0.0010 ± 0.0000
e6[1]	0.0069 ± 0.0000	4.3281 ± 0.0167	0.0503 ± 0.0000	0.0033 ± 0.0000
e7[1]	0.0078 ± 0.0011	2.6919 ± 0.3771	0.0222 ± 0.0006	0.0001 ± 0.0000
e8[1]	0.0048 ± 0.0008	2.3039 ± 0.3913	0.0307 ± 0.0001	0.0013 ± 0.0000
mean	0.0085	4.4462	0.0625	0.0018
std	0.0041	1.5411	0.0408	0.0011

TABLE 8.3: Reconstructed SCM rate constants (min^{-1}) for the 4T1 cell cultures of the Gl1 group, as means and standard deviations over 50 runs of the reg-GN algorithm. The last two lines report mean and standard deviation of each parameter computed over the mean estimates of the eight experiments.

In details, the following comments to the BCM and SCM results of Table 8.2 and Table 8.3 of the Gl1 group, Table 8.4 and Table 8.5 of the Gl2 group, are now in order.

- *Input rates.* The reconstructed values of $\bar{k}_{fi}$ and $\bar{k}^*_{fi}$ are very small, with order of magnitude of 10^{-2} for Gl1 and of 10^{-3} for Gl2. We recall that $\bar{k}_{fi}$ is defined as $\bar{k}_{fi} = k_{if}\, \mathcal{V}_{\text{cyt}}/\mathcal{V}_{\text{i}}$, with $\mathcal{V}_{\text{cyt}} \ll \mathcal{V}_{\text{i}}$, which implies that the smallness of $\bar{k}_{fi}$ is ultimately related to the choice of activities as state variables. Of course, the contribution $\bar{k}_{fi}\, A_i$ cannot be discarded because it is of the order of 10^4 Bq min^{-1}. Similar remarks apply to $\bar{k}^*_{fi}$. The medium values of $\bar{k}_{fi}$ and $\bar{k}^*_{fi}$ in group Gl1 are more than twice the corresponding values in group Gl2. This is consistent with the expected competition between FDG and glucose molecules during cell uptake from the medium. Finally, by looking at a fixed Gl group, for each experiment $\bar{k}_{fi}$ and $\bar{k}^*_{fi}$ are almost equal, showing that the input parameter is independent of the model chosen for the reduction of LT data.

	$\bar{k}_{fi}$	k_{if}	k_{pf}	k_{rp}	k_{fr}
e1[2]	0.0007 ± 0.0000	0.4478 ± 0.0014	0.0762 ± 0.0002	0.7419 ± 0.0314	0.0011 ± 0.0000
e2[2]	0.0037 ± 0.0002	4.1000 ± 0.2389	0.1648 ± 0.0005	2.7640 ± 0.1737	0.0012 ± 0.0000
e3[2]	0.0067 ± 0.0001	4.9148 ± 0.0709	0.0915 ± 0.0002	2.8580 ± 0.2507	0.0011 ± 0.0000
e4[2]	0.0050 ± 0.0001	3.7226 ± 0.1081	0.1030 ± 0.0005	2.0989 ± 0.2556	0.0014 ± 0.0000
e5[2]	0.0004 ± 0.0001	0.3755 ± 0.1708	0.0901 ± 0.0072	0.5544 ± 0.1159	0.0001 ± 0.0000
e6[2]	0.0060 ± 0.0001	3.8472 ± 0.0915	0.0863 ± 0.0002	2.0873 ± 0.1871	0.0039 ± 0.0000
e7[2]	0.0033 ± 0.0000	2.5805 ± 0.0189	0.0305 ± 0.0001	1.7343 ± 0.3394	0.0003 ± 0.0000
e8[2]	0.0028 ± 0.0001	2.5695 ± 0.1682	0.0848 ± 0.0004	1.4337 ± 0.2013	0.0011 ± 0.0000
mean	0.0036	2.8197	0.0909	1.7841	0.0013
std	0.0023	1.6741	0.0369	0.8475	0.0012

TABLE 8.4: Reconstructed BCM rate constants (min^{-1}) for the 4T1 cell cultures of the Gl2 group, as means and standard deviations over 50 runs of the reg-GN algorithm. The last two lines report mean and standard deviation of each parameter computed over the mean estimates of the eight experiments.

	$\bar{k}^*_{fi}$	k^*_{if}	k^*_{pf}	k^*_{fp}
e1[2]	0.0007 ± 0.0000	0.4862 ± 0.0000	0.0121 ± 0.0000	0.0009 ± 0.0000
e2[2]	0.0037 ± 0.0000	4.0784 ± 0.0237	0.0268 ± 0.0000	0.0012 ± 0.0000
e3[2]	0.0068 ± 0.0000	4.9247 ± 0.0251	0.0152 ± 0.0000	0.0011 ± 0.0000
e4[2]	0.0050 ± 0.0001	3.6819 ± 0.0273	0.0169 ± 0.0000	0.0014 ± 0.0000
e5[2]	0.0004 ± 0.0000	0.3802 ± 0.0075	0.0133 ± 0.0002	0.0001 ± 0.0001
e6[2]	0.0060 ± 0.0000	3.7841 ± 0.0260	0.0143 ± 0.0000	0.0039 ± 0.0000
e7[2]	0.0033 ± 0.0000	2.5509 ± 0.0011	0.0051 ± 0.0000	0.0003 ± 0.0000
e8[2]	0.0028 ± 0.0001	2.5560 ± 0.0894	0.0138 ± 0.0000	0.0011 ± 0.0000
mean	0.0036	2.8053	0.0147	0.0012
std	0.0023	1.6572	0.0060	0.0012

TABLE 8.5: Reconstructed SCM rate constants (min^{-1}) for the 4T1 cell cultures of the Gl2 group, as means and standard deviations over 50 runs of the reg-GN algorithm. The last two lines report mean and standard deviation of each parameter computed over the mean estimates of the eight experiments.

- *Output rates.* The estimated k_{if} and k^*_{if} are almost equal in the same Gl experiment, and are of order of unity in both Gl1 and Gl2. The obtained values are higher than expected from comparison with results obtained in normal and cancer tissues (Ishibashi et al., 2016; Reivich et al., 1985; Røe et al., 2010; Rusten et al., 2013). In addition, the group Gl1 shows a mean value of the output parameter almost twice the one of Gl2, which seems to indicate an outgoing transfer of tracer from cells to medium inversely correlated with glucose concentration in the medium. The apparent paradox is explained by the evaluation of the net contribution $-k_{if}A_f + \bar{k}_{fi}A_i$ to the time rate $\dot{A}_f$ (or, for the SCM, $-k^*_{if}A^*_f + \bar{k}^*_{fi}A_i$ in $\dot{A}^*_f$), due to FDG exchange between incubation medium and cytosol, which is strictly positive and greater in Gl1 than in Gl2 (as expected), but rather small. This is consistent with the small decrease rate in time of the medium activity A_i (see Figure 8.2(b)), and the expectation that only a small fraction of the FDG in the medium is consumed by the system of cells.

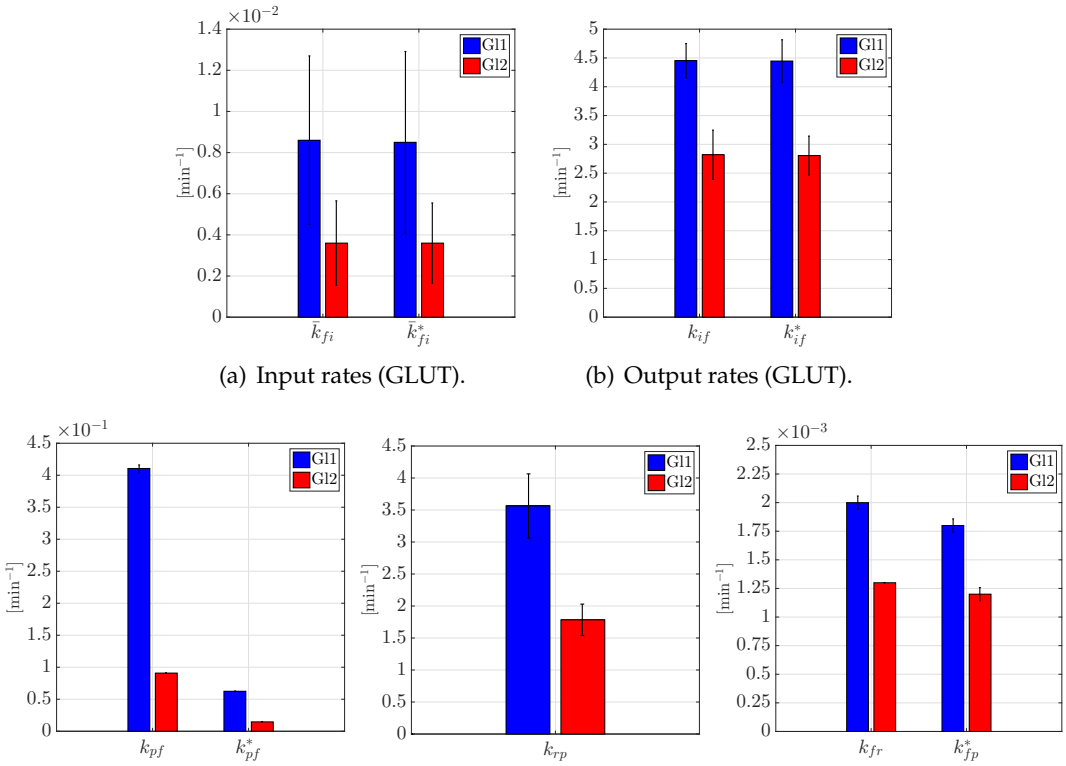

(a) Input rates (GLUT). (b) Output rates (GLUT).

(c) Phosphorylation (HK). (d) BCM ER-input (G6PT). (e) Dephosphorylation (G6Pase).

FIGURE 8.3: Bar plot of the reconstructed rate constants for both the BCM ($\bar{k}_{fi}, k_{if}, k_{pf}, k_{rp}, k_{fr}$) and SCM ($\bar{k}^*_{fi}, k^*_{if}, k^*_{pf}, k^*_{fp}$) and for both groups Gl1 (blue bars) and Gl2 (red bars). Each bar refers to the mean value of the parameter computed over the experiments of the same group, and the error bar identifies the variability of the parameter value with respect to 40% of error on the LT efficiency coefficient ($e = 3 \pm 1.2$ Bq/CPS).

- The result that $\bar{k}_{fi} \simeq \bar{k}^*_{fi}$ and $k_{if} \simeq k^*_{if}$ with respect to the same Gl experiments, shows that the two rate constants cannot be used to discriminate between the two models BCM and SCM. This also implies that the reconstructed tracer exchange between cells and incubation medium is independent of the model applied.

- *Dephosphorylation rates.* Both coefficients k_{fr} and k^*_{fp} refer to dephosphorylation (G6Pase enzyme action), according to the BCM and the SCM, respectively, so that they can be examined together. The estimated values are independent of the model, since k_{fr} and k^*_{fp} are almost coincident for each experiment, and are of the order of 10^{-3} with slightly lower values in Gl2 than Gl1. The corresponding contribution to the rates of change of the activities may be disregarded, as it is often done, following Sokoloff et al., 1977.

- *Phosphorylation rates.* The rate coefficients k_{pf} and k^*_{pf} are related to the process of phosphorylation inside the cytosol (HK enzyme action). Phosphorylation is the mechanism of entrapment of glucose substrate carried out by the cell for energy needs. By looking at the reconstructed values at fixed model, the FDG phosphorylation rate is almost four times faster in Gl1 than Gl2, consistently with the corresponding half of glucose amount available in the medium

and thus the lower competition FDG/glucose. Moreover, the phosphorylation rate is the only kinetic parameter that differs between the reconstructed values of the BCM and of the SCM. Indeed k_{pf} (order of magnitude of 10^{-1}) is systematically greater than k^*_{pf} (order of magnitude of 10^{-2}). The distinct characterization of the phosphorylation process predicted by the competing models is a consequence of the modeling designs: as shown in subsection 7.2.3, under certain assumptions (e.g. conditions (7.22)) which can be considered as satisfied by the parameters and compartment activities obtained, the relation $k^*_{pf} \simeq v k_{pf}$, with $v = 0.17$, holds. The value of k^*_{pf} of the SCM is comparable with well-known results obtained through the Sokoloff model (Reivich et al., 1985; Røe et al., 2010; Rusten et al., 2013; Sokoloff et al., 1977); the value of k_{pf} of the BCM agrees with results of direct measurements of HK enzyme action reconstructed from the literature (Wang et al., 2015; Muzi et al., 2001). This shows that the phosphorylation rate has been underestimated, and that the proposed BCM gives rise to realistic results.

- *ER-input rate.* The parameter k_{rp} for the transfer of FDG6P from cytosol to ER (G6PT enzyme action) is present only in the BCM, and has no equivalent in the SCM. It assumes values of order of unity in both Gl1 and Gl2, showing a relatively fast G6PT action. Moreover, it doubles when glucose concentration in the medium halves, as direct consequence of the competition between the two substrates.

8.2.2 BCM and SCM compartment activities

The difference between models is best evidenced by looking at the time curves of activities in intracellular compartments. Substitution of the reconstructed rate constants and the IF A_i into the analytical solution of the compartmental system of ODEs provides the time-dependent compartment activities: for the BCM, by means of equation (7.6) with the estimated $\bar{\boldsymbol{k}}_{BCM}$, we obtain A_f, A_p, and A_r, where the latter comes from equation (7.5) as $A_r = v\bar{A}_r = 0.17\bar{A}_r$; for the SCM, through equation (7.13) with the estimated $\bar{\boldsymbol{k}}^*_{SCM}$, we get A^*_f and A^*_p.

Figure 8.4 and Figure 8.5 show the model-predicted compartment TACs for experiment e3[1] of the Gl1 group and experiment e2[2] of the Gl2 group, respectively, with the BCM in panel (a) and the SCM in panel (b). The same curves are reported in Figure 8.6 and Figure 8.7 for the BCM and the SCM, respectively, but they are grouped as to compare the Gl1 and Gl2 reconstructed activities in each compartment. Note that experiments e3[1] and e2[2] are obtained at similar injected dose $\mathcal{D}$ and number of cells N_c, and we consider their TACs as representative of all experiments conducted for the related Gl group.

The following considerations on the reconstructed activities indicating FDG localization in the compartments of the BCM and the SCM, for the Gl1 and Gl2 situations, are now in order.

- *Free tracer.* The activities A_f and A^*_f are almost equal at fixed Gl amount, and are nearly constant, with the stationary value reached in the first few minutes of the experiment in both groups. In general, the constant value depends on the experimental situation, and in particular on the glucose concentration in the medium; indeed, as visible in Figure 8.6(a) and Figure 8.7(a), for both models the free FDG amount is found higher in the Gl1 experiment than Gl2, as a consequence of competition with glucose.

- *Phosphorylated tracer.* The activity of phosphorylated tracer in the cytosol predicted by the two competing models is deeply different. The BCM provides a curve A_p which is approximately constant, and almost one order of magnitude smaller than A_f, showing that a small (constant) amount of phosphorylated FDG occupies the cytosol, where the free form of the tracer prevails over the phosphorylated form; however, this also indicates a high efficiency of the process of transfer of tracer molecules from cytosol to ER (i.e. an high k_{rp} rate). In the SCM, the activity A_p^* is almost linear and monotonically increasing; indeed, the phosphorylated compartment contains the greater amount of radioactive molecules and represents the pool where the FDG is accumulated intracellularly. Again, at fixed model, the Gl1 curve is over the Gl2 one (Figure 8.6(b) for the BCM, and Figure 8.7(b) for the SCM).

- *ER tracer.* The ER compartment represents the pool where FDG accumulates for the BCM, as described by the TACs A_r in Figure 8.6(c), which increase in time almost linearly and reach the maximum value at the end-time point. The high value of k_{rp}, seen in both Gl groups, is consistent with the very small (and almost constant) value of the activity A_p, so that the rate of transfer of tracer from the cytosolic-phosphorylated compartment to the ER-localized-phosphorylated compartment, that is $k_{rp}A_p$, is capable of sustaining the growth of A_r. The notable difference in the A_r curves of the Gl groups is coherent: the Gl1 experimental curve of total activity of the cell culture presents a growth rate much greater than the Gl2 one, and the ER activities reflect such uptake trend.

- The activity A_r can be naturally related with the activity A_p^*, as they are the activities of the two pools where tracer accumulates in time, with respect to the two different models. They are quantitatively comparable, although the ER compartment in BCM occupies a different volume with respect to the cytosolic phosphorylated compartment in SCM, specifically a smaller volume ($V_{er} < V_{cyt}$). Indeed, the related concentrations would be different, and in particular C_r bigger than C_p^*. Moreover, the curves A_r and A_p^* mimic the growth of the total cell culture activity $\mathscr{A}_T$, since the other compartments present almost constant activities.

- As to compare the two models, it can be shown that $A_p^* \simeq A_p + A_r$, as direct consequence of the fact that the BCM and SCM are used to explain the same LT data, i.e. $\mathscr{A}_T = A_f + A_p + A_r = A_f^* + A_p^*$ (see subsection 7.2.3), with $A_f \simeq A_f^*$.

Altogether accounting for the documented sequestration of G6Pase in the ER shifts the compartmental description of intracellular FDG kinetics from a standard SCM towards a novel BCM, the latter configuring the same ER as the radioactivity accumulation site. To overcome the limited spatial resolution of radionuclide detection and to corroborate this theoretical finding, we extend our study by verifying whether this same ER fate also applies to the fluorescent 2DG analog 2NBDG (Scussolini et al., 2018b). To this purpose, three cell cultures are exposed to a solution containing glibenclamide as a vital ER probe as well as glucose and 2NBDG at the concentration of 5.5 mM and 50 μM, respectively. Incubation lasts 20, 50 or 90 minutes, before imaging with confocal microscopy with a spatial resolution of 400 nm. Images are analyzed using a dedicated routine of ImageJ and document a progressive increase in the colocalization between the hexose fluorescence and ER signal

(Figure 8.8). Therefore, the BCM prediction of FDG accumulation in the ER is confirmed by independent imaging experiments showing a progressive ER accrual of the fluorescent FDG analog 2NBDG.

A further comment on the BCM characterization of FDG path in cancer cells concerns the ER pool. First, the BCM automatically depicts intracellular FDG accumulation in phosphorylated form inside the ER, as soon as the existence of the ER compartment is admitted, without any forcing contribution. Second, the BCM prediction is confirmed by independent imaging experiments showing a progressive ER accrual of the fluorescent FDG analog 2NBDG (Figure 8.8). Finally, the BCM configuration implies necessarily specific values for the rate constants, and thus for the efficiency of the action of the enzymes processing FDG, which can be different from state-of-the-art values used so far to describe FDG kinetics in cancer tissues.

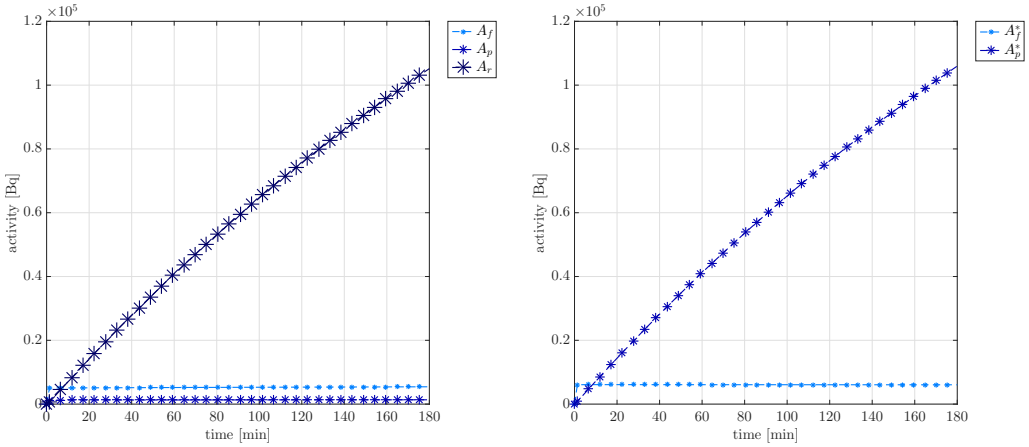

(a) BCM. (b) SCM.

FIGURE 8.4: Model-predicted time curves of the compartment activities for the experiment e3[1] of the Gl1 group: (a) A_f, A_p, and A_r of the BCM; (b) A_f^* and A_p^* of the SCM.

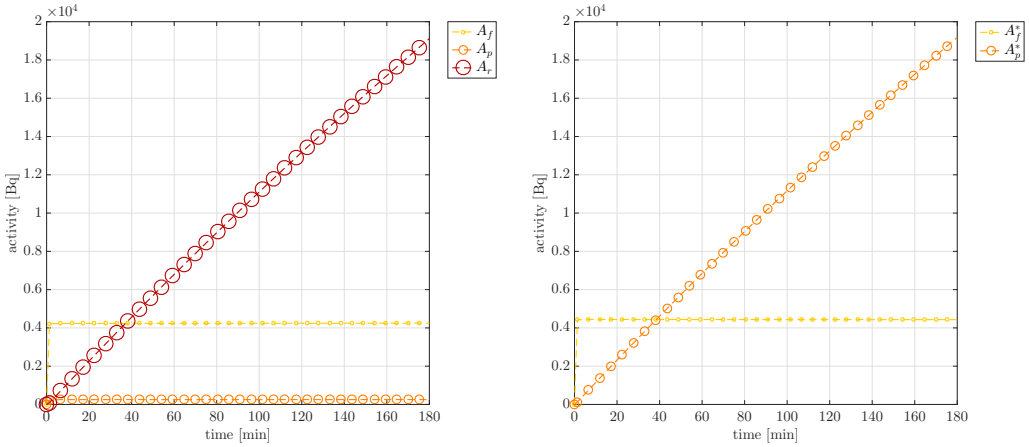

(a) BCM. (b) SCM.

FIGURE 8.5: Model-predicted time curves of the compartment activities for the experiment e2[2] of the Gl2 group: (a) A_f, A_p, and A_r of the BCM; (b) A_f^* and A_p^* of the SCM.

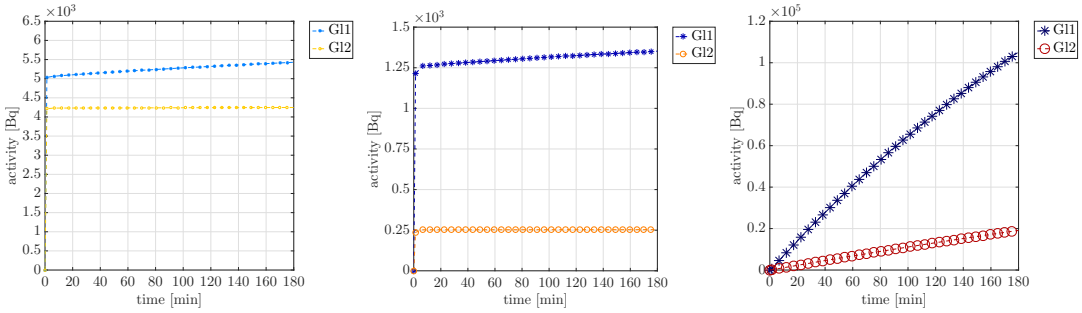

(a) A_f. (b) A_p. (c) A_r.

FIGURE 8.6: Reconstructed TACs of the BCM compartments for experiments e3[1] (Gl1) and e2[2] (Gl2).

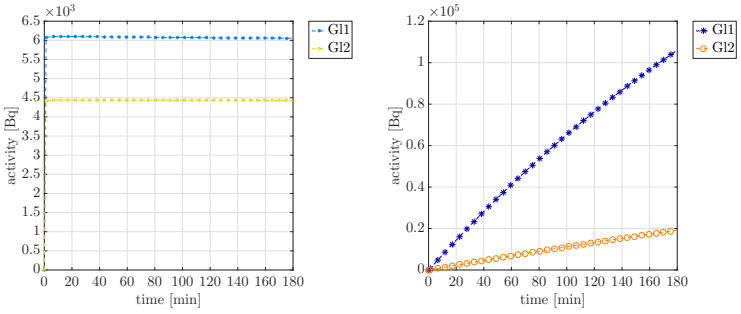

(a) A_f^*. (b) A_p^*.

FIGURE 8.7: Reconstructed TACs of the SCM compartments for experiments e3[1] (Gl1) and e2[2] (Gl2).

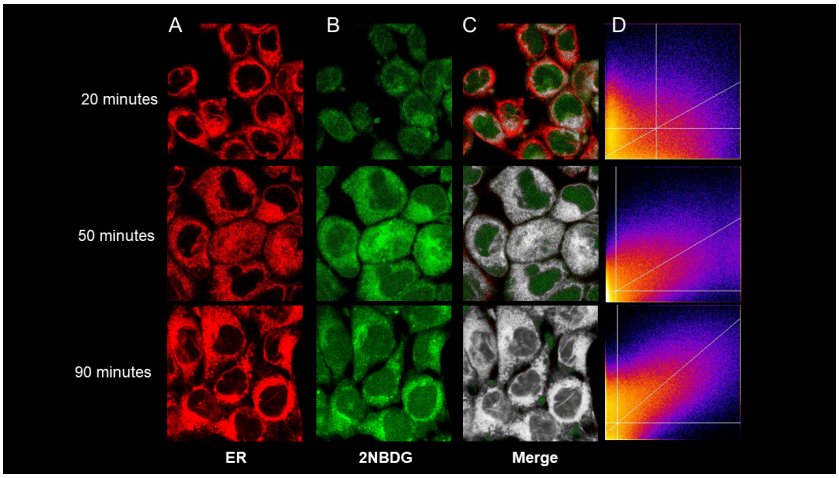

FIGURE 8.8: Imaging confirmation of radioactivity accumulation in ER: column A reports the images obtained with the vital ER staining glybenclamide; column B shows the simultaneous distribution of the fluorescent 2DG analog 2NBDG; the white color in column C identifies the colocalization of ER and 2NBDG signal at a spatial resolution of 250 nm, and column D is the Costes representation of the same images. Images are obtained at 20, 50 and 90 minutes.

Part IV

Molecule-scale

Chapter 9

Molecular Interaction Map for the cell signaling network

Molecular Systems Biology is a cross-disciplinary field of research which aims at explaining cell behavior and function at the level of chemical interactions. Here, the application of chemical reaction networks (CRNs) is required and extensive. In fact, most biological characteristics arise from complex interactions between the cell's numerous constituents, such as proteins, DNA, RNA and small molecules. Hence, there is a need to investigate the chaotic network underlying these processes in order to understand human diseases. A key challenge for biology in the twenty-first century is to model and study complex intracellular biochemical system networks that contribute to the function of a living cell and that underline specific disease mechanisms (Barabási and Oltvai, 2004).

Among the several disorders arising from aberrations in cell regulatory mechanisms, cancer is the most examined, due to its high incidence on the human population. Cancer cell behavior is driven by alterations in the processes, i.e. chemical interactions, that cells use to sense and respond to diverse stimuli. The development of suitable models schematizing the structure and dynamics of cellular biochemical organization can provide some unique insights and predictions into how regulatory and metabolic processes give rise to cancer formation and progression, and can suggest novel strategies for prevention and treatment of malignancy. With this aims, a huge Molecular Interaction Map (MIM) for the colorectal cancer (CRC) has been designed in Tortolina et al., 2015. A MIM is essentially a unambiguous graphical representation of a CRN, used to depict molecular interactions of interest occurring within a cell.

The CRC MIM is probably the largest ever constructed and modeled, at least to our knowledge, and contains an interconnected network of chemical reactions related to the G0-G1-S cell cycle transition, grouped into pathways downstream of the TGFβ, WNT and EGF families of receptor ligands, playing an important role in the CRC pathogenesis. In chemical terms, the MIM is a huge CRN governed by the law of mass action, and therefore, in mathematical terms, a huge non-linear (quadratic) system of ordinary differential equations (ODEs). Using the MIM it is possible to simulate the cancer state by introducing alterations of specific chemical reactions, known as mutations, and to test the effects of targeted drugs, called inhibitors, for the treatment of cancer.

The first section illustrates the biochemical mechanisms by which cell functions are regulated, i.e. the processes underpin the cell signaling, and provides the fundamental chemical notions for the understanding of the intracellular biochemical system networks. In the second section, the features of the MIM model are described. The third section goes deeper in the MIM chemistry by specifying the chemical species interplay, the occurrence of chemical reactions, and the characterization of mutations/inhibitors.

9.1 Cell signaling network

Cell signaling is part of any communication process that governs basic activities of cells and coordinates all cell actions. The mechanism by which stimuli are transmitted through a cell in order to produce a cell response is an intracellular signaling cascade, i.e. a series of chemical reactions within the cell. A *signaling pathway* describes a group of molecules in a cell that work together to control one or more cell functions: after the first molecule in a pathway receives a signal, it activates another molecule, and so on, until the last molecule is activated and the cell function is carried out. Cell signaling research involves studying the spatial distribution and the temporal dynamics of the components of signaling pathways that are activated by extracellular signals in various cell types.

The basic mechanism involving the conversion of a signal from outside the cell to a functional change within the cell is *signal transduction*, by which a chemical or physical signal is transmitted through a cell as a series of molecular events, which ultimately results in a cell response. The chief actors carrying out the duties within the cell are the *proteins*, which perform as structural and motor components, enzymes, signaling molecules, and more in general regulatory molecules. Protein-protein interactions and signal transduction pathways are involved in biological processes at almost every level of cell function.

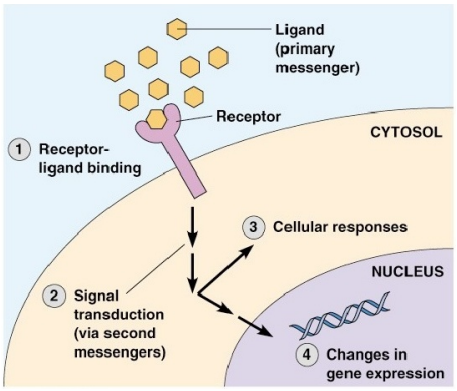

FIGURE 9.1: The signal transduction process for a cell.

The signal transduction process works as in Figure 9.1, and pursues the following steps.

1. The molecules responsible for detecting extracellular chemical signals are cell surface proteins termed *receptors* (signal transducers). Each receptor is linked to a specific cell signaling pathway. When a signaling molecule, known as *ligand* (primary messenger), binds to its corresponding receptor, it activates or inhibits the receptor's associated biochemical pathway.

2. For many cell surface receptors, ligand-receptor interactions are not directly linked to the cell response. The activated receptor must first interact with another protein, called primary effector. Such effectors are often linked to second messengers, which can activate secondary effectors, and so on. The changes elicited by ligand binding in a receptor give rise to a chain of biochemical events along a signaling pathway.

3. The signaling cascade ends with the cell response, as the ultimate physiological effect of the ligand on the cell behavior.

4. The cell responses imply changes in the transcription or translation of genes, and post-translational and conformational changes in proteins, as well as changes in their location.

Each component (or node) of a signaling pathway is classified according to the role it plays with respect to the initial stimulus. When signaling pathways interact with one another they form networks, which allow cell responses to be coordinated, often by combinatorial signaling events.

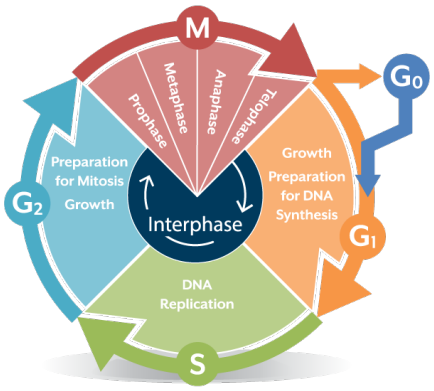

FIGURE 9.2: Schematic representation of the cell cycle phases G0, G1, S, G2, and M (from Myriad myPlan, Salt Lake City, USA).

The signaling pathways are the basic mechanisms controlling cell growth, proliferation, metabolism and many other processes. In other words, cell signaling controls the cell cycle, in which a cell grows, replicates its DNA and divides. The cell cycle, represented in Figure 9.2, consists of four distinct phases: G1 phase in which cell increases in size, S phase (synthesis) for DNA replication, G2 phase in which cell continues to grow, and M phase (mitosis or meiosis) for cell division into two daughter cells. The phase G0 is a resting phase where the cell has left the cycle and has stopped dividing.

Signaling pathways also include mechanisms which ensure that errors therein are corrected, and if not, the cell commits suicide in a systematic cell process known as programmed cell death, or apoptosis. Cancer cells differ from normal body cells in their ability to divide indefinitely and to evade programmed cell death. As a result of *genetic mutations*, in cancer cells the signaling pathways are abnormally activated and the cell regulatory process malfunctions, resulting in uncontrolled cell proliferation. Identification of key factors involved in both apoptosis and cell cycle regulation may help to develop targeted drugs, and drug combinations, able to block the mutated pathways in cancer pathologies.

9.2 The MIM model

At the biochemical level, we may consider a normally differentiated cell as a very complex network of signaling pathways, and a cancer cell as a cell bearing in the order of two dozen mutated pathways (Wood et al., 2007). With the aim of generating a model of signaling mechanisms, we focused on a functionally relevant sub-region of the cell signaling network, in particular the G0-G1-S cell cycle transition (Tortolina et al., 2015), a crucial decisional moment for cell replication, and we modeled an interconnected network downstream three relevant cancer pathways in the CRC: the TGFβ, WNT and EGF pathways.

The signaling network is graphically presented as a MIM. The MIM graphic notation provides a standardized method to draw diagrams for cellular bio-regulatory networks. The first formulation of this kinds of maps was made in Kohn, 1999 for the description of the mammalian cell cycle control and DNA repair systems. The MIM diagram convention "was designed capable of unambiguous representation of networks containing multi-protein complexes, protein modifications, and enzymes that are substrates of other enzymes" (Kohn, 1999). The potential of the MIMs is the ability of showing all of the many interactions in which a given molecule may be involved. Our MIM has been created using the symbol table originally proposed by Aladjem et al., 2004 and Kohn et al., 2006, slightly adapted to fit to some new semantic requirement (Castagnino et al., 2010). The implementation of the MIM followed two phases: a training phase based on fitting the molecular results of more than one hundred, high Impact Factor, pertinent papers; a validation phase for the direct validation on experiments.

The CRC MIM, shown in Figure 9.3, represent a broad structure with a complex connectivity: it includes multiple overlapping pathways, which in turn consider several chemical species involved in a huge number of chemical reactions. Pathways, i.e. paths as simple sequences of molecules that transmit information, are the basic multi-molecular structures of the MIM, through which knowledge of biochemical interactions among proteins and other molecules is organized.

Basically, the MIM model combines three different features.

- The MIM as diagram (see Figure 9.3):
  - each colored boxed node is a chemical species defined as basic, i.e. a species belonging to the set of proteins originating the chain of chemical reactions in which other composed species, bounded-forms of basic species, are chemically created;
  - each arrow with an added node in-between represents a chemical reaction and the complexes involved;
  - a node surrounded by an oval in light yellow indicates a species potentially affected by a mutation;
  - the underlined blue names indicates the targeted inhibitor drugs, relevant in colorectal cancer.
- The MIM as CRN provided by mass action kinetics (see Chapter 2):
  - 447 chemical species (85 basic and 362 composed);
  - 870 chemical reactions (348 reversible and 174 non-reversible reactions), and thus 870 reaction rate constants.

  The CRN graph robustness/sensitivity to random perturbations has been explored in Ambrosi et al., 2013. The intent of the study was to test the degree of tolerance of the network to parameter uncertainty, and the CRC MIM resulted to be a non-isomorphic directed graph: there are privileged directions of propagation of the information, and these privileged directions are recognized at the biological level as the signaling pathways. The CRN dynamics is well-modeled by a non-linear system of ODEs: the CRC MIM system is quadratic with respect to the molar species concentrations, and linear with respect to the reaction rate constants.

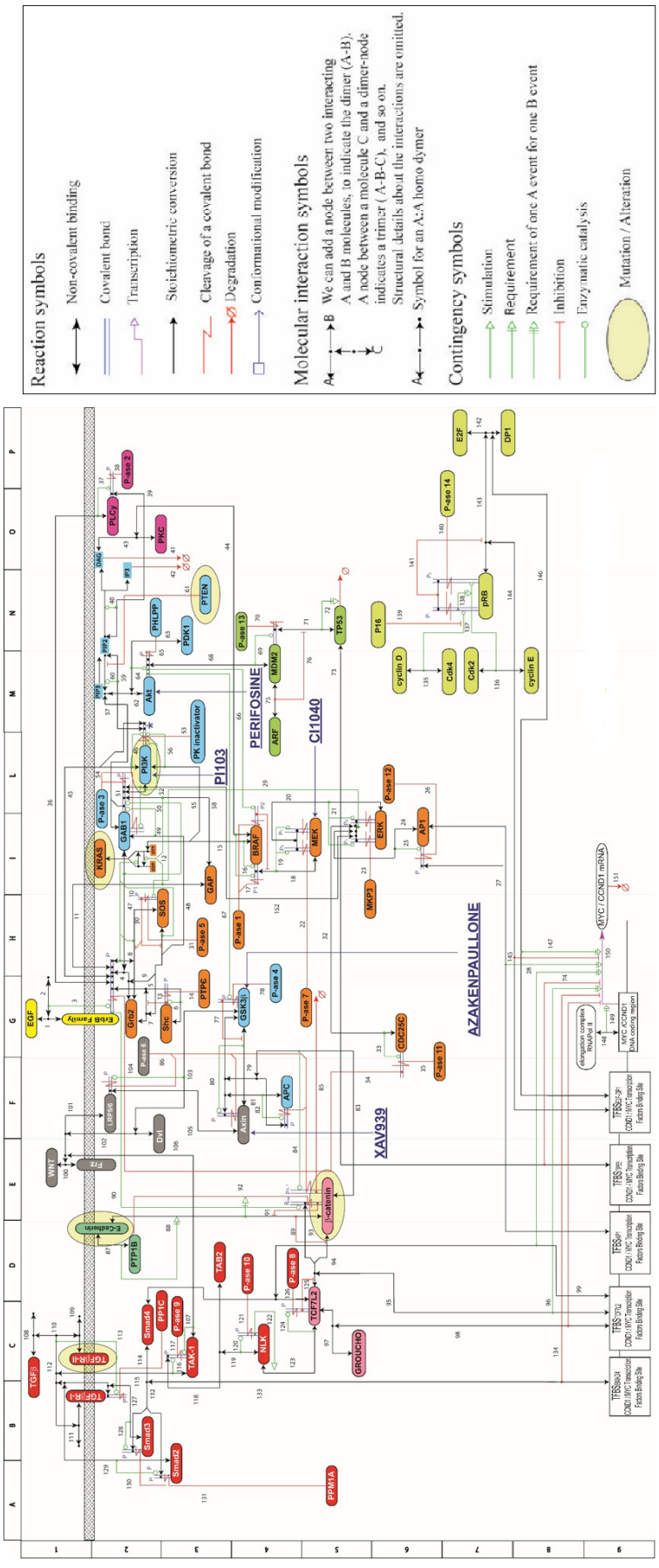

FIGURE 9.3: MIM referring to the TGFβ, WNT and EGF pathways, and the syntactic rules adopted for its construction (from Tortolina et al., 2015).

- The MIM as transcription region controlling the expression of two key oncogenes, MYC (c-myc) and CCND1 (cyclin D1) mRNAs. The function for MYC and CCND1 are reconstructed by using thermo-statistical derivation of a transcription rate (Frank, Carmody, and Kholodenko, 2012), relating the transcription rates of the genes to the concentrations of their upstream transcriptional activator and repressor complexes.

The MIM, applied to CRC, is a huge network but still incomplete with respect to all the possible signaling pathways and chemical interactions supplementing the cell bio-regulatory network. Nevertheless, it can be considered a good starting point. In fact, the CRC MIM can be adapted to represent different types of cancer, and its capabilities go beyond the simple representation of cell signaling network. Starting from an initial physiological condition, the model can be adapted to (i) simulate individual pathologic cancer conditions, implementing individual set of alterations/mutations in relevant oncoproteins, and (ii) test the effects of targeted inhibitor drugs on different cancer mutation profiles in a personalized medicine approach.

9.3 MIM chemistry

At the biochemical level, how does the MIM network works? In order to answer to this question, we need to consider the chemical components involved in the map and account for possible mutations and inhibitors.

9.3.1 MIM chemical components

The CRC MIM, as modeled in Tortolina et al., 2015, considers the signaling network made of three pathways, namely the TGFβ, WNT and EGF pathways.

The TGFβ, WNT and EGF are members of families of ligands, present in the extracellular medium. In particular, the TGFβ and EGF are *growth factors*, naturally occurring substances capable of stimulating cellular growth, proliferation, healing, and cellular differentiation, and WNT is a signaling glycoprotein. The MIM ligands bind to specific transmembrane receptors: the TGFβR-I/TGFβR-II are type I and type II receptors for the TGFβ ligands, FRZ are receptors for WNT ligands, and the ErbB family receptors receive the EGF signal. The chain of biochemical events along the three different signaling pathways involve specific types of chemical species: signaling molecules, kinases, phosphatases, transcription factors, small molecules, and phospholipases.

The list of all CRC MIM chemical components can be found in Tortolina et al., 2015. Here, we describe the basic types of chemical species and chemical reactions present in the CRC MIM. Note that each MIM reaction involves at most two species in the reactant and product complexes.

- In general, suppose to have a simple conversion reaction in which the chemical species A transforms into the species B at reaction rate k_f:

$$A \xrightarrow{k_f} B\,. \tag{9.1}$$

  If the concentration of the species A is constant in time, then the reaction can be rewritten equivalently as

$$\varnothing \xrightarrow{k_f x_A} B\,, \tag{9.2}$$

where the null species $\varnothing$ takes the place of A, and the rate constant becomes $k_f x_A$, with x_A the constant concentration of A.

- The interaction between a ligand L and a receptor R is the reversible reaction

$$L + R \underset{k_r}{\overset{k_f}{\rightleftarrows}} LR \,, \tag{9.3}$$

with rate constants k_f (forward) and k_r (reverse). Since the concentration of the ligand can be considered not consumable, i.e. constant in time, the receptor-ligand reaction is rewritten as

$$R \underset{k_r}{\overset{k_f x_L}{\rightleftarrows}} LR \,, \tag{9.4}$$

where x_L denotes the concentration of the ligand L, and thus the forward reaction rate is modified into the constant product $k_f x_L$.

- The *homodimerization* is a chemical reaction in which two identical molecules join to form a homodimer. If A is a chemical species, the homodimerization of A is given by

$$A + A \rightleftarrows 2A \,. \tag{9.5}$$

- The *phosphorylation* of a protein is the major molecular mechanism through which protein function is regulated in response to extracellular stimuli. The phosphorylation state of a molecule can affect its activity, reactivity, and its ability to bind other molecules. All types of extracellular signals produce most of their diverse effects by regulating phosphorylation of specific proteins, i.e. the signals are propagated through the cell by chains of phosphorylations. A *kinase* is the enzyme responsible for the protein phosphorylation: kinases catalyze the transfer of phosphate groups from high-energy, phosphate-donating molecules, to specific substrates. Let A be a protein, and K a kinase; then the phosphorylation chain of reactions is

$$A + K \rightleftarrows AK \rightarrow AP + K \,, \tag{9.6}$$

where P indicated the phosphate group. The phosphorylation process consists of two steps: one reversible reaction for the creation of the AK complex, and one non-reversible reaction in which the kinase K binds a phosphate group to A and unbinds the phosphorylated protein AP.

- The counterpart of phosphorylation is the *dephosphorylation* process, by which the phosphate group is removed from a phosphorylated protein as a result of the enzyme *phosphatase*. Let AP be a phosphorylated protein, and $Pase$ a generic phosphatase; then the dephosphorylation chain of reactions is

$$AP + Pase \rightleftarrows AP\_Pase \rightarrow A + Pase \,. \tag{9.7}$$

The dephosphorylation process involves a first reversible reaction for the binding of the phosphatase $Pase$ to the phosphorylated protein AP, and a second non-reversible reaction in which the complex AP_Pase dissociates into the dephosphorylated protein A and the phosphatase $Pase$.

- A *transcription factor* is a protein that controls the rate of transcription of genetic information from DNA to mRNA, by binding to a specific DNA sequence. The function of transcription factors is to regulate genes in order to make sure that they are expressed in the right cell at the right time and in the right amount throughout the life of the cell and the organism. Groups of transcription factors function in a coordinated fashion to direct cell division, cell growth, and cell death throughout life.

9.3.2 MIM mutations and inhibitors

The cancer state of a cell can be inserted into the MIM as a set of mutations affecting one or more pathways. Potential mutations belonging to the same pathway are hypothesized as being mutually exclusive (Yeang, McCormick, and Levine, 2008), especially if very close along the pathway. Each pathway might contain a dozen signaling molecules, and, in principle, one of them could be mutated/altered through gain or loss of function. A mutation is the permanent alteration of the nucleotide sequence of the genome, resulting from damages to DNA, as errors during DNA replication. Mutations can result in many different types of change in sequences: mutations in genes can either have no effect, alter the product of a gene, or prevent the gene from functioning properly or completely. One direct effect of a mutation is to change a protein produced by a gene, in such a way that the *mutant protein* results with a single amino acid change or wide-range amino acid changes in the chains of amino acid constituting the protein.

One simple way of modeling a mutation in a signaling pathway is to alter the physiological concentration of the extracellular ligand, as to simulate the transmission to the cell of an abnormal signal, and thus to generate a non-physiological amount of specific phosphorylated proteins. Another typical example of mutation is the one in which the behavior of a mutant protein follows a modification of its dephosphorylation reaction: once the mutant protein is phosphorylated, the related phosphatase does not identify the target phosphorylated molecule and therefore does not bind to the phosphorylated mutant protein. The consequence is an altered production of phosphorylated forms of the mutant protein: the mutant protein is all phosphorylated and the amount of protein in free-form is negligible.

Let denote with $\hat{A}$ the mutated version of the protein A, and with $\hat{A}P$ its phosphorylated form. Let *Pase* be the associated phospahatase. Then, the species $\hat{A}P$ and *Pase* do not interact and the dephosphorylation reaction does not occur:

$$\hat{A}P + Pase \underset{\hat{k}_r}{\overset{\hat{k}_f}{\rightleftharpoons}} \hat{A}P\_Pase \rightarrow \hat{A} + Pase\ . \tag{9.8}$$

This means that the complex $\hat{A}P\_Pase$ is not created and thus $\hat{A}$ is not released. The dephosphorylation reaction is canceled simply by imposing that the forward reaction rate of binding between the phosphorylated mutant protein and the phosphatase is negligible, i.e. $\hat{k}_f = 0$. Following this idea, a set of mutations characterizing a cancer cell coincides mathematically to a suitable mask modifying the set of rate constants, in such a way that the forward reaction rates of interaction between phosphorylated mutant proteins and phosphatases are set to zero.

The MIM considers several *inhibitors* as molecular targeted drugs for the treatment of the colorectal cancer. In general, there exists inhibitor molecules, usually enzymes, with the peculiar function of binding to a protein in order to decrease its activity. Inhibitors can occur naturally in the regulation of metabolism, or can be

implemented as artificial medicinal molecules, simply drugs, with the aim of treating diseases. Targeted cancer therapies aim at blocking the growth of cancer cells by interfering with specific molecules (targets) involved in carcinogenesis and tumor proliferation, rather than by simply acting on all rapidly dividing cells, both normal and cancerous cells, as done by chemotherapy. The advantages of targeted therapies, with respect to standard chemotherapy, rely on the specificity of targeted drugs, designed to interact with their target and not to kill cells, and on the non-cytotoxicity but cytostatic property of blocking tumor cell proliferation.

The development of targeted therapies requires the identification of good targets. One approach to identify potential targets is to determine whether cancer cells produce mutant proteins that drive cancer progression. Once a candidate target has been selected, the next step is to develop a therapy that affects the target by interfering with its ability to promote cancer cell growth or survival. A targeted therapy could both reduce the activity of the target or prevent it from binding to a receptor that it normally activates.

The inhibitors inserted in the MIM act on the chains of chemical reactions in which mutations occur, in order to regulate the transcription of the oncogenes at the end of the signaling cascade. The inhibitors can affect directly the mutant protein or can act on the proteins connected to the mutant one. Let $\hat{A}P$ be the phosphorylated mutant protein, and B a protein that $\hat{A}P$ activates by phosphorylation:

$$\hat{A}P + B \rightleftarrows \hat{A}P\_B \rightarrow \hat{A}P + BP\ . \tag{9.9}$$

If I is an inhibitor, then two possible chemical reactions can be implemented.

1. The targeted molecule is the phosphorylated mutant protein $\hat{A}P$:

$$\hat{A}P + I \rightleftarrows \hat{A}P\_I\ . \tag{9.10}$$

   As a result, the inhibitor decreases the activity of the mutant protein by binding to it, and consequently reduces the amount of downstream phosphorylated proteins activated by $\hat{A}P$. Nevertheless, this approach acts directly on the mutation source, but does not prevent the occurrence of drug resistances which may emerge from mutations in downstream proteins.

2. The targeted molecule is the downstream phosphorylated protein BP:

$$BP + I \rightleftarrows BP\_I\ . \tag{9.11}$$

   The inhibitor binds to BP and prevent its interaction with other proteins.

Obviously, the choice on the type of targets depends on the available inhibitors produced by the pharmaceutical companies. The inhibitor amount to be used should be chosen as to restore the physiological concentration of the phosphorylated proteins. Since the reaction rate constant for the inhibitor-target affinity is known, and fixed, from the pharmacological production, the only way to regulate the inhibitor action is through its concentration. In the case of drug resistances, the solution may be a suitable combination of inhibitors.

Chapter 10

MIM parameterization

The Molecular Interaction Map (MIM) for the colorectal cancer (CRC), as designed in Tortolina et al., 2015, is a huge chemical reaction network (CRN) mathematically modeled by means of non-linear parameter-dependent system of ordinary differential equations (ODEs). The state variables of the system are the concentrations of the chemical species, and the parameters are the reaction rate constants. In a real experimental setting, the measurable quantities are the concentrations of specific chemical species, while the rates of the chemical reactions are unknowns. The reaction rates indicate the chemical affinities between the species and represent the real information source on how the network works. The uncertain knowledge of the reaction parameters makes the need for (i) a mathematical model relating the available data with the unknowns, and this is given by a suitable CRN, and (ii) qualitative and quantitative tools able to estimate reliably the values of the reaction rates.

The estimation of CRN parameters is a non-linear ill-posed inverse problem. In the context of computational systems biology, a lot of methods have been developed for the solution of the network parameterization problem, and several recent research articles deal with this issue. Nevertheless, most of them are simply theoretical, or apply the proposed methods on simple low-dimensional networks. The complexity of our MIM, due to its high dimensionality and its dynamical properties not conforming with well established results on equilibria and stability of CRNs, makes state-of-the-art methods not efficient in reconstructing the model parameters. In fact, the optimization problem of finding the best set of reaction parameters fitting the data on species concentrations is a non-convex problem suffering of many local minima. Moreover, the MIM network seems to suffer from a non-identifiability of the rate constants with respect to the available data. As a preliminary application, we address the problem of parameterizing a single MIM pathway, in particular the TGFβ-pathway, in a simulation setting.

The first section introduces the general problem of estimating the parameters in the computational systems biology framework, providing literature references on methods applicable for the solution of the CRN parameterization. The second section considers the application on the TGFβ-pathway: first, the direct problem is described, and then a first test for estimating the parameters of the associated network is carried out by means of a Bayesian approach.

It should be noticed that the objective of this chapter is just to provide some hints about the kind of mathematics and computational analysis that can be undertaken within this inverse problem framework for systems biology. The systematic investigation of these research paths will be the objective of a further scientific activity out of the one performed during the three years of my PhD program.

10.1 The parameterization inverse problem: generalities

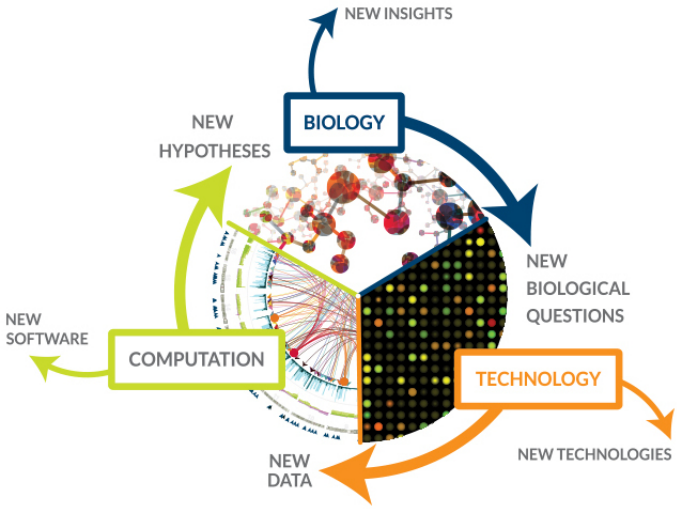

FIGURE 10.1: Computational Systems Biology: biology driving technology driving computation (from Institute for Systems Biology, Seattle, USA).

Computational systems biology is the framework in which biology, technology, and computational methods are integrated with the aim of gaining a better understating of biological phenomena (Figure 10.1). Computational systems biology has two distinct branches: knowledge discovery, or data-mining, which extracts the hidden patterns from huge quantities of experimental data forming hypotheses as a result, and simulation-based analysis, which tests hypotheses with in silico experiments providing predictions to be tested by in vitro and in vivo studies.

A central challenge in computational modeling of biological systems is the determination of the model parameters. The interaction properties and the dynamics of biological systems are described by a mathematical model, fixing the system structure and comprising ODEs with constant parameters. The knowledge of the parameter values is crucial whenever one wants to obtain quantitative, or even qualitative, information from the models. Parameter values may be inaccessible via experiments, or simply unknown. Other variables involved in the model can be assessed: the technology role in computational biology is accomplished by modern high-throughput techniques (e.g., PCR, immunoblotting assays, fluorescent markers, mass spectrometry-based quantitative proteomics) able to provide time-series quantifications of genes, proteins, or metabolites on a cellular level. However, the measurements tend to be very noisy and taken at a limited number of time points. Moreover, the information on model parameters contained in the available data is only implicit and has to be extracted by using efficient and robust computational methods. The solution of this inverse problem is a key issue in computational systems biology.

In general, two different classes of problems can be identified (Engl et al., 2009): (i) parameter estimation from experimental data sets, aiming at determining the parameter values or at least upper and lower bounds, and (ii) qualitative inverse problems, devised to explore the areas in parameter space that give rise to a given qualitative behavior, e.g., multiple steady-state solutions, oscillations, deterministic chaos, etc.

The parameter estimation problem in systems biology is generally formulated as a non-linear optimization problem that minimizes an objective function (Reali, Priami, and Marchetti, 2017; Ashyraliyev et al., 2008), representing the discrepancy between experimental data and model predictions, which are obtained from simulations using the forward model with the estimated parameters. The underlying premise is that the optimal parameter set is the one which gives rise to simulated data matching the experimental observations as well as possible. Computationally, the minimization of the objective function may involve a combination of local (gradient-based) and global (mostly stochastic) methods. Since even the order of magnitude of the parameters may be unknown, it is important to complement the rapid convergence of local optimization algorithms with the comprehensive nature of global search techniques. A general review of local, global, and hybrid methods for parameter estimation in systems biology can be found in Ashyraliyev et al., 2008.

We focus on the parameter estimation inverse problem in biochemical networks, a problem we refer to as *parameterization*. The biochemical networks are mathematically modeled by CRNs, intrinsically characterized by non-linear dynamical systems where the unknown parameters are the reaction rate constants. Parameter estimation in non-linear dynamics is extremely hard. In fact, a large class of CRNs exhibits a wide spectrum of parameter sensitivities, evenly distributed over many orders of magnitude: if a model is highly sensitive to changes in the parameter values, small experimental errors may lead to large deviations in the best fit parameters, even though large differences in experimental outcomes are not observed; if a model is insensitive to alterations in the parameter values, then the experimental outcome may not be appreciably altered by those parameters. An example of sensitivity analysis for parameter estimation in large scale biochemical reaction networks can be found in Fröhlich et al., 2017. The latter remark indicates the ill-posedness of the parameterization inverse problem. Clearly, size and complexity of the network increase the difficulty of parameter identification. When the number of unknown parameters is very large, it is often impossible to find a unique solution to this problem, and the model is non-identifiable. In this case, one finds several sets of parameters, or ranges of values, that are all equally likely to give a good fit with the experimental data. The definitions of a priori and a posteriori identifiability in the context of computational systems biology are illustrated in Ashyraliyev et al., 2008. A comparison of general approaches for testing the parameter identifiability of biological networks in systems biology can be found in Raue et al., 2014. These remarks suggest that the search for the exact individual values of the parameters could be a hopeless task in most cases (Ashyraliyev, Jaeger, and Blom, 2008).

The development of efficient strategies for determining the parameters in a reliable manner is an important mathematical problem with significant practical implications. Various deterministic and stochastic optimization methods have been used to solve the parameterization ill-posed non-linear inverse problem. Examples are linear and non-linear least-squares fitting (Mendes and Kell, 1998), simulated annealing (Kirkpatrick, Gelatt, and Vecchi, 1983), genetic algorithms (Srinivas and Patnaik, 1994), and evolutionary computation (Moles, Mendes, and Banga, 2003). Another considerable class of methods applied to biological systems makes use of the Bayesian approach, especially Monte Carlo techniques, usually in the case of lower-dimensional problems and/or availability of a relatively high number of data samples (Ballnus et al., 2017; Busetto and Buhmann, 2009; Toni et al., 2009). Maximum-likelihood estimation has also been utilized (Bortz and Nelson, 2006; Müller et al., 2004). More recently, the parameter estimation problem for computational biology has been revisited in the framework of control theory, by considering approaches

based on Luenberger-like (Hulhoven, Wouwer, and Bogaerts, 2006), Kalman filter (Lillacci and Khammash, 2010; Sun, Jin, and Xiong, 2008), and high-gain observers (Bullinger and Allgower, 1997).

A recent paper by Reali, Priami, and Marchetti, 2017, reviews the most frequently used methodologies for global optimization that have been successfully applied in computational systems biology. In particular, focusing on a problem with non-linear non-convex objective function and with multiple possible solutions, three algorithms are described: the multi-start non-linear least-squares method based on a Gauss-Newton approach, the random walk Markov Chain Monte Carlo method, and simple Genetic Algorithm. Besides a number of success, the non-linear optimization approach shows a number of limitations. First, the computational cost is very high. Second, although measurement errors can be incorporated into the observation equations, it is difficult to integrate system noise into system equations. Third, due to the high nonlinearity of the dynamics, non-linear optimization for the parameter estimation of CRNs is often multi-modal. Therefore, its solutions may not reach global optimum and often converge to a local optimum.

10.2 Application to the TGFβ-pathway

For the ease of comprehension and handling of both the system equations and the parameterization inverse problem, we consider a single pathway of the MIM developed in Tortolina et al., 2015, namely the TGFβ-pathway.

In this section, we provide the TGFβ-pathway forward model, i.e. the set of chemical components and the system of ODEs composing the associated CRN. Moreover, we analyze the TGFβ-CRN kinetics in qualitative terms, by exploiting the state-of-the-art properties of CRNs illustrated in Section 2.2. Then, we address the problem of parameterizing the TGFβ-CRN: starting from simulated data of dynamic concentrations of the chemical species, we reconstruct a subset of reaction rate constants (precisely, the reverse parameters) by means of a Monte Carlo method, known as single component Metropolis Hastings algorithm, and we show the results with respect to different noise levels on the concentration data. We remark that all the computational part has been implemented in the Matlab programming environment.

10.2.1 TGFβ-pathway direct problem

The TGFβ-pathway contains the signaling cascade downstream the TGFβ family of extracellular ligands. The entire MIM considers highly interconnected pathways, and the complete isolation of one of them is not possible. Hence, a minor part of the adjacent WNT-pathway is also taken into account.

The temporal sequence of the TGFβ-pathway chemical reactions may be described as follows. The TGFβ ligand forms a homodimer, and, simultaneously, the TGFβR-I and TGFβR-II receptors follow a homodimerization. The TGFβ homodimer binds the TGFβR-II homodimer, which in turn binds the TGFβR-I homodimer, phosphorylating it and generating a hexamer. This phosphorylated hexamer binds to the downstream signaling proteins and gives rise to a sequence of phosphorylation reactions. In this way, the extracellular signal is propagated through the pathway.

The MIM for the TGFβ-pathway is represented in Figure 10.2:

- the boxed nodes are the basic species;
- the black dots indicate the composed species;

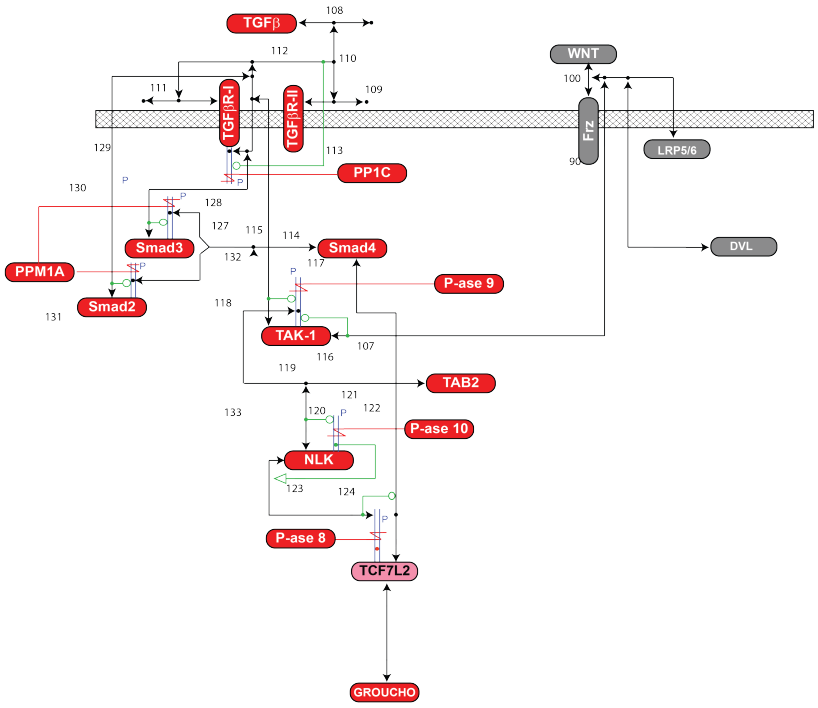

FIGURE 10.2: MIM referring to the TGFβ-pathway.

- the black arrows denote the chemical reactions;
- the green lines stand for phosphorylation;
- the blue parallel lines identify the phosphorylated species;
- the red lines connect the phosphatases and the phosphorylated species for dephosphorylations.

The TGFβ-pathway, together with a small portion of the WNT-pathway, counts for:

- 2 ligands (TGFβ and WNT);
- 50 chemical species (18 basic and 32 composed);
- 65 chemical reactions (26 reversible and 13 non-reversible), and thus 65 reaction rate constants (39 forward and 26 reverse).

The ligands are considered not consumable quantities, and therefore as species which maintain constant concentrations in time. The ligand-receptor interactions for TGFβ and WNT follow the conventions described in subsection 9.3.1: the ligand constant concentration is shifted in multiplying the forward rate constant of the ligand-receptor reaction. The non-reversible reactions appear only in the phosphorylation and dephosphorylation schemes of reactions (illustrated in subsection 9.3.1), and include seven phosphorylations and six dephosphorylations.

In mathematical terms, the CRN associated with the TGFβ-pathway is the list $(\mathcal{S}, \mathcal{C}, \mathcal{R})$, where $\mathcal{S}$ contains the $m = 50$ chemical species, $\mathcal{C}$ is the set of $n = 63$ chemical complexes used and produced in all reactions, and $\mathcal{R}$ collects the $r = 65$ chemical reactions. The ligands are not included in the CRN set of species and not counted as system state variables, since they are inserted in the CRN as known constants.

The CRN kinetics follows the law of mass action, and the network dynamics is well-modeled by a system of ODEs, quadratic in the species concentrations and linear in the reaction rate constants. Following the formalization made in Section 2.2, the TGFβ-CRN system of ODEs can be written as

$$\begin{aligned} \frac{d\boldsymbol{x}}{dt} &= \dot{\boldsymbol{x}} = \boldsymbol{S}\boldsymbol{v}(\boldsymbol{x},\boldsymbol{k}) \\ &= \boldsymbol{Z}\boldsymbol{B}\boldsymbol{v}(\boldsymbol{x},\boldsymbol{k}) \,, \end{aligned} \tag{10.1}$$

where $\boldsymbol{x} \in \mathbb{R}_+^{50}$ is the vector of species concentrations, $\boldsymbol{k} \in \mathbb{R}_+^{65}$ is the vector of reaction rate constants, $\boldsymbol{v}(\boldsymbol{x},\boldsymbol{k}) \in \mathbb{R}_+^{65}$ is the vector of reaction fluxes, $\boldsymbol{S}$ is the 50×65 stoichiometric matrix with elements in $\mathbb{Z}$, $\boldsymbol{Z}$ is the 50×63 complex stoichiometric matrix with elements in $\mathbb{N}$, and $\boldsymbol{B}$ is the 63×65 incidence matrix with elements in $\{-1, 0, 1\}$. Note that the forward rates are associated with the quadratic part of the system and the non-reversible linear part, while the reverse rates settle the reversible linear part.

The initial conditions of system (10.1) are $\boldsymbol{x}(0) \in \mathbb{R}_+^{*50}$ s.t.

$$\boldsymbol{x}(0) = (x_1(0), \ldots, x_m(0))^T \,, \quad \text{with } x_i(0) = \begin{cases} x_{i0} \neq 0 & \text{if } i \text{ basic species} \\ 0 & \text{if } i \text{ composed species} \end{cases} , \tag{10.2}$$

meaning that only basic species have non-zero initial conditions. The total concentrations of the unbounded basic species are needed in order to run the scheme of chemical reactions, and, in some sense, represent the inputs of the system. As time goes by, the species chemical interactions get activated and the initial molecules of basic species are redistributed between the corresponding composed-forms.

The system (10.1) is characterized by *conserved cycles*, defined as vanishing linear combinations of specific differential equations and indicating conserved quantities. The number of conserved cycles coincides with that of the basic species. Indeed, basic species are primary variables initializing the system: at time $t = 0$, the total amount of active substance is retained by the basic species, and at each time point this quantity gets conserved.

The structure of the system of ODEs (10.1) is described by the matrices $\boldsymbol{S}$, $\boldsymbol{Z}$, and $\boldsymbol{B}$. For the TGFβ-CRN system, the linear algebra properties of these matrices are the following:

- $\text{rank}(\boldsymbol{S}) = \min\{m, n\} - \theta = 50 - 18 = 32$, where $m = 50$ the number of species, $n = 65$ the number of reactions, and θ the number of conserved cycles;
- $\text{rank}(\boldsymbol{Z}) = 50$, and hence $\boldsymbol{Z}$ is a full rank matrix;
- $\text{rank}(\boldsymbol{B}) = 39$, i.e. the rank of the incidence matrix equals the number of forward reactions.

The deficiency δ of the TGFβ-CRN can be computed as

$$\delta = \text{rank}(\boldsymbol{B}) - \text{rank}(\boldsymbol{S}) = 7 \,.$$

Therefore, the network is not zero-deficient, and all the results on equilibria and stability stated in subsection 2.2.2 cannot be applied. In other words, the deficiency zero theorem, ensuring at most one asymptotically stable positive steady state for a CRN with deficiency zero, does not hold. For networks with deficiency non-zero, there exists the possibility of multiple positive steady states and also oscillations.

The direct problem of the network consists in determining the time-dependent concentrations of the species for given sets of initial conditions and rate constants. Analytical solutions to non-linear ODEs, as system (10.1), are rarely possible to obtain, and numerical formulas are used. Moreover, the numerical solutions of CRN systems exhibit stiffness, that is, the dynamic step-size adjustments of the explicit Runge-Kutta solver needs to be made smaller in order to achieve stability. Within the software package Matlab, ode15s is a variable-step, variable-order solver based on the numerical differentiation formulas of orders 1 to 5, able to solve stiff differential equations. To give an idea of the type of dynamics retained by the TGFβ-CRN system, Figure 10.3 shows the time-dependent curves of the species concentrations, for given sets of initial conditions and rate constants (the values are chosen as in Tortolina et al., 2015), obtained with the ode15s solver applied to system (10.1).

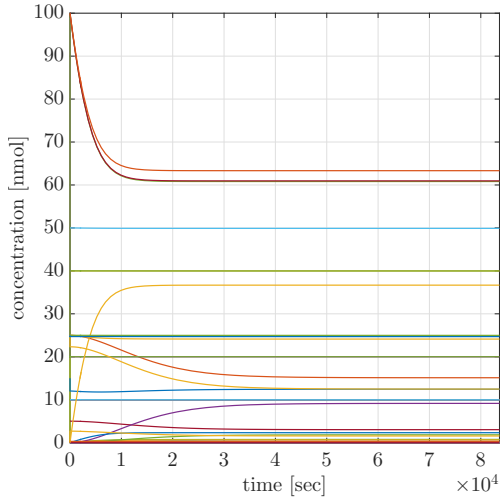

FIGURE 10.3: Time-dependent curves of the species concentrations of the TGFβ-CRN.

In general, by performing different simulations with varying initial values, we have observed that within the dynamics of the MIM-type CRN it is possible to identify a time point $\bar{t} \in (0, t)$ s.t.

- in $[0, \bar{t})$ the concentration curves are in a transitional phase;
- in $[\bar{t}, t)$ the totality of concentration curves are almost constant, i.e. the system equilibrium has been reached.

The time interval $[0, \bar{t})$ in which the concentration curves are still varying, provides information on the speeds of the chemical reactions; the equilibrium interval $[\bar{t}, t)$ fixes the equilibrium constants of the chemical reactions, as ratios of the forward-reverse speeds. In other words, by solving the direct problem, the values of the rate constants, i.e. the speeds, decide the time $\bar{t}$ needed to reach the system equilibrium. Conversely, by formally writing the system (10.1) at equilibrium, $\dot{\boldsymbol{x}} = \boldsymbol{S}\boldsymbol{v} = 0$, it is found that the ratios between linear combinations of rate constants are explicitly determined by the species concentrations corresponding to equilibrium. This fact implies that the equilibrium condition selects a family of rate constants for a given equilibrium point, and all the parameter values satisfying the equilibrium equations return the same equilibrium point (under the same initial conditions). Clearly, the equilibrium of the system does not allow to discriminate the values of each single rate constant.

Appendix D reports all the chemical species, chemical complexes, chemical reactions of the TGFβ-pathway, the system of ODEs of the associated CRN, the expression of the conserved cycles, and the system at equilibrium.

10.2.2 TGFβ-pathway parameterization

The parameterization problem for the TGFβ-pathway is here presented as an optimization problem in which:

- the available data are the time-dependent concentrations of all chemical species of the network $\mathscr{X}(t)$ (nmol), given at predefined time points,

$$\mathscr{X}(t) = (x_1(t), \dots, x_{50}(t))^T \in \mathbb{R}_+^{50}\,, \quad \text{for } t = t_1, \dots, t_T \in \mathbb{R}_+\,;$$

- the unknowns are the reverse reaction rate constants $\boldsymbol{k}_r$ (sec^{-1}),

$$\boldsymbol{k} = (\boldsymbol{k}_f, \boldsymbol{k}_r) \in \mathbb{R}_+^{65}\,, \quad \text{with } \boldsymbol{k}_f \in \mathbb{R}_+^{39}\,, \boldsymbol{k}_r \in \mathbb{R}_+^{26}\,.$$

In some sense, we are characterizing the algebraic structure of the ODEs: the kinetics of the quadratic part of the system, defined by the forward reaction rates $\boldsymbol{k}_f$, is regarded as known and fixed; the kinetics of the linear part of the system, defined by the reverse reaction rates $\boldsymbol{k}_r$, needs to be determined. The set of forward rates includes also the rate constants of the non-reversible reactions, called turnover numbers (i.e. number of substrate molecules converted into a product molecule), which in the MIM case are associated with the phosphorylation/dephosphorylation schemes of reactions and hence with the non-reversible linear part of the system. Then, the forward rates have two distinct units of measure, since the quadratic forward rates are quantified as nmol^{-1} sec^{-1}, and the linear forward rates as sec^{-1}.

We make some remarks before proceeding. Concerning the data, the CRN is considered in a physiological condition, which means that no mutations are taken into account. The idea is to perform a test for parameterizing a healthy network. Nevertheless, in a real experimental framework, measurements over chemical species concentrations are available only for cancer cell lines with specific mutation profiles, and for a limited number of species (usually, non-bounded forms and phosphorylated proteins). Concerning the unknowns, the set of reaction rates is reduced to only the reverse, but this is not an unrealistic hypothesis. Chemically speaking, the value of a forward rate constant is highly stable with respect to the cell signaling, because it represents the probability of encounter of the reactant molecules of a chemical reaction, and these molecules follow a Brownian motion in a viscous continuum fluid (the intracellular matrix is a gel), as stated by the collision theory. Therefore, given the types of molecules involved in a chemical reaction, their probability of association can be regarded as a known variable, and the forward rate is a diffusion rate. Considering the very crowded cellular environment, the very large size of many multi-protein complexes, the fact that only a fraction of protein-protein encounters will be productive, reasonable default values could be a median second-order forward rate constant in the order of 10^{-1}-10^{-3} nmol^{-1} sec^{-1}, and a median first-order forward rate constant in the order of 10^{-1}-10^{0} sec^{-1} (see Castagnino et al., 2010). On the other hand, assessing the value of a reverse rate constant is more difficult. Once the reactants of a chemical reaction collide to form the product, the disruption of their binding follows the Maxwell-Boltzmann distribution, for which the speed of unbinding depends on the level of energy required to separate the bounded molecules. Variations on the speed values can be very large, according

to the strength of binding of the reactants. For example, a strong bound between reactant molecules requires a high energy to be broken and the related speed will be low. The reverse rate is the speed of binding disruption and contains the effective information on the affinity of the chemical species.

The parameterization problem is formulated in the form of least-squares:

$$\min_{\boldsymbol{k}_r} \mathcal{F}(\boldsymbol{k}_r) = \min_{\boldsymbol{k}_r} ||\mathscr{X}(t) - \boldsymbol{x}(t; \boldsymbol{x}_0, \boldsymbol{k}_f, \boldsymbol{k}_r)||_2^2 \,. \tag{10.3}$$

We search for the valued vector $\boldsymbol{k}_r \in \mathbb{R}_+^{26}$ that minimizes the residual objective function $\mathcal{F}(\boldsymbol{k}_r)$, expressing the discrepancy between the dynamic data of species concentrations $\mathscr{X}(t)$ and the forward model predictions $\boldsymbol{x}(t; \boldsymbol{x}_0, \boldsymbol{k}_f, \boldsymbol{k}_r)$, as solutions of the system of ODEs (10.1) depending on the initial conditions $\boldsymbol{x}_0 = \boldsymbol{x}(0) \in \mathbb{R}_+^{*50}$ and the rate constants $(\boldsymbol{k}_f, \boldsymbol{k}_r) \in \mathbb{R}_+^{39} \times \mathbb{R}_+^{26}$. The inverse problem of equation (10.3) is clearly non-linear, since the functional $\mathcal{F}(\boldsymbol{k}_r)$ depends nonlinearly on the unknowns $\boldsymbol{k}_r$. The optimization process to estimate the optimal parameters may be subject to constraints, concerning the values that each parameter can assume, or functional relations among the parameters. In our case, the reverse rate constants cannot be negative.

For the solution of (10.3), we make use of a random walk Markov Chain Monte Carlo (MCMC) method (Brooks et al., 2011), called single component Metropolis Hastings (SCMH) algorithm, first formulated by Metropolis et al., 1953 and then resumed by Hastings, 1970. For a detailed description of stochastic processes, Markov Chains, and Monte Carlo methods refer to Gilks, Richardson, and Spiegelhalter, 1995 and Kaipio and Somersalo, 2006.

In general, Metropolis-Hastings algorithms update all components of the chain of values for unknown parameters at the same time, based on an acceptance/rejection rule, while in the SCMH algorithm the chain is updated component by component (i.e. parameter by parameter). The one-dimensional proposal distributions (one for each parameter) are Gaussian distributions with the present point as the center point and with a variance that has to be decided. Indeed, one crucial issue in Bayesian approaches is how to choose the variance of the proposal distribution: if the selected value is too small then the chain will move too slowly, and virtually all proposed moves will be accepted; if the value is too large then most moves will be rejected, and the chain will usually not move at all. What is needed is a value of the variance between the two extremes, allowing for reasonable-sized proposal moves together with a reasonably acceptance probability. Optimal values for the variance have been analyzed by Gelman, Roberts, and Gilks, 1996 and Roberts and Rosenthal, 2001, following the idea of searching for the optimal acceptance rate (Roberts, Gelman, and Gilks, 1997).

Here we present the SCMH algorithm with a Gaussian proposal distribution for the solution of the CRN parameterization problem (10.3).

Algorithm 10.1. [SCMH]

Step 1. *Initialization.*

- Randomly select a starting point $\boldsymbol{k}_r^{(0)} \in \mathbb{R}_+$.
- Choose the variance σ^2 of the Gaussian distribution.
- Fix the length N of the chain of parameter realizations.

Step 2. *Direct problem.*

- Set $\boldsymbol{k}^{\text{old}} = \boldsymbol{k}_r^{(0)}$.
- Compute the forward model $\boldsymbol{x}^{\text{old}}(t) = \boldsymbol{x}(t; \boldsymbol{x}_0, \boldsymbol{k}_f, \boldsymbol{k}^{\text{old}})$.
- Set the iteration number $i = 1$.

Step 3. *Single component Metropolis step.*
For $j = 1, \ldots, p$, with p the number of parameters.

- Sample a new candidate $\boldsymbol{k}_j^{\text{new}}$ from the normal distribution $N(\boldsymbol{k}_j^{\text{old}}, \sigma^2)$.
- Pick a random number u from the uniform distribution $U([0,1])$.
- Set $\boldsymbol{k}^{\text{new}}$ s.t
$$\boldsymbol{k}_l^{\text{new}} = \begin{cases} \boldsymbol{k}_l^{\text{old}} & \text{if } \; l \neq j \\ \boldsymbol{k}_l^{\text{new}} & \text{if } \; l = j \end{cases} .$$
- Compute the forward model $\boldsymbol{x}^{\text{new}}(t) = \boldsymbol{x}(t; \boldsymbol{x}_0, \boldsymbol{k}_f, \boldsymbol{k}^{\text{new}})$.
- Evaluate the residuals of the old and new realizations, and the ratio between their likelihoods:
$$\begin{aligned} S^{\text{old}} &= \mathcal{F}(\boldsymbol{k}^{\text{old}}) = ||\mathscr{X}(t) - \boldsymbol{x}^{\text{old}}(t)||_2^2 \\ S^{\text{new}} &= \mathcal{F}(\boldsymbol{k}^{\text{new}}) = ||\mathscr{X}(t) - \boldsymbol{x}^{\text{new}}(t)||_2^2 \\ S &= \exp\left(- \frac{(S^{\text{new}} - S^{\text{old}})}{2\sigma^2} \right) . \end{aligned}$$
- Acceptance/rejection rule:
$$\begin{cases} \text{if } \; S^{\text{new}} < S^{\text{old}} \; \text{ or } \; u < S \text{ , then keep } \boldsymbol{k}_j^{\text{new}} \\ \text{otherwise set } \; \boldsymbol{k}_j^{\text{new}} = \boldsymbol{k}_j^{\text{old}} \end{cases} .$$
- Iterate $j = j + 1$.

Step 4. *Update.*

- Store the new realization $\text{chain}(i) = \boldsymbol{k}^{\text{new}}$.
- If $i < N$ then iterate $i = i + 1$ and go to Step 3, otherwise stop.

In general terms, this optimization strategy begins by selecting a random set of parameters (Step 1.), and then evaluating the related model-predicted data (Step 2.). Component by component (Step 3.), this initial (old) set of parameters is updated to a new a set of parameters. Each new candidate is obtained by perturbing the old one through random normally distributed coefficients. When the new set of parameters is generated, its forward model is evaluated. Then, both residuals for the old and new set of parameters are computed. If the new residual is smaller then the previous, the new set of parameters is always accepted. If not, the ratio between the likelihoods of the old and new realizations is compared with a uniformly distributed random number: if the random number is smaller than the ratio of the likelihoods then the new set of parameters is accepted. The latter rule allows the method to randomly accept values that are not better in terms of residual and to escape local minima. In the long run, the method will return back to the previous value if it was the global solution, otherwise it continues the exploration of the space of parameters.

The accepted parameters are stored at each iteration in the chain of realizations (Step 4.), representing the posterior distributions of parameter estimates. The convergence of SCMH is slow, since it is not guaranteed that the optimization process escapes quickly from local solutions. Consequently, the method is stopped after a predefined number of iterations.

In our implementation of the SCMH algorithm, we set the subsequent options.

- The initial random guesses of parameter values are selected within a predefined range of orders of magnitude.
- The variance of the Gaussian distribution is chosen as the optimal value $\sigma^2 = (2.38)^2$, as proposed by Gelman, Roberts, and Gilks, 1996 for an optimal acceptance rate of 0.234.
- The maximum number of iterations is fixed at $N = 10^3$.
- The single component Metropolis steps are not performed with a prescribed order, but are carried out with random directions obtained by permuting the indexed vector $(1, \dots, p)$.

The test on the parameterization of the TGFβ-pathway follows the scheme below.

1. Select ground truth values for the reverse rate constants $\boldsymbol{k}_r \in \mathbb{R}_+^{26}$.
2. Given the known values of the forward rate constants $\boldsymbol{k}_f \in \mathbb{R}_+^{39}$, and the initial conditions $\boldsymbol{x}_0 = \boldsymbol{x}(0) \in \mathbb{R}_+^{*50}$ for the species concentrations, numerically solve the system of ODEs (10.1) by means of the Matlab solver `ode15s`, and get the continuous dynamic data $\mathscr{X}(t) \in \mathbb{R}_+^{50}$.
3. Select discrete time points $t_1, \dots, t_T \in \mathbb{R}_+$, in particular $T = 11$ points chosen as $t_1 = 5$, $t_2 = 10$, $t_3 = 20$, $t_4 = 30$, $t_5 = 60$, $t_6 = 90$, $t_7 = 120$, $t_8 = 180$, $t_9 = 240$, $t_{10} = 360$, $t_{11} = 480$ minutes, and collect the related concentration data $\mathscr{X} = (\mathscr{X}(t_1), \dots, \mathscr{X}(t_T))$, s.t. $\mathscr{X}(t_i) \in \mathbb{R}_+^{50}\ \forall i = 1, \dots, T$.
4. Add white Gaussian noise to the discrete data, by means of the Matlab function `awgn` with a specific signal-to-noise ratio, to obtain the noisy data.
5. Solve the parameterization inverse problem (10.3) by means of the SCMH optimization procedure (Algorithm 10.1)
6. The optimal set of reverse parameters returned by the SCMH algorithm is the best in terms of residual.

We perform different simulations, based on the level of noise on the discrete data; in particular, we consider Gaussian noise with a signal-to-noise ratio from 90 dB to 50 dB. The results are reported in Table 10.1, where means and standard deviations for each parameter are computed over different reconstructions obtained by varying the starting point of the SCMH algorithm. We recall that the list of reaction rate constants for the TGFβ-CRN is reported in Table D.3 of Appendix D. In general, increasing the noise level on the concentration data obviously returns worst estimates and higher standard deviations. However, a subset of parameters does not follow this trend, and are equally well reconstructed regardless of the noise. On the contrary, other parameters widely suffer the perturbations on the data. This distinct attitude indicates the multiple parameter sensitivities of the TGFβ-CRN.

	g.t.	90 dB	80 dB	70 dB	60 dB	50 dB
k_{1r}	0.010	0.019 ± 0.029	0.017 ± 0.021	0.032 ± 0.011	0.026 ± 0.017	0.026 ± 0.023
k_{2r}	0.030	0.055 ± 0.010	0.054 ± 0.030	0.040 ± 0.016	0.049 ± 0.018	0.064 ± 0.031
k_{3r}	0.010	0.032 ± 0.012	0.033 ± 0.006	0.019 ± 0.019	0.021 ± 0.024	0.027 ± 0.038
k_{5r}	0.100	0.152 ± 0.196	0.063 ± 0.076	0.109 ± 0.127	0.068 ± 0.059	0.114 ± 0.122
k_{6r}	0.100	0.100 ± 0.000	0.101 ± 0.002	0.099 ± 0.001	0.100 ± 0.000	0.099 ± 0.001
k_{7r}	0.100	0.100 ± 0.000	0.100 ± 0.000	0.100 ± 0.000	0.100 ± 0.000	0.100 ± 0.001
k_{9r}	0.100	0.425 ± 0.353	0.353 ± 0.254	0.269 ± 0.192	0.203 ± 0.092	0.314 ± 0.289
k_{11r}	0.100	0.656 ± 0.412	0.676 ± 0.265	0.574 ± 0.402	0.689 ± 0.177	0.607 ± 0.498
k_{13r}	1.000	1.746 ± 0.828	3.407 ± 2.339	3.963 ± 2.029	5.327 ± 4.335	7.861 ± 2.204
k_{15r}	1.000	1.951 ± 0.689	2.508 ± 1.852	1.406 ± 0.965	3.889 ± 1.270	3.915 ± 2.219
k_{17r}	1.000	1.398 ± 0.845	1.257 ± 0.142	1.431 ± 0.927	1.314 ± 0.663	1.637 ± 0.559
k_{19r}	1.000	1.117 ± 0.305	0.851 ± 0.080	1.256 ± 0.450	3.080 ± 4.644	4.393 ± 3.653
k_{21r}	0.010	0.010 ± 0.000	0.010 ± 0.000	0.009 ± 0.009	0.009 ± 0.001	0.009 ± 0.002
k_{22r}	0.010	0.009 ± 0.002	0.007 ± 0.005	0.006 ± 0.004	0.008 ± 0.003	0.012 ± 0.013
k_{23r}	10.00	13.12 ± 12.55	22.01 ± 8.067	17.45 ± 4.144	24.79 ± 4.535	24.94 ± 1.754
k_{25r}	10.00	13.01 ± 13.99	21.59 ± 7.339	14.82 ± 10.96	23.83 ± 7.628	15.76 ± 12.38
k_{27r}	0.100	0.095 ± 0.117	0.144 ± 0.109	0.043 ± 0.024	0.063 ± 0.038	0.062 ± 0.047
k_{28r}	1.000	1.946 ± 1.574	7.239 ± 2.548	2.870 ± 4.214	2.668 ± 1.740	4.146 ± 0.899
k_{30r}	0.040	0.040 ± 0.000	0.039 ± 0.000	0.041 ± 0.001	0.043 ± 0.009	0.040 ± 0.008
k_{31r}	0.040	0.039 ± 0.000	0.040 ± 0.000	0.039 ± 0.001	0.038 ± 0.007	0.041 ± 0.009
k_{32r}	0.040	0.040 ± 0.000	0.040 ± 0.000	0.040 ± 0.000	0.040 ± 0.001	0.039 ± 0.002
k_{33r}	10.00	14.92 ± 8.209	11.51 ± 2.206	13.63 ± 8.159	12.19 ± 5.609	16.41 ± 5.189
k_{35r}	10.00	18.39 ± 9.047	10.14 ± 3.677	11.24 ± 4.336	17.75 ± 4.973	14.19 ± 7.925
k_{36r}	10.00	10.69 ± 8.892	10.52 ± 4.103	7.286 ± 4.421	15.39 ± 11.76	18.67 ± 15.05
k_{38r}	10.00	13.59 ± 4.842	14.80 ± 3.873	15.54 ± 7.356	10.04 ± 1.769	13.03 ± 1.285
k_{39r}	1.000	0.985 ± 0.018	0.959 ± 0.060	0.971 ± 0.011	0.989 ± 0.014	0.969 ± 0.021

TABLE 10.1: Ground truth (g.t.) and reconstructed reverse rate constants (sec^{-1}) of the TGFβ-CRN from noisy dynamic data of species concentrations, affected by Gaussian noise with a signal-to-noise ratio from 90 dB to 50 dB, by means of the SCMH algorithm. Means and standard deviations are computed over different SCMH runs with varying starting point.

Open issues

This final chapter aims to briefly outline the many open issues raised by the data-driven multi-scale inverse problems for Systems Medicine discussed in this Thesis.

The tissue-scale reference tissue model (RTM) is a powerful tool in the analysis of [^{18}F]-fluorodeoxyglucose (FDG) Positron Emission Tomography (PET) data. Comparison of tracer uptake between the reference tissue (RT) and the target tissue (TT) avoids explicit determination of the time concentration curve of arterial blood, working as input function (IF) for the compartmental system. In addition, correlation of tracer kinetics in two nearby tissues is capable of reducing distortions in the interpretation of FDG uptake, influenced by physiological or pharmacological conditions and uptake by different organs. In this Thesis, the RTM based on a one-compartment RT and a two-compartment TT, with given non-vanishing blood volume fractions, was considered. The developed method for the reduction of the RTM led to a unique, stable, and robust determination of the kinetic parameters. Further developments can extend the RTM to pixel-wise applications, which means that dependence of the rate constants on PET image positions can be explicitly accounted. Moreover, in view of availability of human PET data, the RTM approach can be used when the RT and TT signals are evaluated only on asymptotic values.

Tissue-scale parametric imaging methods improve the quality of information achievable from PET images, since they are capable of showing the tracer metabolism at local level, i.e. pixel-wise. Starting from the design of compartmental models suitable to describe the tracer kinetics in a predefined physiological system, parametric imaging techniques process dynamic PET images and estimate the spatial distribution of the kinetic parameters identified by the model. This Thesis implemented a parametric imaging tool integrating pre-processing methods, for noise reduction and image segmentation, and optimization of non-linear inverse problems for the reduction of multi-compartment models. The resulted imaging procedure realized an automatic pipeline, whose main advantages are in (i) its notable degree of generality, since in principle it may be applied to models made of several compartments, (ii) providing maps of all model parameters, (iii) reconstructing a large set of kinetic parameters, and (iv) accounting for different models in non-overlapping regions of the same image. Further developments of the proposed parametric imaging method are concerned with several issues. From the numerical viewpoint, the computational burden can be reduced by means of ad hoc designed implementations that will allow a technological platform able to deal not only with dynamic 2D images but also with full dynamic 3D data, in a context closer to the clinical application. From the modeling viewpoint, this approach can be extended to the direct parametric imaging problem, whereby the input data are the PET count sinograms and not the reconstructed PET images. Finally, from the clinical viewpoint, the imaging procedure can be adopted for applications to a notable quantity of data, coming from animal and human measurements.

For the analysis of FDG and glucose uptake by cultured cancer cells from LigandTracer (LT) data, this Thesis proposed a cell-scale biochemically-driven compartmental model (BCM). The BCM originated from an effort of reproducing basic features of FDG kinetics in a single cell, and emphasized the role of the endoplasmic reticulum (ER), where dephosphorylation of tracer occurs, which was not considered in previous models. To this aim, an additional compartment for phosphorylated tracer in ER was introduced in the model, besides the two standard compartments for free and phosphorylated tracer in cytosol. The BCM was adopted for the reduction of LT data, under varying FDG and glucose concentrations in the liquid medium where cancer cells were seeded. As a result, the predictions of the BCM revealed an accumulation of FDG in phosphorylated form in the ER compartment, and a relatively small amount of phosphorylated tracer outside the ER. As to cell biology, an immediate next application of the BCM is obtained when the composition of the medium is changed through the injection of pharmacological molecules in order to examine effects induced on FDG (and perhaps glucose) consumption. As to diverse employment of the BCM, tissue PET data can be considered. The BCM may be modified to handle specific complex physiologies, and may be inserted in tissue-scale approaches, such as reference tissue formulations and parametric imaging analysis. Although endowed with new realistic features, the BCM has to be regarded as a simplification with respect to the effective biochemical path followed by FDG inside cells, and further refinements are still possible. Nevertheless, as to the mathematical formulation, the BCM may represent the starting point for the development of a finer and more detailed model able to depict faithfully the FDG and glucose destiny in cancer cells.

Within the filed of Molecular Systems Biology, this Thesis presented a molecule-scale Molecular Interaction Map (MIM) for the signaling network of a colorectal cancer cell. As a first application, the parameterization a limited portion of the MIM chemical reaction network (CRN), for the estimation of the reaction rates from protein concentration data, was discussed. The potentiality of the MIM are considerable. The CRN given by the MIM is actually huge, but can be widened to include more signaling pathways and to represent the interaction mechanisms of a generic cell. Indeed, the MIM can embody a virtual cell, by which specific conditions are realized: a cancer state of the cell can be generated through the imposition of peculiar genetic mutations, and the effects of therapies can be evaluated through the addition of inhibitor targeted drugs. In this scenario, the MIM constitutes a concrete effort towards personalized medicine. From the mathematical viewpoint, there is still a lot to do. In order to estimate reliably the reaction rate constants, in a unique and stable way, from partial data on different cancer cell lines, even affected by a large amount of noise, robust computational methods need to be developed. Besides, from a technological viewpoint, a pipeline for the simulation of the pharmacological action is required: given an individual cancer profile, provided by its set of mutations, automatically determine the set of inhibitor drugs, in combined forms, and their concentrations, to re-establish the optimal physiological condition. The MIM open the way for a new research direction, both for clinical medicine, biology, and applied mathematics.

Appendix A

Proof of identifiability of RTM

We formally prove Theorem 4.1.1 for the identifiability of the reference tissue model (RTM). Identifiability of the RTM corresponds to uniqueness of the vector of rate constants $\boldsymbol{k}_{RTM} = (k_{Rb}, k_{fb}, k_{bf}, k_{mf}, k_{fm})^T \in \mathbb{R}^5_+$, given the data of tracer concentration $\mathscr{C}_T$ in the target tissue (TT) and $\mathscr{C}_R$ in the reference tissue (RT), and the related blood volume fractions V_{bT} and V_{bR}. The blood input function (IF) C_b is introduced in order to connect the RT and the TT.

We recall the model equations needed for the subsequent analysis:

$$\begin{gathered} \dot{\boldsymbol{C}} = \boldsymbol{M}\boldsymbol{C} + k_{fb}\boldsymbol{e}_1 C_b\,, \quad \boldsymbol{C}(0) = 0 \\ \boldsymbol{C} = \begin{pmatrix} C_f \\ C_m \end{pmatrix}, \quad \boldsymbol{M} = \begin{pmatrix} -(k_{bf} + k_{mf}) & k_{fm} \\ k_{mf} & -k_{fm} \end{pmatrix}, \quad \boldsymbol{e}_1 = \begin{pmatrix} 1 \\ 0 \end{pmatrix}; \end{gathered} \tag{A.1}$$

$$\dot{C}_b = -\gamma k_{Rb} C_b + \frac{1}{V_{bR}}(\dot{\mathscr{C}}_R + \lambda k_{Rb}\mathscr{C}_R)\,, \quad \gamma = (V_{bR}^{-1} - 1) + \lambda\,; \tag{A.2}$$

$$\mathscr{C}_T(t; \mathscr{C}_R, \boldsymbol{k}_{RTM}) = \boldsymbol{\alpha}^T \boldsymbol{C}(t; \mathscr{C}_R, \boldsymbol{k}_{RTM}) + V_{bT} C_b(t; \mathscr{C}_R, k_{Rb})\,, \quad \boldsymbol{\alpha} = \begin{pmatrix} 1 - V_{bT} \\ 1 - V_{bT} \end{pmatrix}. \tag{A.3}$$

The parameter λ is known from the asymptotic Logan plot approach on the RT.

The discussion on uniqueness is based on the differential form (A.1) and the equation connecting the model to the data (A.3). We consider the Laplace transform of (A.1) and (A.3) in order to reduce our identifiability problem to the identification of the coefficients of a rational fraction.

Denote by $\mathcal{L}(f)$ the Laplace transform of the function f. Under suitable assumptions of regularity, the Laplace transform of system (A.1) takes the form

$$(s\boldsymbol{I}_2 - \boldsymbol{M})\mathcal{L}(\boldsymbol{C}) = k_{fb}\boldsymbol{e}_1 \mathcal{L}(C_b)\,, \tag{A.4}$$

where

$$\mathcal{L}(C_b) = \frac{1}{V_{bR}} \frac{s + \lambda k_{Rb}}{s + \gamma k_{Rb}} \mathcal{L}(\mathscr{C}_R) \tag{A.5}$$

thanks to (A.2), and where $\boldsymbol{I}_2 \in M_2(\{0,1\})$ is the 2×2 identity matrix. Left multiplication by the inverse of $(s\boldsymbol{I}_2 - \boldsymbol{M})$ provides $\mathcal{L}(\boldsymbol{C})$. Replacing $\mathcal{L}(\boldsymbol{C})$ and $\mathcal{L}(C_b)$ into the Laplace transform of (A.3), which relates the measured data to the solution $\boldsymbol{C}$, gives

$$\mathcal{L}(\mathscr{C}_T) = \frac{V_{bT}}{V_{bR}} \left(\frac{k_{fb}}{V_{bT}} \boldsymbol{\alpha} (s\boldsymbol{I}_2 - \boldsymbol{M})^{-1} \boldsymbol{e}_1 + 1 \right) \frac{s + \lambda k_{Rb}}{s + \gamma k_{Rb}} \mathcal{L}(\mathscr{C}_R)\,. \tag{A.6}$$

After substitution of the definitions of $\boldsymbol{\alpha}$, $\boldsymbol{e}_1$, and $\boldsymbol{M}$, equation (A.6) may be expressed in the equivalent form

$$\frac{V_{bR}}{V_{bT}} \frac{\mathcal{L}(\mathscr{C}_T)}{\mathcal{L}(\mathscr{C}_R)} = \frac{Q(s; \boldsymbol{k}_{RTM})}{D(s; \boldsymbol{k}_{RTM})}, \tag{A.7}$$

where $D(s;\boldsymbol{k}_{RTM})$ and $Q(s;\boldsymbol{k}_{RTM})$ are polynomials in s, parameterized by the components of $\boldsymbol{k}_{RTM}$, defined as

$$\begin{aligned} Q(s;\boldsymbol{k}_{RTM}) &= s^3 + (\bar{k}_{fb} + \lambda k_{Rb} + k_{bf} + k_{mf} + k_{fm})s^2 \\ &+ (\lambda k_{Rb}(\bar{k}_{fb} + k_{bf} + k_{mf} + k_{fm}) + \bar{k}_{fb}(k_{mf} + k_{fm}) + k_{bf}k_{fm})s \\ &+ \lambda k_{Rb}(\bar{k}_{fb}(k_{mf} + k_{fm}) + k_{bf}k_{fm}) \,, \end{aligned} \tag{A.8}$$

and

$$\begin{aligned} D(s;\boldsymbol{k}_{RTM}) &= s^3 + (\bar{k}_{Rb} + \lambda k_{Rb} + k_{bf} + k_{mf} + k_{fm})s^2 \\ &+ ((\bar{k}_{Rb} + \lambda k_{Rb})(k_{bf} + k_{mf} + k_{fm}) + k_{bf}k_{fm})s \\ &+ (\bar{k}_{Rb} + \lambda k_{Rb})k_{bf}k_{fm} \,, \end{aligned} \tag{A.9}$$

where D is also the characteristic polynomial of $\boldsymbol{M}$, and

$$\bar{k}_{fb} = (V_{bT}^{-1} - 1)k_{fb} \,, \quad \bar{k}_{Rb} = (V_{bR}^{-1} - 1)k_{Rb} \,. \tag{A.10}$$

We recall that λ is a fixed, known parameter and we also note explicitly that the left-hand side of (A.7) is only dependent on measurable given data.

Suppose $\boldsymbol{h}_{RTM} = (h_{Rb}, h_{fb}, h_{bf}, h_{mf}, h_{fm})^T \in \mathbb{R}^5_+$ is an alternative choice of RTM rate coefficients consistent with the data of the problem. This means that an equation of the form (A.7) is necessarily satisfied, which implies that

$$\frac{V_{bR}}{V_{bT}} \frac{\mathcal{L}(\mathscr{C}_T)}{\mathcal{L}(\mathscr{C}_R)} = \frac{Q(s;\boldsymbol{k}_{RTM})}{D(s;\boldsymbol{k}_{RTM})} = \frac{Q(s;\boldsymbol{h}_{RTM})}{D(s;\boldsymbol{h}_{RTM})}. \tag{A.11}$$

The discussion of uniqueness for the RTM is based on (A.11); specifically, it is shown that (A.11) does imply $\boldsymbol{h}_{RTM} = \boldsymbol{k}_{RTM}$.

Assume that the rational fraction (A.11) is irreducible, i.e. the polynomials D and Q are coprime; therefore, the rational fraction Q/D is irreducible. Next we observe that $D(s;\boldsymbol{k}_{RTM})$ and $D(s;\boldsymbol{h}_{RTM})$ have the same leading coefficient, and the same condition holds for the polynomials $Q(s;\boldsymbol{k}_{RTM})$ and $Q(s;\boldsymbol{h}_{RTM})$. This implies that equation (A.11) is verified if and only if

$$D(s;\boldsymbol{h}_{RTM}) = D(s;\boldsymbol{k}_{RTM}) \,, \quad Q(s;\boldsymbol{h}_{RTM}) = Q(s;\boldsymbol{k}_{RTM}) \,, \tag{A.12}$$

and equations (A.12) are equivalent to the following system:

$$\bar{h}_{Rb} + \lambda h_{Rb} + \phi_h = \bar{k}_{Rb} + \lambda k_{Rb} + \phi_k \tag{A.13a}$$
$$(\bar{h}_{Rb} + \lambda h_{Rb})\phi_h + h_{bf}h_{fm} = (\bar{k}_{Rb} + \lambda k_{Rb})\phi_k + k_{bf}k_{fm} \tag{A.13b}$$
$$(\bar{h}_{Rb} + \lambda h_{Rb})h_{bf}h_{fm} = (\bar{k}_{Rb} + \lambda k_{Rb})k_{bf}k_{fm} \tag{A.13c}$$
$$\bar{h}_{fb} + \lambda h_{Rb} + \phi_h = \bar{k}_{fb} + \lambda k_{Rb} + \phi_k \tag{A.13d}$$
$$\lambda h_{Rb}(\bar{h}_{fb} + \phi_h) + \bar{h}_{fb}(h_{mf} + h_{fm}) + h_{bf}h_{fm} = \lambda k_{Rb}(\bar{k}_{fb} + \phi_k) + \bar{k}_{fb}(k_{mf} + k_{fm}) + k_{bf}k_{fm} \tag{A.13e}$$
$$\lambda h_{Rb}(\bar{h}_{fb}(h_{mf} + h_{fm}) + h_{bf}h_{fm}) = \lambda k_{Rb}(\bar{k}_{fb}(k_{mf} + k_{fm}) + k_{bf}k_{fm}) \tag{A.13f}$$

for $\boldsymbol{h}_{RTM}$ in terms of $\boldsymbol{k}_{RTM}$, where $\phi_h = h_{bf} + h_{mf} + h_{fm}$ and $\phi_k = k_{bf} + k_{mf} + k_{fm}$.

By comparison with (A.13a), equation (A.13d) can be replaced by

$$\bar{h}_{fb} - \bar{h}_{Rb} = \bar{k}_{fb} - \bar{k}_{Rb} \,. \tag{A.14}$$

First, let us solve the sub-system (A.13a)–(A.13c) with respect to $\bar{h}_{Rb} + \lambda h_{Rb} = \gamma h_{Rb}$. We find three solutions:

$$\begin{aligned} \gamma h_{Rb}^{(1)} &= \gamma k_{Rb} \,, \\ \gamma h_{Rb}^{(2,3)} &= \frac{\phi_k \pm \sqrt{\phi_k^2 - 4 k_{bf} k_{fm}}}{2} \,. \end{aligned} \tag{A.15}$$

Solution $h_{Rb}^{(1)}$ leads to $\boldsymbol{h}_{RTM}^{(1)} = \boldsymbol{k}_{RTM}$. Solutions $h_{Rb}^{(2,3)}$ a priori define two distinct sets of solution. Nevertheless, we can observe that, by replacing (A.13d) in (A.13e) and comparing to (A.13f), we obtain

$$(k_{Rb} - h_{Rb}) \Big((\lambda h_{Rb})^2 - (\bar{k}_{fb} + \phi_k) \lambda h_{Rb} + \bar{k}_{fb} (k_{mf} + k_{fm}) + k_{bf} k_{fm} \Big) = 0 \,. \tag{A.16}$$

Therefore, to be solutions of the system (A.13a)–(A.13f), the three solutions defined in (A.15) have to satisfy (A.16). For $h_{Rb}^{(1)} = k_{Rb}$, equation (A.16) is easily satisfied. For $h_{Rb}^{(2,3)}$, equation (A.16) becomes

$$(\lambda h_{Rb}^{(2,3)})^2 - (\bar{k}_{fb} + \phi_k) \lambda h_{Rb}^{(2,3)} + \bar{k}_{fb} (k_{mf} + k_{fm}) + k_{bf} k_{fm} = 0 \,. \tag{A.17}$$

This equation (once $\bar{k}_{fb}$ and ϕ_k are explicated), represents a constraint on the components of $\boldsymbol{k}_{RTM}$, that, in general (i.e. if $\boldsymbol{k}_{RTM}$ is generic), is not satisfied.

Appendix B

Proof of identifiability of renal model

Theorem 5.1.2 ensures identifiability of the renal three-compartment non-catenary model, under the hypothesis C_t, k_{tm}, and k_{ut} fixed. These modeling assumptions are obtained from physiological properties holding for the kidneys, and are essential in order to prove uniqueness of $\boldsymbol{k}_K = (k_{fa}, k_{ma}, k_{af}, k_{mf}, k_{fm}, k_{tm}, k_{ut})^T \in \mathbb{R}^7_+$ given the pixel-wise renal tracer concentration $\mathscr{C}_K$, the arterial region of interest (ROI) input function (IF) C_a^{ROI}, and the constant renal blood volume fraction V_{bK}.

We recall the model equations needed for the subsequent analysis:

$$\begin{aligned} &\dot{\boldsymbol{C}} = \boldsymbol{M}\boldsymbol{C} + \boldsymbol{W}\,, \quad \boldsymbol{C}(0) = 0\,, \\ &\boldsymbol{C} = \begin{pmatrix} C_f \\ C_m \\ C_t \end{pmatrix}\,, \quad \boldsymbol{M} = \begin{pmatrix} -(k_{af}+k_{mf}) & k_{fm} & 0 \\ k_{mf} & -(k_{fm}+k_{tm}) & 0 \\ 0 & k_{tm} & -k_{ut} \end{pmatrix}\,, \\ &\boldsymbol{W} = k_{fa}C_a^{\mathrm{ROI}}\boldsymbol{e}_1 + k_{ma}C_a^{\mathrm{ROI}}\boldsymbol{e}_2\,, \quad \boldsymbol{e}_1 = \begin{pmatrix} 1 \\ 0 \\ 0 \end{pmatrix}\,, \quad \boldsymbol{e}_2 = \begin{pmatrix} 0 \\ 1 \\ 0 \end{pmatrix}\,; \end{aligned} \tag{B.1}$$

$$\mathscr{C}_K(t; C_a^{\mathrm{ROI}}, \boldsymbol{k}_K) = \boldsymbol{\alpha}^T \boldsymbol{C}(t; C_a^{\mathrm{ROI}}, \boldsymbol{k}_K) + V_{bK}C_a^{\mathrm{ROI}}(t)\,, \quad \boldsymbol{\alpha} = \begin{pmatrix} 1-V_{bK} \\ 1-V_{bK} \\ 1-V_{bK} \end{pmatrix}\,. \tag{B.2}$$

Since k_{tm} and k_{ut} are assumed to be fixed, we have to prove uniqueness of the remaining five coefficients $(k_{fa}, k_{ma}, k_{af}, k_{mf}, k_{fm})^T \in \mathbb{R}^5_+$. In explicit form, the system of ODEs (B.1) takes the form

$$\begin{cases} \dot{C}_f = -(k_{af}+k_{mf})C_f + k_{fm}C_m + k_{fa}C_a^{\mathrm{ROI}} \\ \dot{C}_m = k_{mf}C_f - (k_{fm}+\alpha)C_m + k_{ma}C_a^{\mathrm{ROI}} \\ \dot{C}_t = k_{tm}C_m - k_{ut}C_t \end{cases}\,. \tag{B.3}$$

Assuming that the concentrations are sufficiently regular, we take the Laplace transform of the differential equations (B.3):

$$\begin{cases} (s+k_{af}+k_{mf})\mathcal{L}(C_f) - k_{fm}\mathcal{L}(C_m) = k_{fa}\mathcal{L}(C_a^{\mathrm{ROI}}) \\ -k_{mf}\mathcal{L}(C_f) + (s+k_{fm}+k_{tm})\mathcal{L}(C_m) = k_{ma}\mathcal{L}(C_a^{\mathrm{ROI}}) \\ (s+k_{ut})\mathcal{L}(C_t) - k_{tm}\mathcal{L}(C_m) = 0 \end{cases}\,, \tag{B.4}$$

where $\mathcal{L}(f)$ denotes the Laplace transform of the function f. Solving (B.4) with respect to $\mathcal{L}(C_f)$, $\mathcal{L}(C_m)$, and $\mathcal{L}(C_t)$, we get

$$\mathcal{L}(C_f) = \frac{k_{fa}(s + k_{fm} + k_{tm}) + k_{ma}k_{fm}}{D(s; \boldsymbol{k}_K)} \mathcal{L}(C_a^{\text{ROI}}) \,, \tag{B.5a}$$

$$\mathcal{L}(C_m) = \frac{k_{ma}(s + k_{af} + k_{mf}) + k_{fa}k_{mf}}{D(s; \boldsymbol{k}_K)} \mathcal{L}(C_a^{\text{ROI}}) \,, \tag{B.5b}$$

$$\mathcal{L}(C_t) = \frac{k_{tm}}{s + k_{ut}} \mathcal{L}(C_m) \,, \tag{B.5c}$$

where

$$D(s; \boldsymbol{k}_K) = (s + k_{af} + k_{mf})(s + k_{fm} + k_{tm}) - k_{mf}k_{fm} \tag{B.6}$$

is the characteristic polynomial of $\boldsymbol{M}$. Moreover, by comparing (B.5b) and (B.5c), we get

$$\mathcal{L}(C_t) = \frac{k_{tm}}{s + k_{ut}} \frac{k_{ma}(s + k_{af} + k_{mf}) + k_{fa}k_{mf}}{D(s; \boldsymbol{k}_K)} \mathcal{L}(C_a^{\text{ROI}}) \,. \tag{B.7}$$

Then, we take the Laplace transform of equation (B.2):

$$\frac{\mathcal{L}(\mathscr{C}_K) - V_{bK}\mathcal{L}(C_a^{\text{ROI}})}{1 - V_{bK}} = \mathcal{L}(C_f) + \mathcal{L}(C_m) + \mathcal{L}(C_t) \,, \tag{B.8}$$

where the left-hand side is a known function of s, independent of the constants $\boldsymbol{k}_K$.

Now, suppose $\boldsymbol{h}_K = (h_{fa}, h_{ma}, h_{af}, h_{mf}, h_{fm}, h_{tm}, h_{ut})^T \in \mathbb{R}_+^7$, s.t. $h_{tm} = k_{tm}$ and $h_{ut} = k_{ut}$, is an alternative choice of rate coefficients consistent with the data of the problem. We make explicit the dependence of the compartment concentrations on the rate constants $\boldsymbol{k}_K$ or $\boldsymbol{h}_K$. The condition C_t fixed implies that $C_t(\boldsymbol{k}_K) = C_t(\boldsymbol{h}_K)$, whence it follows that

$$\mathcal{L}(C_t(\boldsymbol{k}_K)) = \mathcal{L}(C_t(\boldsymbol{h}_K)) \,. \tag{B.9}$$

Equation (B.5c) implies

$$\mathcal{L}(C_m) = \frac{s + k_{ut}}{k_{tm}} \mathcal{L}(C_t) \,,$$

and, since k_{tm} and k_{ut} are fixed, and equation (B.9) holds, it follows also that

$$\mathcal{L}(C_m(\boldsymbol{k}_K)) = \mathcal{L}(C_m(\boldsymbol{h}_K)) \,. \tag{B.10}$$

From equation (B.8), it is found that

$$\mathcal{L}(C_f(\boldsymbol{k}_K)) + \mathcal{L}(C_m(\boldsymbol{k}_K)) + \mathcal{L}(C_t(\boldsymbol{k}_K)) = \mathcal{L}(C_f(\boldsymbol{h}_K)) + \mathcal{L}(C_m(\boldsymbol{h}_K)) + \mathcal{L}(C_t(\boldsymbol{h}_K)) \,. \tag{B.11}$$

Therefore, because of (B.9) and (B.10), equation (B.11) reduces to

$$\mathcal{L}(C_f(\boldsymbol{k}_K)) = \mathcal{L}(C_f(\boldsymbol{h}_K)) \,. \tag{B.12}$$

Now, substitution of (B.7) into (B.9) leads to

$$\frac{k_{ma}(s + k_{af} + k_{mf}) + k_{fa}k_{mf}}{D(s; \boldsymbol{k}_K)} = \frac{h_{ma}(s + h_{af} + h_{mf}) + h_{fa}h_{mf}}{D(s; \boldsymbol{h}_K)} \,, \tag{B.13}$$

and substitution of (B.5a) into (B.12) gives

$$\frac{k_{fa}(s+k_{fm}+k_{tm})+k_{ma}k_{fm}}{D(s;\boldsymbol{k}_K)} = \frac{h_{fa}(s+h_{fm}+k_{tm})+h_{ma}h_{fm}}{D(s;\boldsymbol{h}_K)} \,. \tag{B.14}$$

Assume that the two rational fractions (B.13) and (B.14) are irreducible, i.e. the polynomials

$$P(s;\boldsymbol{k}_K) = k_{ma}(s+k_{af}+k_{mf})+k_{fa}k_{mf} \tag{B.15}$$

$$Q(s;\boldsymbol{k}_K) = k_{fa}(s+k_{fm}+k_{tm})+k_{ma}k_{fm} \tag{B.16}$$

are both coprime with $D(s;\boldsymbol{k}_K)$. Moreover, the leading coefficients of $D(s;\boldsymbol{k}_K)$ and $D(s;\boldsymbol{h}_K)$ are identical, as well as those of $P(s;\boldsymbol{k}_K)$ and $P(s;\boldsymbol{h}_K)$, $Q(s;\boldsymbol{k}_K)$ and $Q(s;\boldsymbol{h}_K)$. Therefore, equations (B.13)–(B.14) holds if and only if

$$D(s;\boldsymbol{h}_K) = D(s;\boldsymbol{k}_K)\,, \quad P(s;\boldsymbol{h}_K) = P(s;\boldsymbol{h}_K)\,, \quad Q(s;\boldsymbol{h}_K) = Q(s;\boldsymbol{h}_K)\,. \tag{B.17}$$

We obtain the links between the two sets of parameters, i.e. the system

$$\begin{aligned}
h_{af}+h_{mf}+h_{fm}+k_{tm} &= k_{af}+k_{mf}+k_{fm}+k_{tm}\\
h_{af}h_{fm}+(h_{af}+h_{mf})k_{tm} &= k_{af}k_{fm}+(k_{af}+k_{mf})k_{tm}\\
h_{ma} &= k_{ma}\\
h_{ma}(h_{af}+h_{mf})+h_{fa}h_{mf} &= k_{ma}(k_{af}+k_{mf})+k_{fa}k_{mf}\\
h_{fa} &= k_{fa}\\
h_{fa}(h_{fm}+k_{tm})+h_{ma}h_{fm} &= k_{fa}(k_{fm}+k_{tm})+k_{ma}k_{fm}
\end{aligned}$$

which holds if and only if

$$k_{fa}=h_{fa}\,,\; k_{ma}=h_{ma}\,,\; k_{af}=h_{af}\,,\; k_{mf}=h_{mf}\,,\; k_{fm}=h_{fm}\,.$$

Appendix C

Proof of identifiability of BCM

We want to prove Theorem 7.2.1 for the identifiability of the biochemically-driven compartmental model (BCM) applied to LigandTracer (LT) data of cultured cells. The aim is to ensure uniqueness of the rate constants $\bar{\boldsymbol{k}}_{BCM} = (\bar{k}_{fi}, k_{if}, k_{pf}, k_{rp}, k_{fr})^T \in \mathbb{R}^5_+$, given the data of total tracer activity in the cell culture $\mathscr{A}_T$ and in the incubation liquid medium A_i.

We recall the model equations needed for the subsequent analysis:

$$\begin{gathered}\dot{\boldsymbol{A}} = \boldsymbol{M}\boldsymbol{A} + \bar{k}_{fi}A_i\boldsymbol{e}_1\,, \quad \boldsymbol{A}(0) = 0\,, \\ \boldsymbol{A} = \begin{pmatrix} A_f \\ A_p \\ \bar{A}_r \end{pmatrix}\,, \quad \boldsymbol{M} = \begin{pmatrix} -(k_{if}+k_{pf}) & 0 & k_{fr} \\ k_{pf} & -k_{rp} & 0 \\ 0 & k_{rp} & -k_{fr} \end{pmatrix}\,, \quad \boldsymbol{e}_1 = \begin{pmatrix} 1 \\ 0 \\ 0 \end{pmatrix} \\ \bar{A}_r = \frac{1}{v}A_r\,, \quad v = \frac{V_{er}}{V_{cyt}}\,, \quad \bar{k}_{fi} = k_{fi}\frac{V_{cyt}}{V_i}\,;\end{gathered} \tag{C.1}$$

$$\mathscr{A}_T(t) = \boldsymbol{\alpha}^T\boldsymbol{A}(t; A_i, \bar{\boldsymbol{k}}_{BCM})\,, \quad \boldsymbol{\alpha} = \begin{pmatrix} 1 \\ 1 \\ v \end{pmatrix}\,. \tag{C.2}$$

The discussion of uniqueness is based on the analysis of the Laplace transform of the differential equations (C.1), and equation (C.2) stating the connection between formal expression of the solutions and LT data.

We denote by $\mathcal{L}(f)$ the Laplace transform of the function f. Assuming that suitable regularity conditions are satisfied, the Laplace transform of system (C.1) leads to the linear system

$$\begin{cases} (s+k_{if}+k_{pf})\mathcal{L}(A_f) - k_{fr}\mathcal{L}(\bar{A}_r) = \bar{k}_{fi}\mathcal{L}(A_i) \\ -k_{pf}\mathcal{L}(A_f) + (s+k_{rp})\mathcal{L}(A_p) = 0 \\ -k_{rp}\mathcal{L}(A_p) + (s+k_{fr})\mathcal{L}(\bar{A}_r) = 0 \end{cases}\,, \tag{C.3}$$

and the Laplace transform of equation (C.2) gives

$$\mathcal{L}(\mathscr{A}_T) = \mathcal{L}(A_f) + \mathcal{L}(A_p) + v\mathcal{L}(\bar{A}_r)\,. \tag{C.4}$$

The solution of the linear system (C.3) is

$$\mathcal{L}(A_f) = \frac{\bar{k}_{fi}}{D(s;\bar{\boldsymbol{k}}_{BCM})}(s+k_{rp})(s+k_{fr})\mathcal{L}(A_i)\,, \tag{C.5}$$

$$\mathcal{L}(A_p) = \frac{\bar{k}_{fi}}{D(s;\bar{\boldsymbol{k}}_{BCM})}k_{pf}(s+k_{fr})\mathcal{L}(A_i)\,, \tag{C.6}$$

$$\mathcal{L}(\bar{A}_r) = \frac{\bar{k}_{fi}}{D(s;\bar{\boldsymbol{k}}_{BCM})}k_{pf}k_{rp}\mathcal{L}(A_i)\,, \tag{C.7}$$

where

$$D(s;\bar{\boldsymbol{k}}_{BCM}) = s^3 + (k_{if}+k_{pf}+k_{rp}+k_{fr})s^2 + [(k_{if}+k_{pf})(k_{rp}+k_{fr})+k_{rp}k_{fr}]s + k_{if}k_{rp}k_{fr}\,, \tag{C.8}$$

is the characteristic polynomial of $\boldsymbol{M}$. Substitution of the expressions (C.5)–(C.7) of $\mathcal{L}(A_f)$, $\mathcal{L}(A_p)$, and $\mathcal{L}(\bar{A}_r)$ into equation (C.4) yields the necessary condition

$$\frac{\mathcal{L}(\mathscr{A}_T)}{\mathcal{L}(A_i)} = \frac{\bar{k}_{fi}Q(s;\bar{\boldsymbol{k}}_{BCM})}{D(s;\bar{\boldsymbol{k}}_{BCM})}\,, \tag{C.9}$$

where

$$Q(s;\bar{\boldsymbol{k}}_{BCM}) = s^2 + (k_{pf}+k_{rp}+k_{fr})\,s + (k_{pf}\,+k_{rp})\,k_{fr} + v\,k_{pf}\,k_{rp}\,. \tag{C.10}$$

If $\bar{\boldsymbol{h}}_{BCM} = (\bar{h}_{fi}, h_{if}, h_{pf}, h_{rp}, h_{fr})^T \in \mathbb{R}^5_+$ is another vector of rate coefficients consistent with the same LT data, it follows that the right-hand side of (C.9) in terms of $\bar{\boldsymbol{k}}_{BCM}$ and in terms of $\bar{\boldsymbol{h}}_{BCM}$ are equal. With obvious meaning of symbols, we have

$$\frac{\bar{k}_{fi}\,Q(s;\bar{\boldsymbol{k}}_{BCM})}{D(s;\bar{\boldsymbol{k}}_{BCM})} = \frac{\bar{h}_{fi}Q(s;\bar{\boldsymbol{h}}_{BCM})}{D(s;\bar{\boldsymbol{h}}_{BCM})}\,. \tag{C.11}$$

Assume that D and Q are coprime. Moreover, the leading coefficients of $D(s;\bar{\boldsymbol{k}}_{BCM})$ and $D(s;\bar{\boldsymbol{h}}_{BCM})$ are identical, as well as those of $Q(s;\bar{\boldsymbol{k}}_{BCM})$ and $Q(s;\bar{\boldsymbol{h}}_{BCM})$. Then, equation (C.11) holds if and only if

$$\bar{h}_{fi} = \bar{k}_{fi}\,, \quad D(s;\bar{\boldsymbol{h}}_{BCM}) = D(s;\bar{\boldsymbol{k}}_{BCM})\,, \quad Q(s;\bar{\boldsymbol{h}}_{BCM}) = Q(s;\bar{\boldsymbol{k}}_{BCM})\,, \tag{C.12}$$

equivalent to the system

$$\bar{h}_{fi} = \bar{k}_{fi} \tag{C.13a}$$

$$h_{if}+h_{pf}+h_{rp}+h_{fr} = k_{if}+k_{pf}+k_{rp}+k_{fr} \tag{C.13b}$$

$$(h_{if}+h_{pf})(h_{rp}+h_{fr})+h_{rp}h_{fr} = (k_{if}+k_{pf})(k_{rp}+k_{fr})+k_{rp}k_{fr} \tag{C.13c}$$

$$h_{if}h_{rp}h_{fr} = k_{if}k_{rp}k_{fr} \tag{C.13d}$$

$$h_{pf}+h_{rp}+h_{fr} = k_{pf}+k_{rp}+k_{fr} \tag{C.13e}$$

$$(h_{pf}+h_{rp})h_{fr}+vh_{pf}h_{rp} = (k_{pf}+k_{rp})k_{fr}+vk_{pf}k_{rp} \tag{C.13f}$$

for $\bar{\boldsymbol{h}}_{BCM}$ in terms of $\bar{\boldsymbol{k}}_{BCM}$.

Comparison between (C.13b) and (C.13e) shows that $h_{if} = k_{if}$. As a consequence, (C.13d) reduces to $h_{rp}h_{fr} = k_{rp}k_{fr}$.

Next $h_{rp}+h_{fr}$ is determined from (C.13e) in terms of h_{pf}, and substituted into equation (C.13c), which takes the form of a vanishing polynomial of degree two, in

the unknown h_{pf}. The corresponding solutions are:

$$h_{pf}^{(1)} = k_{pf} \ , \quad h_{pf}^{(2)} = -k_{if} + k_{rp} + k_{fr} \ .$$

If $h_{pf}^{(1)} = k_{pf}$, it is easily shown that $h_{rp}^{(1)} = k_{rp}$ and $h_{fr}^{(1)} = k_{fr}$, which implies $\bar{\boldsymbol{h}}_{BCM}^{(1)} = \bar{\boldsymbol{k}}_{BCM}$.

If $h_{pf}^{(2)} \leq 0$ this solution is not admissible. If $h_{pf}^{(2)} > 0$, then equations (C.13e) and (C.13f) reduce to a linear system for the unknowns $h_{rp}^{(2)}$ and $h_{fr}^{(2)}$. The solution is

$$h_{rp}^{(2)} = \frac{1}{1-v}\left(k_{if} - k_{pf}\frac{k_{fr} + vk_{rp}}{-k_{if} + k_{rp} + k_{fr}}\right) \ , \quad h_{fr}^{(2)} = k_{if} - h_{rp}^{(2)} \ .$$

If at least one between $h_{rp}^{(2)}$ and $h_{fr}^{(2)}$ is negative or vanishing, then $h_{pf}^{(2)}$ gives rise to a vector solution which not admissible. If $h_{rp}^{(2)}$ and $h_{fr}^{(2)}$ are positive then the compatibility condition

$$h_{rp}^{(2)}(k_{if} - h_{rp}^{(2)}) = k_{rp}k_{fr} \tag{C.14}$$

must be satisfied. Thus we conclude that the solution reconstructed from $h_{pf}^{(2)}$ is not admissible, unless the data satisfy equation (C.14). In other words, equation (C.14) is a constraint on the components of the parameter vector $\bar{\boldsymbol{k}}_{BCM}$ that, in general (i.e. if $\bar{\boldsymbol{k}}_{BCM}$ is generic), is not satisfied.

Appendix D

TGFβ-pathway CRN

We provide the chemical structure of the TGFβ-pathway chemical reaction network (CRN), as list of chemical species, chemical complexes, chemical reactions, and as system of ordinary differential equations (ODEs) characterized by conserved cycles. Moreover, we show the equations of the TGFβ-CRN system at equilibrium to give evidence of a priori restrictions on the reaction rate constants.

We recall the TGFβ system dimensions: 50 chemical species (18 basic and 32 composed), 63 chemical complexes, 65 chemical reactions (26 reversible and 13 non-reversible), and thus 65 reaction rate constants (39 forward and 26 reverse). Before reporting the details of the TGFβ-CRN, we make some remarks.

- The conserved cycles equal the number of basic chemical species, and each basic species concentration appears in one and only one cycle.
- The equations of the conserved cycles may be used to reduce the number of state variables of the CRN system: (1) each equation sets to zero a weighted sum of time derivatives of the species concentrations; (2) this equation can be integrated in time to obtain a formal expression in which the concentration of the only basic species is written as function of other species concentrations; (3) this explicit expression can be substituted in the system of ODEs.
- The integrated equations of the conserved cycles express the time-dependent concentration of each basic species as its initial non-negligible value at time $t = 0$ minus the time-dependent species concentrations involved in its cycle.
- The system of ODEs at equilibrium $\dot{\boldsymbol{x}} = \boldsymbol{S}\boldsymbol{v} = 0$ counts for a total number of 50 equations, of which only 32 ($= \text{rank}(\boldsymbol{S})$) are linearly independent.
- The equilibrium equations allow to fix the ratios between linear combinations of rate constants, as determined from the species concentrations at equilibrium. Alternatively, the equilibrium equations establish constraints on a subset of rate constants:
  - the 26 reverse parameters can be written as functions of the 39 forward;
  - 6 equations fix 6 forward parameters of the 13 non-reversible reactions.

  There remains a total of 33 free (non-constrained) forward parameters.
- The equilibrium equations select a family of rate constants for a given equilibrium point. In other words, all the parameter values satisfying the equilibrium equations return the same equilibrium point (with the same initial conditions).

D.1 Chemical species

Name	Variable	Type
TGF	x_{i1}	basic (ligand - constant)
WNT	x_{i2}	basic (ligand - constant)
2TGF	x_1	composed
2TBR2	x_2	composed
2TGF_2TBR2	x_3	composed
2TBR1	x_4	composed
2TGF_2TBR2_2TBR1	x_5	composed
2TGF_2TBR2_2TBR1P	x_6	composed (P)
PP1C	x_7	basic (phosphatase)
SMAD2	x_8	basic
2TGF_2TBR2_2TBR1P_SMAD2	x_9	composed
TBR1	x_{10}	basic (receptor)
TBR2	x_{11}	basic (receptor)
SMAD2P	x_{12}	composed (P)
SMAD3	x_{13}	basic
2TGF_2TBR2_2TBR1P_SMAD3	x_{14}	composed
SMAD3P	x_{15}	composed (P)
TAK	x_{16}	basic
2TGF_2TBR2_2TBR1P_TAK	x_{17}	composed
TAKP	x_{18}	composed (P)
NLK	x_{19}	basic
NLKP	x_{20}	composed (P)
TCFLEF	x_{21}	basic
NLKP_TCFLEF	x_{22}	composed
TCFLEFP	x_{23}	composed (P)
P8	x_{24}	basic (phosphatase)
TCFLEFP_P8	x_{25}	composed
P9	x_{26}	basic (phosphatase)
TAKP_P9	x_{27}	composed
NLKP_P10	x_{28}	composed
P10	x_{29}	basic (phosphatase)
SMAD4	x_{30}	basic
SMAD2P_SMAD4	x_{31}	composed
SMAD3P_SMAD4	x_{32}	composed
PP1A	x_{33}	basic (phosphatase)
SMAD3P_PP1A	x_{34}	composed
SMAD2P_PP1A	x_{35}	composed
2TBR1P	x_{36}	composed (P)
2TBR1P_PP1C	x_{37}	composed
FRZ	x_{38}	basic (receptor)
WNT_FRZ	x_{39}	composed
LRP6	x_{40}	basic
WNT_FRZ_LRP6	x_{41}	composed
DVL	x_{42}	basic
WNT_FRZ_LRP6_DVL	x_{43}	composed
WNT_FRZ_LRP6_TAK	x_{44}	composed
TAB	x_{45}	basic
TAKP_TAB	x_{46}	composed
TAKP_TAB_NLK	x_{47}	composed
GROUCHO	x_{48}	basic
GROUCHO_TCFLEF	x_{49}	composed
SMAD4_TCFLEF	x_{50}	composed

TABLE D.1: List of TGFβ-pathway chemical species: chemical name, variable as concentration, and type of chemical species.

D.2 Chemical complexes

Name	Variable	Value
~~TGF + TGF~~ ∅	–	x_{i1}^2
2TGF	C_1	x_1
2TGF + 2TBR2	C_2	x_1x_2
2TGF_2TBR2	C_3	x_3
2TGF_2TBR2 + 2TBR1	C_4	x_3x_4
2TGF_2TBR2_2TBR1	C_5	x_5
2TGF_2TBR2_2TBR1P	C_6	x_6
2TGF_2TBR2_2TBR1P + SMAD2	C_7	x_6x_8
2TGF_2TBR2_2TBR1P_SMAD2	C_8	x_9
TBR1 + TBR1	C_9	x_{10}^2
2TBR1	C_{10}	x_4
TBR2 + TBR2	C_{11}	x_{11}^2
2TBR2	C_{12}	x_2
2TGF_2TBR2_2TBR1P + SMAD2P	C_{13}	x_6x_{12}
2TGF_2TBR2_2TBR1P + SMAD3	C_{14}	x_6x_{13}
2TGF_2TBR2_2TBR1P_SMAD3	C_{15}	x_{14}
2TGF_2TBR2_2TBR1P + SMAD3P	C_{16}	x_6x_{15}
2TGF_2TBR2_2TBR1P + TAK	C_{17}	x_6x_{16}
2TGF_2TBR2_2TBR1P_TAK	C_{18}	x_{17}
2TGF_2TBR2_2TBR1P + TAKP	C_{19}	x_6x_{18}
NLKP + TCFLEF	C_{20}	$x_{20}x_{21}$
NLKP_TCFLEF	C_{21}	x_{22}
NLKP + TCFLEFP	C_{22}	$x_{20}x_{23}$
TCFLEFP + P8	C_{23}	$x_{23}x_{24}$
TCFLEFP_P8	C_{24}	x_{25}
TCFLEF + P8	C_{25}	$x_{21}x_{24}$
TAKP + P9	C_{26}	$x_{18}x_{26}$
TAKP_P9	C_{27}	x_{27}
TAK + P9	C_{28}	$x_{16}x_{26}$
NLKP + P10	C_{29}	$x_{20}x_{29}$
NLKP_P10	C_{30}	x_{28}
NLK + P10	C_{31}	$x_{19}x_{29}$
SMAD2P + SMAD4	C_{32}	$x_{12}x_{30}$
SMAD2P_SMAD4	C_{33}	x_{31}
SMAD3P + SMAD4	C_{34}	$x_{15}x_{30}$
SMAD3P_SMAD4	C_{35}	x_{32}
SMAD3P + PP1A	C_{36}	$x_{15}x_{33}$
SMAD3P_PP1A	C_{37}	x_{34}
SMAD3 + PP1A	C_{38}	$x_{13}x_{33}$
SMAD2P + PP1A	C_{39}	$x_{12}x_{33}$
SMAD2P_PP1A	C_{40}	x_{35}
SMAD2 + PP1A	C_{41}	x_8x_{33}
2TGF_2TBR2 + 2TBR1P	C_{42}	x_3x_{36}
2TBR1P + PP1C	C_{43}	$x_{36}x_7$
2TBR1P_PP1C	C_{44}	x_{37}
2TBR1 + PP1C	C_{45}	x_4x_7
~~WNT + FRZ~~ FRZ	C_{46}	$x_{i2}x_{38}$
WNT_FRZ	C_{47}	x_{39}
WNT_FRZ + LRP6	C_{48}	$x_{39}x_{40}$
WNT_FRZ_LRP6	C_{49}	x_{41}
WNT_FRZ_LRP6 + DVL	C_{50}	$x_{41}x_{42}$
WNT_FRZ_LRP6_DVL	C_{51}	x_{43}
WNT_FRZ_LRP6 + TAK	C_{52}	$x_{41}x_{16}$
WNT_FRZ_LRP6_TAK	C_{53}	x_{44}
WNT_FRZ_LRP6 + TAKP	C_{54}	$x_{41}x_{18}$
TAKP + TAB	C_{55}	$x_{18}x_{45}$
TAKP_TAB	C_{56}	x_{46}
TAKP_TAB + NLK	C_{57}	$x_{46}x_{19}$
TAKP_TAB_NLK	C_{58}	x_{47}
TAKP_TAB + NLKP	C_{59}	$x_{46}x_{20}$
GROUCHO + TCFLEF	C_{60}	$x_{48}x_{21}$
GROUCHO_TCFLEF	C_{61}	x_{49}
SMAD4 + TCFLEF	C_{62}	$x_{30}x_{21}$
SMAD4_TCFLEF	C_{63}	x_{50}

TABLE D.2: List of TGFβ-pathway chemical complexes: chemical form, variable as complex involved in a reaction, and value as product of species concentrations.

D.3 Chemical reactions

Reaction	Variable	Flux
~~$\text{TGF} + \text{TGF} \overset{k_{1f}}{\underset{k_{1r}}{\rightleftarrows}} 2\text{TGF}$~~ $\varnothing \overset{k_{1f}x_{i1}^2}{\underset{k_{1r}}{\rightleftarrows}} 2\text{TGF}$	$R_{1f}\colon \varnothing \to C_1$	$v_{1f} = k_{1f}x_{i1}^2$
	$R_{1r}\colon C_1 \to \varnothing$	$v_{1r} = k_{1r}x_1$
$2\text{TGF} + 2\text{TBR2} \overset{k_{2f}}{\underset{k_{2r}}{\rightleftarrows}} 2\text{TGF\_2TBR2}$	$R_{2f}\colon C_2 \to C_3$	$v_{2f} = k_{2f}x_1x_2$
	$R_{2r}\colon C_3 \to C_2$	$v_{2r} = k_{2r}x_3$
$2\text{TGF\_2TBR2} + 2\text{TBR1} \overset{k_{3f}}{\underset{k_{3r}}{\rightleftarrows}} 2\text{TGF\_2TBR2\_2TBR1}$	$R_{3f}\colon C_4 \to C_5$	$v_{3f} = k_{3f}x_3x_4$
	$R_{3r}\colon C_5 \to C_4$	$v_{3r} = k_{3r}x_5$
$2\text{TGF\_2TBR2\_2TBR1} \overset{k_{4f}}{\to} 2\text{TGF\_2TBR2\_2TBR1P}$	$R_{4f}\colon C_5 \to C_6$	$v_{4f} = k_{4f}x_5$
$2\text{TGF\_2TBR2\_2TBR1P} + \text{SMAD2} \overset{k_{5f}}{\underset{k_{5r}}{\rightleftarrows}} 2\text{TGF\_2TBR2\_2TBR1P\_SMAD2}$	$R_{5f}\colon C_7 \to C_8$	$v_{5f} = k_{5f}x_6x_8$
	$R_{5r}\colon C_8 \to C_7$	$v_{5r} = k_{5r}x_9$
$\text{TBR1} + \text{TBR1} \overset{k_{6f}}{\underset{k_{6r}}{\rightleftarrows}} 2\text{TBR1}$	$R_{6f}\colon C_9 \to C_{10}$	$v_{6f} = k_{6f}x_{10}^2$
	$R_{6r}\colon C_{10} \to C_9$	$v_{6r} = k_{6r}x_4$
$\text{TBR2} + \text{TBR2} \overset{k_{7f}}{\underset{k_{7r}}{\rightleftarrows}} 2\text{TBR2}$	$R_{7f}\colon C_{11} \to C_{12}$	$v_{7f} = k_{7f}x_{11}^2$
	$R_{7r}\colon C_{12} \to C_{11}$	$v_{7r} = k_{7r}x_2$
$2\text{TGF\_2TBR2\_2TBR1P\_SMAD2} \overset{k_{8f}}{\to} 2\text{TGF\_2TBR2\_2TBR1P} + \text{SMAD2P}$	$R_{8f}\colon C_8 \to C_{13}$	$v_{8f} = k_{8f}x_9$
$2\text{TGF\_2TBR2\_2TBR1P} + \text{SMAD3} \overset{k_{9f}}{\underset{k_{9r}}{\rightleftarrows}} 2\text{TGF\_2TBR2\_2TBR1P\_SMAD3}$	$R_{9f}\colon C_{14} \to C_{15}$	$v_{9f} = k_{9f}x_6x_{13}$
	$R_{9r}\colon C_{15} \to C_{14}$	$v_{9r} = k_{9r}x_{14}$
$2\text{TGF\_2TBR2\_2TBR1P\_SMAD3} \overset{k_{10f}}{\to} 2\text{TGF\_2TBR2\_2TBR1P} + \text{SMAD3P}$	$R_{10f}\colon C_{15} \to C_{16}$	$v_{10f} = k_{10f}x_{14}$
$2\text{TGF\_2TBR2\_2TBR1P} + \text{TAK} \overset{k_{11f}}{\underset{k_{11r}}{\rightleftarrows}} 2\text{TGF\_2TBR2\_2TBR1P\_TAK}$	$R_{11f}\colon C_{17} \to C_{18}$	$v_{11f} = k_{11f}x_6x_{16}$
	$R_{11r}\colon C_{18} \to C_{17}$	$v_{11r} = k_{11r}x_{17}$
$2\text{TGF\_2TBR2\_2TBR1P\_TAK} \overset{k_{12f}}{\to} 2\text{TGF\_2TBR2\_2TBR1P} + \text{TAKP}$	$R_{12f}\colon C_{18} \to C_{19}$	$v_{12f} = k_{12f}x_{17}$
$\text{NLKP} + \text{TCFLEF} \overset{k_{13f}}{\underset{k_{13r}}{\rightleftarrows}} \text{NLKP\_TCFLEF}$	$R_{13f}\colon C_{20} \to C_{21}$	$v_{13f} = k_{13f}x_{20}x_{21}$
	$R_{13r}\colon C_{21} \to C_{20}$	$v_{13r} = k_{13r}x_{22}$
$\text{NLKP\_TCFLEF} \overset{k_{14f}}{\to} \text{NLKP} + \text{TCFLEFP}$	$R_{14f}\colon C_{21} \to C_{22}$	$v_{14f} = k_{14f}x_{22}$
$\text{TCFLEFP} + \text{P8} \overset{k_{15f}}{\underset{k_{15r}}{\rightleftarrows}} \text{TCFLEFP\_P8}$	$R_{15f}\colon C_{23} \to C_{24}$	$v_{15f} = k_{15f}x_{23}x_{24}$
	$R_{15r}\colon C_{24} \to C_{23}$	$v_{15r} = k_{15r}x_{25}$
$\text{TCFLEFP\_P8} \overset{k_{16f}}{\to} \text{TCFLEF} + \text{P8}$	$R_{16f}\colon C_{24} \to C_{25}$	$v_{16f} = k_{16f}x_{25}$
$\text{TAKP} + \text{P9} \overset{k_{17f}}{\underset{k_{17r}}{\rightleftarrows}} \text{TAKP\_P9}$	$R_{17f}\colon C_{26} \to C_{27}$	$v_{17f} = k_{17f}x_{18}x_{26}$
	$R_{17r}\colon C_{27} \to C_{26}$	$v_{17r} = k_{17r}x_{27}$
$\text{TAKP\_P9} \overset{k_{18f}}{\to} \text{TAK} + \text{P9}$	$R_{18f}\colon C_{27} \to C_{28}$	$v_{18f} = k_{18f}x_{27}$
$\text{NLKP} + \text{P10} \overset{k_{19f}}{\underset{k_{19r}}{\rightleftarrows}} \text{NLKP\_P10}$	$R_{19f}\colon C_{29} \to C_{30}$	$v_{19f} = k_{19f}x_{20}x_{29}$
	$R_{19r}\colon C_{30} \to C_{29}$	$v_{19r} = k_{19r}x_{28}$
$\text{NLKP\_P10} \overset{k_{20f}}{\to} \text{NLK} + \text{P10}$	$R_{20f}\colon C_{30} \to C_{31}$	$v_{20f} = k_{20f}x_{28}$
$\text{SMAD2P} + \text{SMAD4} \overset{k_{21f}}{\underset{k_{21r}}{\rightleftarrows}} \text{SMAD2P\_SMAD4}$	$R_{21f}\colon C_{32} \to C_{33}$	$v_{21f} = k_{21f}x_{12}x_{30}$
	$R_{21r}\colon C_{33} \to C_{32}$	$v_{21r} = k_{21r}x_{31}$
$\text{SMAD3P} + \text{SMAD4} \overset{k_{22f}}{\underset{k_{22r}}{\rightleftarrows}} \text{SMAD3P\_SMAD4}$	$R_{22f}\colon C_{34} \to C_{35}$	$v_{22f} = k_{22f}x_{15}x_{30}$
	$R_{22r}\colon C_{35} \to C_{34}$	$v_{22r} = k_{22r}x_{32}$

Reaction	Variable	Flux
SMAD3P + PP1A $\underset{k_{23r}}{\overset{k_{23f}}{\rightleftarrows}}$ SMAD3P_PP1A	$R_{23f}: C_{36} \to C_{37}$	$v_{23f} = k_{23f} x_{15} x_{33}$
	$R_{23r}: C_{37} \to C_{36}$	$v_{23r} = k_{23r} x_{34}$
SMAD3P_PP1A $\overset{k_{24f}}{\to}$ SMAD3 + PP1A	$R_{24f}: C_{37} \to C_{38}$	$v_{24f} = k_{24f} x_{34}$
SMAD2P + PP1A $\underset{k_{25r}}{\overset{k_{25f}}{\rightleftarrows}}$ SMAD2P_PP1A	$R_{25f}: C_{39} \to C_{40}$	$v_{25f} = k_{25f} x_{12} x_{33}$
	$R_{25r}: C_{40} \to C_{39}$	$v_{25r} = k_{25r} x_{35}$
SMAD2P_PP1A $\overset{k_{26f}}{\to}$ SMAD2 + PP1A	$R_{26f}: C_{40} \to C_{41}$	$v_{26f} = k_{26f} x_{35}$
2TGF_2TBR2 + 2TBR1P $\underset{k_{27r}}{\overset{k_{27f}}{\rightleftarrows}}$ 2TGF_2TBR2_2TBR1P	$R_{27f}: C_{42} \to C_6$	$v_{27f} = k_{27f} x_3 x_{36}$
	$R_{27r}: C_6 \to C_{42}$	$v_{27r} = k_{27r} x_6$
2TBR1P + PP1C $\underset{k_{28r}}{\overset{k_{28f}}{\rightleftarrows}}$ 2TBR1P_PP1C	$R_{28f}: C_{43} \to C_{44}$	$v_{28f} = k_{28f} x_{36} x_7$
	$R_{28r}: C_{44} \to C_{43}$	$v_{28r} = k_{28r} x_{37}$
2TBR1P_PP1C $\overset{k_{29f}}{\to}$ 2TBR1 + PP1C	$R_{29f}: C_{44} \to C_{45}$	$v_{29f} = k_{29f} x_{37}$
~~WNT + FRZ $\underset{k_{30r}}{\overset{k_{30f}}{\rightleftarrows}}$ WNT_FRZ~~ FRZ $\underset{k_{30r}}{\overset{k_{30f} x_{i2}}{\rightleftarrows}}$ WNT_FRZ	$R_{30f}: C_{46} \to C_{47}$	$v_{30f} = k_{30f} x_{i2} x_{38}$
	$R_{30r}: C_{47} \to C_{46}$	$v_{30r} = k_{30r} x_{39}$
WNT_FRZ + LRP6 $\underset{k_{31r}}{\overset{k_{31f}}{\rightleftarrows}}$ WNT_FRZ_LRP6	$R_{31f}: C_{48} \to C_{49}$	$v_{31f} = k_{31f} x_{39} x_{40}$
	$R_{31r}: C_{49} \to C_{48}$	$v_{31r} = k_{31r} x_{41}$
WNT_FRZ_LRP6 + DVL $\underset{k_{32r}}{\overset{k_{32f}}{\rightleftarrows}}$ WNT_FRZ_LRP6_DVL	$R_{32f}: C_{50} \to C_{51}$	$v_{32f} = k_{32f} x_{41} x_{42}$
	$R_{32r}: C_{51} \to C_{50}$	$v_{32r} = k_{32r} x_{43}$
WNT_FRZ_LRP6 + TAK $\underset{k_{33r}}{\overset{k_{33f}}{\rightleftarrows}}$ WNT_FRZ_LRP6_TAK	$R_{33f}: C_{52} \to C_{53}$	$v_{33f} = k_{33f} x_{41} x_{16}$
	$R_{33r}: C_{53} \to C_{52}$	$v_{33r} = k_{33r} x_{44}$
WNT_FRZ_LRP6_TAK $\overset{k_{34f}}{\to}$ WNT_FRZ_LRP6+ TAKP	$R_{34f}: C_{53} \to C_{54}$	$v_{34f} = k_{34f} x_{44}$
TAKP + TAB $\underset{k_{35r}}{\overset{k_{35f}}{\rightleftarrows}}$ TAKP_TAB	$R_{35f}: C_{55} \to C_{56}$	$v_{35f} = k_{35f} x_{18} x_{45}$
	$R_{35r}: C_{56} \to C_{55}$	$v_{35r} = k_{35r} x_{46}$
TAKP_TAB + NLK $\underset{k_{36r}}{\overset{k_{36f}}{\rightleftarrows}}$ TAKP_TAB_NLK	$R_{36f}: C_{57} \to C_{58}$	$v_{36f} = k_{36f} x_{46} x_{19}$
	$R_{36r}: C_{58} \to C_{57}$	$v_{36r} = k_{36r} x_{47}$
TAKP_TAB_NLK $\overset{k_{37f}}{\to}$ TAKP_TAB + NLKP	$R_{37f}: C_{58} \to C_{59}$	$v_{37f} = k_{37f} x_{47}$
GROUCHO + TCFLEF $\underset{k_{38r}}{\overset{k_{38f}}{\rightleftarrows}}$ GROUCHO_TCFLEF	$R_{38f}: C_{60} \to C_{61}$	$v_{38f} = k_{38f} x_{48} x_{21}$
	$R_{38r}: C_{61} \to C_{60}$	$v_{38r} = k_{38r} x_{49}$
SMAD4 + TCFLEF $\underset{k_{39r}}{\overset{k_{39f}}{\rightleftarrows}}$ SMAD4_TCFLEF	$R_{39f}: C_{62} \to C_{63}$	$v_{39f} = k_{39f} x_{30} x_{21}$
	$R_{39r}: C_{63} \to C_{62}$	$v_{39r} = k_{39r} x_{50}$

TABLE D.3: List of TGFβ-pathway chemical reactions: reaction in chemical form, variable as function between chemical complexes, and flux as product of reaction rate constants and species concentrations. The notations follow the convention of f for forward and r for reverse, both in the reaction, flux, and rate constant variables. Coupled forward-reverse components have the same index number.

D.4 System of ODEs: $\dot{x} = Sv$

$$\dot{x_1} = v_{1f} - v_{1r} - v_{2f} + v_{2r} \tag{D.4.1}$$
$$\dot{x_2} = -v_{2f} + v_{2r} + v_{7f} - v_{7r} \tag{D.4.2}$$
$$\dot{x_3} = v_{2f} - v_{2r} - v_{3f} + v_{3r} - v_{27f} + v_{27r} \tag{D.4.3}$$
$$\dot{x_4} = -v_{3f} + v_{3r} + v_{6f} - v_{6r} + v_{29f} \tag{D.4.4}$$
$$\dot{x_5} = v_{3f} - v_{3r} - v_{4f} \tag{D.4.5}$$
$$\dot{x_6} = v_{4f} - v_{5f} + v_{5r} + v_{8f} - v_{9f} + v_{9r} + v_{10f} - v_{11f} + v_{11r} + v_{12f} + v_{27f} - v_{27r} \tag{D.4.6}$$
$$\dot{x_7} = -v_{28f} + v_{28r} + v_{29f} \tag{D.4.7}$$
$$\dot{x_8} = -v_{5f} + v_{5r} + v_{26f} \tag{D.4.8}$$
$$\dot{x_9} = v_{5f} - v_{5r} - v_{8f} \tag{D.4.9}$$
$$\dot{x_{10}} = -2v_{6f} + 2v_{6r} \tag{D.4.10}$$
$$\dot{x_{11}} = -2v_{7f} + 2v_{7r} \tag{D.4.11}$$
$$\dot{x_{12}} = v_{8f} - v_{21f} + v_{21r} - v_{25f} + v_{25r} \tag{D.4.12}$$
$$\dot{x_{13}} = -v_{9f} + v_{9r} + v_{24f} \tag{D.4.13}$$
$$\dot{x_{14}} = v_{9f} - v_{9r} - v_{10f} \tag{D.4.14}$$
$$\dot{x_{15}} = v_{10f} - v_{22f} + v_{22r} - v_{23f} + v_{23r} \tag{D.4.15}$$
$$\dot{x_{16}} = -v_{11f} + v_{11r} + v_{18f} - v_{33f} + v_{33r} \tag{D.4.16}$$
$$\dot{x_{17}} = v_{11f} - v_{11r} - v_{12f} \tag{D.4.17}$$
$$\dot{x_{18}} = v_{12f} - v_{17f} + v_{17r} + v_{34f} - v_{35f} + v_{35r} \tag{D.4.18}$$
$$\dot{x_{19}} = v_{20f} - v_{36f} + v_{36r} \tag{D.4.19}$$
$$\dot{x_{20}} = -v_{13f} + v_{13r} + v_{14f} - v_{19f} + v_{19r} + v_{37f} \tag{D.4.20}$$
$$\dot{x_{21}} = -v_{13f} + v_{13r} + v_{16f} - v_{38f} + v_{38r} - v_{39f} + v_{39r} \tag{D.4.21}$$
$$\dot{x_{22}} = v_{13f} - v_{13r} - v_{14f} \tag{D.4.22}$$
$$\dot{x_{23}} = v_{14f} - v_{15f} + v_{15r} \tag{D.4.23}$$
$$\dot{x_{24}} = -v_{15f} + v_{15r} + v_{16f} \tag{D.4.24}$$
$$\dot{x_{25}} = v_{15f} - v_{15r} - v_{16f} \tag{D.4.25}$$
$$\dot{x_{26}} = -v_{17f} + v_{17r} + v_{18f} \tag{D.4.26}$$
$$\dot{x_{27}} = v_{17f} - v_{17r} - v_{18f} \tag{D.4.27}$$
$$\dot{x_{28}} = v_{19f} - v_{19r} - v_{20f} \tag{D.4.28}$$
$$\dot{x_{29}} = -v_{19f} + v_{19r} + v_{20f} \tag{D.4.29}$$
$$\dot{x_{30}} = -v_{21f} + v_{21r} - v_{22f} + v_{22r} - v_{39f} + v_{39r} \tag{D.4.30}$$
$$\dot{x_{31}} = v_{21f} - v_{21r} \tag{D.4.31}$$
$$\dot{x_{32}} = v_{22f} - v_{22r} \tag{D.4.32}$$
$$\dot{x_{33}} = -v_{23f} + v_{23r} + v_{24f} - v_{25f} + v_{25r} + v_{26f} \tag{D.4.33}$$
$$\dot{x_{34}} = v_{23f} - v_{23r} - v_{24f} \tag{D.4.34}$$
$$\dot{x_{35}} = v_{25f} - v_{25r} - v_{26f} \tag{D.4.35}$$
$$\dot{x_{36}} = -v_{27f} + v_{27r} - v_{28f} + v_{28r} \tag{D.4.36}$$
$$\dot{x_{37}} = v_{28f} - v_{28r} - v_{29f} \tag{D.4.37}$$
$$\dot{x_{38}} = -v_{30f} + v_{30r} \tag{D.4.38}$$
$$\dot{x_{39}} = v_{30f} - v_{30r} - v_{31f} + v_{31r} \tag{D.4.39}$$
$$\dot{x_{40}} = -v_{31f} + v_{31r} \tag{D.4.40}$$
$$\dot{x_{41}} = v_{31f} - v_{31r} - v_{32f} + v_{32r} - v_{33f} + v_{33r} + v_{34f} \tag{D.4.41}$$
$$\dot{x_{42}} = -v_{32f} + v_{32r} \tag{D.4.42}$$
$$\dot{x_{43}} = v_{32f} - v_{32r} \tag{D.4.43}$$
$$\dot{x_{44}} = v_{33f} - v_{33r} - v_{34f} \tag{D.4.44}$$
$$\dot{x_{45}} = -v_{35f} + v_{35r} \tag{D.4.45}$$
$$\dot{x_{46}} = v_{35f} - v_{35r} - v_{36f} + v_{36r} + v_{37f} \tag{D.4.46}$$
$$\dot{x_{47}} = v_{36f} - v_{36r} - v_{37f} \tag{D.4.47}$$
$$\dot{x_{48}} = -v_{38f} + v_{38r} \tag{D.4.48}$$
$$\dot{x_{49}} = v_{38f} - v_{38r} \tag{D.4.49}$$
$$\dot{x_{50}} = v_{39f} - v_{39r} \tag{D.4.50}$$

D.5 Conserved cycles

The conserved cycles are linear combinations of specific differential equations equal to zero, and indicate conserved quantities.

$$\dot{x_7} + \dot{x_{37}} = 0 \tag{D.5.1}$$
$$\dot{x_8} + \dot{x_9} + \dot{x_{12}} + \dot{x_{31}} + \dot{x_{35}} = 0 \tag{D.5.2}$$
$$2 \cdot \dot{x_4} + 2 \cdot \dot{x_5} + 2 \cdot \dot{x_6} + 2 \cdot \dot{x_9} + \underline{\dot{x_{10}}} + 2 \cdot \dot{x_{14}} + 2 \cdot \dot{x_{17}} + 2 \cdot \dot{x_{36}} + 2 \cdot \dot{x_{37}} = 0 \tag{D.5.3}$$
$$2 \cdot \dot{x_2} + 2 \cdot \dot{x_3} + 2 \cdot \dot{x_5} + 2 \cdot \dot{x_6} + 2 \cdot \dot{x_9} + \underline{\dot{x_{11}}} + 2 \cdot \dot{x_{14}} + 2 \cdot \dot{x_{17}} = 0 \tag{D.5.4}$$
$$\dot{x_{13}} + \dot{x_{14}} + \dot{x_{15}} + \dot{x_{32}} + \dot{x_{34}} = 0 \tag{D.5.5}$$
$$\dot{x_{16}} + \dot{x_{17}} + \dot{x_{18}} + \dot{x_{27}} + \dot{x_{44}} + \dot{x_{46}} + \dot{x_{47}} = 0 \tag{D.5.6}$$
$$\dot{x_{19}} + \dot{x_{20}} + \dot{x_{22}} + \dot{x_{28}} + \dot{x_{47}} = 0 \tag{D.5.7}$$
$$\dot{x_{21}} + \dot{x_{22}} + \dot{x_{23}} + \dot{x_{25}} + \dot{x_{49}} + \dot{x_{50}} = 0 \tag{D.5.8}$$
$$\dot{x_{24}} + \dot{x_{25}} = 0 \tag{D.5.9}$$
$$\dot{x_{26}} + \dot{x_{27}} = 0 \tag{D.5.10}$$
$$\dot{x_{29}} + \dot{x_{28}} = 0 \tag{D.5.11}$$
$$\dot{x_{30}} + \dot{x_{31}} + \dot{x_{32}} + \dot{x_{50}} = 0 \tag{D.5.12}$$
$$\dot{x_{33}} + \dot{x_{34}} + \dot{x_{35}} = 0 \tag{D.5.13}$$
$$\dot{x_{38}} + \dot{x_{39}} + \dot{x_{41}} + \dot{x_{43}} + \dot{x_{44}} = 0 \tag{D.5.14}$$
$$\dot{x_{40}} + \dot{x_{41}} + \dot{x_{43}} + \dot{x_{44}} = 0 \tag{D.5.15}$$
$$\dot{x_{42}} + \dot{x_{43}} = 0 \tag{D.5.16}$$
$$\dot{x_{45}} + \dot{x_{46}} + \dot{x_{47}} = 0 \tag{D.5.17}$$
$$\dot{x_{48}} + \dot{x_{49}} = 0 \tag{D.5.18}$$

By integrating in time the conserved cycle equations, the following formal explicit expressions for the concentrations of the basic species are obtained. The dependence on the time variable is omitted but implied.

$$x_7 = x_7(0) - x_{37} \tag{D.5.19}$$
$$x_8 = x_8(0) - (x_9 + x_{12} + x_{31} + x_{35}) \tag{D.5.20}$$
$$x_{10} = x_{10}(0) - 2 \cdot (x_4 + x_5 + x_6 + x_9 + x_{14} + x_{17} + x_{36} + x_{37}) \tag{D.5.21}$$
$$x_{11} = x_{11}(0) - 2 \cdot (x_2 + x_3 + x_5 + x_6 + x_9 + x_{14} + x_{17}) \tag{D.5.22}$$
$$x_{13} = x_{13}(0) - (x_{14} + x_{15} + x_{32} + x_{34}) \tag{D.5.23}$$
$$x_{16} = x_{16}(0) - (x_{17} + x_{18} + x_{27} + x_{44} + x_{46} + x_{47}) \tag{D.5.24}$$
$$x_{19} = x_{19}(0) - (x_{20} + x_{22} + x_{28} + x_{47}) \tag{D.5.25}$$
$$x_{21} = x_{21}(0) - (x_{22} + x_{23} + x_{25} + x_{49} + x_{50}) \tag{D.5.26}$$
$$x_{24} = x_{24}(0) - x_{25} \tag{D.5.27}$$
$$x_{26} = x_{26}(0) - x_{27} \tag{D.5.28}$$
$$x_{29} = x_{29}(0) - x_{28} \tag{D.5.29}$$
$$x_{30} = x_{30}(0) - (x_{31} + x_{32} + x_{50}) \tag{D.5.30}$$
$$x_{33} = x_{33}(0) - (x_{34} + x_{35}) \tag{D.5.31}$$
$$x_{38} = x_{38}(0) - (x_{39} + x_{41} + x_{43} + x_{44}) \tag{D.5.32}$$
$$x_{40} = x_{40}(0) - (x_{41} + x_{43} + x_{44}) \tag{D.5.33}$$
$$x_{42} = x_{42}(0) - x_{43} \tag{D.5.34}$$
$$x_{45} = x_{45}(0) - (x_{46} + x_{47}) \tag{D.5.35}$$
$$x_{48} = x_{48}(0) - x_{49} \tag{D.5.36}$$

D.6 System at equilibrium: $\dot{x} = Sv = 0$

$$v_{1f} - v_{1r} = 0 \qquad \frac{k_{1r}}{k_{1f}} = \frac{x_{i1}^2}{x_1} \qquad k_{1r} = k_{1f}\frac{x_{i1}^2}{x_1} \tag{D.6.1}$$

$$v_{2f} - v_{2r} = 0 \qquad \frac{k_{2r}}{k_{2f}} = \frac{x_1 x_2}{x_3} \qquad k_{2r} = k_{2f}\frac{x_1 x_2}{x_3} \tag{D.6.2}$$

$$v_{3f} - v_{3r} - v_{4f} = 0 \qquad \frac{k_{3r} + k_{4f}}{k_{3f}} = \frac{x_3 x_4}{x_5} \qquad k_{3r} = k_{3f}\frac{x_3 x_4}{x_5} - k_{4f} > 0 \tag{D.6.3}$$

$$v_{5f} - v_{5r} - v_{8f} = 0 \qquad \frac{k_{5r} + k_{8f}}{k_{5f}} = \frac{x_6 x_8}{x_9} \qquad k_{5r} = k_{5f}\frac{x_6 x_8}{x_9} - k_{8f} > 0 \tag{D.6.4}$$

$$v_{6f} - v_{6r} = 0 \qquad \frac{k_{6r}}{k_{6f}} = \frac{x_{10}^2}{x_4} \qquad k_{6r} = k_{6f}\frac{x_{10}^2}{x_4} \tag{D.6.5}$$

$$v_{7f} - v_{7r} = 0 \qquad \frac{k_{7r}}{k_{7f}} = \frac{x_{11}^2}{x_2} \qquad k_{7r} = k_{7f}\frac{x_{11}^2}{x_2} \tag{D.6.6}$$

$$v_{9f} - v_{9r} - v_{10f} = 0 \qquad \frac{k_{9r} + k_{10f}}{k_{9f}} = \frac{x_6 x_{13}}{x_{14}} \qquad k_{9r} = k_{9f}\frac{x_6 x_{13}}{x_{14}} - k_{10f} > 0 \tag{D.6.7}$$

$$v_{11f} - v_{11r} - v_{12f} = 0 \qquad \frac{k_{11r} + k_{12f}}{k_{11f}} = \frac{x_6 x_{16}}{x_{17}} \qquad k_{11r} = k_{11f}\frac{x_6 x_{16}}{x_{17}} - k_{12f} > 0 \tag{D.6.8}$$

$$v_{13f} - v_{13r} - v_{14f} = 0 \qquad \frac{k_{13r} + k_{14f}}{k_{13f}} = \frac{x_{20} x_{21}}{x_{22}} \qquad k_{13r} = k_{13f}\frac{x_{20} x_{21}}{x_{22}} - k_{14f} > 0 \tag{D.6.9}$$

$$v_{15f} - v_{15r} - v_{16f} = 0 \qquad \frac{k_{15r} + k_{16f}}{k_{15f}} = \frac{x_{23} x_{24}}{x_{25}} \qquad k_{15r} = k_{15f}\frac{x_{23} x_{24}}{x_{25}} - k_{16f} > 0 \tag{D.6.10}$$

$$v_{17f} - v_{17r} - v_{18f} = 0 \qquad \frac{k_{17r} + k_{18f}}{k_{17f}} = \frac{x_{18} x_{26}}{x_{27}} \qquad k_{17r} = k_{17f}\frac{x_{18} x_{26}}{x_{27}} - k_{18f} > 0 \tag{D.6.11}$$

$$v_{19f} - v_{19r} - v_{20f} = 0 \qquad \frac{k_{19r} + k_{20f}}{k_{19f}} = \frac{x_{20} x_{29}}{x_{28}} \qquad k_{19r} = k_{19f}\frac{x_{20} x_{29}}{x_{28}} - k_{20f} > 0 \tag{D.6.12}$$

$$v_{21f} - v_{21r} = 0 \qquad \frac{k_{21r}}{k_{21f}} = \frac{x_{12} x_{30}}{x_{31}} \qquad k_{21r} = k_{21f}\frac{x_{12} x_{30}}{x_{31}} \tag{D.6.13}$$

$$v_{22f} - v_{22r} = 0 \qquad \frac{k_{22r}}{k_{22f}} = \frac{x_{15} x_{30}}{x_{32}} \qquad k_{22r} = k_{22f}\frac{x_{15} x_{30}}{x_{32}} \tag{D.6.14}$$

$$v_{23f} - v_{23r} - v_{24f} = 0 \qquad \frac{k_{23r} + k_{24f}}{k_{23f}} = \frac{x_{15} x_{33}}{x_{34}} \qquad k_{23r} = k_{23f}\frac{x_{15} x_{33}}{x_{34}} - k_{24f} > 0 \tag{D.6.15}$$

$$v_{25f} - v_{25r} - v_{26f} = 0 \qquad \frac{k_{25r} + k_{26f}}{k_{25f}} = \frac{x_{12} x_{33}}{x_{35}} \qquad k_{25r} = k_{25f}\frac{x_{12} x_{33}}{x_{35}} - k_{26f} > 0 \tag{D.6.16}$$

$$v_{27f} - v_{27r} + v_{4f} = 0 \qquad k_{27r} = \frac{k_{27f} x_3 x_{36} + k_{4f} x_5}{x_6} \tag{D.6.17}$$

$$v_{28f} - v_{28r} - v_{29f} = 0 \qquad \frac{k_{28r} + k_{29f}}{k_{28f}} = \frac{x_{36} x_7}{x_{37}} \qquad k_{28r} = k_{28f}\frac{x_{36} x_7}{x_{37}} - k_{29f} > 0 \tag{D.6.18}$$

$$v_{30f} - v_{30r} = 0 \qquad \frac{k_{30r}}{k_{30f}} = \frac{x_{i2} x_{38}}{x_{39}} \qquad k_{30r} = k_{30f}\frac{x_{i2} x_{38}}{x_{39}} \tag{D.6.19}$$

$$v_{31f} - v_{31r} = 0 \qquad \frac{k_{31r}}{k_{31f}} = \frac{x_{39} x_{40}}{x_{41}} \qquad k_{31r} = k_{31f}\frac{x_{39} x_{40}}{x_{41}} \tag{D.6.20}$$

$$v_{32f} - v_{32r} = 0 \qquad \frac{k_{32r}}{k_{32f}} = \frac{x_{41} x_{42}}{x_{43}} \qquad k_{32r} = k_{32f}\frac{x_{41} x_{42}}{x_{43}} \tag{D.6.21}$$

$$v_{33f} - v_{33r} - v_{34f} = 0 \qquad \frac{k_{33r} + k_{34f}}{k_{33f}} = \frac{x_{41} x_{16}}{x_{44}} \qquad k_{33r} = k_{33f}\frac{x_{41} x_{16}}{x_{44}} - k_{34f} > 0 \tag{D.6.22}$$

$$v_{35f} - v_{35r} = 0 \qquad \frac{k_{35r}}{k_{35f}} = \frac{x_{18} x_{45}}{x_{46}} \qquad k_{35r} = k_{35f}\frac{x_{18} x_{45}}{x_{46}} \tag{D.6.23}$$

$$v_{36f} - v_{36r} - v_{37f} = 0 \qquad \frac{k_{36r} + k_{37f}}{k_{36f}} = \frac{x_{46} x_{19}}{x_{47}} \qquad k_{36r} = k_{36f}\frac{x_{46} x_{19}}{x_{47}} - k_{37f} > 0 \tag{D.6.24}$$

$$v_{38f} - v_{38r} = 0 \qquad \frac{k_{38r}}{k_{38f}} = \frac{x_{48} x_{21}}{x_{49}} \qquad k_{38r} = k_{38f}\frac{x_{48} x_{21}}{x_{49}} \tag{D.6.25}$$

$$v_{39f} - v_{39r} = 0 \qquad \frac{k_{39r}}{k_{39f}} = \frac{x_{30} x_{21}}{x_{50}} \qquad k_{39r} = k_{39f}\frac{x_{30} x_{21}}{x_{50}} \tag{D.6.26}$$

$$v_{14f} - v_{16f} = 0 \qquad \frac{k_{16f}}{k_{14f}} = \frac{x_{22}}{x_{25}} \qquad k_{16f} = k_{14f}\frac{x_{22}}{x_{25}} \tag{D.6.27}$$

$$v_{10f} - v_{24f} = 0 \qquad \frac{k_{24f}}{k_{10f}} = \frac{x_{14}}{x_{34}} \qquad k_{24f} = k_{10f}\frac{x_{14}}{x_{34}} \tag{D.6.28}$$

$$v_{8f} - v_{26f} = 0 \qquad \frac{k_{26f}}{k_{8f}} = \frac{x_{9}}{x_{35}} \qquad k_{26f} = k_{8f}\frac{x_{9}}{x_{35}} \tag{D.6.29}$$

$$v_{4f} - v_{29f} = 0 \qquad \frac{k_{29f}}{k_{4f}} = \frac{x_{5}}{x_{37}} \qquad k_{29f} = k_{4f}\frac{x_{5}}{x_{37}} \tag{D.6.30}$$

$$v_{12f} - v_{18f} + v_{34f} = 0 \qquad\qquad k_{34f} = \frac{k_{18f}x_{27} - k_{12f}x_{17}}{x_{44}} > 0 \tag{D.6.31}$$

$$v_{20f} - v_{37f} = 0 \qquad \frac{k_{37f}}{k_{20f}} = \frac{x_{28}}{x_{47}} \qquad k_{37f} = k_{20f}\frac{x_{28}}{x_{47}} \tag{D.6.32}$$

Bibliography

Aladjem, M.I. et al. (2004). "Molecular Interaction Maps–A Diagrammatic Graphical Language for Bioregulatory Networks". In: *Science Signaling* 2004.222, pe8. DOI: 10.1126/stke.2222004pe8.

Ambrosi, C. De et al. (2013). "Parameter space exploration within dynamic simulations of signaling networks". In: *Mathematical biosciences and engineering* 10.1, pp. 103–120. DOI: 10.3934/mbe.2013.10.103.

Angeli, D., P. De Leenheer, and E. Sontag (2010). "Graph-theoretic characterizations of monotonicity of chemical networks in reaction coordinates". In: *Journal of Mathematical Biology* 61.4, pp. 581–616. DOI: 10.1007/s00285-009-0309-0.

Annibaldi, A. and C. Widmann (2010). "Glucose metabolism in cancer cells". In: *Current Opinion in Clinical Nutrition and Metabolic Care* 13.4, pp. 466–470. DOI: 10.1097/MCO.0b013e32833a5577.

Arceo, C.P.P. et al. (2015). "Chemical reaction network approaches to Biochemical Systems Theory". In: *Mathematical Biosciences* 269, pp. 135–152. DOI: 110.1016/j.mbs.2015.08.022.

Ashyraliyev, M., J. Jaeger, and J.G. Blom (2008). "Parameter estimation and determinability analysis applied to Drosophila gap gene circuits". In: *BMC Systems Biology* 2.83. DOI: 10.1186/1752-0509-2-83.

Ashyraliyev, M. et al. (2008). "Systems biology: parameter estimation for biochemical models". In: *The FEBS Journal* 276.4, pp. 886–902. DOI: 10.1111/j.1742-4658.2008.06844.x.

Bailey, D.L. et al. (2005). *Positron Emission Tomography: Basic Sciences*. Springer-Verlag London. DOI: 10.1007/b136169.

Ballnus, B. et al. (2017). "Comprehensive benchmarking of Markov chain Monte Carlo methods for dynamical systems". In: *BMC Systems Biology* 11.1, p. 63. DOI: 10.1186/s12918-017-0433-1.

Barabási, A.L. and Z.N. Oltvai (2004). "Network biology: understanding the cell's functional organization". In: *Nature Reviews Genetics* 5, pp. 101–113. DOI: 10.1038/nrg1272.

Basu, A. et al. (2000). "Effects of type 2 diabetes on the ability of insulin and glucose to regulate splanchnic and muscle glucose metabolism: evidence for a defect in hepatic glucokinase activity". In: *Diabetes* 49.2, pp. 272–283. DOI: 10.2337/diabetes.49.2.272.

Bauer, F., T. Hohage, and A. Munk (2009). "Iteratively Regularized Gauss-Newton Method for Nonlinear Inverse Problems with Random Noise". In: *SIAM Journal on Numerical Analysis* 47.3, pp. 1827–1846. DOI: 10.1137/080721789.

Bertero, M. and P. Boccacci (1998). *Introduction to Inverse Problems in Imaging*. IOP Publishing Bristol.

Berthollet, C.L. (1803). *Essai de statique chimique*. Paris, France.

Bertoldo, A. et al. (2001). "Kinetic modeling of [18F]FDG in skeletal muscle by PET: a four-compartment five-rate-constant model". In: *American Journal of Physiology-Endocrinology and Metabolism* 281.3, E524–E536. DOI: 10.1152/ajpendo.2001.281.3.E524.

Björke, H. and K. Andersson (2006a). "Automated, high-resolution cellular retention and uptake studies in vitro". In: *Applied Radiation and Isotopes* 64.8, pp. 901–905. DOI: 10.1016/j.apradiso.2006.03.002.

— (2006b). "Measuring the affinity of a radioligand with its receptor using a rotating cell dish with in situ reference area". In: *Applied Radiation and Isotopes* 64.1, pp. 32–37. DOI: 10.1016/j.apradiso.2005.06.007.

Bortz, D.M. and P.W. Nelson (2006). "Model Selection and Mixed-Effects Modeling of HIV Infection Dynamics". In: *Bulletin of Mathematical Biology* 68.8, pp. 2005–2025. DOI: 10.1007/s11538-006-9084-x.

Boyd, S. and L. Vandenberghe (2004). *Convex optimization*. Cambridge university press.

Brooks, S. et al. (2011). *Handbook of Markov Chain Monte Carlo*. Chapman & Hall/CRC press.

Bruker (2012). "Albira Imaging". In: *Bruker Albira Imaging System User Manual*.

Bullinger, E. and F. Allgower (1997). "An adaptive high-gain observer for nonlinear systems". In: *Proceedings of the 36th IEEE Conference on Decision and Control* 5, pp. 4348–4353. DOI: 10.1109/CDC.1997.649541.

Busetto, A.G. and J.M. Buhmann (2009). "Stable Bayesian Parameter Estimation for Biological Dynamical Systems". In: *2009 International Conference on Computational Science and Engineering* 1, pp. 148–157. DOI: 10.1109/CSE.2009.134.

Cairns, R.A., I.S. Harris, and T.W. Mak (2011). "Regulation of cancer cell metabolism". In: *Nature Reviews Cancer* 11.2, pp. 85–95. DOI: 10.1038/nrc2981.

Carson, R.E. (2005). "Tracer Kinetic Modeling in PET". In: *Positron Emission Tomography: Basic Sciences*. Ed. by P.E. Valk D.L. Bailey D.W. Townsend and M.N. Maisey. Springer London, pp. 127–159. DOI: 10.1007/1-84628-007-9_6.

Carson, R.E. and K. Lange (1985). "Comment: the EM parametric image reconstruction algorithm". In: *Journal of the American Statistical Association* 80.389, pp. 20–22. DOI: 10.1080/01621459.1985.10477120.

Castagnino, N. et al. (2010). "Dynamic Simulations of Pathways Downstream of ERBB-Family, Including Mutations and Treatments: Concordance with Experimental Results". In: *Current Cancer Drug Targets* 10.7, pp. 737–757. DOI: 10.2174/156800910793605848.

Cherry, S.R., J.A. Sorenson, and M.E. Phelps (2012). *Physics in Nuclear Medicine*. Elsevier Health Sciences.

Chou, J.Y., H.S. Jun, and B.C. Mansfield (2010). "Glycogen storage disease type I and G6Pase-β deficiency: etiology and therapy". In: *Nature Reviews Endocrinology* 6, pp. 676–688. DOI: 10.1038/nrendo.2010.189.

Csala, M., G. Bánhegyi, and A. Benedetti (2006). "Endoplasmic reticulum: A metabolic compartment". In: *FEBS Letters* 580.9, pp. 2160–2165. DOI: 10.1016/j.febslet.2006.03.050.

Csala, M. et al. (2007). "Transport and transporters in the endoplasmic reticulum". In: *Biochimica et Biophysica Acta (BBA) - Biomembranes* 1768.6, pp. 1325–1341. DOI: 10.1016/j.bbamem.2007.03.009.

Delbary, F. and S. Garbarino (2018). "Compartmental analysis of dynamic nuclear medicine data: regularization procedure and application to physiology". In: *Inverse Problems in Science and Engineering* 0.0, pp. 1–19. DOI: 10.1080/17415977.2018.1512603.

Delbary, F., S. Garbarino, and V. Vivaldi (2016). "Compartmental analysis of dynamic nuclear medicine data: models and identifiability". In: *Inverse Problems* 32.12, p. 125010. DOI: 10.1088/0266-5611/32/12/125010.

Domijan, M. and M. Kirkilionis (2008). "Graph theory and qualitative analysis of reaction networks". In: *Networks & Heterogeneous Media* 3.2, pp. 295–322. DOI: 10.3934/nhm.2008.3.295.

Engl, H.W. et al. (2009). "Inverse problems in systems biology". In: *Inverse Problems* 25.12, p. 123014. DOI: 10.1088/0266-5611/25/12/123014.

Feinberg, M. (1972). "Complex balancing in general kinetic systems". In: *Archive for Rational Mechanics and Analysis* 49.3, pp. 187–194. DOI: 10.1007/BF00255665.

— (1979). "Lectures on chemical reaction networks". In: *University of Wisconsin*. URL: http://www.crnt.osu.edu/LecturesOnReactionNetworks.

— (1987). "Chemical reaction network structure and the stability of complex isothermal reactors –I. The deficiency zero and deficiency one theorems". In: *Chemical Engineering Science* 42.10, pp. 2229–2268. DOI: 10.1016/0009-2509(87)80099-4.

— (1995). "The existence and uniqueness of steady states for a class of chemical reaction networks". In: *Archive for Rational Mechanics and Analysis* 1332.4, pp. 311–370. DOI: 10.1007/BF00375614.

Frank, T.D., A.M. Carmody, and B.N. Kholodenko (2012). "Versatility of Cooperative Transcriptional Activation: A Thermodynamical Modeling Analysis for Greater-Than-Additive and Less-Than-Additive Effects". In: *PLOS ONE* 7.4, pp. 1–15. DOI: 10.1371/journal.pone.0034439.

Fröhlich, F. et al. (2017). "Scalable Parameter Estimation for Genome-Scale Biochemical Reaction Networks". In: *PLOS Computational Biology* 13.1, pp. 1–18. DOI: 10.1371/journal.pcbi.1005331.

Garbarino, S. et al. (2014). "A novel description of FDG excretion in the renal system: application to metformin-treated models". In: *Physics in Medicine & Biology* 59.10, p. 2469. DOI: 10.1088/0031-9155/59/10/2469.

Garbarino, S. et al. (2015). "A new compartmental method for the analysis of liver FDG kinetics in small animal models". In: *EJNMMI Research* 5, pp. 35–44. DOI: 10.1186/s13550-015-0107-1.

Garnier, C. (1897). "Les filaments basaux des cellules glandulaires. Note préliminaire". In: *Bibliographie anatomique* 5, pp. 278–289.

Gelman, A., G.O. Roberts, and W.R. Gilks (1996). "Efficient Metropolis jumping rules". In: *Bayesian Statistics 5*. Ed. by J.M. Bernardo et al. Oxford University Press, New York, pp. 599–607.

Ghosh, A. et al. (2002). "The catalytic center of glucose-6-phosphatase. HIS176 is the nucleophile forming the phosphohistidine-enzyme intermediate during catalysis". In: *The Journal of Biological Chemistry* 277.36, pp. 32837–32842. DOI: 10.1074/jbc.M201853200.

Gilks, W.R., S. Richardson, and D. Spiegelhalter (1995). *Markov chain Monte Carlo in Practice*. Chapman & Hall/CRC Interdisciplinary Statistics.

Ginovart, N. et al. (2001). "Positron Emission Tomography Quantification of [11C]-DASB Binding to the Human Serotonin Transporter: Modeling Strategies". In: *Journal of Cerebral Blood Flow & Metabolism* 21.11, pp. 1342–1353. DOI: 10.1097/00004647-200111000-00010.

Golish, S. Raymond et al. (2001). "A Fast Nonlinear Method for Parametric Imaging of Myocardial Perfusion by Dynamic 13N-Ammonia PET". In: *Journal of Nuclear Medicine* 42.6, pp. 924–931. URL: http://jnm.snmjournals.org/content/42/6/924.

Golub, G.H., M. Heath, and G. Wahba (1979). "Generalized Cross-Validation as a Method for Choosing a Good Ridge Parameter". In: *Technometrics* 21.2, pp. 215–223. DOI: 10.1080/00401706.1979.10489751.

Hastings, W.K. (1970). "Monte Carlo Sampling Methods Using Markov Chains and Their Applications". In: *Biometrika* 57, pp. 97–109. DOI: 10.1093/biomet/57.1.97.

Hearon, J.Z. (1963). "THEOREMS ON LINEAR SYSTEMS". In: *Annals of the New York Academy of Sciences* 108.1, pp. 36–68. DOI: 10.1111/j.1749-6632.1963.tb13364.x.

Hindel, S. et al. (2017). "Validation of Blood Volume Fraction Quantification with 3D Gradient Echo Dynamic Contrast-Enhanced Magnetic Resonance Imaging in Porcine Skeletal Muscle". In: *PLoS One* 12.1, e0170841. DOI: 10.1371/journal.pone.0170841.

Horn, F. (1972). "Necessary and sufficient conditions for complex balancing in chemical kinetics". In: *Archive for Rational Mechanics and Analysis* 49.3, pp. 172–186. DOI: 10.1007/BF00251225.

Horn, F. and R. Jackson (1972). "General mass action kinetics". In: *Archive for Rational Mechanics and Analysis* 47.2, pp. 81–116. DOI: 10.1007/BF00255664.

Hudson, H.M. and R.S. Larkin (1994). "Accelerated image reconstruction using ordered subsets of projection data". In: *IEEE Transactions on Medical Imaging* 13.4, pp. 601–609. DOI: 10.1109/42.363108.

Huesman, R.H. et al. (1998). "Kinetic parameter estimation from SPECT cone-beam projection measurements". In: *Physics in Medicine & Biology* 43.4, p. 973. DOI: 10.1088/0031-9155/43/4/024.

Hulhoven, X., A.V. Wouwer, and Ph. Bogaerts (2006). "Hybrid extended Luenberger-asymptotic observer for bioprocess state estimation". In: *Chemical Engineering Science* 61.21, pp. 7151–7160. DOI: 10.1016/j.ces.2006.06.018.

Iozzo, P. et al. (2003). "Effects of Metformin and Rosiglitazone Monotherapy on Insulin-Mediated Hepatic Glucose Uptake and Their Relation to Visceral Fat in Type 2 Diabetes". In: *Diabetes Care* 26.7, pp. 2069–2074. DOI: 10.2337/diacare.26.7.2069.

Ishibashi, K. et al. (2016). "Alteration of the regional cerebral glucose metabolism in healthy subjects by glucose loading". In: *Human Brain Mapping* 37.8, pp. 2823–28324. DOI: 10.1002/hbm.23210.

Joshi, B. and A. Shiu (2015). "A Survey of Methods for Deciding Whether a Reaction Network is Multistationary". In: *Mathematical Modelling of Natural Phenomena* 10.5, pp. 47–67. DOI: 10.1051/mmnp/201510504.

Kaipio, J. and E. Somersalo (2006). *Statistical and computational inverse problems*. Springer Science & Business Media. DOI: 10.1007/b138659.

Kamasak, M.E. et al. (2005). "Direct reconstruction of kinetic parameter images from dynamic PET data". In: *IEEE Transactions on Medical Imaging* 24.5, pp. 636–650. DOI: 10.1109/TMI.2005.845317.

Kirkpatrick, S., C.D. Gelatt, and M.P. Vecchi (1983). "Optimization by simulated annealing". In: *Science* 220, pp. 671–680.

Kohn, Kurt W et al. (2006). "Depicting combinatorial complexity with the molecular interaction map notation". In: *Molecular Systems Biology* 2.1, p. 51. DOI: 10.1038/msb4100088.

Kohn, K.W. (1999). "Molecular Interaction Map of the Mammalian Cell Cycle Control and DNA Repair Systems". In: *Molecular Biology of the Cell* 10.8, pp. 2703–2734. DOI: 10.1091/mbc.10.8.2703.

Lackner, R. et al. (1984). "A problem in the radiochemical assay of glucose-6-phosphatase in muscle". In: *Biochemical Journal* 218.2, pp. 649–651. DOI: 10.1042/bj2180649.

Lalush, D.S. and M.N. Wernick (2004). "Iterative Image Reconstruction". In: *Emission Tomography: The Fundamentals of PET and SPECT*. Ed. by M.N. Wernick and J.N.

Aarsvold. Academic Press, pp. 443–472. DOI: 10.1016/B978-012744482-6.50024-7.

Lammertsma, A.A. and S.P. Hume (1996). "Simplified Reference Tissue Model for PET Receptor Studies". In: *NeuroImage* 4.3, pp. 153–158. DOI: 10.1006/nimg.1996.0066.

Levenberg, K. (1944). "A METHOD FOR THE SOLUTION OF CERTAIN NON-LINEAR PROBLEMS IN LEAST SQUARES". In: *Quarterly of Applied Mathematics* 2.2, pp. 164–168. URL: http://www.jstor.org/stable/43633451.

Lillacci, G. and M. Khammash (2010). "Parameter Estimation and Model Selection in Computational Biology". In: *PLoS Computational Biology* 6.3, e1000696. DOI: 10.1371/journal.pcbi.1000696.

Limber, M.A. et al. (1995). "Direct reconstruction of functional parameters for dynamic SPECT". In: *IEEE Transactions on Nuclear Science* 42.4, pp. 1249–1256. DOI: 10.1109/23.467872.

Ljung, L. and T. Glad (1994). "On global identifiability for arbitrary model parametrizations". In: *Automatica* 30.2, pp. 265–276. DOI: 10.1016/0005-1098(94)90029-9.

Logan, J. (2003). "A review of graphical methods for tracer studies and strategies to reduce bias". In: *Nuclear Medicine and Biology* 30.8, pp. 833–844. DOI: 10.1016/S0969-8051(03)00114-8.

Logan, J. et al. (1990). "Graphical Analysis of Reversible Radioligand Binding from Time-Activity Measurements Applied to [N-11C-Methyl]-(–)-Cocaine PET Studies in Human Subjects". In: *Journal of Cerebral Blood Flow & Metabolism* 10.5, pp. 740–747. DOI: 10.1038/jcbfm.1990.127.

Lotka, A.J. (1909). "Contribution to the Theory of Periodic Reactions". In: *The Journal of Physical Chemistry* 14.3, pp. 271–274. DOI: 10.1021/j150111a004.

— (1925). *Elements of Physical Biology*. Williams and Wilkins, Baltimore.

Luisier, F., T. Blu, and M. Unser (2011). "Image Denoising in Mixed Poisson–Gaussian Noise". In: *IEEE Transactions on Image Processing* 20.3, pp. 696–708. DOI: 10.1109/TIP.2010.2073477.

Marini, C. et al. (2016). "Discovery of a novel glucose metabolism in cancer: The role of endoplasmic reticulum beyond glycolysis and pentose phosphate shunt". In: *Scientific Reports* 6.25092. DOI: 10.1038/srep25092.

Marquardt, D.W. (1962). "An Algorithm for Least-Squares Estimation of Nonlinear Parameters". In: *Journal of the Society for Industrial and Applied Mathematics* 11.2, pp. 431–441. DOI: 10.1137/0111030.

Massollo, M. et al. (2013). "Metformin Temporal and Localized Effects on Gut Glucose Metabolism Assessed Using 18F-FDG PET in Mice". In: *Journal of Nuclear Medicine* 54.2, pp. 259–266. DOI: 10.2967/jnumed.112.106666.

Mendes, P. and D. Kell (1998). "Non-linear optimization of biochemical pathways: applications to metabolic engineering and parameter estimation". In: *Bioinformatics* 14.10, pp. 869–883.

Meneton, P. et al. (2000). "Renal physiology of the mouse". In: *American Journal of Physiology-Renal Physiology* 278.3, F339–F351. DOI: 10.1152/ajprenal.2000.278.3.F339.

Mertens, K. et al. (2012). "In vitro 2-deoxy-2-[18F]fluoro-D-glucose uptake: practical considerations". In: *Cancer Biotherapy and Radiopharmaceuticals* 27.3, pp. 183–188. DOI: 10.1089/cbr.2011.1125.

Metropolis, N. et al. (1953). "Equation of State Calculations by Fast Computing Machines". In: *The Journal of Chemical Physics* 21.6, pp. 1087–1092. DOI: 10.1063/1.1699114.

Miao, H. et al. (2011). "On Identifiability of Nonlinear ODE Models and Applications in Viral Dynamics". In: *SIAM Review* 53.1, pp. 3–39. DOI: 10.1137/090757009.

Milo, R. and R. Phillips (2015). *Cell Biology by the Numbers*. Garland Science New York, pp. 59–62.

Moles, C.G., P. Mendes, and J.R. Banga (2003). "Parameter Estimation in Biochemical Pathways: A Comparison of Global Optimization Methods". In: *Genome Research* 13.11, pp. 2467–2474. DOI: 10.1101/gr.1262503.

Montet, X. et al. (2007). "Tomographic Fluorescence Imaging of Tumor Vascular Volume in Mice". In: *Radiology* 242.3, pp. 751–758. DOI: 10.1148/radiol.2423052065.

Morris, E.D. et al. (2004). "Kinetic Modeling in Positron Emission Tomography". In: *Emission Tomography: The Fundamentals of PET and SPECT*. Ed. by M.N. Wernick and J.N. Aarsvold. Academic Press, pp. 499–540. DOI: 10.1016/B978-012744482-6.50026-0.

Müller, T.G. et al. (2004). "Tests for cycling in a signalling pathway". In: *Journal of the Royal Statistical Society: Series C (Applied Statistics)* 53.4, pp. 557–568. DOI: 10.1111/j.1467-9876.2004.05148.x.

Muzi, M. et al. (2001). "Kinetic characterization of hexokinase isoenzymes from glioma cells: implications for FDG imaging of human brain tumors". In: *Nuclear Medicine and Biology* 28.2, pp. 107–116. DOI: 10.1016/S0969-8051(00)00201-8.

Natterer, F. (2001). "Inversion of the attenuated Radon transform". In: *Inverse Problems* 17.1, p. 113. DOI: 10.1088/0266-5611/17/1/309.

Nocedal, J. and S. Wright (2006). *Numerical Optimization*. 2nd ed. Springer-Verlag New York. DOI: 10.1007/978-0-387-40065-5.

Ollinger, J.M. and J.A. Fessler (1997). "Positron-emission tomography". In: *IEEE Signal Processing Magazine* 14.1, pp. 43–55. DOI: 10.1109/79.560323.

O'Sullivan, F. (1999). "Use of ridge regression for improved estimation of kinetic constants from PET data". In: *IEEE Transactions on Medical Imaging* 18.2, pp. 115–125. DOI: 10.1109/42.759111.

Patlak, C.S., R.G. Blasberg, and J.D. Fenstermacher (1983). "Graphical Evaluation of Blood-to-Brain Transfer Constants from Multiple-Time Uptake Data". In: *Journal of Cerebral Blood Flow & Metabolism* 3.1, pp. 1–7. DOI: 10.1038/jcbfm.1983.1.

Porter, K.R., A. Claude, and E.F. Fullam (1945). "A study of tissue culture cells by electron microscopy: methods and preliminary observations". In: *The Journal of Experimental Medicine* 81.3, pp. 233–246. DOI: 10.1084/jem.81.3.233.

Qiao, H. et al. (2007). "Kidney Modelling for FDG Excretion with PET". In: *International Journal of Biomedical Imaging* 2007.63234, 4 pages. DOI: 10.1155/2007/63234.

Rao, S., A.J. van der Schaft, and B. Jayawardhana (2013). "A graph-theoretical approach for the analysis and model reduction of complex-balanced chemical reaction networks". In: *Journal of Mathematical Chemistry* 51.9, pp. 2401–2422. DOI: 0.1007/s10910-013-0218-8.

Raue, A. et al. (2014). "Comparison of approaches for parameter identifiability analysis of biological systems". In: *Bioinformatics* 30.10, pp. 1440–1448. DOI: 10.1093/bioinformatics/btu006.

Reader, A.J. and J. Verhaeghe (2014). "4D image reconstruction for emission tomography". In: *Physics in Medicine & Biology* 59.22, R371. DOI: 10.1088/0031-9155/59/22/R371.

Reali, F., C. Priami, and L. Marchetti (2017). "Optimization Algorithms for Computational Systems Biology". In: *Frontiers in Applied Mathematics and Statistics* 3.6. DOI: 10.3389/fams.2017.00006.

Reivich, M. et al. (1985). "Glucose metabolic rate kinetic model parameter determination in humans: the lumped constants and rate constants for [^{18}F]Fluorodeoxyglucose

and [^{11}C]Deoxyglucose". In: *Journal of Cerebral Blood Flow & Metabolism* 5.2, pp. 179–192. DOI: 10.1038/jcbfm.1985.24.

Roberts, G.O., A. Gelman, and W.R. Gilks (1997). "Weak convergence and optimal scaling of random walk Metropolis algorithms". In: *The Annals of Applied Probability* 7.1, pp. 110–120. DOI: 10.1214/aoap/1034625254.

Roberts, G.O. and J.S. Rosenthal (2001). "Optimal scaling for various Metropolis-Hastings algorithms". In: *Statistical Science* 16.4, pp. 351–367. DOI: 10.1214/ss/1015346320.

Røe, K. et al. (2010). "Preclinical dynamic ^{18}F-FDG PET - tumor characterization and radiotherapy response assessment by kinetic compartmental analysis". In: *Acta Oncologica* 49.7, pp. 914–921. DOI: 10.3109/0284186X.2010.498831.

Rusten, E. et al. (2013). "Quantitative dynamic 18FDG-PET and tracer ki- netic analysis of soft tissue sarcomas". In: *Acta Oncologica* 52.6, pp. 1160–1167. DOI: 10.3109/0284186X.2012.728713.

Santarelli, M.F., V. Positano, and L. Landini (2017). "Measured PET Data Characterization with the Negative Binomial Distribution Model". In: *Journal of Medical and Biological Engineering* 37.3, pp. 299–312. DOI: 10.1007/s40846-017-0236-2.

Schmidt, K.C. and F.E. Turkheimer (2002). "Kinetic modeling in positron emission tomography". In: *The Quarterly Journal of Nuclear Medicine and Molecular Imaging* 46.1, pp. 70–85.

Scussolini, M. et al. (2017). "A physiology-based parametric imaging method for FDG–PET data". In: *Inverse Problems* 33.12, p. 125010. DOI: 10.1088/1361-6420/aa9544.

Scussolini, M. et al. (2018a). "FDG kinetics in cells and tissues: a biochemically-driven compartmental approach". In: *arXiv.org* q-bio.arXiv:1803.05025v1. URL: https://arxiv.org/abs/1803.05025v1.

Scussolini, M. et al. (2018b). "G6Pase location in the endoplasmic reticulum: Implications on compartmental analysis of FDG uptake in cancer cells". In: *Scientific Reports* (submitted).

Scussolini, M. et al. (2018c). "Reference Tissue Models for FDG–PET Data: Identifiability and Solvability". In: *IEEE Transactions on Radiation and Plasma Medical Sciences* 2.3, pp. 177–186. DOI: 10.1109/TRPMS.2018.2801029.

Shepp, L.A. and Y. Vardi (1982). "Maximum Likelihood Reconstruction for Emission Tomography". In: *IEEE Transactions on Medical Imaging* 1.2, pp. 113–122. DOI: 10.1109/TMI.1982.4307558.

Shreve, P.D., Y. Anzai, and R.L. Wahl (1999). "Pitfalls in Oncologic Diagnosis with FDG PET Imaging: Physiologic and Benign Variants". In: *RadioGraphics* 19.1, pp. 61–77. DOI: 10.1148/radiographics.19.1.g99ja0761.

Sokoloff, L. et al. (1977). "The [14C]deoxyglucose method for the measurement of local cerebral glucose utilization: theory, procedure, and normal values in the conscious and anesthetized albino rat". In: *Journal of Neurochemistry* 28.5, pp. 897–916. DOI: 10.1111/j.1471-4159.1977.tb10649.x.

Srinivas, M. and L.M. Patnaik (1994). "Genetic algorithms: a survey". In: *Computer* 27.6, pp. 17–26. DOI: 10.1109/2.294849.

Sun, X., L. Jin, and M. Xiong (2008). "Extended Kalman Filter for Estimation of Parameters in Nonlinear State-Space Models of Biochemical Networks". In: *PLoS ONE* 3.11, e3758. DOI: 10.1371/journal.pone.0003758.

Thie, J.A., G.T. Smith, and K.F. Hubner (1997). "Linear least squares compartmental-model-independent parameter identification in PET". In: *IEEE Transactions on Medical Imaging* 16.1, pp. 11–16. DOI: 10.1109/42.552051.

Tichauer, K.M. et al. (2012a). "Advantages of a dual-tracer model over reference tissue models for binding potential measurement in tumors". In: *Physics in Medicine & Biology* 57.20, pp. 6647–6659. DOI: 10.1088/0031-9155/57/20/6647.

Tichauer, K.M. et al. (2012b). "In Vivo Quantification of Tumor Receptor Binding Potential with Dual-Reporter Molecular Imaging". In: *Molecular Imaging and Biology* 14.5, pp. 584–592. DOI: 10.1007/s11307-011-0534-y.

Tichauer, K.M. et al. (2014). "Accounting for pharmacokinetic differences in dual-tracer receptor density imaging". In: *Physics in Medicine & Biology* 59.10, p. 2341. DOI: 10.1088/0031-9155/59/10/2341.

Tikhonov, A.N., A. Goncharsky, and V.V. Stepanovand A.G. Yagola (1995). *Numerical Methods for the Solution of Ill-Posed Problems*. Springer Netherlands. DOI: 10.1007/978-94-015-8480-7.

Tomasi, G. et al. (2012). "Double-input compartmental modeling and spectral analysis for the quantification of positron emission tomography data in oncology". In: *Physics in Medicine & Biology* 57.7, pp. 1889–1906. DOI: 10.1088/0031-9155/57/7/1889.

Toni, T. et al. (2009). "Approximate Bayesian computation scheme for parameter inference and model selection in dynamical systems". In: *Journal of The Royal Society Interface* 6, pp. 187–202. DOI: 10.1098/rsif.2008.0172.

Tortolina, L. et al. (2015). "Advances in dynamic modeling of colorectal cancer signaling-network regions, a path toward targeted therapies". In: *Oncotarget* 6.7, pp. 5041–5058. DOI: 10.18632/oncotarget.3238.

Tsoumpas, C., F.E. Turkheimer, and K. Thielemans (2008). "Study of direct and indirect parametric estimation methods of linear models in dynamic positron emission tomography". In: *Medical Physics* 35.4, pp. 1299–1309. DOI: 10.1118/1.2885369.

Ullah, M. (2011). "Biochemical Reaction Networks". In: *Stochastic Approaches for Systems Biology*. Ed. by P.E. Valk D.L. Bailey D.W. Townsend and M.N. Maisey. Springer New York, pp. 23–52. DOI: 10.1007/978-1-4614-0478-1_2.

van der Schaft, A.J., S. Rao, and B. Jayawardhana (2013). "On the mathematical structure of balanced chemical reaction networks governed by mass action kinetics". In: *SIAM Journal on Applied Mathematics* 73.2, pp. 953–973. DOI: 10.1137/11085431X.

— (2016). "A network dynamics approach to chemical reaction networks". In: *International Journal of Control* 89.4, pp. 731–745. DOI: 10.1080/00207179.2015.1095353.

Vander-Heiden, M.G., L.C. Cantley, and C.B. Thompson (2009). "Understanding the Warburg effect: the metabolic requirements of cell proliferation". In: *Science* 324.5930, pp. 1029–1033. DOI: 10.1126/science.11608099.

van't Hoff, J. H. (1877). "Die Grenzebene, ein Beitrag zur Kenntniss der Esterbildung". In: *Berichte der deutschen chemischen Gesellschaft* 10.1, pp. 669–678. DOI: 10.1002/cber.187701001185.

Vanzi, E. et al. (2004). "Kinetic parameter estimation from renal measurements with a three-headed SPECT system: a simulation study". In: *IEEE Transactions on Medical Imaging* 23.3, pp. 363–373. DOI: 10.1109/TMI.2004.824149.

Vogel, C. (2002). *Computational Methods for Inverse Problems*. Society for Industrial and Applied Mathematics. DOI: 10.1137/1.9780898717570.

Volterra, V. (1928). "Variations and Fluctuations of the Number of Individuals in Animal Species living together". In: *ICES Journal of Marine Science* 3.1, pp. 3–51. DOI: 10.1093/icesjms/3.1.3.

Waage, P. and C.M. Gulberg (1986). "Studies concerning affinity". In: *Journal of chemical education* 63.12, p. 1044. DOI: 10.7150/thno.5130.

Wang, G. and J. Qi (2013). "Direct Estimation of Kinetic Parametric Images for Dynamic PET". In: *Theranostics* 3.10, pp. 802–815. DOI: 10.7150/thno.5130.

Wang, Q. et al. (2015). "A reaction-diffusion simulation model of [18F]FDG PET imaging for the quantitative interpretation of tumor glucose metabolism". In: *Computational Methods for Molecular Imaging*. Ed. by F. Gao, K. Shi, and S. Li. Vol. 22. Springer New York, pp. 123–137. DOI: 10.1007/978-3-319-18431-9_13.

Warburg, O. (1927). "THE METABOLISM OF TUMORS IN THE BODY". In: *The Journal of General Physiology* 8.6, pp. 519–530. DOI: 10.1085/jgp.8.6.519.

Watabe, H. et al. (2006). "PET kinetic analysis—compartmental model". In: *Annals of Nuclear Medicine* 20.9, p. 583. DOI: 10.1007/BF02984655.

Wood, L.D. et al. (2007). "The Genomic Landscapes of Human Breast and Colorectal Cancers". In: *Science* 318.5853, pp. 1108–1113. DOI: 10.1126/science.1145720.

Xia, X. and C.H. Moog (2003). "Identifiability of nonlinear systems with application to HIV/AIDS models". In: *IEEE Transactions on Automatic Control* 48.2, pp. 330–336. DOI: 10.1109/TAC.2002.808494.

Yates, J.W.T. (2006). "Structural Identifiability of Physiologically Based Pharmacokinetic Models". In: *Journal of Pharmacokinetics and Pharmacodynamics* 33.4, pp. 421–439. DOI: 10.1007/s10928-006-9011-7.

Yeang, C.H., F. McCormick, and A. Levine (2008). "Combinatorial patterns of somatic gene mutations in cancer". In: *The Faseb Journal* 22.8, pp. 2605–2622. DOI: 10.1096/fj.08-108985.

Zanotti-Fregonara, P. et al. (2011). "Image-Derived Input Function for Brain PET Studies: Many Challenges and Few Opportunities". In: *Journal of Cerebral Blood Flow & Metabolism* 31.10, pp. 1986–1998. DOI: 10.1038/jcbfm.2011.107.

Zhou, Y., S.C. Huang, and M. Bergsneider (2001). "Linear ridge regression with spatial constraint for generation of parametric images in dynamic positron emission tomography studies". In: *IEEE Transactions on Nuclear Science* 48.1, pp. 125–130. DOI: 10.1109/23.910842.

Zhou, Y. et al. (2002). "Improved Parametric Image Generation Using Spatial-Temporal Analysis of Dynamic PET Studies". In: *NeuroImage* 15.3, pp. 697–707. DOI: 10.1006/nimg.2001.1021.

Zhou, Y. et al. (2003). "Linear regression with spatial constraint to generate parametric images of ligand-receptor dynamic PET studies with a simplified reference tissue model". In: *NeuroImage* 18.4, pp. 975–989. DOI: 10.1016/S1053-8119(03)00017-X.

Zhou, Y. et al. (2007). "Using a reference tissue model with spatial constraint to quantify [11C]Pittsburgh compound B PET for early diagnosis of Alzheimer's disease". In: *NeuroImage* 36.2, pp. 298–312. DOI: 10.1016/j.neuroimage.2007.03.004.